Nanosecond, femtosecond (fs) and fs filamentation LIBS studies combined with machine learning for the identification of plastic waste and standoff detection of HEMs

A thesis submitted to

University of Hyderabad

Towards partial fulfillment for the degree of

Doctor of Philosophy

in

Physics

By

Rajendhar Junjuri
(14ACPA05)

हैदराबाद विश्वविद्यालय
University of Hyderabad

प्रतिष्ठित संस्थान
INSTITUTION OF EMINENCE

Under the supervision of

Dr. G. Manoj Kumar

Advanced Centre of Research in High Energy Materials (ACRHEM)

School of Physics, University of Hyderabad

Hyderabad 500046, Telangana, India.

July 2020

A thesis entitled

Nanosecond, femtosecond (fs) and fs filamentation LIBS studies combined with machine learning for the identification of plastic waste and standoff detection of HEMs

Submitted to

University of Hyderabad

Towards partial fulfillment for the degree of

Doctor of Philosophy

in

Physics

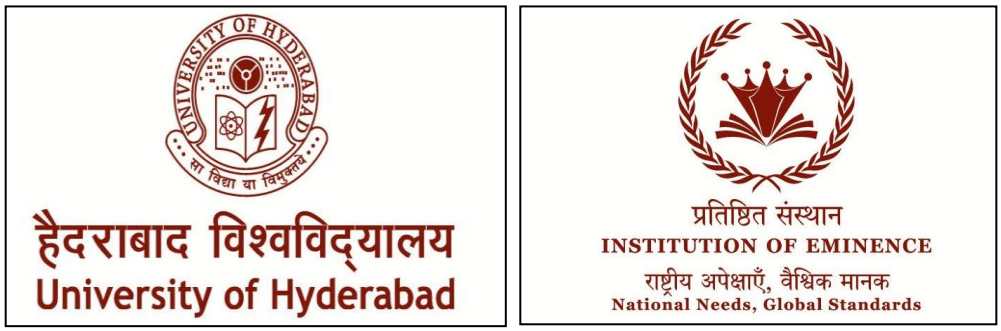

By

Rajendhar Junjuri (14ACPA05)

Under the supervision of

Dr. G. Manoj Kumar

Advanced Centre of Research in High Energy Materials (ACRHEM)

School of Physics, University of Hyderabad

Hyderabad 500046, Telangana, India.

July 2020

Dedicated to Amma-Nanna

&

Chelle- Bava

Declaration

I, **Rajendhar Junjuri**, hereby declare that the work reported in this thesis entitled **"Nanosecond, femtosecond (fs) and fs filamentation LIBS studies combined with machine learning for the identification of plastic waste and standoff detection of HEMs"** is original and has been carried out by me under the supervision of **Dr. G. Manoj Kumar**, Assistant professor in ACRHEM (School of Physics), University of Hyderabad, Hyderabad, Telangana, India, as per the Ph.D. ordinances of the University, which is also free from plagiarism. I further declare that this work has not submitted for the award of a research degree at any other University. I hereby agree that my thesis can be deposited in Shodhganga/INFLIBNET.

A report on plagiarism statistics from the University Librarian is enclosed.

30/06/2020

(Rajendhar Junjuri)

Reg. No: 14ACPA05

1/7/2020

Dr. G. Manoj Kumar

Thesis Supervisor

ACRHEM,

School of Physics,

University of Hyderabad.

Dr.G. Manoj Kumar

Advanced Centre of Research in High Energy Materials

University of Hyderabad

Hyderabad-500 046. Telangana, India

Dr. G. Manoj Kumar
Associate Professor
Tel.: + 91-40-23138837
Fax: + 91-40-23012800
E-mail: manoj@uohyd.ac.in

ACRHEM
University of Hyderabad,
Prof. C. R. Rao Road,
Gachibowli,
Hyderabad – 500 046,
Telangana, India.

Certificate

This is to certify that the thesis entitled **"Nanosecond, femtosecond (fs) and fs filamentation LIBS studies combined with machine learning for the identification of plastic waste and standoff detection of HEMs"** being submitted to the University of Hyderabad by **Rajendhar Junjuri** (Reg. No. **14ACPA05**), for the award of the degree of **Doctor of Philosophy in Physics**, is a record of bonafide work carried out by him under my supervision and is free of plagiarism.

The thesis has not been submitted previously in part or in full to this or any other University or Institution for the award of any degree or diploma.

1/7/2020

Dr. G. Manoj Kumar
(Supervisor)

Dr.G. Manoj Kumar
Advanced Centre of Research in High Energy Materials
University of Hyderabad
Hyderabad-500 046. Telangana, India

Director
ACRHEM

Director
ACRHEM

Dean
School of Physics

DEAN
School of Physics
University of Hyderabad
HYDERABAD - 500 046

CERTIFICATE

This is to certify that the thesis entitled **"Nanosecond, femtosecond (fs) and fs filamentation LIBS studies combined with machine learning for the identification of plastic waste and standoff detection of HEMs"** submitted by **Rajendhar Junjuri** bearing registration number **14ACPA05** in partial fulfillment of the requirements for the award of **Doctor of Philosophy in physics at ACRHEM, School of Physics, University of Hyderabad** is a bonafide work carried out by him under my supervision and guidance. This thesis is free from plagiarism and has not been submitted previously in part or in full to this or any other University or Institution for the award of any degree or diploma.

Further, the student has the following publications before submission of the thesis for adjudication:

1. **Rajendhar Junjuri**, S.A. Rashkovskiy, M.K. Gundawar, "Dependence of radiation decay constant of laser produced copper plasma on focal position", Physics of Plasmas, (2020). **(Chapter 3).**
2. **Rajendhar Junjuri,** C. Zhang, I. Barman, M.K. Gundawar, "Identification of post-consumer plastics using laser-induced breakdown spectroscopy", Polymer Testing, (2019). **(Chapter 4).**
3. **Rajendhar Junjuri**, M.K. Gundawar, A.K. Myakalwar, "Standoff detection of explosives at 1 m using laser induced breakdown spectroscopy", Defence Science Journal, (2017). **(Chapter 5).**
4. **Rajendhar Junjuri,** A. Prakash Gummadi, M. Kumar Gundawar, "Single-shot compact spectrometer based standoff LIBS configuration for explosive detection using artificial neural networks ", Optik, (2020). **(Chapter 5).**
5. **Rajendhar Junjuri,** M.K. Gundawar, "Femtosecond laser-induced breakdown spectroscopy studies for the identification of plastics", Journal of Analytical Atomic Spectrometry, (2019). **(Chapter 6).**
6. **Rajendhar Junjuri,** M.K. Gundawar "Laser produced plasma diagnosis for classification of optical isomers", International Conference on Fibre Optics and Photonics, OSA conference proceedings, (2016).
7. **Rajendhar Junjuri**, Tarai A.K, Dhobley A, M.K. Gundawar, "Identification of the calcified tissues using LIBS", Workshop on Recent Advances in Photonics-2019, SPIE conference proceedings. (2020).
8. **Rajendhar Junjuri**, Gummadi A.K, M.K., Gundawar, "Identification of the explosive mixtures using LIBS", International Conference on Optics & Electro-Optics-2019, Springer conference proceedings (In Press).

Also, made presentations in the following conferences:

1. **Rajendhar Junjuri,** M.K. Gundawar, **"**Rapid identification of the plastics using LIBS", 10th Euro-Mediterranean Symposium on LIBS, 2019, Czech Republic. (**Secured top 4th position globally in LIBS data analysis competition** conducted by conference organizers, results published in Spectrochimica Acta Part B: Atomic Spectroscopy).
2. **Rajendhar Junjuri,** M.K. Gundawar, "Fs and ns LIBS Studies of Postconsumer Plastics", MeghnadSaha Memorial International Symposium-cum-Workshop on LIBS, 2018. University of Allahabad, Allahabad. (**Awarded with best oral presentation**).
3. **Rajendhar Junjuri,** M.K. Gundawar, "LIBS based standoff detection of explosives", 2015, Recent Advances in optics conference, University of Hyderabad, Hyderabad (**Awarded with best poster presentation**).

The following courses have taken as part of the course work:

Course No.	Course offered at	Title of the Course	Credits	Pass/Fail
PY804	School of Physics	Advanced Electromagnetic theory	4	Pass
AC807	ACRHEM	Research Methodology	4	Pass
AC808	ACREHM	Non-linear Optics	4	Pass
AC810	ACRHEM	Introduction to high energy materials	4	Pass

1/7/2020

Supervisor,
Dr. G. Manoj Kumar,
Associate Professor,
ACRHEM, University of Hyderabad,
Hyderabad, India.

Dr.G. Manoj Kumar
Advanced Centre of Research in High Energy Materials
University of Hyderabad
Hyderabad-500 046. Telangana, India

Director,
ACRHEM,
University of Hyderabad,
Hyderabad,
India.

Director
ACRHEM

Dean,
School of Physics,
University of Hyderabad,
Hyderabad,
India.

DEAN
School of Physics
University of Hyderabad
HYDERABAD - 500 046

Acknowledgements

First and foremost, I would like to express my sincere gratitude to my supervisor, **Dr. G. Manoj Kumar,** for his exceptional guidance, motivation, and unconditional support in carrying out this research work. His passion for the research and questioning nature made me understand the basics of the underlying physics which I truly enjoyed. I consider myself blessed for getting a chance to pursue my research studies with him.

It is my pleasure to thank the present director, **Dr. V. Kameswara Rao,** and former directors of ACRHEM for their support in all aspects towards completion of this work. I also thank the Dean, School of Physics (SoP), UoH, for academic support.

I sincerely thank my doctoral committee members **Dr. P. Prem Kiran** and **Dr. N. Sriram Gopal** for their invaluable suggestions in and out of the doctoral committee meetings. I would also thank Dr. Harsha for on and off discussions.

I would like to thank the Defence Research and Development Organization (DRDO), India for providing me the financial support (through ACRHEM) all through my Ph.D.

I would like to express my gratitude for **Dr. Ishan Barman** & Mr. Chi Zhang Massachusetts Institute of Technology, USA, for the analysis of plastics using PLS-DA. A special thanks go for **Prof. Sergey A. Rashkovskiy**, Tomsk State University, Russia for making me understand the experimental results with his theoretical support.

I would like to thank, **Dr. Arnab Sarkar** & Mr. Manjeet Singh, BARC, Mumbai for providing the high-resolution spectrometer facility for analysing the various samples.

I thank **Mr. P. Sudhakar sir**, Spark institute for motivating me to be in physics by his lectures and for his constant support throughout these years.

I thank **DST –SERB** for providing the travel grant to attend the EMSLIBS conference, and I thank the **EMSLIBS organizers** for providing the financial support the accommodation. Further, I thank the **HORIBA & JNCASR,** Bangalore for selecting me for the summer school program on Raman spectroscopy. I also thank the **RRACT,** Indore for selecting me for the winter school on "Ultrahigh Intensity Laser Produced Plasmas: Physics and Applications".

I thank all the teaching staff of ACRHEM and SoP for conducting the classes and explaining the nitty-gritty things in the core subjects. I would also like to thank all the non-teaching staff of ACRHEM and SoP for their co-operation as when required.

I acknowledge Mr. M. Shiva for assisting in surface profile studies. I would like to acknowledge Ms. Reshma for assisting in Raman studies. I acknowledge Mr. Kumar & Mrs. Gomati for assisting me in TG-DTA studies.

I would like to thank my lab members, Arun Prakash, Akash Tarai, Sai Krishna. and Rohith for their support. I especially thank Arun for helping in carrying out the standoff LIBS measurements. Special thanks go to Anubham, and Dr. M. Ashwin Kumar for teaching the Matlab programming and a thorough input in learning the various aspects of the LIBS experiments and for several fruitful discussions.

I would like to thank my seniors Dr. S. Sreedhar, Dr. E. Nageswara Rao, Dr. Y. Balaji, Dr. Ch. Leela, Dr. E. Narasimha Rao, Dr. G. K and Dr. Hamad for several fruitful discussions. Special thanks go to Dr. S. A. Kalam, Dr. Sai Shiva, Dr. E. Manikanta, Dr, P. Venkateshwarulu and Dr. V. Rakesh for endless discussions which helped me in clarifying many doubts that I encountered in understanding the experimental observations.

I would like to thank my friends/roommates Dr. Kalam, Dr. Ravi Kiran, Dr. Chandu, Dr. Esitha, Damarla, Naga, Mahi, and Azmath for their help in carrying out this research work, sharing their joy and my pain in these years. Without their company and help, these years would have been much tougher. I would also like to thank my juniors/colleagues Lingam, Samuel, Yellu, Bharathi, Phani, Moses, Praveen, Deepanajan, Menchu, Sarang, Rajesh and all others for their support.

I also thank my endearing friends Bhushan, Krishna, Venu, Ramana, Johny, Gouse, Mogulappa, Jai Kumar, Bhaskar, Kiran, Jayakar, Sudha, Shiva, Venkat, Raju, Ajay, Vijay, Praveen, Sai, Naheem, Venaktesham, Rajesh, and Hari, for their motivation and support throughout my education career. Their support at all the odd times in my personal life is invaluable.

I would like to thank my **Pinni –Babai** and loving sisters **Naga & Rachana** for their unconditional love and support throughout my life.

I'm fortunate to have loving sister **Mrs. Rani** and brother in law **Mr. Ranjth** in my life. Their unconditional love, endless support, and encouragement gave me the strength to achieve my ambitions.

Most importantly I am unambiguously grateful to my loving family. I am indebted to my Father **Mr. Lingam** (He is my first teacher) & Mother **Mrs. Anjamma** for their love, support, and prayers throughout my life**.** They are my strength.

Finally, I would like to thank the almighty God for his blessings throughout my entire life.

Preface

Spectroscopy is a branch of physics that deals with the interaction of electromagnetic radiation (EM) with matter[1]. Spectroscopic studies provide deep insights into the properties of the analyte (samples/materials) considered for the investigation. It finds application in a wide range of interests such as medicine, chemistry, biology, nanotechnology, materials science, environmental studies, and physics. The invention of the laser in the early 1960s has opened up new avenues in the field of spectroscopy[2]. Laser-matter interaction has become exciting research filed which has revolutionized the different research areas like photonics, nanoengineering, semiconductor physics, plasma dynamics, chemistry, and optical physics, etc. The interaction of high-intensity laser pulse on the sample results in the formation of transient, inhomogeneous, hot, and luminous plasma also referred to as laser-induced plasma (LIP)[3]. Instantly after the formation of LIP, it expands into the surrounding medium and cools down with the emission of intense EM radiation (in $\sim$0.5 -1 μs) accompanied by the generation of a shock wave (in $\sim$3-5 μs) which immediately decays to acoustic signal (in $\sim$20-40 μs). The characteristic emission from the plasma (after $\sim$ 0.5 μs) provides the atomic elemental information of the sample and this analytical spectroscopic technique called as the Laser-induced breakdown spectroscopy (LIBS)[4, 5].

The initial LIBS experiments were carried out by Cross and Brech in 1962[6]. Radziemski et al. have critically reviewed and presented the historical development as well as the significant progress achieved in the LIBS technique[7]. A single laser pulse is sufficient to create the plasma which acts as a rich source of spectral emissions resulting in the LIBS spectrum. A typical LIBS spectrum spans over 200-1000 nm which covers the characteristic emissions starting from UV to IR. The elemental assignment of the spectral peaks can be accomplished with the aid of the 'NIST Atomic Spectra Database' [8]. The measurement of spectral line emissions provides qualitative and quantitative information about the elemental constituents of the sample. As an analytical technique, it has many advantages over other conventional atomic spectroscopic methods such as in-situ multi-elemental detection in a single shot, rapid analysis, nearly non-destructive nature, and can analyze the samples regardless of their physical state i.e. solid or liquid or gas [9]. LIBS can detect all

the elements in the periodic table as they emit light of characteristic frequencies when excited but limited only by the power of the laser as well as the sensitivity and wavelength range of the spectrograph. The unique features of LIBS are practically minimal sample preparation and the capability to perform real-time standoff/remote analysis by employing an intense pulsed laser beam on to the sample where the physical access to the sample is not possible albeit optical access can be envisaged. These key attributes make it as a promising cutting-edge technique for the concentration measurements and material identification applications.

The emission line intensity of a particular element in the LIBS spectra can be utilized for the concentration measurements with the aid of the calibration curve approach. In this method, a spectral line (at a characteristic wavelength) intensity is measured as a function of increasing the analyte concentration for preparing a 'standard calibration curve' which can be further utilized to find the concentration of the unknown sample. Alternatively, the calibration-free LIBS technique[10] can be employed to estimate the concentration of all the major and minor elements present in the sample [11] which in principle avoids the pressing need for the matrix-matched standard samples. One of the most interesting uses of LIBS is the identification/classification of material from a collection of materials of interest[12][13] using various machine learning/ multivariate algorithms. It finds the applications in different fields namely, defence [14-16], space exploration [17], archaeology [18], biology [19, 20], nuclear materials[21], medical diagnosis[22], soil analysis[23], and forensic studies[24], etc.

The present thesis mainly focuses on the identification of the high energy materials (HEMs)/explosives[25] in standoff mode and plastics waste [26, 27] in near filed using different machine learning/multivariate approaches for homeland security and environmental applications respectively. It also proposes a theoretical model for the kinetic evolution of the plasma and validates results with the experimental data in the initial chapters. Further, it discusses the exploration of fs LIBS application for the plastics identification. It also presents the spatial and temporal characterization of Cu plasma produced by fs filaments in ambient air aiming at futuristic standoff measurements for the HEMs identification.

Over the decades, various HEMs and improvised explosive devices (IED) are being used for the bomb blasts which is a major threat from the anti-social elements[25]. Thus the discrimination of HEMs and their labelling is a primary concern to every country for the safeguard of their citizens. Further, their identification also avoids illegal transport which is an immediate requirement for minimising the terrorist activities around the globe [28-31]. Moreover, identification of HEMs is a prior task at transport checkpoints and public meetings to avoid unwanted incidents which mitigate the damage to the public and their property. Post bomb analysis for the HEMs trace identification helps the forensic interrogation. LIBS can serve as an efficient labelling tool for this application owing to its intrinsic unique capability of probing the samples in standoff mode which is an immediate and primary requirement. Few research groups around the world are working towards the in situ identification of the HEM's[16, 32, 33] as well as the standoff detection[34, 35]. However, only very few works have been devoted to the standoff identification of HEMs. To the best of my knowledge, only double-pulse LIBS (DP-LIBS) configurations with big telescopic arrangements have been deployed for the standoff measurements. The utilization of the DP LIBS systems for the standoff investigation has enhanced the signal strength [36] however, the total system size is huge [37]. Hence in this thesis, a compact single-shot standoff LIBS (ST-LIBS) detection system has been developed. The preliminary studies were performed at 1 m[25] and further, it extended to a standoff distance of 6.5 m. The overall size of the developed ST-LIBS system is reduced because of the use of a single pulse laser system and a just a convex lens. Further, the cost also greatly reduces due to the usage of a non-gated compact CCD spectrometer, which is an essential factor in making a low-cost portable LIBS system. The first task of the HEMs identification is to identify whether the given sample is a HEM or not, later to label it as a specific HEM. Explosive identification poses challenges due to the wide variety of the interferent organic non HEMs. Besides that the nitro rich ambient environment leads to complex formation however it is inevitable for the standoff measurements. Hence, in the current thesis, five HEMs and nineteen organic non-HEMs were considered for the analysis and identified utilizing machine learning algorithms. Among all non-HEMs, plastics can be considered to be potentially interfering agents for the identification of HEMs as they are commonly used as transport containers/boxes in airports and public transport systems [38].

Further, the recognition of plastics waste is demonstrated as their identification is a crucial and primary step in the recycling process. Most of the LIBS studies reported in the literature have investigated the standard plastics purchased from the companies with the aid of Echelle based ICCD spectrometers and multichannel gated CCD spectrometers [39-44]. However, single-shot identification of post-consumer plastics with low-cost CCD detection systems are not explored[42]. Hence in the thesis, the performance of LIBS evaluated for the identification of post-consumer plastic waste obtained from local recycling as their identification is more relevant to the actual scenario instead of considering standard plastics purchased from the company/industry[26]. A systematic investigation has been performed with the CCD and ICCD based LIBS detection system and evaluated their performance with different machine learning algorithms in single-shot and ten shot average mode. Further, the fs LIBS is explored for the identification of plastic waste[26]. The fs filaments can propagate and deliver energies over very long distances without any diffraction effects, demonstrates it as a potential candidate for the remote sensing applications compared to the conventional ns laser pulses. Hence, the basic characterization of the fs filaments produced by different lenses has been performed.

Chapter 1 presents an overview of the atomic emission spectroscopy (AES) and the LIBS technique. It also briefly discusses the theoretical background of the LIP and LIBS. The last section presents the various LIBS data analysis methods used in the thesis.

Chapter 2 provides a comprehensive overview of the different laser sources, and spectrometers used for the LIBS experiment in the thesis work. As well as, different components deployed for the LIBS setup and the timing scheme used in LIBS studies are briefly discussed.

Chapter 3 presents a theoretical model for the kinetic evolution of the LIP. A theory of radiative relaxation mechanism is considered to explain the decay in temperature of the plasma. For this investigation, the LIBS experiment is performed on the Cu sample in the ambient atmosphere and evaluated the performance of the proposed model at three different focal positions. The initial sections of the chapter briefly discuss the plasma temperature and electron density measurement techniques along with thermodynamic equilibrium conditions. Further, the details of the proposed model are explained in the last section.

Chapter 4 is an application towards the sensing of post-consumer plastics obtained from a local recycling plant. Initially, all the samples were characterized by TG-DTA and Raman studies to evaluate their identity. Further, a systematic study was done with the aim of reducing the data acquisition and analysis time, along with the cost, size, and weight of the LIBS detection system. For this investigation, the LIBS experiments were performed in single-shot and the accumulation of ten shots mode. Also, the spectral emissions were captured by an Echelle spectrograph equipped with ICCD and a low cost, compact and portable Czerny Turner CCD spectrometer. Ratiometric and correlation analysis yielded partial discrimination. The results from PCA have shown excellent discrimination. Further, ANN has demonstrated that individual identification accuracies/rates up to ~99 % can be obtained. The data acquired with ICCD in the accumulation of ten shots have shown average identification accuracies ~97 % nevertheless, similar performance can be accomplished with the CCD spectrometer in even a single-shot acquisition. The analysis performed with the CCD detector in single-shot mode resulted in a reduction of overall time by ~ 15 compared to the ICCD. Further, the ANN analysis in conjunction with features selection based on the RF algorithm exhibited average accuracies close (only less by ~1.5 %) to the total data, albeit it drastically reduced the investigation times for the data recorded with ICCD. Furthermore, the detectors/collection system size, weight, and cost also can be reduced by ~ 10 times by employing a CCD spectrometer. Finally, the results demonstrated here can be utilized in making a compact, and low-cost LIBS system for the rapid identification (testing time only ~ 10 ms) of plastics with higher accuracies for the real-time application.

Chapter 5 discusses the development of the standoff LIBS (ST-LIBS) system for the identification of explosives using ns laser as an excitation source. Initially, the ST-LIBS experiments were performed on five explosives at 1 m distance with the Mechelle spectrometer. C/H and H/O ratios have shown a good correlation, finally, an excellent classification has been attained by employing the PCA. Further, the ST-LIBS measurements (a set of five explosives & potentially interfering nineteen non-explosives) were performed by extending the probing distance to 6.5 m. A two-lens system has been optimized and utilized for focusing the laser beam. Later a single plano-convex lens in conjunction with a small non-gated CCD spectrometer was utilized for analysing the

optical response. Further, the 2d scatter plot analysis and the results obtained from the PCA technique has demonstrated an excellent separation among the explosives as well as explosives and non-explosives. The identification accuracies of over 98 % were achieved among the explosives with the ANN algorithm. Despite the huge similarities in the spectral features of the explosives and non-explosives, the achieved false positive and false negative rates are less than 6 %.

Chapter 6 explores the extending fs-LIBS for the discrimination of plastics waste and characterization of the Cu plasma produced by different fs filament intensities. A strong positive linear correlation (Pearsons'r=0.90) is observed between the spectral features of the molecular bands CN and C_2 to the C-C bonds. PCA has been utilized for the exploratory analysis where excellent segregation was achieved. ANN model was constructed and evaluated by exploiting five different spectral windows/regions. The average identification rates obtained for all samples are in the range of 97 to 99 % depending on the spectral window. The correct prediction rates with 100 % accuracy were achieved when ten prominent spectral features were employed. Further, it presents the preliminary studies of the filamentation induced breakdown spectroscopy (FIBS) on the Cu metal target at various filament focusing conditions. The filaments of various intensities were generated with the aid of three different focusing lenses. Further, the FIBS measurements were carried out for each filament at three different positions along the length. The investigation has demonstrated that the maximum spectral line intensity for Cu plasma is attained at the central part of the filament. It also revealed that the persistence time of the spectral lines is highest for the centre of the filament.

Chapter 7 comprehends the inferences derived from the research work carried out in the thesis as well as the future plan.

References

1. W. Demtröder, "Atoms, molecules and photons", Springer**2010**.
2. W.T. Silfvast, "Laser fundamentals", Cambridge university press**2004**.
3. D.A. Cremers, and A.K. Knight, "Laser-Induced Breakdown Spectroscopy", Wiley Online Library**2006**.
4. H.R. Griem, "Principles of plasma spectroscopy", Cambridge University Press**2005**.
5. J.P. Singh, and S.N. Thakur, "Laser-induced breakdown spectroscopy", Elsevier**2007**.
6. F. Brech, and L. Cross, "Optical microemission stimulated by a ruby laser", Appl. Spectrosc, 16, **1962**.
7. L.J. Radziemski, "From LASER to LIBS, the path of technology development", Spectrochimica Acta Part B: Atomic Spectroscopy, 57, **2002**.
8. R. Junjuri, M.K. Gundawar, and A.K. Myakalwar, "Standoff Detection of Explosives at 1 m using Laser Induced Breakdown Spectroscopy", Defence Science Journal, 67, **2017**.
9. A.W. Miziolek, V. Palleschi, and I. Schechter, "Laser induced breakdown spectroscopy", Cambridge university press**2006**.
10. E. Tognoni, G. Cristoforetti, S. Legnaioli *et al.*, "Calibration-free laser-induced breakdown spectroscopy: state of the art", Spectrochimica Acta Part B: Atomic Spectroscopy, 65, **2010**.
11. Z. Hao, L. Liu, R. Zhou *et al.*, "One-point and multi-line calibration method in laser-induced breakdown spectroscopy", Optics express, 26, **2018**.
12. A.K. Myakalwar, S.K. Anubham, S.K. Paidi *et al.*, "Real-time fingerprinting of structural isomers using laser induced breakdown spectroscopy", Analyst, 141, **2016**.
13. L. Radziemski, and D. Cremers, "A brief history of LIBS: from the concept of atoms to LIBS 2012", Spectrochimica Acta Part B: Atomic Spectroscopy, 87, **2013**.
14. J.L. Gottfried, F.C. De Lucia, C.A. Munson *et al.*, "LIBS for detection of explosives residues: a review of recent advances, challenges, and future prospects", Analytical and bioanalytical chemistry, 395, **2009**.
15. R. Junjuri, A.K. Myakalwar, and M.K. Gundawar, "Standoff Detection of Explosives at 1 m using Laser Induced Breakdown Spectroscopy", Defence Science Journal, 67, **2017**.
16. A.K. Myakalwar, N. Spegazzini, C. Zhang *et al.*, "Less is more: Avoiding the LIBS dimensionality curse through judicious feature selection for explosive detection", Scientific reports, 5, **2015**.
17. S. Sharma, A. Misra, P. Lucey *et al.*, "Combined remote LIBS and Raman spectroscopy at 8.6 m of sulfur-containing minerals, and minerals coated with hematite or covered with basaltic dust", Spectrochimica Acta Part A: Molecular and Biomolecular Spectroscopy, 68, **2007**.
18. A. Giakoumaki, K. Melessanaki, and D. Anglos, "LIBS in archaeological science—applications and prospects", Analytical and bioanalytical chemistry, 387, **2007**.
19. V.K. Singh, and A.K. Rai, "Prospects for laser-induced breakdown spectroscopy for biomedical applications: a review", Lasers in medical science, 26, **2011**.
20. D. Thomas, S. Surendran, and N. Vasa, "Nanosecond laser induced breakdown spectroscopy for biofouling analysis and classification of fouling constituents", Spectrochimica Acta Part B: Atomic Spectroscopy, **2020**.
21. A. Sarkar, D. Alamelu, and S.K. Aggarwal, "Determination of trace constituents in thoria by laser induced breakdown spectrometry", Journal of Nuclear Materials, 384, **2009**.
22. M. Bonta, J.J. Gonzalez, C.D. Quarles *et al.*, "Elemental mapping of biological samples by the combined use of LIBS and LA-ICP-MS", Journal of Analytical Atomic Spectrometry, 31, **2016**.
23. J. El Haddad, M. Villot-Kadri, A. Ismaël *et al.*, "Artificial neural network for on-site quantitative analysis of soils using LIBS", Spectrochimica Acta Part B: Atomic Spectroscopy, 79-80, **2013**.

24. M.M. El-Deftar, N. Speers, S. Eggins *et al.*, "Assessment and forensic application of laser-induced breakdown spectroscopy (LIBS) for the discrimination of Australian window glass", Forensic science international, 241, **2014**.
25. M.K. Gundawar, R. Junjuri, and A.K. Myakalwar, "Standoff Detection of Explosives at 1 m using Laser Induced Breakdown Spectroscopy", Defence Science Journal, 67, **2017**.
26. R. Junjuri, C. Zhang, I. Barman *et al.*, "Identification of post-consumer plastics using laser-induced breakdown spectroscopy", Polymer Testing, 76, **2019**.
27. R. Junjuri, and M.K.K. Gundawar, "Femtosecond laser induced breakdown spectroscopy studies for the identification of the plastics", Journal of Analytical Atomic Spectrometry, **2019**.
28. S. Almaviva, A. Palucci, V. Lazic *et al.*, "LIBS for the remote detection of explosives at level of fingerprints", Optical Sensing and Detection IV, International Society for Optics and Photonics, **2016**.
29. F.C. De Lucia, and J.L. Gottfried, "Classification of explosive residues on organic substrates using LIBS", Applied optics, 51, **2012**.
30. I. Gaona, J. Serrano, J. Moros *et al.*, "Range-adaptive standoff recognition of explosive fingerprints on solid surfaces using a supervised learning method and LIBS", Analytical chemistry, 86, **2014**.
31. J.L. Gottfried, F.C. De Lucia Jr, C.A. Munson *et al.*, "Strategies for residue explosives detection using LIBS", Journal of Analytical Atomic Spectrometry, 23, **2008**.
32. J.S. Caygill, F. Davis, and S.P. Higson, "Current trends in explosive detection techniques", Talanta, 88, **2012**.
33. V. Lazic, A. Palucci, S. Jovicevic *et al.*, "Analysis of explosive and other organic residues by LIBS", Spectrochimica Acta Part B: Atomic Spectroscopy, 64, **2009**.
34. J. Laserna, R.F. Reyes, R. González *et al.*, "Study on the effect of beam propagation through atmospheric turbulence on standoff nanosecond LIBS measurements", Optics express, 17, **2009**.
35. S. Wallin, A. Pettersson, H. Östmark *et al.*, "Laser-based standoff detection of explosives: a critical review", Analytical and bioanalytical chemistry, 395, **2009**.
36. R. Ahmed, and M. Baig, "A comparative study of enhanced emission in double pulse laser induced breakdown spectroscopy", Optics & Laser Technology, 65, **2015**.
37. J.L. Gottfried, F.C. De Lucia, C.A. Munson *et al.*, "Double-pulse standoff LIBS for versatile hazardous materials detection", Spectrochimica Acta Part B: Atomic Spectroscopy, 62, **2007**.
38. Q. Wang, G. Teng, C. Li *et al.*, "Identification and classification of explosives using semi-supervised learning and LIBS", Journal of Hazardous Materials, **2019**.
39. J. Anzano, I. Gornushkin, B. Smith *et al.*, "Laser-induced plasma spectroscopy for plastic identification", Polymer engineering & science, 40, **2000**.
40. M.A. Gondal, and M.N. Siddiqui, "Identification of different kinds of plastics using LIBS for waste management", Journal of Environmental Science and Health Part A, 42, **2007**.
41. S. Grégoire, M. Boudinet, F. Pelascini *et al.*, "Laser-induced breakdown spectroscopy for polymer identification", Analytical and bioanalytical chemistry, 400, **2011**.
42. K. Liu, D. Tian, C. Li *et al.*, "A review of laser-induced breakdown spectroscopy for plastic analysis", TrAC Trends in Analytical Chemistry, 110, **2019**.
43. K. Liu, D. Tian, H. Wang *et al.*, "Rapid classification of plastics by LIBS coupled with PLS-DA based on variable importance (VI-PLS-DA)", Analytical Methods, 11, **2019**.
44. V. Unnikrishnan, K. Choudhari, S.D. Kulkarni *et al.*, "Analytical predictive capabilities of LIBS with PCA for plastic classification", RSC Advances, 3, **2013**.

Abbreviations

LIP	Laser Induced Plasma
LIB	Laser induced breakdown
LIBS	Laser induced breakdown spectroscopy
ST-LIBS	Standoff Laser- Induced Breakdown Spectroscopy
DP-LIBS	Double Pulse- Laser Induced Breakdown Spectroscopy
CF-LIBS	Calibration Free- Laser Induced Breakdown Spectroscopy
AES	Atomic Emission Spectroscopy
XRF	X-Ray Fluorescence
ICP	Inductively Coupled Plasma
EDS	Energy-Dispersive X-Ray Spectroscopy
MIP	Microwave-Induced Plasma
DCP	Direct-Current Plasma
NIR	Near-Infrared Spectroscopy
TE	Thermodynamic Equilibrium
LTE	Local Thermodynamic Equilibrium
IB	Inverse Bremsstrahlung
Fs/fs	Femtosecond
Ps/ps	Picosecond
Ns/ns	Nanosecond
RSD	Relative Standard Deviation
SNR	Signal To Noise Ratio
PCA	Principal Component Analysis
ANN	Artificial Neural Network
RF	Random Forest
KNN	K-Nearest Neighbour
PLS-DA	Partial Least Squares Discriminant Analysis
SIMCA	Soft Independent Modelling of Class Analogy
SPA	Successive Projection Algorithm
ROC	Receiver Operating Characteristic
GA	Genetic Algorithm
SW	Stepwise Formulation
VI	Variable Importance
IG	Information Gain
RDR	Residual Discriminatory Region
PCs	Principal Components
TP	True Positive Rate
FN	False Negative Rate
TN	True Negative Rate
FP	False Positive Rate

RGA	Regenerative Amplifier
CPA	Chirped Pulse Amplification
ICCD	Intensified Charge-Coupled Device
CCD	Charge Coupled Device
LTSD	Lens to Sample Distance
FWHM	Full Width at Half Maximum
IRICS	International Resin Identification Coding System
TG-DTA	Thermogravimetric Differential Thermal Analysis
ATS	Accumulation of Ten Laser Shots
SS	Single Shot
NA	Numerical Aperture
BFL	Back Focal Length
F#	F-Number
ACCR	Average of Correct Classification Rate
PVC	Polyvinyl Chloride
HIP	High Impact Polystyrene
PP	Polypropylene
LD/LDPE	Low Density Polyethylene
ABS	Acrylonitrile Butadiene Styrene
PS	Polystyrene
HD/HDPE	High Density Polyethylene
PET	Polyethylene Terephthalate
PC	Polycarbonate
PPCP	Polypropylene Co-Polymer
PU	Polyurethane
PTFE	PolyTetraFluoroEthylene
POM	PolyOxyMethylene
PMMA	PolyMethylMethacrylate
PA	Polyamide
POE	PolyOxyEthylene
NTP	Novatein Thermoplastic Protein
RDX	1, 3, 5-Trinitroperhydro-1, 3, 5-Triazine
HMX	1, 3, 5, 7-Tetranitro-1, 3, 5, 7-Tetrazocane
TNT	2-Methyl-1, 3, 5-Trinitrobenzene
CL-20	Hexanitrohexaazaisowurtzitane
AN	Ammonium Nitrate
NTO	3-Nitro-1, 2, 4- Triazole-5-One
DNT	2, 4- Dinitrotoluene
HEMs	High Energy Materials
IEDs	Improvised Explosive Devices

CHAPTER 1 : Introduction

This chapter presents an overview of the atomic emission spectroscopy (AES) and laser induced breakdown spectroscopy (LIBS) technique. It also briefly discusses the theoretical background of the laser induced plasma (LIP) and LIBS. The last section presents the various LIBS data analysis methods such as 2D scatter plot approach, principal component analysis (PCA), Artificial neural network (ANN), and Random Forest algorithm.

1.1 Introduction

Atomic emission spectroscopy (AES) is an analytical technique that can find applications in a wide range of disciplines [1-3]. It is the study of radiation emitted by the excited atoms and ions where each element has characteristic emission wavelength(s). Different excitation sources such as sparks, arcs, flames, and plasma are being used depending on the application of interest. The following are the basic steps involved in the elemental analysis [4]

1. Vaporization/atomization of the given sample
2. Excitation of the atoms/ions
3. Detection of the radiation from the excited species
4. Utilize the radiation for the concentration measurements or material identification

Various AES techniques such as X-ray fluorescence (XRF), inductively coupled plasma (ICP-AES), energy-dispersive X-ray spectroscopy (EDS), microwave-induced plasma (MIP-AES), direct-current plasma (DCP-AES), and arc/spark-AES are being utilized in different applications[1-3, 5]. Every technique has its own advantages and limitations, for example, ICP –AES has excellent analytical performance, however, it is destructive where the sample needs to be dissolved in acids that are hazardous for the environment too. Further, atomization and excitation sources need to be different for analyzing the samples. Similarly, most of the techniques need rigorous sample preparation methods, time-consuming, and require significant laboratory support facilities.

When a laser pulse of sufficient intensity focused onto the surface of a sample, results in instantaneous thermalization, & evaporation of the minute amount material, which leads to the formation of the plasma [6-8]. Plasma is a state of matter constituted by electrons, ionized, and neutrals species. The spectroscopic analysis of the optical emissions from the plasma called as laser induced breakdown spectroscopy (LIBS). In principle, LIBS technique is similar to that of other conventional plasma-based AES methods, such as ICP-AES, MIP-AES, and DCP-AES. However, in LIBS, the sample does not need to be transported into the plasma source as compared to others; indeed the plasma produced on the sample surface makes it a simpler method because the atomization/vaporization and excitation processes are performed by a laser pulse in a single step[8, 9]. In recent times, LIBS technique has gained the attention of the international research community owing to its inherent advantages like little sample preparation, nearly non-destructive nature, and single-shot multi-elemental detection. All these characteristics together have enabled LIBS as a more robust technique for real-time, in situ, and standoff measurements compared to other conventional laser-based spectroscopic techniques. The stochastic nature of the plasma and matrix effects is the limitations in contrast to conventional techniques. However, numerous studies are under investigation to explore the possibilities to overcome these limitations and further to improve the analytical capabilities of the LIBS technique [10].

1.2 Processes involved in laser induced breakdown

Laser-induced breakdown of the material occurs when the intensity of the focused laser beam exceeds the threshold value which depends on the nature of the material, wavelength, and duration of the laser pulse[11, 12]. Typically, the breakdown threshold is of the order of $GWcm^{-2}$. This phenomenon involves a complex interaction of the light with the matter leading to the ablation of material and formation of plasma[13]. The process of laser ablation i.e. the process of ejection of material from the sample surface upon the interaction of the laser pulse with the matter is still under investigation [14-17]. Further, the generation and evolution of LIPs depend on numerous factors such as material properties (conductivity, hardness, and physical state, etc.), parameters of the laser (pulse duration, fluence, rep rate, and wavelength, etc.), laser beam focusing conditions,

and ambient gas properties (reactivity, pressure, conductivity, and density, etc.)[18-20]. The pictorial representation of the laser ablation, formation, and growth of the LIP with the interaction of the ns and fs laser pulses are shown in Fig. 1.1[21]. The laser ablation phenomenon happens over several orders of magnitude in time, starting from fs (electronic absorption of incident laser pulse) to ms (particle condensation). The formation of LIP through the laser ablation involves the following processes: laser absorption, bond breaking, plasma formation, plasma expansion, emission of radiation, and particulate formation[7].

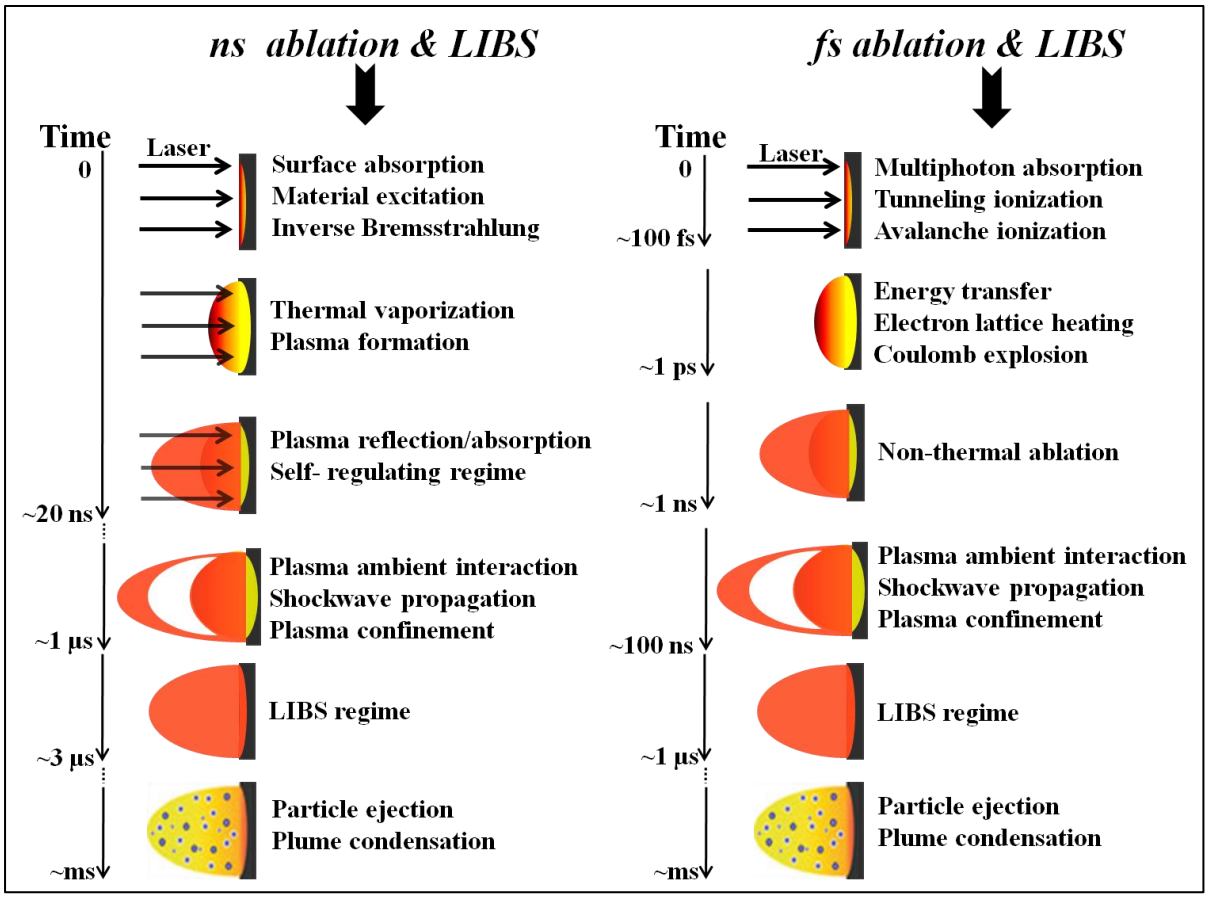

Fig. 1.1. Various processes involved in LIP during and after the interaction of laser pulse (ns & fs) with the matter. (Figure reproduced from Harilal et al [21]).

Drastic differences between fs and ns laser ablation processes are observed due to the significant differences in pulse duration. In the case of ns laser, seed electrons in the focal region of the laser pulse initiate the absorption process at fs time scales[22], and further, it is followed by the inverse Bremsstrahlung (IB) absorption process. IB absorption is the predominant mechanism responsible for laser absorption with matter[23], and IB absorption coefficient is given as

$$\alpha_{IB}(cm^{-1}) = 1.37 \times 10^{-35} \lambda^3 \, N_e^{\,2} \, T^{1/2} \tag{1.1}$$

where λ is the "wavelength of the laser(μm)", N_e is "electron density (cm^{-3})" and T is "plasma temperature (eV)".

As seen in equation 1.1, the IB absorption predominantly depends on the laser wavelength and varies as a function of λ^3. Apart from that, photoionization also contributes to the absorption albeit at higher irradiance and lower wavelengths. Approximately ~ 100 ps after laser energy deposition, the surface temperature of the solid increases and lead to a sequential phase transition from solid to liquid and liquid to vapor. i.e the thermal vaporization is the dominant mechanism in ns laser ablation ($\sim 10^8$- 10^9 W/cm^2). Further, the plasma shielding process could be possible at higher irradiance during the formation of LIP with ns laser as irradiance source where the rising part of the laser pulse creates the plasma and trailing part gets absorbed by the LIP. Plasma shielding prevents the interaction of the later part of the laser pulse with the sample hence results in a lower ablation rate nevertheless; it reheats the plasma and leads to the rise in plasma temperature and background of the LIBS signal. Further, the reheating also increases the lifetime of plasma and provides the emissions for a longer time with higher intensity.

Fs ablation (at intensities $> 10^{13}$ W/cm^2) is governed by various mechanisms depending on the availability of free electrons i.e. Multiphoton absorption, impact ionization, avalanche ionization, and Coulomb explosion. The multi-photon absorption is a non-linear process and its absorption coefficient is given by the following equation

$$\alpha_{MP}(cm^{-1}) = \sum_n 7.9 \times \left(\frac{E_n}{h\nu}\right)^3 \left(\frac{\chi}{E_n}\right)^{1/2} N_n \tag{1.2}$$

where E_n and N_n are the "energy" and "number density of the excited state n", and χ is "ionization potential of the atom"

In the case of metals, the free electron can directly absorb the laser energy and creates hot-electron plasma whereas in the case of semiconductors and dielectrics aforementioned mechanisms are responsible for the generation of the plasma. In the strong-field regime, the superposition of the laser electric field and the nuclear Coulomb field results in an oscillating finite potential barrier through which bound electrons can tunnel, thus escaping

the atom. Therefore, at higher intensities, Coulomb explosion leads to the ablation of the material which is a non-thermal melting process. This process can be investigated by x-ray diffraction and time-resolved reflectivity methods [24]. The duration of the fs pulse is much shorter than characteristic 'relaxation times' such as 'electron heat conduction time', 'electron-to-ion energy transfer time', and consequently the hydrodynamic/expansion time. Indeed, all of these mechanisms typically happen in the order of several ps after the termination of the laser pulse. Hence, the fs ablation greatly reduces the thermal damage as well as the heat-affected zone on the sample surface due to the negligible heat conduction. Consequently, fs laser pulses offer the better the spatial resolution compared to ns pulses. The latest investigations revealed that the submicron scale fs laser ablation can be performed for the chemical analysis[25].

Plasma shielding is negligible in fs LIBS compared to ns and results in the formation of the lower temperature plasma. The absence of plasma shielding favors the formation of molecular spectra with lower background whereas atomization and ionization are dominant for the ns LIBS. Smaller sized crater formation with reduced thermal effects (negligible heat transfer from the irradiated area), minimal plasma air interaction, and low ablation threshold are advantages in fs ablation. These attributes make it is as a promising technique for various applications including LIBS such as nanoparticle generation, laser direct writing, and pulsed laser deposition[26-28].

1.3 Radiation emitted from the LIP

The evolution of the LIP is accompanied by intense electromagnetic radiation in ultraviolet-visible and near-infrared regions and also by the generation of sound and shock waves [29-31]. The radiation comprises the emissions from the continuum and discrete lines of excited atoms, neutrals, ionic, and molecular species present in the plasma. The wavelength(s) of the emitted light represent(s) the elemental constituents of the given sample. The radiation has a major contribution from the continuum emission at the early stage of plasma evolution[32]. It is observed due to the free–free (Bremsstrahlung emission) and free-bound transitions[33]. The deceleration of electron in the vicinity of another coulomb filed emits the Bremsstrahlung radiation. Whereas, free-bound transitions occur when a free electron recombines into the bound states of an ion which is also referred to as

radiative recombination. The continuum emission can be avoided while recording the spectra with gated detectors. As mentioned earlier, the continuum is prevailed in the ns LIBS compared to the fs LIBS due to the reheating caused by the plasma shielding process.

As the plasma evolves the continuum decreases and line radiation becomes predominant. It is observed due to the bound-bound transition. i.e. the de-excitation events of the ions and neutral species in the plasma emit characteristic line radiation. Further, the emission of molecular features (mostly CN & C_2) also observed in the spectra of organic samples such as plastics and explosives. Various studies have demonstrated that CN emissions are observed due to recombination and C_2 species are formed due to fragmentation of the C=C dimers[34-36].

All these spectral features are in combination with different analysis methods are useful for a variety of applications. The main motive of applying the LIBS technique for the real-world application is

1. To find a certain element is present in the sample or not.
2. Quantitative measurements of the analyte in a sample – for the estimation of concentration.
3. Identify the class/type of the material – for the classification of the samples.

The present thesis focuses on the identification of the materials/samples for the different applications. In the next sections, various data analysis methods utilized in the present thesis are discussed in detail.

1.4 LIBS data analysis methods

LIBS being atomic emission spectroscopy method, it is challenging to work with organic samples like plastics, amino acids, and explosives, etc., as their LIBS spectra look similar and complicate their identification. It is attributed to sharing similar elemental constituents (C, H, N, and O) with a different stoichiometric composition. However, the problem pertinent to the classification can be tackled by the chemometrics/multivariate/ machine learning approaches. It meets the requirements of a LIBS analyst for the classification as well as quantification related applications. The rich spectral information available in the LIBS spectra combined with bi variate[37, 38] and multivariate analysis [39] has proved it as

an efficient tool in sorting and discriminating the variety of classes of the materials. The following multivariate methods such as principal component analysis (PCA)[40, 41]2, partial least squares discriminant analysis decision (PLS-DA)[42, 43], soft independent modelling of class analogy (SIMCA)[44], random forest and artificial neural networks (ANN) [38, 45, 46], etc., have been widely utilized for the identification of materials in different applications. For the present thesis, 2D scatter plot analysis, PCA, ANN, and RF methods are used for the classification of the samples where the first two are unsupervised and remaining are supervised in nature. The unsupervised methods can be used as data exploratory approaches whereas the supervised algorithms learn from labelled training data, and predicts the outcomes for unseen data for the real-time application.

1.4.1 2D Scatter plot analysis

The 2D scatter plot approach visualizes the clusters present in data distributed among the scattering space defined by the two specific spectral lines. It explores the data in lower dimensional space by plotting the intensity of the one spectral line on the x-axis and the other spectral line intensity on the y-axis as shown in Fig. 1.2. The 2D[39] and 3D[47] scatter plot approaches were employed in literature to discriminate the bacteria and explosive samples respectively. The 2D hyperspace visualization exploits the essential information of the total data which also creates a simple and reduced way of graphical representation. However, the performance of the analysis rests on the spectral features considered for the analysis. The line selection can be performed based on the prior knowledge of the spectral emission acquired from the plasma.

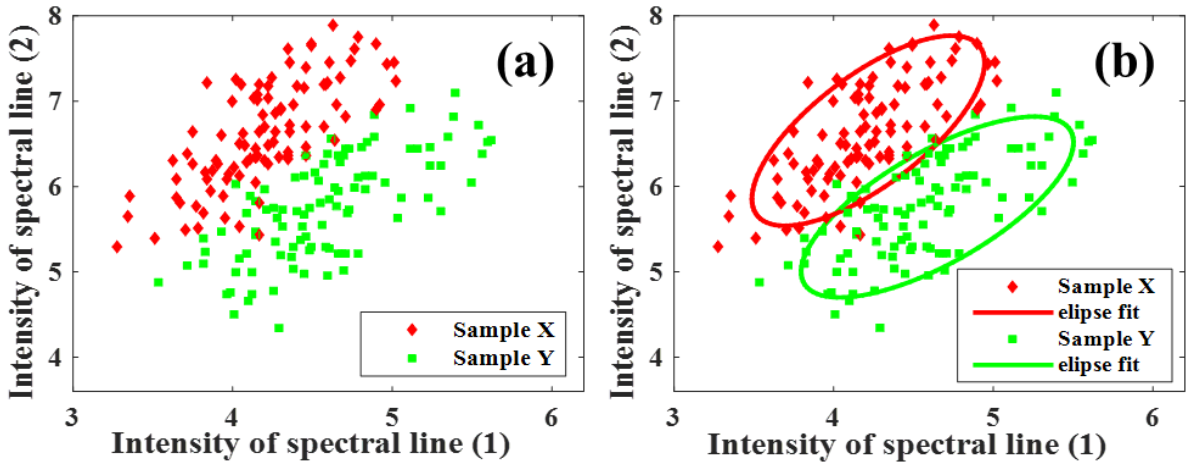

Fig. 1.2. a) 2D scatter plot visualization. b) With the ellipse fit around the clusters.

For example, it is better to avoid the spectral lines of impurities, self-absorbed emissions, and the lines which have a chance to interfere with the spectral lines of the other elements, etc. Further, a numerical/statistical parameter, residual discriminatory region (RDR) has been defined for the quantitative evaluation of the discriminatory power of a 2D scatter plot method for a set of two samples[47, 48]. It is the sum of the ratios of the area of the overlapped region to the area of the fitted ellipse of the two samples respectively as given equation 1.3.

$$RDR = \frac{A_o}{A_x} + \frac{A_o}{A_y} \tag{1.3}$$

Where, A_X, A_Y, and A_o represent the area of the fitted ellipse of sample X, Y, and overlap region between the X &Y samples respectively.

The least-square fitting method has been employed to find the best fit of the ellipse for the scattered data of each sample with a confidence of 95 % as shown in Fig. 1.2(b). The area estimated from the ellipse fit has been utilized for finding the RDR value. In general, the range of values of the RDR parameter spans over 0 to 2. A value of close to zero indicates very good separation among the clusters and can be considered as an efficient classification. On the contrary, an RDR $\sim$2 represents the complete ($\sim$100 %) overlap of both the clusters.

1.4.2 Principle component analysis

Principle component analysis (PCA) is one of the widely employed chemometric technique which finds the patterns buried in input data in a large number of variables[49]. It is a simple nevertheless powerful visualization tool that explores the data in a lower dimension space and has the capability of clustering of several materials[50]. A recent article reviewed and highlighted the extensive use of PCA in combination with the LIBS technique for the discrimination of the materials in different applications such as explosives identification[38, 44, 51], soil analysis[52], plastics sorting[41, 43] and alloys discrimination[53], etc [54]. The prime objective of the PCA is dimensionality reduction of a given dataset which initially comprises a huge number of variables/features. In principle, dimensionality reduction can be accomplished by orthogonal transformation of a set of

data into the new coordinate system called as principal components (PCs) and the new variables in it treated as scores. The PCs are the directions along which the variation in the data is maximum. The detailed flowchart of the PCA algorithm is shown in Fig. 1.3.

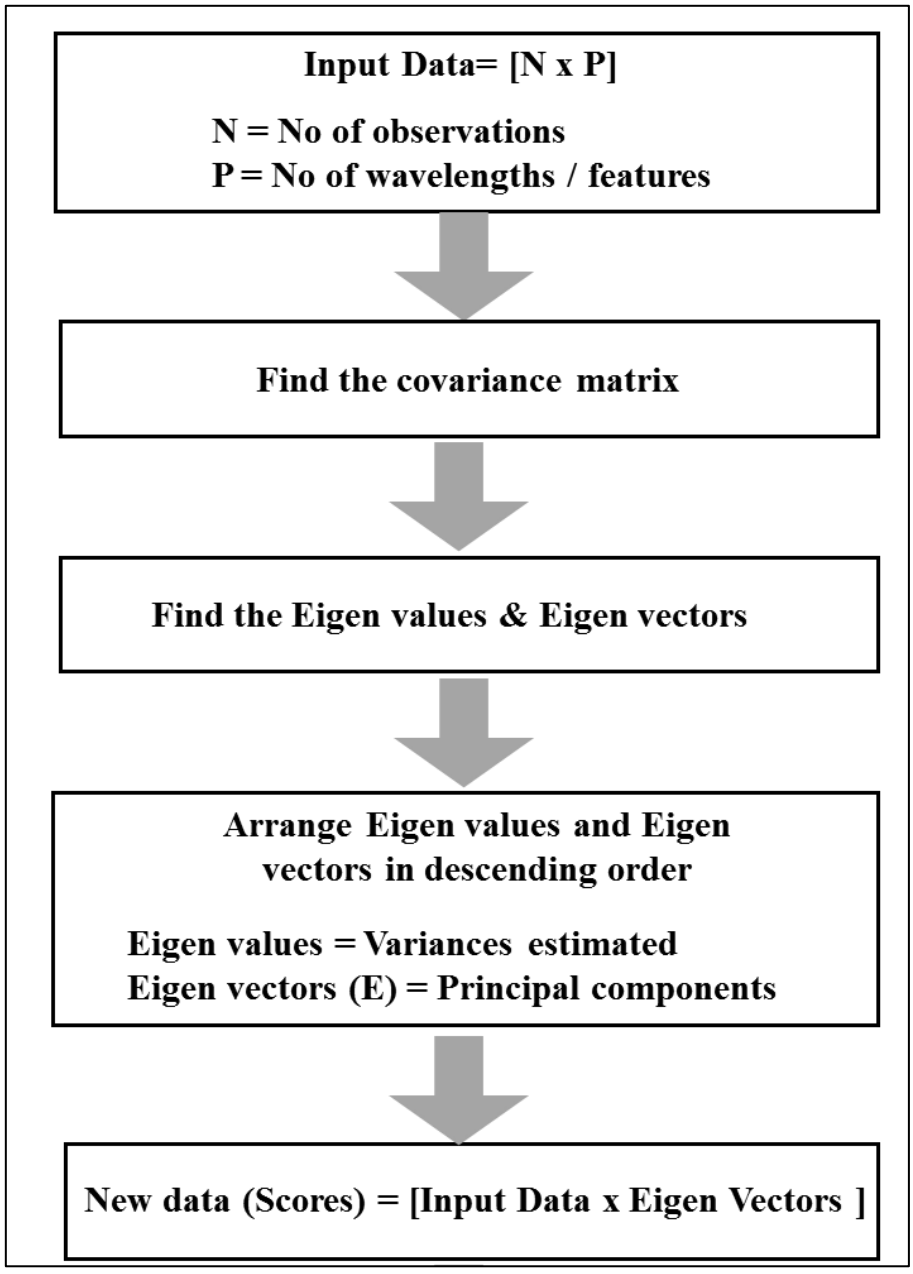

Fig. 1.3. Flow chart representation of the PCA algorithm.

PCA demonstrates the classifying capability by correlating dominant spectral features with the output PCs. However, it should worth considering that most of the variance present in input data can be retained by the first few PCs only irrespective of the dimensionality reduction[40, 42]. For example, the pictorial representation of the dimensionality reduction in layman interpretation is shown in Fig. 1.4.

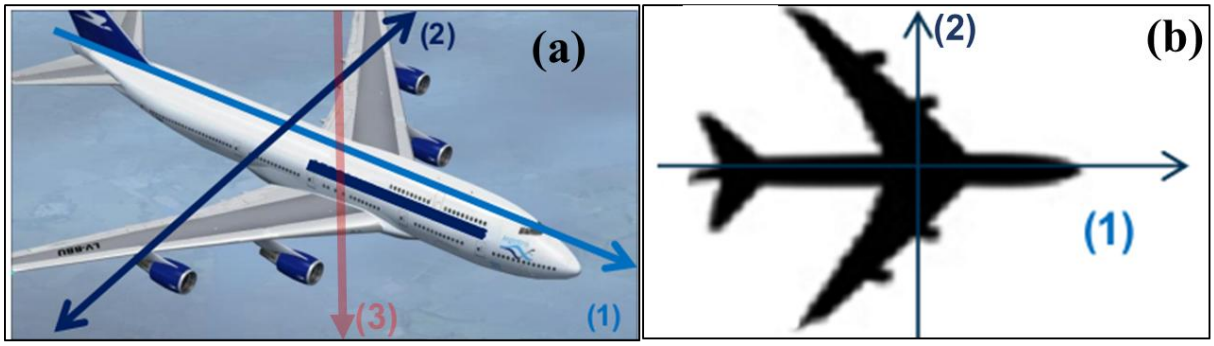

Fig. 1.4. The pictorial representation of dimensionality reduction in layman interpretation. Areoplane visualization in a) 3D space and b) 2D space.

It visualizes the image of an areoplane in 3d space (Fig. 1.4(a)) and 2d space (Fig. 1.4(b)). It is evident from the figure; the image can be still identified as an areoplane even after transformation/rotation from 3D to 2D space. i.e the information is still preserved even after the reduction of one dimension. The rotation of axis is used in various disciplines of physics such as the moment of inertia tensor for rigid body dynamics, polarizing ellipsoid for Raman spectroscopy, and polarizability ellipsoid for double refraction, etc. Further, the PCs are ordered/aligned in a way such that the maximum variance is explained by the first PC and followed by the subsequent PCs. By utilizing a few PCs, each sample can be represented by relatively few variables instead of thousands and it is called as a score plot. The score plot makes it possible to visually assess the similarities and differences between samples and determine whether it can be clustered or not for the classification.

1.4.3 Artificial neural network

Artificial neural network (ANN) is a non-parametric supervised learning algorithm, exploited in the identification and pattern recognition applications such as weather forecasting, process control, and image identification, etc. [55]. In LIBS community, it has been extensively utilized for the classification of a variety of samples namely, pharmaceutical tablets[56], bacteria[55], explosives[57], isomers[44] and plastics[58] and quantification of elements[59] in the diverse field of applications. It serves as an information processing paradigm analogous to the way the biological nervous system computes the information. It develops a nonlinear mathematical model by the capability of achieving meaningful relationships among the input and target variables through

supervised learning. The architecture of ANN comprises a huge number of interconnected processing elements called neurons which are fundamental for the building and operation of a neural network. In biological system architecture, the units communicate with each other by the synapse. This is analogous to a bridge/junction which can transmit the chemical signals converted from electrical impulse/signals to neighboring nod[60]. In ANN, weight (interneuron connection strengths) and bias stimulated as a synapse. Every synapse connects the one unit of a particular layer to the second unit of another layer. It should be noted that the neurons of a specific layer cannot be linked together. ANN has the capability to organize the network by changing the interneuron connection strengths (weights) by the knowledge acquired through the learning process[61].

Numerous theoretical and experimental works have been demonstrated that a single hidden layer of ANN is adequate for approximating any complex nonlinear-function [62, 63]. Hence for the thesis, a three-layer neural network with the feed forward-backward propagation approach has been utilized[64]. In the first step, the LIBS data was fed to the first layer of the network as the input. The output obtained from the first layer was fed to the second layer which is also referred to as a hidden layer. Further, the extracted information is accessed by the output layer which is in charge to generate the prediction of the analyte. i.e. third layer. The typical schematic of the three-layer ANN model is shown in Fig. 1.5.

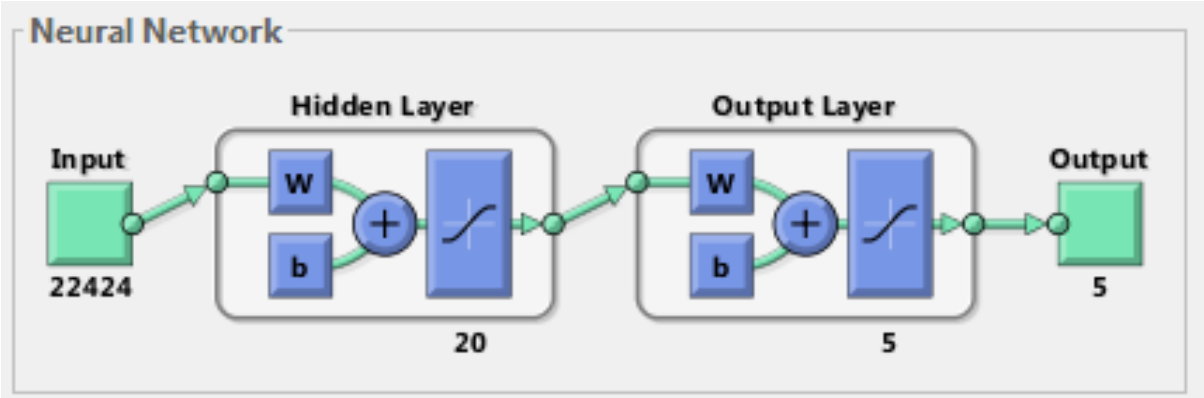

Fig. 1.5. Typical schematic of the three-layer ANN model. It is an interface of the ANN algorithm in MatLab environment.

The input contains the 22424 variables/wavelengths (it may change depending on the requirement) and target class labels for each sample. A class label is a discrete attribute

allotted for the sample in binary form for the classification approach. Fig. 1.5 contains a hidden layer with 20 neurons, and the number of neurons can be optimized for better performance. The output '5' corresponds to five samples. Initially, the data set was divided into training (70%), testing (15 %), and validation (15%) sets. This random selection of the input data in each iteration minimizes the biasing and can lead to better identification accuracy. The training dataset used for the training of network and predictive ability of the network is estimated by the validation dataset. In the first iteration, the forward propagation approach of the algorithm initiates with random values of the bias and weights. Then, the output predicted by the ANN is compared with the actual input and the corresponding error has been utilized in a back-propagation approach for adjusting the values of the weights and bias for the second iteration. This process continues until the error converges to a minimum threshold value as shown in Fig. 1.6. Finally, the test data evaluates the performance of the trained network.

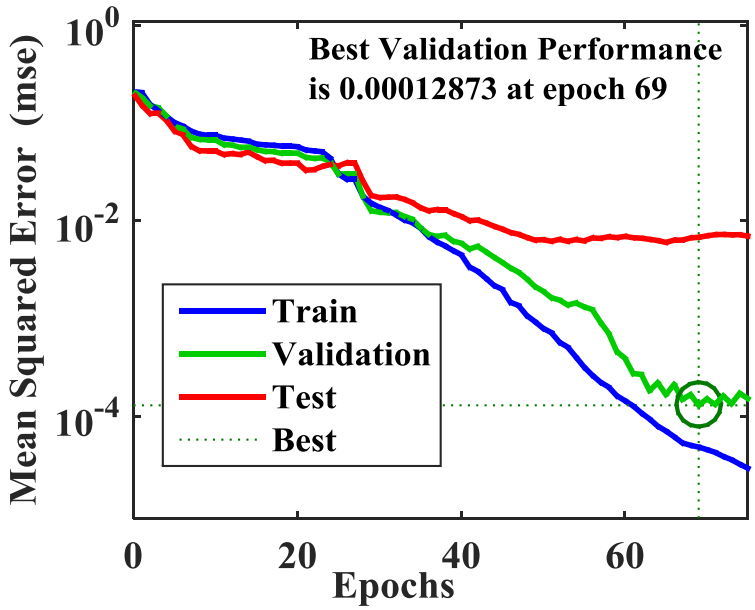

Fig. 1.6. Performance plot of the trained ANN model. The circle in the plot represents the best validation at 69 epoch.

The final predictive output of the ANN is given in the form of a confusion matrix. It is a table that represents the performance of the classification model quantitatively. The confusion matrix generated for the 1000 observations (100 for each sample, a total of five samples) with 22424 variables as input is shown in Fig. 1.7. The diagonal elements in green color represent the correct rate of each sample whereas off-diagonal elements represent the

miss-classification rate. For example, in the case of 1st sample, the correct labelling rate is 100 % and the miss-classification rate is 0 % whereas it is 99 % and 1 % respectively for the 3rd sample as shown in Fig. 1.7.

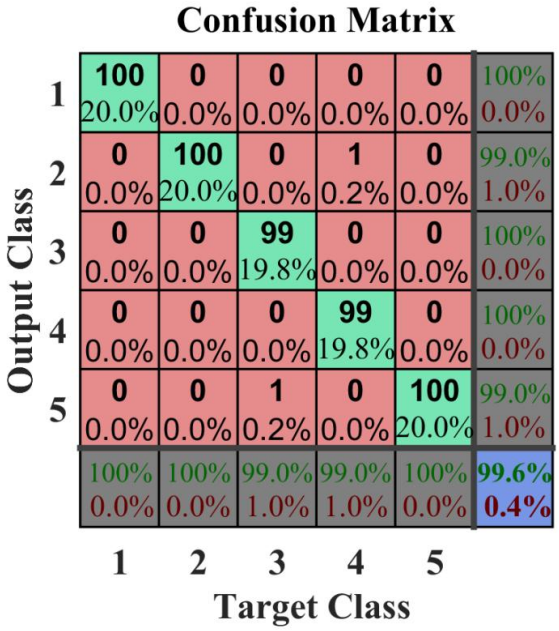

Fig. 1.7. Confusion matrix generated by the ANN. A total of 1000 spectra (five samples with each 100 spectra) were given as input to the model.

Further, few decision making statistical parameters can be derived from the confusion matrix. It helps in minimizing the arbitrariness and to evaluate the performance of the ANN[40, 57]. Sensitivity and specificity are the two performance metrics used for the evaluation process. Sensitivity is defined for the group/class 'A' as the - number of samples identified as Class 'A' divide by the total number of actual samples belongs to Class 'A'.

$$\text{Sensitivity} = TP/(TP + FN) \tag{1.4}$$

Where TP is the true positive rate and FN is the false negative rate

Specificity is determined as the number of samples identified as not belonging to Class A/ number of actual samples not belonging to Class A.

$$\text{Specificity} = TN/(TN + FP) \tag{1.5}$$

Where, TN is the true negative rate and FP is the false positive rate

Accuracy is an important global metric for the decision making in discrimination procedure which is defined as the

$$\text{Accuracy} = (TP + TN)/(TP + TN + FN + FP) \tag{1.6}$$

Precision is the ratio of the number of true positives to the total number of positive test results.

$$\text{Precision} = TP/(TP + FP) \tag{1.8}$$

The increase in the input data size will lead to more complexity for the ANN, as well as the increase in computing time. However, this problem is tackled by selecting the proper spectral input to chemometric/multivariate methods. An efficient identification of explosives[65], geological samples[44], and plastics[59, 66] has been already demonstrated in literature with the aid of feature selection. In the next section, the Random forest is considered for the feature selection algorithm.

1.4.4 Random forest (RF)

The LIBS spectrum of plastic is shown in Fig. 1.8 (a). It is noticed from the figure, all the variables (data points) generated in the spectra are not significant for example, 220-245 nm and 590-650 nm spectral region is noise only and not contributing to any of the emission lines. Consequently, it would be beneficial to restrict the analysis to only some selected features of interest by eliminating irrelevant and unreliable variables for better outcomes. The number of variables required for efficient analytical performance can be chosen by the various feature selection methods. It can be done manually by creating an apriori subjected to the expertise on the analytical methods or employing any well-established multivariate statistical techniques that are reported in the literature [40, 44, 67, 68]. Numerous studies have been reported in LIBS literature for the classification of various samples based on different feature selection algorithms such as successive projection algorithm (SPA), genetic algorithm (GA), stepwise formulation (SW) and random forest (RF), etc, [40, 44, 67, 68]. These methods resulted in achieving the correct labelling rates as similarly as 100 % data deployed for the classification. Apart from the efficient classification, it has also demonstrated that the computational workload can be reduced by 10 -100 times[68] depending on the samples and section algorithms.

For the present thesis, the method of variable importance (VI) obtained from the RF algorithm has been chosen for the feature selection. VI represents the statistical significance of each variable in the data. RF is an ensemble-based decision tree algorithm proposed by

Breiman. It is not only used for finding the significant variables present in the entire dataset but also for regression and classification applications[69]. It precisely finds the pattern buried in the input data that replicates the useful information by properly guiding and training through supervised learning. The choice of growing 'number of trees' in RF depends on the application of interest. The trees grow independently and randomly by selecting the "bootstrapped dataset". i.e. In the bootstrap method, the observations randomly selected while building the tree and some of the observations are removed. Further, the "removed observations" are replaced by repeating the other observations. The removed samples are called as "out of bag sample" and it is used for estimating the efficiency of the grown decision tree.

Further, each tree is grown by selecting a variable and corresponding information gain (IG) is estimated. Similarly, the IG is estimated for all the variables, and a variable with the highest IG is considered as the root node while building the tree. At each node, it spits into further based on the IG estimation without considering the variable corresponding to the root node. This process repeats until the leaf node reaches. VI is estimated by the sum of the decrease in error when split by a variable. It should not that the variables are randomly selected during the construction of each tree. The VI acquired from the developed RF model possesses a huge impact on opting for the input variables for the analysis[67]. The VI estimated for the spectra of plastic is shown in Fig. 1.8 (b).

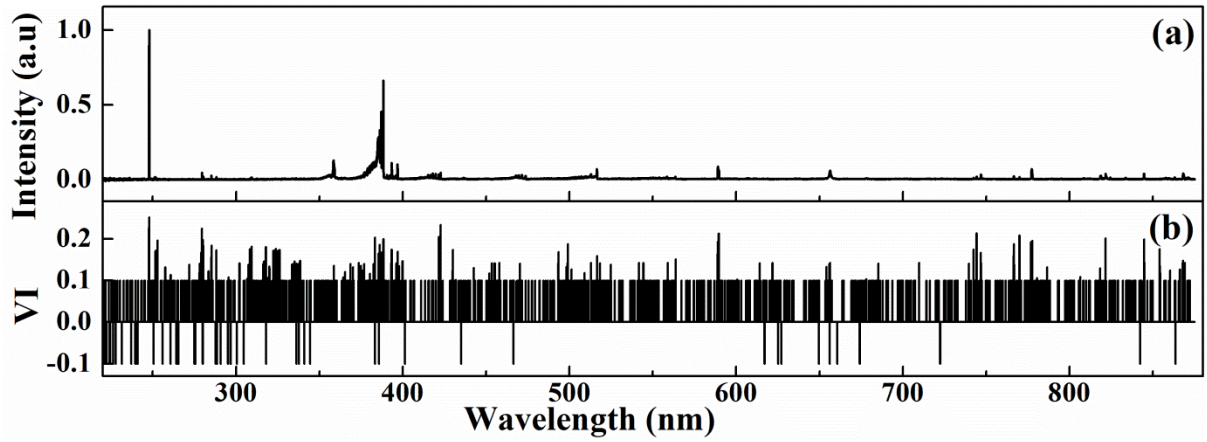

Fig. 1.8. a) LIBS spectra of a plastic. b) The respective variable importance (VI) estimated by the RF model using 50 trees.

The highest value of VI in the plot corresponds to the most significant variable of the total dataset and the variables with lower value are trivial. It is evident from Fig. 1.8 (b), ~93.6 % of total variables are having zero VI value, and can be easily eliminated from the dataset

without any ambiguity. Moreover, selecting input variables based on VI can avoid overfitting which can be utilized in improving the performance of the multivariate technique. As the true variables are more important and efficient compared to the noisy ones considered for the analysis. Also, employing VI for the multivariate analysis can significantly reduce the computational times (training and testing) as well as data storage requirements.

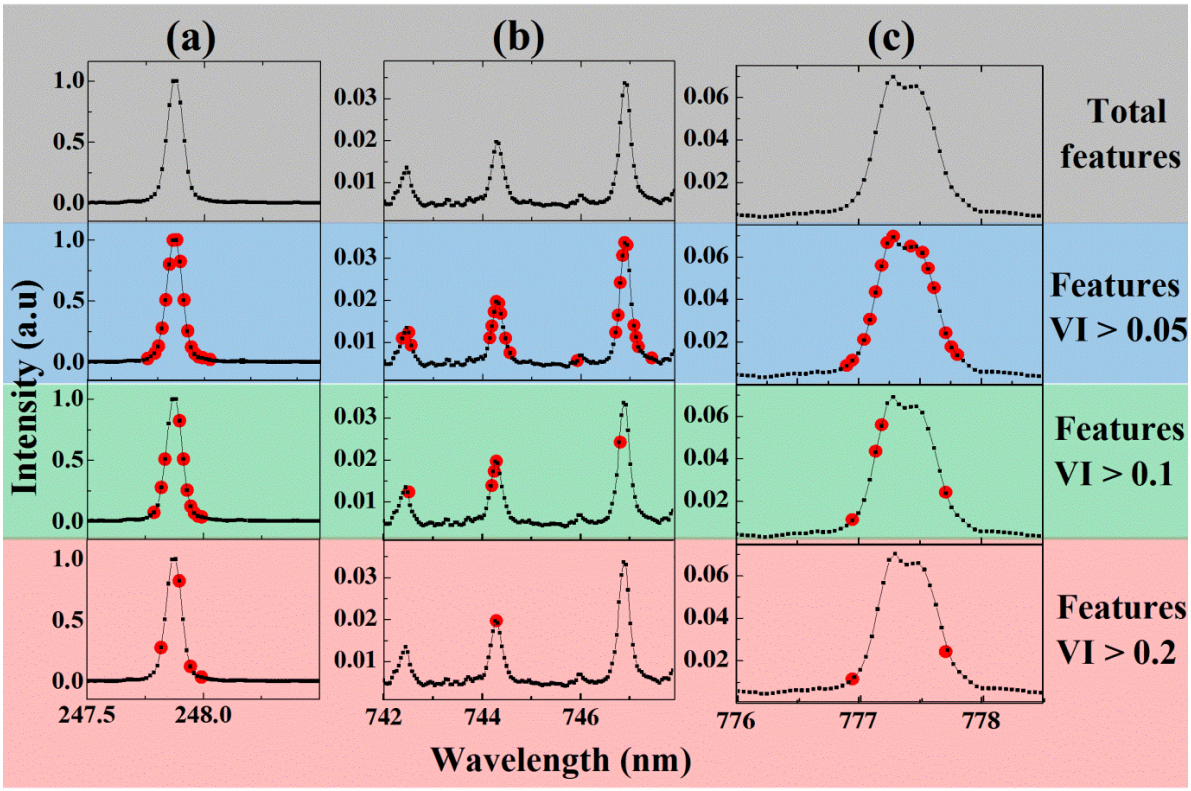

Fig. 1.9. (a, b & c) Represent the spectral lines of carbon, nitrogen, and oxygen respectively. Black rectangles represent the total variables of the spectral line. Red dots correspond to features selected by varying the different threshold values of VI. Blue, green and red color strips represent the features selected with VI thresholds of 0.05, 0.1, and 0.2 respectively.

Fig. 1.8 (a) shows the LIBS spectra (220-880 nm) of plastic whereas Fig. 1.9 (a-c) represent the emission lines of carbon (247.5- 249 nm), nitrogen (742- 748 nm) and oxygen (776-778.5 nm) respectively. Only these spectral windows are shown in the figure for the better visualization of the selected features obtained from VI. The features can be chosen by keeping a certain value of the threshold for VI however it depends on the application of interest. For example, the blue strip in Fig. 1.9 represents the features (red dots) selected with VI threshold of 0.05. It is evident from the figure, all the features selected based on VI lie within the peak region only irrespective of the threshold, and the variables from the baseline are not contributed to the feature selection due to zero VI value. Hence, it is

asserted that the feature selection picks the most important variables from the spectra, not the noisy one. Further, the number of variables is decreasing with the increasing threshold value of VI as shown in Fig. 1.9 and the results are given in Table 1.1. It is evident from Table 1.1, the no of variables are drastically reduced for the VI >0.1 and 0.2 compared to the total no of variables.

Table 1.1. No of variables obtained using feature selection based on VI for the carbon, nitrogen, and oxygen lines.

Spectral line	Wavelength window (nm)	Total no of variables	No of variables obtained with features selection		
			VI>0.05	VI>0.1	VI>0.2
Carbon	247.5- 249	65	16	10	4
Nitrogen	742- 748	129	24	6	1
Oxygen	776- 778.5	53	17	4	4

In feature selection, if the threshold is very high it leads to the selection of a very less number of variables which deteriorates the performance of the classification model. At another extreme, the low threshold results in opting in a huge number of features nevertheless increase the computational time. For example (see Table 1.2), the features extracted with VI >0.2 correspond to only 0.1 % of total data and reduced the workload by more than two orders for the classification of the plastics using ANN. Nevertheless, it deteriorated results due to very less number of features compared to the 100 % data as given in Table 1.2. Further, the analysis performed with features (VI > 0.05) has shown the classification performance close to the total data and reduced the computational times by more than order. Hence, an optimal number of features need to be selected with the compromise between classification rate and computational time as well as it also, depends on the requirements of the user.

Table 1.2. The identification rates obtained using feature selection based on VI. ANN is used for the analysis.

Spectral input	Data (%)	Classification rate (%)	Training time (S)	Testing time (ms)
Total data	100	96.95	43.8	42.9
Thresold-0.05	6.4	95.10	2.6	13.5
Thresold-0.15	0.4	92.27	0.5	11.5
Thresold-0.2	0.1	79.43	0.4	11.5

1.5 References

1. A.F. LAGALANTE, "Atomic emission spectroscopy: A tutorial review", Applied Spectroscopy Reviews, 34, **2004**.
2. C. Xinkun, "Atomic Emission Spectroscopy [J]", Chinese Journal of Analysis Laboratory, 4, **1991**.
3. D. Devia, L. Rodriguez-Restrepo, and E.R. Parra, "Methods employed in optical emission spectroscopy analysis: a review", Ingeniería y ciencia, 11, **2015**.
4. M.S.H. Akash, and K. Rehman, "Essentials of Pharmaceutical Analysis", Springer.
5. J.D. Winefordner, I.B. Gornushkin, T. Correll *et al.*, "Comparing several atomic spectrometric methods to the super stars: special emphasis on laser induced breakdown spectrometry, LIBS, a future super star", Journal of Analytical Atomic Spectrometry, 19, **2004**.
6. H.R. Griem, "Validity of local thermal equilibrium in plasma spectroscopy", Physical review, 131, **1963**.
7. J.P. Singh, and S.N. Thakur, "Laser-induced breakdown spectroscopy", Elsevier**2007**.
8. D.A. Cremers, and A.K. Knight, "Laser-Induced Breakdown Spectroscopy", Wiley Online Library**2006**.
9. E. Rodriguez-Celis, I. Gornushkin, U. Heitmann *et al.*, "Laser induced breakdown spectroscopy as a tool for discrimination of glass for forensic applications", Analytical and bioanalytical chemistry, 391, **2008**.
10. D.W. Hahn, and N. Omenetto, "Laser-induced breakdown spectroscopy (LIBS), part I: review of basic diagnostics and plasma–particle interactions: still-challenging issues within the analytical plasma community", Applied spectroscopy, 64, **2010**.
11. D.W. Hahn, and N. Omenetto, "Laser-induced breakdown spectroscopy (LIBS), part II: review of instrumental and methodological approaches to material analysis and applications to different fields", Applied spectroscopy, 66, **2012**.
12. D.H. Gili, and A.A. Dougal, "Breakdown minima due to electron-impact ionization in super-high-pressure gases irradiated by a focused giant-pulse laser", Physical Review Letters, 15, **1965**.
13. J. Hermann, A. Lorusso, A. Perrone *et al.*, "Simulation of emission spectra from nonuniform reactive laser-induced plasmas", Physical Review E, 92, **2015**.
14. J.C. Miller, "Laser ablation: principles and applications", Springer Science & Business Media**2013**.
15. B. Rethfeld, D.S. Ivanov, M.E. Garcia *et al.*, "Modelling ultrafast laser ablation", Journal of Physics D: Applied Physics, 50, **2017**.
16. T.A. Labutin, V.N. Lednev, A.A. Ilyin *et al.*, "Femtosecond laser-induced breakdown spectroscopy", Journal of Analytical Atomic Spectrometry, 31, **2016**.
17. R.E. Russo, X. Mao, J.J. Gonzalez *et al.*, "Laser ablation in analytical chemistry", ACS Publications, **2013**.
18. D. Díaz, A. Molina, and D. Hahn, "Effect of laser irradiance and wavelength on the analysis of gold-and silver-bearing minerals with laser-induced breakdown spectroscopy", Spectrochimica Acta Part B: Atomic Spectroscopy, 145, **2018**.
19. K. Anoop, S. Harilal, R. Philip *et al.*, "Laser fluence dependence on emission dynamics of ultrafast laser induced copper plasma", Journal of Applied Physics, 120, **2016**.

20. R. Noll, "Laser-induced breakdown spectroscopy", Laser-Induced Breakdown Spectroscopy, Springer**2012**.
21. S.S. Harilal, J.R. Freeman, P.K. Diwakar *et al.*, "Femtosecond laser ablation: Fundamentals and applications", Laser-Induced Breakdown Spectroscopy, Springer**2014**.
22. D. Patel, P. Pandey, and R. Thareja, "Stoichiometric investigations of laser-ablated brass plasma", Applied optics, 51, **2012**.
23. J.J. Chang, and B.E. Warner, "Laser-plasma interaction during visible-laser ablation of methods", Applied physics letters, 69, **1996**.
24. K. Sokolowski-Tinten, and D. Von Der Linde, "Ultrafast phase transitions and lattice dynamics probed using laser-produced x-ray pulses", Journal of Physics: Condensed Matter, 16, **2004**.
25. V. Zorba, X. Mao, and R.E. Russo, "Laser wavelength effects in ultrafast near-field laser nanostructuring of Si", Applied Physics Letters, 95, **2009**.
26. E. Millon, O. Albert, J. Loulergue *et al.*, "Growth of heteroepitaxial ZnO thin films by femtosecond pulsed-laser deposition", Journal of Applied Physics, 88, **2000**.
27. C.-H. Lin, L. Jiang, Y. Chai *et al.*, "Fabrication of microlens arrays in photosensitive glass by femtosecond laser direct writing", Applied Physics A, 97, **2009**.
28. A.V. Kabashin, and M. Meunier, "Synthesis of colloidal nanoparticles during femtosecond laser ablation of gold in water", Journal of Applied Physics, 94, **2003**.
29. A.W. Miziolek, V. Palleschi, and I. Schechter, "Laser induced breakdown spectroscopy", Cambridge University Press**2006**.
30. A. Miloshevsky, S.S. Harilal, G. Miloshevsky *et al.*, "Dynamics of plasma expansion and shockwave formation in femtosecond laser-ablated aluminum plumes in argon gas at atmospheric pressures", Physics of Plasmas, 21, **2014**.
31. S. Harilal, G. Miloshevsky, P. Diwakar *et al.*, "Experimental and computational study of complex shockwave dynamics in laser ablation plumes in argon atmosphere", Physics of Plasmas, 19, **2012**.
32. X.L. Mao, M.A. Shannon, A.J. Fernandez *et al.*, "Temperature and emission spatial profiles of laser-induced plasmas during ablation using time-integrated emission spectroscopy", Applied Spectroscopy, 49, **1995**.
33. M. Sabsabi, and P. Cielo, "Quantitative analysis of aluminum alloys by laser-induced breakdown spectroscopy and plasma characterization", Applied Spectroscopy, 49, **1995**.
34. S. Harilal, R.C. Issac, C. Bindhu *et al.*, "Optical emission studies of species in laser-produced plasma from carbon", Journal of Physics D: Applied Physics, 30, **1997**.
35. S. Harilal, R.C. Issac, C. Bindhu *et al.*, "Temporal and spatial evolution of C2 in laser induced plasma from graphite target", Journal of applied physics, 80, **1996**.
36. J. Serrano, J. Moros, and J.J. Laserna, "Molecular signatures in femtosecond laser-induced organic plasmas: comparison with nanosecond laser ablation", Physical Chemistry Chemical Physics, 18, **2016**.
37. S. Sai Shiva, C. Leela, P. Prem Kiran *et al.*, "The effects of electron thermal radiation on laser ablative shock waves from aluminum plasma into ambient air", Physics of Plasmas, 23, **2016**.
38. M.K. Gundawar, R. Junjuri, and A.K. Myakalwar, "Standoff Detection of Explosives at 1 m using Laser Induced Breakdown Spectroscopy", Defence Science Journal, 67, **2017**.

39. S. Sreedhar, M.K. Gundawar, and S.V. Rao, "Laser induced breakdown spectroscopy for classification of high energy materials using elemental intensity ratios", Defence Science Journal, 64, **2014**.
40. V.K. Unnikrishnan, K.S. Choudhari, S.D. Kulkarni *et al.*, "Analytical predictive capabilities of Laser Induced Breakdown Spectroscopy (LIBS) with Principal Component Analysis (PCA) for plastic classification", RSC Advances, 3, **2013**.
41. V. Unnikrishnan, K. Choudhari, S.D. Kulkarni *et al.*, "Analytical predictive capabilities of laser induced breakdown spectroscopy (LIBS) with principal component analysis (PCA) for plastic classification", RSC Advances, 3, **2013**.
42. P. Pořízka, J. Klus, E. Képeš *et al.*, "On the utilization of principal component analysis in laser-induced breakdown spectroscopy data analysis, a review", Spectrochimica Acta Part B: Atomic Spectroscopy, 148, **2018**.
43. R. Junjuri, C. Zhang, I. Barman *et al.*, "Identification of post-consumer plastics using laser-induced breakdown spectroscopy", Polymer Testing, **2019**.
44. A.K. Myakalwar, N. Spegazzini, C. Zhang *et al.*, "Less is more: Avoiding the LIBS dimensionality curse through judicious feature selection for explosive detection", Scientific reports, 5, **2015**.
45. A.K. Myakalwar, S. Sreedhar, I. Barman *et al.*, "Laser-induced breakdown spectroscopy-based investigation and classification of pharmaceutical tablets using multivariate chemometric analysis", Talanta, 87, **2011**.
46. N.C. Dingari, I. Barman, A.K. Myakalwar *et al.*, "Incorporation of support vector machines in the LIBS toolbox for sensitive and robust classification amidst unexpected sample and system variability", Analytical chemistry, 84, **2012**.
47. J. Serrano, J. Moros, C. Sánchez *et al.*, "Advanced recognition of explosives in traces on polymer surfaces using LIBS and supervised learning classifiers", Analytica chimica acta, 806, **2014**.
48. M. Baudelet, J. Yu, M. Bossu *et al.*, "Discrimination of microbiological samples using femtosecond laser-induced breakdown spectroscopy", Applied physics letters, 89, **2006**.
49. H. Abdi, and L.J. Williams, "Principal component analysis", Wiley interdisciplinary reviews: computational statistics, 2, **2010**.
50. R. Bro, and A.K. Smilde, "Principal component analysis", Analytical Methods, 6, **2014**.
51. A.K. Shaik, N.R. Epuru, H. Syed *et al.*, "Femtosecond laser induced breakdown spectroscopy based standoff detection of explosives and discrimination using principal component analysis", Opt. Express, 26, **2018**.
52. S.C. Jantzi, and J.R. Almirall, "Characterization and forensic analysis of soil samples using laser-induced breakdown spectroscopy (LIBS)", Analytical and bioanalytical chemistry, 400, **2011**.
53. A.K. Shaik, Ajmathulla, and V.R. Soma, "Discrimination of bimetallic alloy targets using femtosecond filament-induced breakdown spectroscopy in standoff mode", Opt. Lett., 43, **2018**.
54. I. Gaona, J. Serrano, J. Moros *et al.*, "Range-adaptive standoff recognition of explosive fingerprints on solid surfaces using a supervised learning method and laser-induced breakdown spectroscopy", Analytical chemistry, 86, **2014**.
55. A.K. Myakalwar, N.C. Dingari, R.R. Dasari *et al.*, "Non-gated laser induced breakdown spectroscopy provides a powerful segmentation tool on concomitant treatment of characteristic and continuum emission", PloS one, 9, **2014**.

56. K. Sudheer, A. Gosain, D. Mohana Rangan *et al.*, "Modelling evaporation using an artificial neural network algorithm", Hydrological Processes, 16, **2002**.
57. D. Marcos-Martinez, J. Ayala, R. Izquierdo-Hornillos *et al.*, "Identification and discrimination of bacterial strains by laser induced breakdown spectroscopy and neural networks", Talanta, 84, **2011**.
58. A.K. Myakalwar, S.K. Anubham, S.K. Paidi *et al.*, "Real-time fingerprinting of structural isomers using laser induced breakdown spectroscopy", Analyst, 141, **2016**.
59. M. Boueri, V. Motto-Ros, W.Q. Lei *et al.*, "Identification of polymer materials using laser-induced breakdown spectroscopy combined with artificial neural networks", Applied Spectroscopy, 65, **2011**.
60. S.Y. Oh, F.-Y. Yueh, and J.P. Singh, "Quantitative analysis of tin alloy combined with artificial neural network prediction", Applied Optics, 49, **2010**.
61. F. Rezaei, P. Karimi, and S. Tavassoli, "Effect of self-absorption correction on LIBS measurements by calibration curve and artificial neural network", Applied Physics B, 114, **2014**.
62. S.S. Haykin, "Neural networks and learning machines", Pearson Upper Saddle River, NJ, USA:**2009**.
63. J. El Haddad, M. Villot-Kadri, A. Ismaël *et al.*, "Artificial neural network for on-site quantitative analysis of soils using laser induced breakdown spectroscopy", Spectrochimica Acta Part B: Atomic Spectroscopy, 79-80, **2013**.
64. H. Zheng, L. Jiang, H. Lou *et al.*, "Application of artificial neural network (ANN) and partial least-squares regression (PLSR) to predict the changes of anthocyanins, ascorbic acid, Total phenols, flavonoids, and antioxidant activity during storage of red bayberry juice based on fractal analysis and red, green, and blue (RGB) intensity values", Journal of agricultural and food chemistry, 59, **2010**.
65. C.M. Bishop, "Pattern recognition and machine learning", springer**2006**.
66. S.-L. Lui, and A. Koujelev, "Accurate identification of geological samples using artificial neural network processing of laser-induced breakdown spectroscopy data", Journal of Analytical Atomic Spectrometry, 26, **2011**.
67. M.J.C. Pontes, J. Cortez, R.K.H. Galvão *et al.*, "Classification of Brazilian soils by using LIBS and variable selection in the wavelet domain", Analytica Chimica Acta, 642, **2009**.
68. K. Liu, D. Tian, H. Wang *et al.*, "Rapid classification of plastics by laser-induced breakdown spectroscopy (LIBS) coupled with partial least squares discrimination analysis based on variable importance (VI-PLS-DA)", Analytical Methods, 11, **2019**.
69. L. Breiman, "Random forests", Machine learning, 45, **2001**.

CHAPTER 2 : Experimental details

This chapter provides a comprehensive overview of the different laser sources, and spectrometers used for the LIBS experiment in the present thesis work. It comprises the details of nanosecond (ns, SpitLight-1200, M/S Innolas) and femtosecond (fs, Libra, M/S Coherent) laser systems. It also presents the details of the gated Mechelle spectrograph (Mechelle 5000, M/S Andor technologies) and nongated Czerny Turner spectrometers (Maya 2000, M/S Ocean optics). As well as, different components deployed for the LIBS setup and the timing scheme used in LIBS studies are briefly discussed.

2.1 Details of the laser

Two laser systems (ns & fs) were utilized for the experiments presented in this thesis. The ns LIBS studies are presented in chapters 3, 4, and 5 and fs LIBS experiments are described in chapter 6.

2.1.1 Nanosecond laser system

A Nd: YAG laser (SpitLight-1200, M/S Innolas) was utilized for carrying out the ns LIBS experiments. The laser system comprises three parts 1) Oscillator 2) Pre-amplifier, and 3) Main amplifier. The schematic of the optical layout is presented in Fig. 2.1[1].

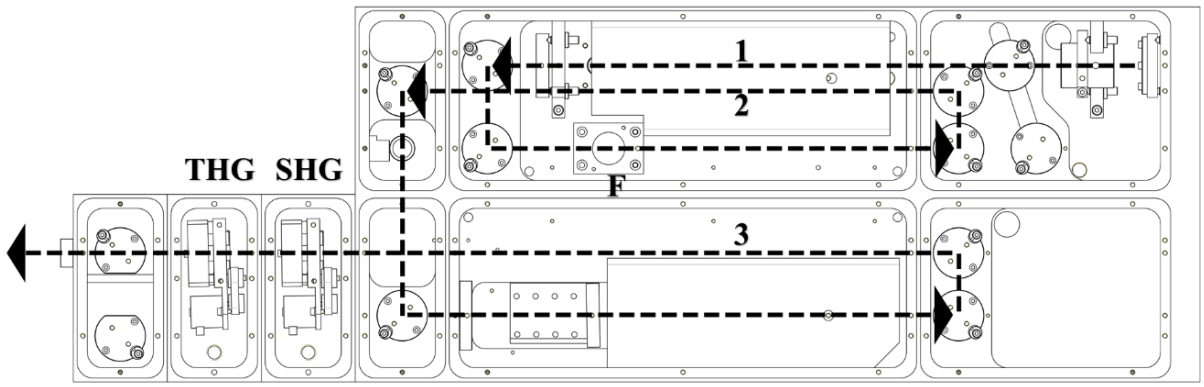

Fig. 2.1.The schematic of the optical layout of the ns laser system. 1, 2 & 3 correspond to the beam path of the oscillator, pre-amplifier and main amplifier. 'F' is the Faraday isolator. SHG, and THG correspond to the assemblies of second and third harmonic crystals respectively.

The Neodymium (Nd) ions are doped in yttrium aluminum garnet ($Y_3Al_5O_{12}$) where it acts as the gain medium and $Y_3Al_5O_{12}$ corresponds to the host material[2]. It has high optical quality as well as thermal conductivity which favors the making of high repetition pulsed lasers (up to 100 Hz). The doping concentration is ~ 0.725 % by weight. The laser operates at a fundamental wavelength of 1064 nm with the maximum energy of 1200 mJ. It can be operated at 532, 355, and 266 nm wavelengths however; only 1064 & 532 nm wavelengths are used by the standoff and in-situ LIBS experiments respectively. It is a four-level laser system where the emission of fundamental wavelength at 1064 nm has been observed due to the transition of the atoms from lasing levels of $4F_{3/2} \rightarrow 4\ I_{11/2}$ [2, 3]. The lifetime of the metastable state is ~ 230 μs. The maximum repetition rate of the current laser system is 10 Hz albeit for the experiments it is operated at 1 Hz. The ns pulse is generated with the aid of the Q-switching technique[2] where the pulse duration is measured with the photodiode as shown in Fig. 2.2(a) and it is found to be ~ 8 ns (According to specification it is ~7 ns). The gain medium (one Nd: YAG rod) is optically pumped by a Xenon flash lamp and the duration of the flash pulse is ~ 200 µs as shown in Fig. 2.2(b).

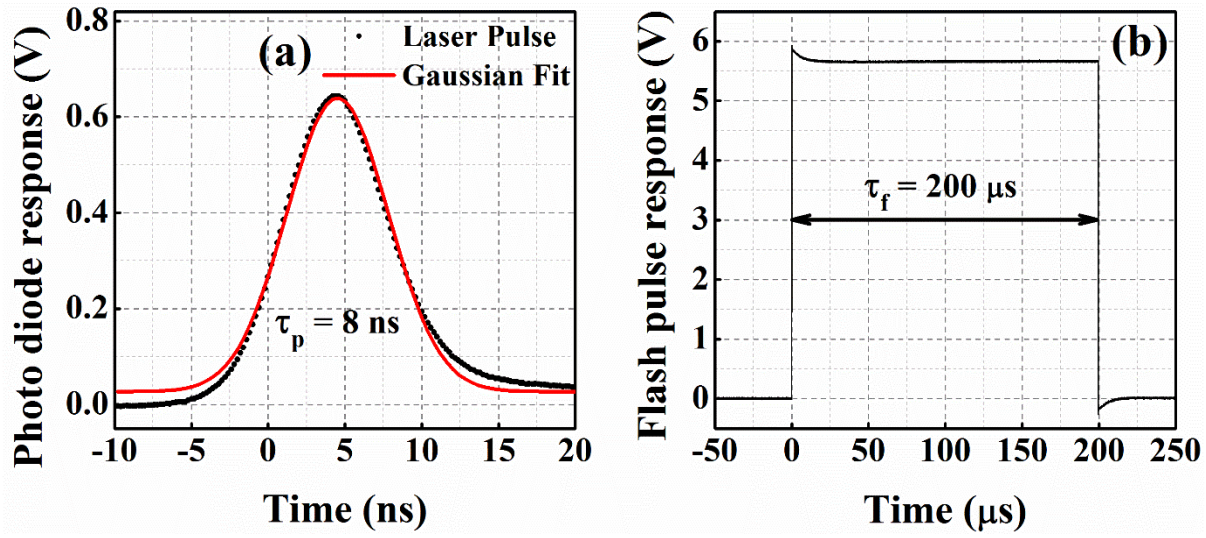

Fig. 2.2. a) The photodiode response/signal of the ns laser pulse. b) The response of the Xenon flash lamp. τ_p & τ_f correspond to the duration of the laser pulse and flash lamp respectively.

The energy of 300 mJ/pulse can be achieved in the oscillator. Further, the laser beam gets amplified in the pre-amplifier where the pulse energy gets doubled, and finally, the pulse energy of 1200 mJ @ 1064 nm can be obtained after the final amplification process. An

external chiller is connected to the laser system to remove the heat generated in the lasing process. The fundamental wavelength (1064 nm) is converted to 532 and 355 nm by using second and third harmonic crystals respectively. For the present work, the 532 nm laser beam is obtained by passing the 1064 nm laser beam through KD*P crystal where the conversion efficiency is ~43 %. Fs laser system is described in the next section.

2.1.2 Femtosecond laser system

A commercial compact fs laser system (Libra, M/s Coherent) was utilized for the fs as well as filamentation LIBS experiments[4] and the optical bench layout is shown in Fig. 2.3. It is a class IV ultrafast Ti: Sapphire laser system which operates at a repetition rate of 1 kHz and wavelength centered at 800 nm with the beam diameter of ~ 9 mm. It delivers pulses of ~35 fs duration with the maximum energy of 4 mJ/pulse which corresponds to the average power of 4 W. It comprises four modules 1) Oscillator/seed laser (Vitesse), 2) Pump laser (Evolution), 3) Regenerative amplifier (RGA), and 4) stretcher and compressor region which are integrated into one box.

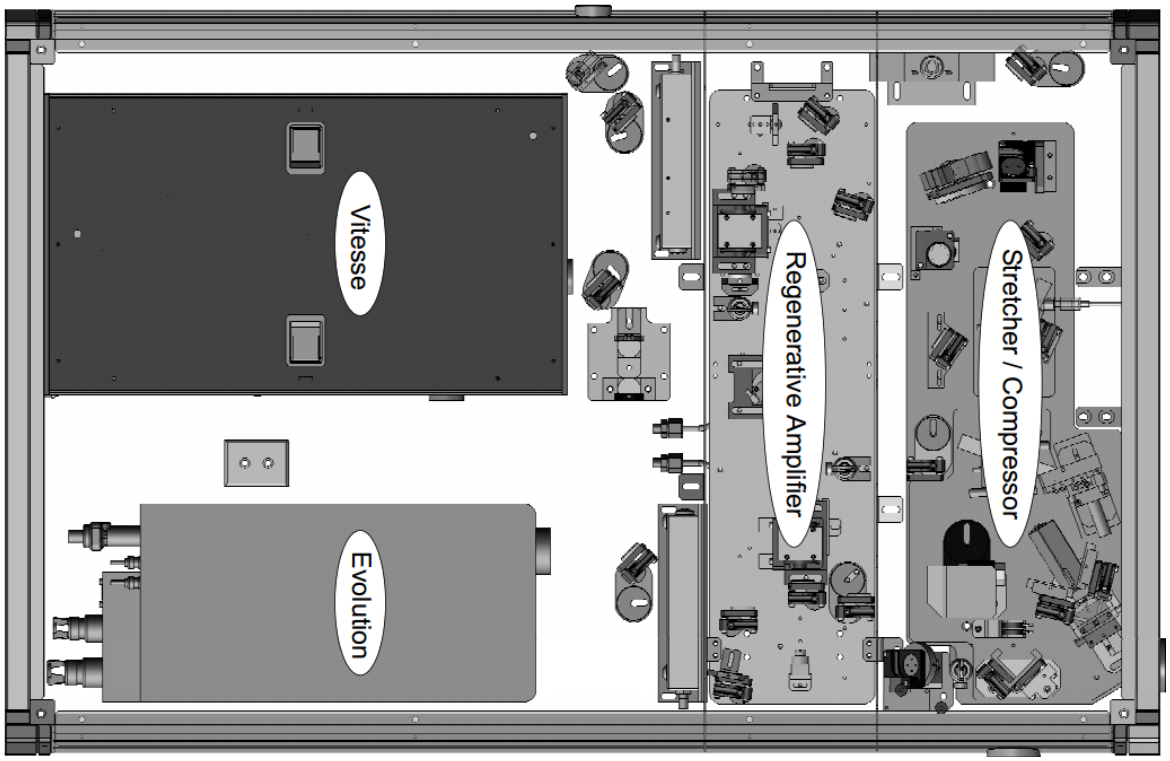

Fig. 2.3. The optical bench assembly of the Libra fs laser system.

2.1.2.a Oscillator (Vitesse)

It is a compact ultrafast Ti: Sapphire laser which serves as a seed laser/oscillator in the Libra[4]. It is a modelocked fs laser system with a pulse duration of ~100 fs, a repetition rate of 80 MHz and an average power of 300 mW. The emitted laser wavelength is centered at 800 nm with an optimum bandwidth of 30 nm. The Ti ions are doped into the host material of sapphire (Al_2O_3) with concentrations in the range of 0.1-0.5%[5]. The gain medium has an absorption spectrum bandwidth of 400-650 nm, and the emission spectrum starts at 650 nm[6]. The laser emission at a particular wavelength is selected by using an etalon/optical wedge. Apart from that, the tuning range is influenced by coating on the mirrors/optical components, input power losses, quality of pump beam, losses in the cavity, and ambient absorption, etc. Vitesse consists of three major parts 1) a sealed optical cavity with a Verdi laser system which acts as a pump laser. 2) A power tracking mirror and 3) Verdi Pumped Ultra-Fast [VPUF] laser head. The layout of the Vitesse laser head is illustrated in Fig. 2.4.

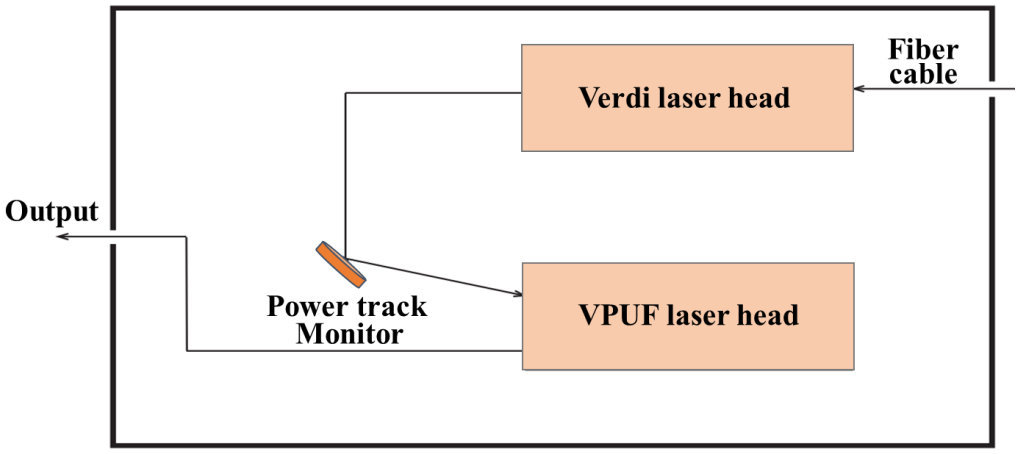

Fig. 2.4. The schematic of the Vitesse laser head.

Both VPUF and Verdi are sealed by the manufacturer for the best performance of the laser over the long lifetime. The Verdi laser operates at the wavelength of 532 nm with the power of 2 W. It contains a Neodymium Yttrium orthovanadate (Nd: YVO_4) crystal which serves as a gain medium. The Verdi is pumped by an array of diode lasers and produces a continuous laser beam operating at the fundamental wavelength of 1064 nm. Further, the laser beam converted to 532 nm by propagating the fundamental beam

through a second harmonic crystal Lithium Triborate (LiB_3O_5-LBO). The LBO crystal maintained at 148°C temperature by a resistive based heating system. The LBO has a high damage threshold compared to the other SHG crystal as well as it offers non-critical phase-matching and provides a larger acceptance angle for the higher efficiency. The power tracking system utilizes a Piezo driven mirror for maintaining the optimum pump beam alignment into the VPUF head. The VPUF is a sealed cavity which comprises of a Ti: Sapphire crystal and negative dispersion mirrors (NDM). The multiple light reflection from the NDMs ensures the negative dispersion compensation which is essential to generate sub 100 fs pulses. The Kerr-Lens Modelocking (KLM) that is a passive modelocking technique is responsible for modelocking in Vitesse[7]. The cavity is sealed to avoid environmental contamination as well for the stability of the laser power.

2.1.2.b Pump Laser (Evolution)

It is an Nd: YLF (Nd: $LiYF_4$, yttrium lithium fluoride) solid-state laser used as a pump laser for the amplifier module. It has an upper-level lifetime twice that of Nd: YAG laser ~ 470 μs which results in achieving twice the pulse energy of Nd: YAG laser however relatively with a lower repetition rate. Apart from that, low thermal lensing and natural "birefringence" favours in generating laser with high beam quality. The narrow spectral emission from the diode laser in contrast to the emissions from the arc lamps provides the most effective pumping scheme. Besides that, with no/minimal diode light falling outside of the absorption band of the gain medium results in negligible waste heat production. Acousto-optic Q-switching technique allows the generation of the laser pulse. It provides the fundamental wavelength at 1053 nm which corresponds to the transition of $4F_{3/2} \rightarrow I_{11/2}$. The frequency doubling (527 nm) is achieved by propagating the 1053 nm laser via an LBO crystal.

2.1.2.c Regenerative amplifier (RGA)

The RGA is based on the Legend Elite TM platform (M/s Coherent, USA). The amplifier is compactly designed and enclosed in a module with an active cooling system[4]. It exhibits excellent stability and less sensitive to the changes in ambient temperature. The RGA system inherently contains a Synchronized Delay Generator (SDG) system which

not only controls the functioning of Pockels cells for the seed laser but also synchronizes the pump laser. The seed pulse from Vitesse is get amplified in RGA with the aid of pump beam from evolution focused onto the gain medium and round trips. The technical details of the oscillator and amplifier laser beam are presented in Table 2.1.

Table 2.1. Laser beam parameters of the fs oscillator and amplifier.

S. No	Parameters	Oscillator	Amplifier
1	Pulse duration	~ 100 fs	~ 100 fs
2	Rep rate	80 MHz	1 kHz
3	Beam diameter	~ 3 mm	~ 9 mm
4	Maximum energy per pulse	~ 7 nJ	~ 4 mJ
5	Polarization	Horizontal	Horizontal

2.1.2.d Stretcher & Compressor - Chirped pulse amplification (CPA)

The stretcher and compressor are integrated into a single box system within a robust modular enclosure. The energy of the oscillator pulse (~ 7 nJ) is enhanced by a factor of ~ 10^6 in RGA through the CPA technique as depicted in Fig. 2.5.

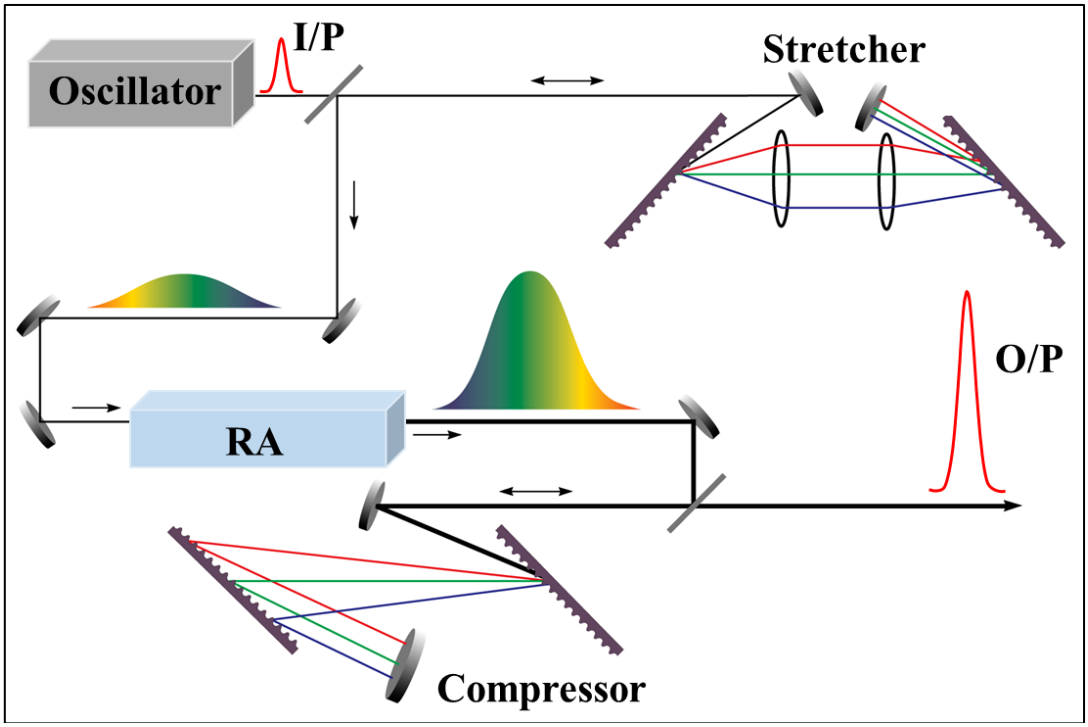

Fig. 2.5. Typical schematic of the CPA technique[8, 9]. I/P-Input pulse, O/P-Output pulse.

The laser pulse from the oscillator serves as a seed and gets amplified in RGA. As aforementioned Ti: Sapphire crystal is used as a gain medium in RGA also. During this amplification process, the fs pulses can lead to the self-focusing phenomenon due to the high intensity and prone to damage the optical components as well as the gain medium. Hence, to avoid the damage of laser components in the cavity of RGA, the fs pulses need to be stretched significantly (fs to ps). Thus, the peak power of the laser beam reduces by several orders and favours in achieving amplification without any damage to the laser system. In CPA, the grating design of the stretching compartment alters the fs pulses such that the blue components travel longer distances compared to the red components and results in stretching the pulses[8, 9]. For the present configuration, the pulses from the oscillator (~ 100 fs @ 80 MHz) stretches to (~100 ps @ 80 MHz) which reduces the peak power by 10^3 times and hence the damage can be prevented. Further, the RF signal generated from the seed pulse of the oscillator synchronizes the Pockels cell and switches the pulses from the oscillator/stretcher to RGA. Besides that, the repetition rate of amplified pulses can be varied in the range of these 10 to 1 kHz with the aid of the Pockels cell. After the amplification in the RGA, the laser pulses were compressed in the compressor region. The process of compression is exactly opposite to the stretching in which the gratings are aligned in such that higher frequencies travel the shorter distance in order to "catch up" with the lower frequencies. Thus, the pulse compresses to the initial time scales and for the present laser system, the seed pulse of few nJ is get amplified to ~4 mJ (@ 1 kHz in RA[4].

2.2 Details of the spectrometers

Mechelle spectrometer equipped with an intensified charge-coupled device (ICCD) detector and Czerny-turner (CT) spectrometer coupled with charge-coupled device (CCD) detector is utilized for the LIBS experiments carried out in the thesis. Both the spectrometers are rugged and no moving parts (optical elements) present in it. The complete technical details and specifications of both the spectrometers are given in Table 2.2.

Table 2.2. Various parameters of the Mechelle ICCD spectrometer and Czerny-turner (CT) CCD spectrometer.

S. No	Parameter	ICCD System	CCD System
1	Spectrograph model	ME-5000 (M/s Andor)	Maya-2000 (M/s Ocean optics)
2	Detector model	istar, DH334T-18U-E3, & DH734-18U-03	Hamamatsu S9840, back-thinned FFT-CCD
3	F number	7	4
4	Entrance slit (μm)	50	50
5	Resolution @ 500 nm	0.1	1
6	CCD format	1024X1024	2048 X 64
7	Pixel size (μm)	13 X 13	14 X 14
8	Detector cooling ^{o}C	-30	Not required
9	Gating & time resolution	Yes	No
10	Spectral range (nm)	230-880	300-900
11	Weight (Kg)	~ 15	~ 1
12	Size (10^3 cm^{-3})	~ 9.1	~ 0.8
13	Minimum integration time	2 ns	6 ms

2.2.1 Mechelle spectrometer

Mechelle spectrometer (ME-5000 & M/S Andor) coupled to ICCD was utilized for all the gated LIBS experiments. It has been a workhorse for the LIBS technique in various applications owing to its ruggedness and wide spectral coverage in single acquisition with a higher resolution. The iStar ICCD (DH334T-18U-E3 & M/S Andor) was attached to the Echelle spectrograph in case of fs LIBS experiments whereas iStar ICCD (DH734-18U-03 & M/S Andor) was utilized in case of ns LIBS experiments. It has a minimum time resolution (operating gate width for the acquiring the LIBS spectra) of 2 ns. An Echelle grating combined with prism serves as a dispersive element in the spectrometer. This combination (prism + grating=grism) disperses the light in 2D space, and projects on to the ICCD. The Echelle grating has lees grove density, blazed, and works at higher-order diffraction for achieving the higher resolution. The spectrometer offers a resolution of 0.1 nm at 500 nm with the wide spectral range starting from UV (220 nm) to NIR (800 nm) in one acquisition. The spectrometer was calibrated for the wavelength using Mercury (Hg)-Argon (Ar) standard lamp. Further, the intensity correction of the whole detection system (spectrograph + ICCD) was done by deploying the Deuterium-Halogen lamp. The calibration was performed at the temperature of 25 ^{O}C and was operated at 25 $\pm$ 3 ^{O}C for the better performance.

2.2.2 Czerny-turner (CT) spectrometer

A Czerny-turner CCD spectrometer (Maya-2000, & M/s Ocean Optics) was used as non – gated detection system in the LIBS experiments. Primarily, the cost makes it a promising tool for the real-time implementation of the LIBS technique in the diverse field of applications. As well as the compact size and less weight promotes it as a portable system for miniaturized LIBS applications. It covers the spectral range of ~ 300 -1050 nm in a single shot with a resolution of 1 nm at 500 nm. It offers the minimum integration time of ~6 ms to acquire the spectra however, the accumulation option is not provided. It has peak quantum efficiency > 90 % at 650 nm and bit a low quantum efficiency (< 40 %) in the UV region. A grating has been used in the optical design of the spectrometer to disperse the light and CCD is utilized as the detector. The added advantage of the Maya-2000 is it does not require a cooling system for the CCD.

2.3 LIBS experimental setup

In the present thesis, the LIBS experiments were performed with the ns[10, 11] and fs[12] lasers depending on the application of interest. As well as in each case, the spectra were acquired with the gated[12] and non-gated[13] detectors as aforementioned. The typical processes involved in LIBS as a function of time with respect to laser pulse is shown in Fig. 2.6 and the time represented in the graph is not to the scale. The gating option avoids the huge continuum emissions from the plasma in earlier time scales which otherwise saturates and damages the detector. In general delay time of ~0.2-1 μs was employed in the experiments presented in this thesis. Further, the gated detection system enables the acquisition of the spectra at different delay times for the temporal characterization of plasma. It is essential to understand the kinetic evolution of the plasma properties which is most useful in CF-LIBS experiments for the concentration measurements[14].

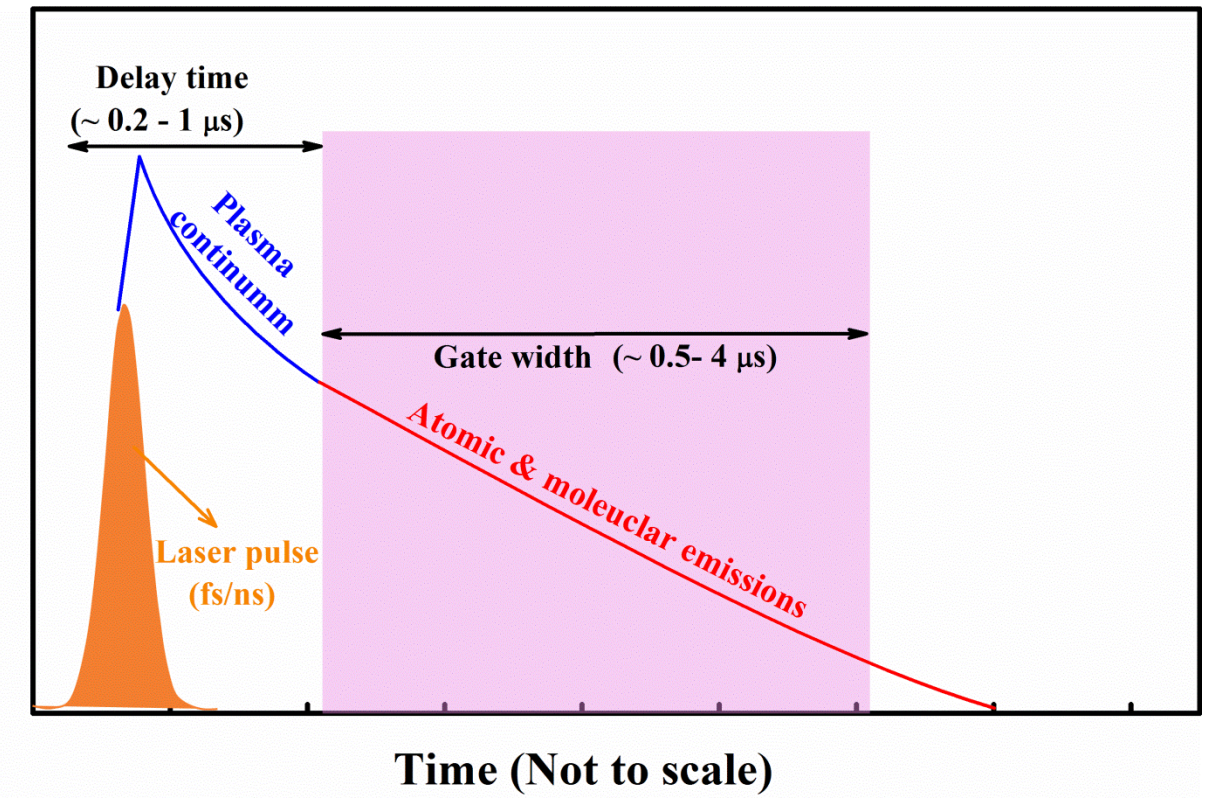

Fig. 2.6. The timing diagram of the LIP and typical LIBS spectra acquisition parameters. Delay time refers to the delay between the arrival of the laser pulse on to the sample and the starting time of the collection of LIP emissions. Gate width refers to typical integration time for acquiring the LIBS spectrum.

2.3.1 Gated LIBS setup

The typical schematic of the ns-gated LIBS experimental setup is shown in Fig. 2.7. The fs-gated setup looks similar to the ns-gated except for the wavelength and delay generator hence it is not shown here[12]. Only near field setups are described in the current chapter and the description of standoff systems[10] and their optimization[13] is shown in their respective chapters. In brief, the laser beam (fs/ns) was guided by a set of mirrors from the laser head and a Plano-convex lens focuses it on to the sample surface. The focal length of the lens, energy of the laser pulse, and acquisition parameters are different for the different experimental conditions. The sample was mounted on an X-Y translational stage which was connected to a motion controller (ESP-300 M/s Newport). The movement of the stage provides a fresh spot for each laser shot which was controlled and operated by the inbuilt LabView program. This movement/scanning avoids the formation of a deep crater on the sample surface and ensures the better reproducibility of acquiring LIBS spectra on a shot to shot basis.

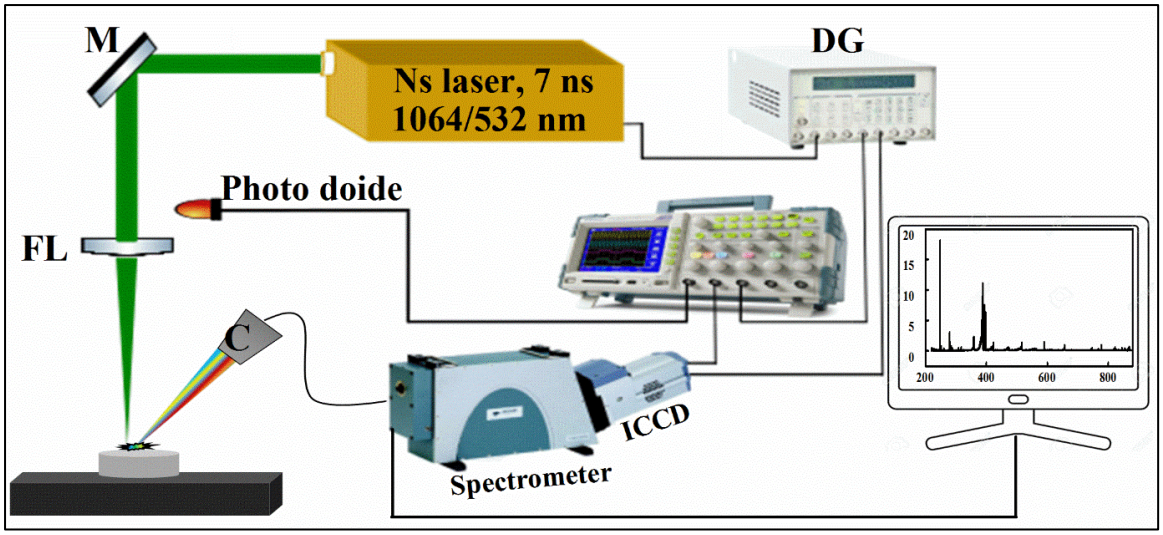

Fig. 2.7. Typical schematic of the ns-gated LIBS experimental setup. C-Collection optics/system, FL – Focusing lens, M – Mirror, and DG- Delay generator (it is SDG for fs LIBS).

However, the moving/scanning speed was varied with respect to the experimental conditions. The spectral emissions from the plasma were collected using collection optics/system (ME-OPT-007 M/s Andor) which was coupled to the spectrometers (separately for gated and non-gated spectrometers) via an optical fiber of core diameter 600 μm. The collection system was kept at 45° relative to the incident laser beam and a diode laser beam was guided through it via an optical fiber to adjust and optimize it. The spectra were acquired with Mechelle spectrograph equipped with the ICCD ('DH334T-18U-E3, for fs' & 'DH734-18U-03, for ns').

A delay generator ('DG-645 & M/S Stanford research systems for ns' and 'SDG elite, & M/S Coherent for fs') was utilized to synchronize the laser pulse/system to the ICCD. Initially, it was triggered by a Pockels pulse from the laser. Further, the ICCD was triggered by a TTL pulse (0-5 V, with a rise time of ~2 ns) generated from the delay generator. All these time events were monitored in an oscilloscope (TDS-2024B & M/S Tektronix) and a screenshot (picture of oscilloscope display) is presented in Fig. 2.8. An InGaAs PIN photodiode (DET-410, & M/S ThorLabs) with a rise time of ~ 5 ns deployed for monitoring the laser pulse. The photodiode response (orange color pulse in Fig. 2.8) represents the arrival of the laser pulse on to the sample and it was taken as a reference point of time for the spectral/signal acquisition. The temporal delay between the laser pulse and the ICCD gate opening (Magenta color pulse) can be changed through

either delay generator or ICCD which can be observed in the oscilloscope as shown in Fig. 2.8. The time gap between the rising part of the delay generator TTL trigger pulse (Cyan colour) and the ICCD gate opening is referred to as the insertion delay of the ICCD and for the current configuration, it was ~ 35 ns.

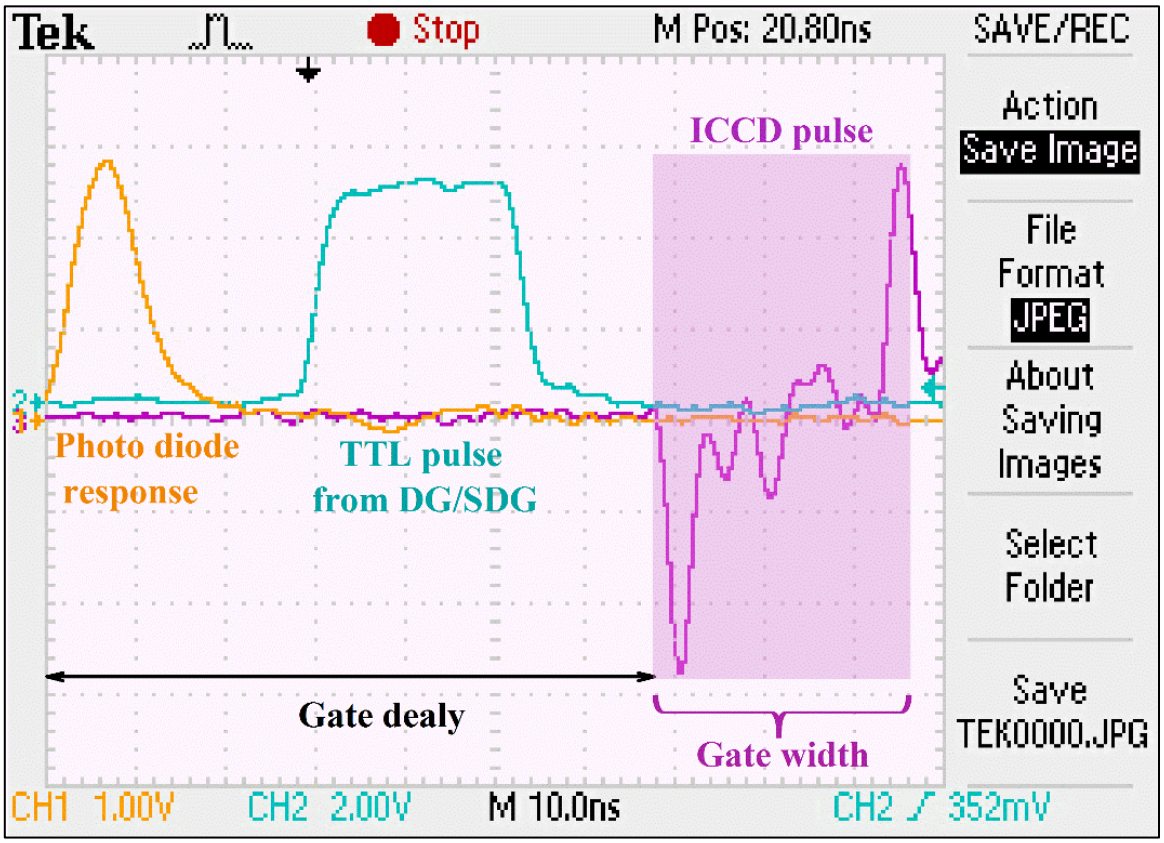

Fig. 2.8. An oscilloscope screenshot for monitoring the different time events of LIBS data acquisition. The ICCD gate width was set to 25 ns for the illustration.

2.3.2 Non - gated LIBS setup

The optical layout of the ns non-gated LIBS experimental setup is shown in Fig. 2.9. The fs non-gated appears similar to ns except for wavelength hence not shown in here. A Czerny Turner CCD spectrometer (Maya-2000, & M/s Ocean optics) was utilized for acquiring the spectra in the non-gated LIBS experiments[13]. Being a non-gated spectrometer it acquires the optical emissions not only from the plasma but also from the laser beam focused on to the sample. The 532/800/1064 nm notch filters have been used to avoid the pump beam in the LIBS spectra depending on the experimental conditions. Apart from that, the non-gated LIBS spectra inherently contain a large contribution from continuum emissions.

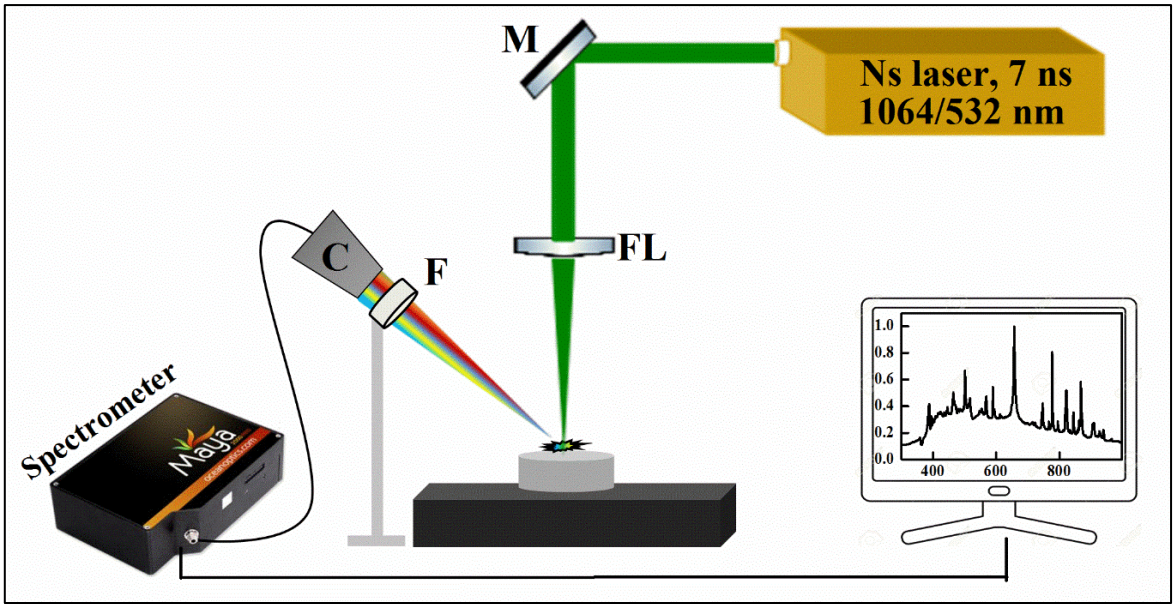

Fig. 2.9. The non-gated LIBS setup. C-Collection optics/system, FL – Focusing lens, M – Mirror, F- Notch Filter (532/800/1064 nm).

It is observed due to the acquiring the Bremsstrahlung emissions in the early time scales of the plasma evolution which can be avoided in the spectral measurements with gated spectrometers. A software was provided by the manufacturer to record the spectra and it is synchronized to the PC by a USB connection. However, the saving process requires a lengthy time and it is a tedious job. A LabView program was designed for the automatic spectral measurements to avoid the difficulties in saving. This program enables the rapid acquisition of the LIBS spectra and as well as minimizes the experimental errors that occur during the spectral acquisition process. The spectrometer provides the threshold intensity approach (it refers to spectra only saved when the intensity of any peak reaches above a certain threshold value of intensity) to save the spectrum automatically through LabView environment.

2.4 Summary

A brief overview of fs and ns lasers systems is presented in this chapter. As well as the details of fs and ns LIBS experimental setups and their components are described. The specifications and the comparison of gated & non – gated spectrometers are presented. The gating scheme and the timing diagram of the LIBS setup are explained in detail.

2.5 References

1. "Innolas laser", https://www.innolas-laser.com/Products/Lamp-Pumped Lasers/SpitLightHighPower.html?s=DE2BE16CC36E00766120516A82E092BFA2D2C65A.
2. W.T. Silfvast, "Laser fundamentals", Cambridge university press**2004**.
3. W. Koechner, "Solid-state laser engineering", Springer**2013**.
4. "Coherent, Operator's Manual: Libra Ultrafast Amplifier Laser System", http://lasers.coherent.com/lasers/libra-manual.
5. S. Thakur, and D. Rai, "Atom, Laser and Spectroscopy", PHI Learning Pvt. Ltd.**2013**.
6. "Dual-Mode Ti:Sa laser", https://www3.mpifr-bonn.mpg.de/div/submmtech/heterodyne/photonic_laser/dualmodeTiSa.html.
7. T. Brabec, C. Spielmann, P. Curley *et al.*, "Kerr lens mode locking", Optics letters, 17, **1992**.
8. "CPA technique", https://en.wikipedia.org/wiki/Chirped_pulse_amplification.
9. D. Strickland, and G. Mourou, "Compression of amplified chirped optical pulses", Optics communications, 55, **1985**.
10. M.K. Gundawar, R. Junjuri, and A.K. Myakalwar, "Standoff Detection of Explosives at 1 m using Laser Induced Breakdown Spectroscopy", Defence Science Journal, 67, **2017**.
11. R. Junjuri, C. Zhang, I. Barman *et al.*, "Identification of post-consumer plastics using laser-induced breakdown spectroscopy", Polymer Testing, 76, **2019**.
12. R. Junjuri, and M.K.K. Gundawar, "Femtosecond laser induced breakdown spectroscopy studies for the identification of the plastics", Journal of Analytical Atomic Spectrometry, **2019**.
13. A.P.G. Rajendhar Junjuri, Manoj Kumar Gundawar, "Single-Shot Compact Spectrometer Based Standoff LIBS Configuration For Explosive Detection Using Artificial Neural Networks", Optik –International Journal for Light and Electron Optics, **2020**.
14. E. Mal, R. Junjuri, M.K. Gundawar *et al.*, "Optimization of temporal window for application of calibration free-laser induced breakdown spectroscopy (CF-LIBS) on copper alloys in air employing a single line", Journal of Analytical Atomic Spectrometry, 34, **2019**.

CHAPTER 3 : Plasma diagnostic studies and a theoretical model for the temporal evolution of LIP

This chapter presents a theoretical model for the kinetic evolution of the LIP. A theory of radiative relaxation mechanism is considered to explain the decay in temperature of the plasma. For this investigation, the LIBS experiment is performed on the copper sample in the ambient atmosphere and evaluated the performance of the proposed model at three different focal positions. First, the experimental data is utilized for estimating the electron density, plasma temperature, radiation decay constant, and ablated mass. Further, the results from the experimental data are compared and evaluated with the model. The initial sections of the chapter briefly discuss the plasma temperature and electron density measurement techniques along with thermodynamic equilibrium conditions. Further, the details of the proposed model are explained in the last section.

Part of this chapter's work has been published as following journal article.

***Rajendhar Junjuri**, S.A. Rashkovskiy, M.K. Gundawar, "Dependence of radiation decay constant of laser produced copper plasma on focal position", Physics of Plasmas, (2020).*

3.1 Introduction

The LIP is highly transient, inhomogeneous, and very complex owing to the occurrence of various processes simultaneously in it. However, it can be spatially and temporally characterized by estimating the temperature and electron density which are considered as the two important properties of the LIP[1]. The temporal characterization of LIP is a valuable tool to gain information about plasma evolution and utilization of the complex sources of radiation from the plasma [2-4]. Several plasma characterization methods/techniques have been reported in the literature depending on the application of interest for the measurement of plasma parameters of LIP. Some of these are Langmuir probe[5], Thomson scattering[6], beam deflection[7], laser interferometry[8], fast imaging[9, 10], laser-induced fluorescence[11] and LIBS technique[12, 13], etc. Among all, LIBS can be considered as a simplest and nonintrusive analytical spectroscopic technique to study the dynamics of the LIP as it utilizes the intrinsic spectral emissions from the plasma. It can work as a non-contact diagnostic tool that does not require any external perturbation for the estimation of the plasma temperature and electron density. The analysis of the optical emissions emanated from the LIP based on the assumption of local thermodynamic equilibrium(LTE) condition allows the measurement of the electron density and plasma temperature[14]. The initial part of this chapter presents the same, where the optical emissions from the plasma are being utilized for the measurement of the aforementioned plasma properties.

The interest in modeling the kinetic evolution of LIP is growing due to its impressive number of applications such as starting from chemical analysis of the materials to medical therapy, from the production of micro or nano-structuring of surfaces/objects to the generation of energetic particles, from the research toward astrophysical investigation to the nuclear fusion studies[15]. The temporal characterization of LIP has paramount importance for improving the analytical performance of the following applications: (i) Laser-induced breakdown spectroscopy (LIBS) [16-18], (ii) Laser direct writing [19], (iii) Pulsed laser deposition [20], (iv) Generation of plasma light sources[21, 22], (v) Material processing[23] and (vi) Nanoparticle and cluster production[24, 25]. However, the kinetic evolution of the plasma properties imperatively depend on the characteristics of the laser

pulse, lens to sample distance (LTSD), ambient environment, various physical and chemical properties of the sample[26]. Especially, the LTSD can significantly affect the plasma parameters where the position of the sample surface with respect to the focused laser beam waist changes and leads to the variation of power density at the interaction zone. Also, by investigating the influence of LTSD on plasma properties, one can adjust the experimental conditions for achieving the optimum analytical performance. The evolution of the hierarchy of the fundamental processes involving in the expansion of the plasma plume makes the investigation indeed complex and theoretical works/studies are desirable for understanding the experimental data[23]. Nevertheless, only a little effort has been spent in understanding the kinetic evolution of the plasma properties and a systematic investigation is not performed in literature. Hence, it is of great importance to explore the kinetic evolution of plasma properties in both theoretical and experimental studies. In this complex framework of LIP, the present study aims at proposing theoretical modeling of the LIP and to delineate possible scenarios occurring in it which find application in the wide range of LIPs.

Multari *et al*. studied the influence of the LTSD on LIP in the ambient environment using spherical and cylindrical lenses. It was revealed that the amount of ablation, emission-line strengths, and the plasma temperature depend strongly on the LTSD for two lenses [27]. Li *et al* investigated the effect of the focal spot size on the kinetic evolution of the laser-produced Cu plasma. It was demonstrated that the expansion dynamics are similar, irrespective of the position of the target whether it is in front of the focal point or in the background when the spot size is the same[28]. Harilal *et al* have explored the effect of spot size on the conversion efficiency (CE) of LIP of Sn where the better CE was noticed away from the actual focal position[29]. It has been demonstrated that it is extremely important to study and understand the temporal evolution of excited species in the plasma (neutrals and ions) as these will acts as debris in the Sn plasma-based extreme ultraviolet (EUV) source. In another study, the variation of LTSD has shown a significant change in plasma temperature. It was ascribed to the plasma plume expansion as well as the shape at different LSTDs [2, 3]. Apart from that, it was observed that the change in ionic line intensity is more prominent compared to the neutral lines for the Zn target excited with the ns pulse [30].

In the present study, the effect of changing the lens position by small distances compared to the Raleigh range of the focused laser beam on the characteristic properties of Cu plasma is investigated. As well as a theoretical model for the kinetic evolution of the plasma temperature is proposed. The initial part (Section 3.2) of this chapter delineates the plasma diagnostic methods. The Boltzmann method (assuming LTE condition) is used for the estimation of the plasma temperature. The Stark broadening of the emission line is used for the estimation of electron density [1, 31, 32]. The subsequent section (3.4), present the results on intensity, decay time, temperature, electron density, and mass ablation studies. The last section (3.5) presents the theory of relaxation of the radiation model for the kinetic evolution of the plasma and validated with the experimental data.

3.2 Plasma diagnostic studies

3.2.1 An overview of thermodynamic equilibrium (TE) in plasma

The formation and evolution/expansion of the LIP involves various processes such as photo-excitation/ionization, collision excitation/ionization, radiative and three-body recombination, de-excitation, and Bremsstrahlung emission, etc. The LIP goes through a phase of strong ionization during the interaction laser pulse whereas recombination is dominant during plasma plume expansion and cooling[15]. Under thermodynamic equilibrium (TE), the whole plasma system which consists of atoms, electrons, ions, and radiation can be explained by the statistical mechanics, where the equilibrium distributions are described by a single temperature.

i.e., all the processes involved in LIP will be in equilibrium with each other in complete TE condition. It is possible only when the rate of each process is the same as that of the inverse processes which is also called as a “principle of detail balance”. For example, the collisional excitation and radiative decay are two inverse processes involved in the plasma evolution which lead to the population and de-population of the species respectively.

In TE, the “particle velocity distribution” has a Maxwellian distribution as given in equation 3.1

$$f(v) = 4\Pi v^2 \left(\frac{m}{2\Pi k_B T} \right)^{\frac{3}{2}} \exp^{\left(-\frac{mv^2}{2k_B T} \right)} \tag{3.1}$$

where, k_B is "Boltzmann constant", T is "temperature", v & m are "speed" and "mass" of the particle respectively.

The relative population distribution of the plasma species i.e., ions and electrons are governed by the following distribution (equation 3.2)

$$N_i = N_o \frac{g_i}{U(T)} \exp\left(-\frac{E_i}{k_B T} \right) \tag{3.2}$$

where, g_i, E_i and N_i represent the "statistical weight", "energy", and "population" of the corresponding (i^{th}) level respectively. $U(T)$, and N_o are "partition function", and the "total number density of the species" respectively.

The population of any particular species in different ionization states can be determined by the Saha–Eggert equation as given in equation 3.3

$$\frac{N_e N^{z+1}}{N^z} = 2\frac{U^{z+1}}{U_z} \left(\frac{2\Pi m k_B T}{h^2} \right)^{\frac{3}{2}} \exp\left(-\frac{E_z + E_{z+1} - \chi}{k_B T} \right) \tag{3.3}$$

where, N^z and N^{z+1} are correspond to the number density of z^{th}, $(z+1)^{th}$ ionization states respectively. N_e is "number density of the electrons", χ is "first ionization of an isolated system", h is "Planck's constant".

Finally, the photon energy can be determined by the "Planck's radiation law" at temperature (T), where the spectral energy density in the vacuum is given by equation 3.4

$$\varepsilon(v) = \frac{8\Pi h v^3}{c^3 (e^{hv/k_B T} - 1)} \tag{3.4}$$

Where c is "speed of the light".

However, most of the laboratory-based LIPs are non-homogeneous and highly transient in nature and can't be in complete TE condition. The plasma should be optically thick in order to achieve the radiative equilibrium. Although, it is not followed in LIP where the radiation/photons are get escaped from the plasma and deviates from the "planks radiation

law". However, if the energy loosed in the radiation process less than the other process then the Maxwell and Saha–Boltzmann distributions still be a valid approach for characterizing the LIP which is known as a "local thermodynamic equilibrium" (LTE). Under LTE, the population and depopulation of the atoms in the excited state, are dominated by electron collisions rather than the radiative process[33]. The minimum electron density, a necessary but not sufficient condition required to follow LTE is given by Mcwhirter criterion[34] as –

$$N_e \geq 1.6\times10^{12} T^{1/2} (\Delta E)^3 \tag{3.5}$$

Where ΔE (eV) is the energy difference between spectral line transitions.

The plasma can be considered as optical thin only if the emitted radiation is without being absorbed. If it is thick, the radiation emitted from the core of the plasma gets absorbed by the outer layer where the atoms are in relatively less temperature region. Thus, the emission lines will show a dip at the center of the spectral line which is also called as "self-absorption". The branching ratio is determined to verify the "optical thin condition" and it is given in equation 3.6

$$\left(\frac{I_{ij}}{I_{mn}}\right)=\left(\frac{\lambda_{mn}}{\lambda_{ij}}\frac{A_{ij}}{A_{mn}}\frac{g_i}{g_m}\right)\exp\left(-\frac{E_i-E_m}{kT}\right) \tag{3.6}$$

Where λ_{ij}, A_{ij}, E_i, and I_{ij} represent the "wavelength", "transition probability", "upper energy level", and "intensity" of the corresponding spectral line respectively. m & i and n & j correspond to the upper and lower energy levels of a particular transition respectively. If the spectral transitions considered for the analysis possess the same upper energy level then the equation 3.6 can be modified as equation 3.7

$$\left(\frac{I_{ij}}{I_{mn}}\right)=\left(\frac{\lambda_{mn}}{\lambda_{ij}}\frac{A_{ij}}{A_{mn}}\frac{g_i}{g_m}\right) \tag{3.7}$$

The plasma can be considered to be optically thin only if the experimental intensity ratio matches with the theoretical ratio as given in equation (3.7).

3.2.2 Measurement of plasma temperature

The temperature and electron density are the characteristic properties of plasma which influence the spectral emissions of the plasma[35]. Under LTE, the population of neutral or ionic species at a particular temperature follows a Boltzmann distribution as given in equation 3.2. The integrated intensity of the emitted radiation from the plasma at a wavelength is given by

$$I_{ij} = \frac{N_o hcg_i A_{ij}}{\lambda_{ij} Z(T)} \exp\left(-\frac{E_i}{k_B T}\right) \tag{3.8}$$

where, h, Z(T), k_B, and T are "Planck's constant (eV S)", "partition function", "Boltzmann constant (eV K^{-1})", and "excitation temperature (K)" respectively. λ_{ij}, A_{ij}, E_i, and I_{ij} represents the "wavelength (nm)", "transition probability (s^{-1})", "upper energy level (eV)", and "integrated intensity" of the corresponding spectral line respectively. i and j correspond to the upper and lower energy level of the spectral transition respectively. The plasma temperature has been estimated from the Boltzmann plot method as given by the equation (3.9)

$$\ln\left(\frac{I_{ij}}{A_{ij}}\frac{\lambda_{ij}}{g_i}\right) = -\frac{E_i}{k_B T} + \ln\left(\frac{hcN_o}{Z(T)}\right) \tag{3.9}$$

All the spectroscopic parameters (A_{ij}, g_i, and E_i) of the corresponding spectral transitions are available in the NIST database[36]. The Boltzmann plot obtained by fitting the experimental data to a straight line (X=E_i, Y=$\ln(I_{ij}\lambda_{ij} / A_{ij}g_i)$, and the temperature estimated from the slope of the fitted line (slope = $1/k_B T$). Fitting the experimental data to linear approximation not only validates the assumption of a Boltzmann distribution but also serves as a crosscheck for the errors in transition probability value or line assignment[21, 37]. In general, only two lines are sufficient for the linear fit provided by those lines have their energy levels are well separated from each other[21, 37]. However, the accuracy in plasma temperature estimated from the Boltzmann plot can be improved by considering the more number of spectral transitions which are also having the upper energy level well separated from each other. Also, the transition which terminates to the ground state needs to be eliminated from the analysis otherwise the self-absorption leads to incorrect measurement of plasma temperature.

3.2.3 Measurement of electron density

Electron density is another characteristic parameter of the plasma which has been determined from full–width at half maximum (FWHM) of the Stark broadening of the spectral line [38]. The width and shape of the spectral lines are influenced by collisional processes[17]. Three mechanisms can contribute to the broadening of the spectral lines viz, natural, Doppler, and Stark broadening. However, the broadening corresponding to the natural linewidth is extremely small and can be neglected. The Doppler broadening ($\Delta\lambda_D$) can be determined from equation 3.10

$$\Delta\lambda_D = 7.16\times\lambda_{ij}\times10^{-7}\sqrt{\frac{T}{M}} \tag{3.10}$$

where M is the atomic mass in a.m.u. It is found from the literature the broadening corresponding to Doppler Effect is in the order of ~ 1-10 pm which is very small compared resolution of the spectrometer (throughout the thesis, "Andor-Mechelle" and "Ocean optics-Maya" spectrometers are deployed for the experiments which are having a resolution of 100 pm and 1000 pm at 500 nm respectively) and can be neglected. Hence, among the three mechanisms considered, only Stark broadening can be utilized for the estimation of the electron density. The energy levels of the spectral emission from the LIP are get shifted by the impact of electric fields produced from the plasma species (electrons and ions) and leads to spectral broadening which is also called as "Stark broadening". The electron density is calculated using the FWHM of the spectral line according to Stark broadening as shown in equation (3.11)

$$\Delta\lambda_{1/2} = 2\omega\frac{N_e}{10^{16}} + 3.5A\left(\frac{N_e}{10^{16}}\right)^{\frac{1}{4}}\left[1-1.2N_D^{\frac{-1}{3}}\right]\omega\left(\frac{N_e}{10^{16}}\right) \tag{3.11}$$

where 'A' is the "ion broadening parameter" and N_D is "number of particles" in the Debye sphere. By neglecting the small contribution of ions, equation (3.11) can be simplified as

$$\Delta\lambda_{1/2} = 2\omega\frac{N_e}{10^{16}} \tag{3.12}$$

where ω is the "impact width parameter", $\Delta\lambda_{1/2}$ is "FWHM" of the corresponding spectral line, and N_e is "electron density".

In the next sections, details of the experiment as well as the results are discussed.

3.3 Experimental details

The schematic of the LIBS experimental setup is shown in Chapter2 (Fig. 2.6.) [39]. The laser beam (7 ns, 532 nm, and 90 mJ/pulse) was focused onto the Cu sample by using a Plano-convex lens of focal length 15 cm. The lens was mounted on a translation stage which allowed its movement along the laser beam propagation direction. The experiment was performed at three focusing conditions which are represented by X_0, X_1, and X_2 as shown in the inset in Fig. 3.1. However, the movement of focal position is within the Raleigh range and the estimated value of the Raleigh range is found to be ~ 9 mm. Only the lens was moved with the aid of the micrometer screw to change the focal position with respect to the sample surface. X_0 is the centre of the plasma produced in ambient air in the absence of the Cu sample. .i.e. the position represents the centre of the beam waist. The plasma length was scanned using a translation stage to locate this centre. X_1 represents the position of the Cu sample surface at 1.5 mm above/before the X_0 whereas X_2 corresponds to the position below/after X_0 as shown in the inset in Fig. 3.1. The motivation behind considering the three positions to study the effect of focal position on plasma properties and to evaluate the proposed theoretical model for different conditions.

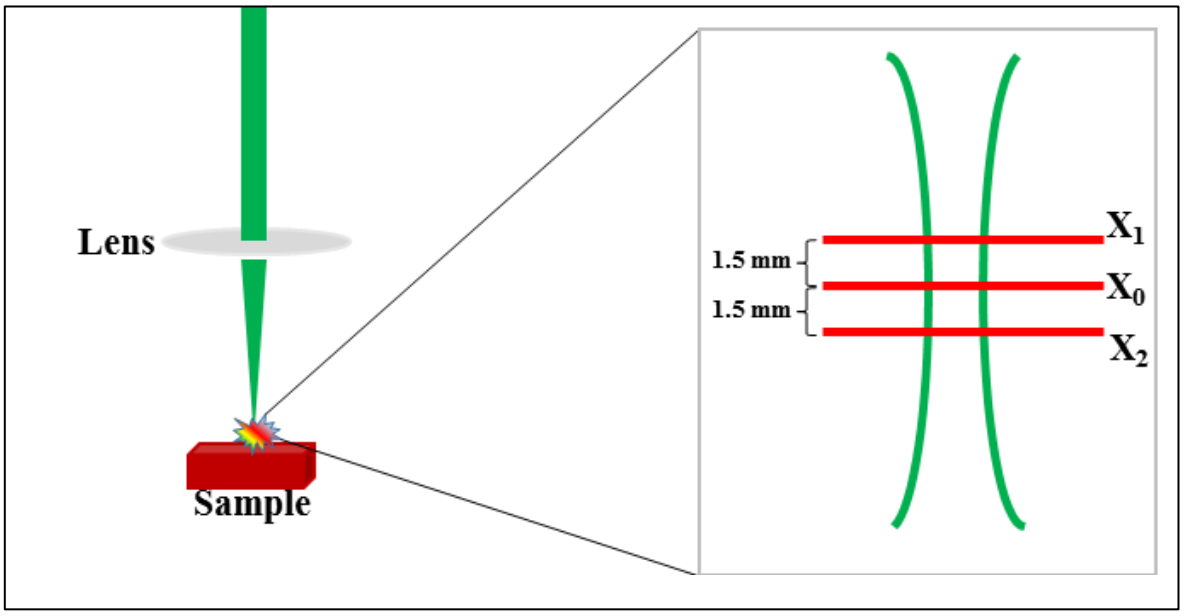

Fig. 3.1. The schematic of the typical LIBS experimental setup. The inset represents the focused laser beam waist.

The LIBS spectra were recorded in two modes viz, 1) Time integrated, and 2) Time-resolved/evolution. A total of 20 spectra for each mode were recorded where each spectrum is acquired by accumulating the ten consecutive laser shots to improve the signal to noise ratio. The ICCD gain was set to be 100. The time-integrated spectra recorded with the gate delay of 0.5 μs and a gate width of 2 μs whereas the time evolution spectra were recorded in the temporal window 0.5 – 4.5 μs in steps of 0.5 μs with a constant gate width of 0.5 μs.

3.4 Results and discussion

3.4.1 Description of the LIBS spectral lines

A typical Cu LIBS spectrum recorded at X_0, X_1, and X_2 is shown in Fig. 3.2. The LIBS spectra look similar but with a change in spectral line intensities for the three positions. The spectrum is visualized in two separate spectral windows of 250-400 nm (Fig. 3.2a) and 400-800 nm (Fig. 3.2b) with different intensity scales for the better view of the spectral lines.

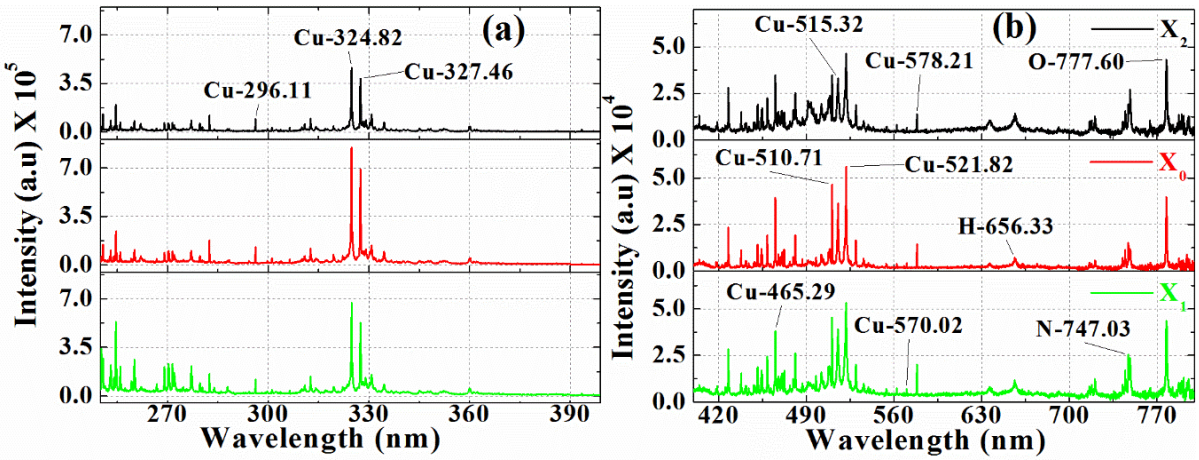

Fig. 3.2. The Cu LIBS spectra acquired at X_0, X_1, and X_2. (a) & (b) correspond to the 250-400 & 400-800 nm spectral windows respectively. The intensity scales are considered different for two graphs for better visualization.

The energy level diagram of the Cu is shown in Fig. 3.3 in which all the prominent transitions are presented. The spectrum is composed of numerous Cu strong lines such as 578.35, 521.82, 515.32, 510.71, 465.29, 327.46 324.82, and 296.11 nm. The spectral emissions from the air plasma (Hydrogen, Nitrogen, and Oxygen) also appeared in the

spectra and represented at their characteristic wavelengths (H-656.33, N-747.03, and O-777.60 nm. Two dominant Cu lines viz., 324.82, and 327.46 nm are prevailed in the first part of the spectrum (250-400 nm) with the former having a higher intensity. The second part comprises the various other strong Cu lines along with the spectral features of omnipresent elements. It is observed that the spectral intensities are highest at X_0 and least at X_2 whereas the intensities at X_1 are lying between the intensities at X_0 and X_2. It can be explained as follows. In the case of X_2, the sample surface is located after the X_0 (i.e. the exact focus is ahead of the sample surface as shown in Fig. 3.1) in contrast to X_1 and X_0.

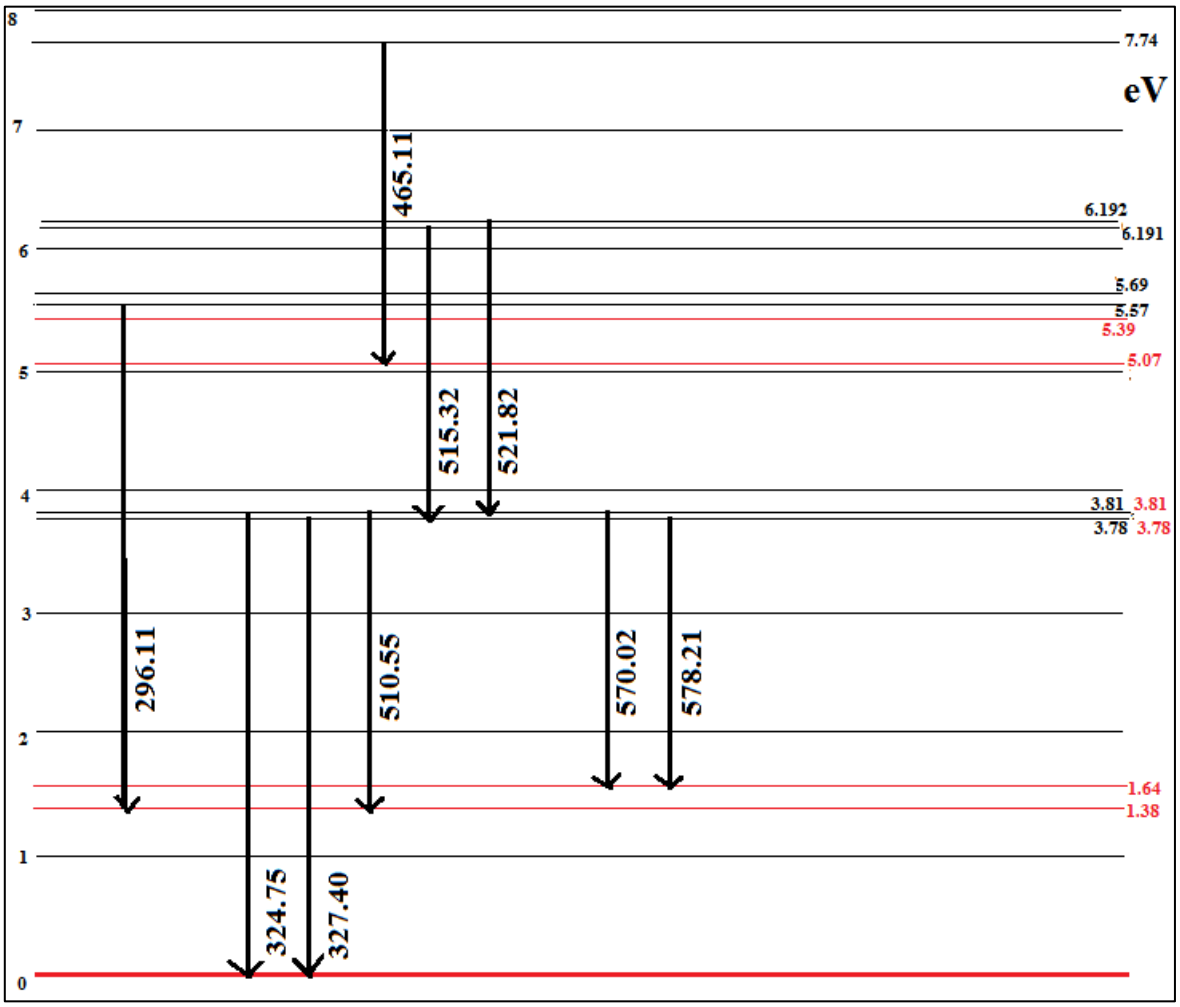

Fig. 3.3. Energy level diagram of the Cu neutral transitions. Red and black colors correspond to the lower and upper energy levels of the particular transition respectively.

In this scenario, the laser-induced breakdown occurs in ambient air which is similar to the absence of a copper sample. As a result, the main absorption of laser energy is utilized in the formation of air plasma, which shields the surface of the sample from the direct

interaction of the laser beam. Thus, in these conditions, the ablation of the sample happens owing to the heat entering from the discharge zone to the sample surface as a result of heat conduction and thermal radiation. The amount of this heat is much less than compared to the amount of heat entering the sample under the direct interaction of laser bean on its surface. It is confirmed by evaluating the efficiency of Cu evaporation under the influence of laser radiation (see Table 3.3).

As aforementioned X_0 corresponds to the sample surface kept at the exact focal position and X_1 represent the sample surface is located before the X_0 (i.e. is the exact focus is behind the sample surface as shown in the inset in Fig. 3.1) Thus, at X_1 and X_0, the laser pulse directly interacts with the sample surface leads to the plasma formation. As a result, the efficiency of Cu evaporation under the action of the laser pulse and mass of evaporated Cu is higher compared to the X_2 (see Table 3.3). It results in the formation of plasma with higher spectral line intestines at X_0 and X_1 compared to the X_2. Further, in order to estimate the stability in laser energy coupling to the sample surface (i.e. LIB) at X_0, X_1, and X_2, the intensities of four strong lines (324.82, 327.46, 510.17, and 515.32 nm) are compared and illustrated as a bar graph in Fig. 3.4(a-d).

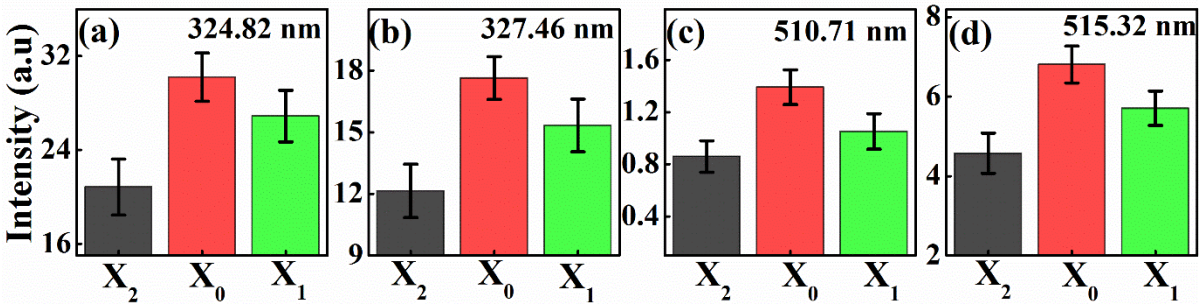

Fig. 3.4. The comparison of the four spectral line intensities. a) 324.82 nm, b) 327.46 nm, c) 510.71 and d) 515.32 nm.

Here, the intensity of a spectral line refers to the area obtained from the Lorentzian fit of the corresponding peak. The error bar in Fig. 3.4 represents the standard deviation of the intensities of the corresponding emission line obtained from the twenty spectral measurements. It is noticed that the variation of intensities from one spectrum to another is in the order of ~ 10 % which ascertains the stability of the spectral measurements at three LTSDs[40]. A similar trend is noticed for the other spectral features also thus not

shown in here. In the next sections, the kinetic evolution of the Cu spectral lines, plasma temperature, and electron densities at three focusing are explored.

3.4.2 Temporal evolution of the plasma

During the expansion of LIP in the ambient gas, the plasma cools down by emitting the intense electromagnetic (EM) radiation and also by the generation of sound and shock waves [9, 41, 42]. The LIP radiation comprising of a continuum as well as discrete lines of atomic and ionic emissions of the constituent elements of the target depending on the acquisition delay time. The time evolution spectra recorded in the time window of 0.5 – 5 μs in steps of 0.5 μs at X_0, X_1, and X_2, is presented in Fig. 3.5(a-f). The kinetic decay of five strong spectral lines (324.82, 327.46, 510.17, 515.32, and 521.82 nm) are shown in Fig. 3.5(a-f). A strong continuum is prevailed in the spectra at the initial times (at 500 ns) due to the Bremsstrahlung emissions and it is decreased with increasing delay time as shown in Fig. 3.5(a-f). The spectral intensities decreases during the expansion of the plasma due to the decrease in plasma temperature. It also happens due to the de-excitation of the plasma species during the collisions. It is noticed that spectral emissions at X_0 focal position are persisting for a longer time in comparison to the other two positions. The times required to reach 50 % of the initial intensity (it is the area under the peak) for all the lines at X_0, X_1, and X_2 are given in Table 3.1.

Table 3.1. Time (μs) required for the decay of spectral line intensities to 50 % of their initial value.

	324.82 nm	327.46 nm	510.71 nm	515.32 nm	521.82 nm
X_2	1.05	1.12	1.24	0.96	1.03
X_1	0.95	0.95	1.32	1.17	1.14
X_0	1.2	1.23	1.72	1.28	1.36

The intensities of the 324.82, and 327.46 nm lines decrease to 50 % of its initial intensity within 1.25 μs and up to 10 % within 5 μs. The intensity of 510.71 nm line decreases to 50 % of its initial value within 2 μs and have shown a higher lifetime among all spectral lines. The decay of spectral line intensities are in general modelled to exponential decay in the literature however no theoretical model developed to explain the decay to the best of my

knowledge. In the subsequent sections the plasma properties are determined and a theoretical model was developed for the decay of plasma temperature.

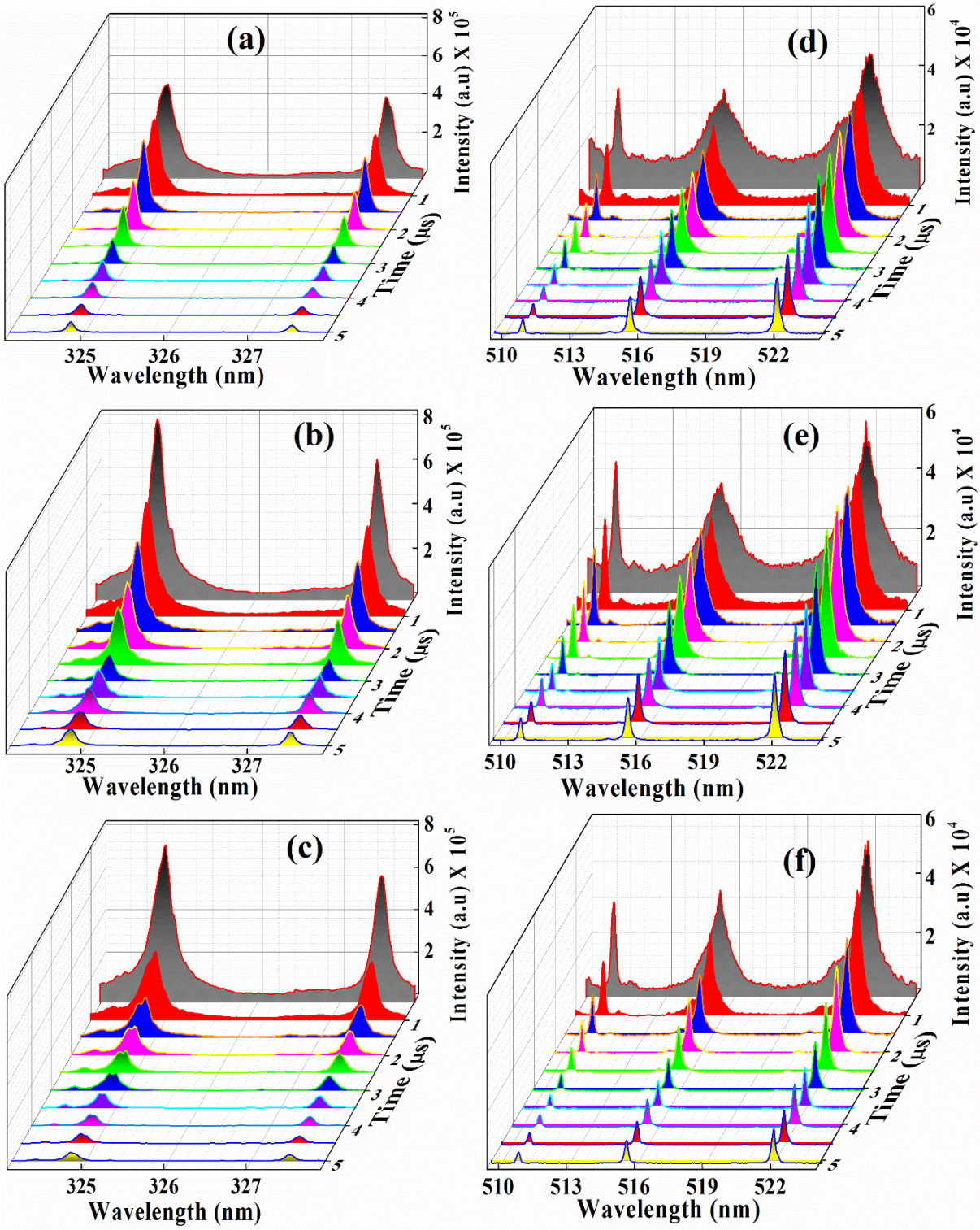

Fig. 3.5. Time evolution of the Cu 324.82, 327.46 nm spectral lines at a) X_2, b) X_0, and c) X_1. Time evolution of the Cu 510.71, 515.32 & 521.82 nm spectral lines at d) X_2, e) X_0, and f) X_1.

3.4.3 Temporal evolution of the plasma temperature

Four Cu neutral lines at 465.11, 510.17, 515.32, and 521.82 nm were chosen for the measurement of plasma temperature. The required spectroscopic parameters of the corresponding spectral lines were taken from the NIST database and the same presented in Table 3.2.

Table 3.2. Spectroscopic parameters of the Cu lines. Relative line intensity intended to represent the strengths of the corresponding lines of a Cu as they would appear in emission.

S.No	Wavelength (nm)		A_{ij}	g_i	(E_i)Energy (eV)		Relative line intensity
	Observed	Actual	$(s^{-1})*10^7$		Upper	Lower	
1	465.29	465.11	3.8	8	7.737	5.072	2000
2	510.71	510.55	0.2	4	3.817	1.389	1500
3	515.32	515.33	6.0	4	6.191	3.786	2000
4	521.82	521.82	7.5	6	6.192	3.817	2500

The 2nd and 3rd columns of Table 3.2 represent the wavelengths of the spectral transitions observed and standard values taken from the NIST database respectively. The Boltzmann plot constructed by using four lines at three focal positions at 500 ns delay is depicted in Fig. 3.6(a). The symbols represent the actual data and the solid/dotted line corresponds to the linear fit. The same procedure has been performed for the remaining delays and also for twenty spectral measurements.

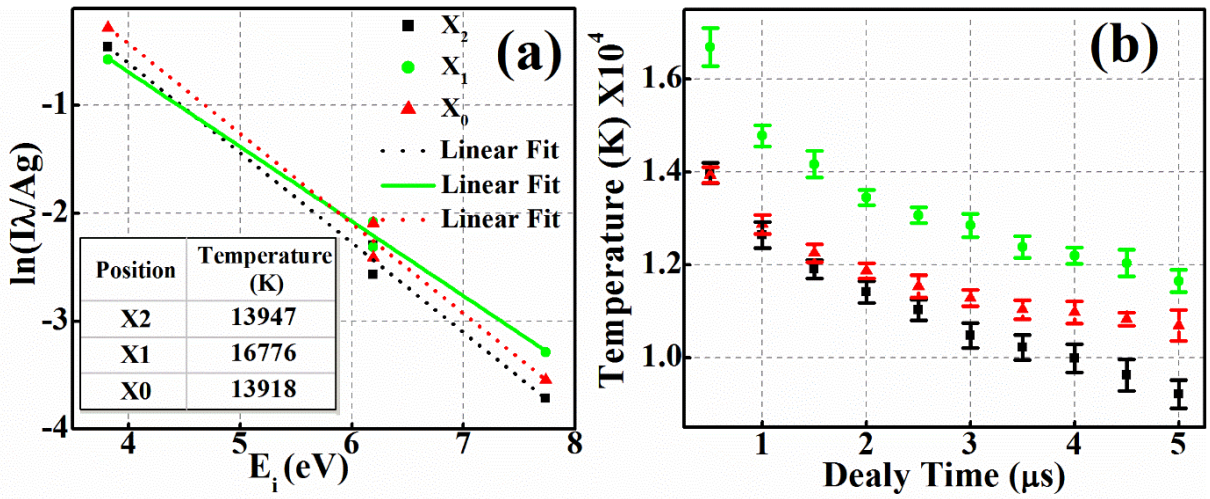

Fig. 3.6. a) Boltzmann plot obtained at three positions at 500 ns delay time. b) The variation of the plasma temperature with time.

Each time, this dependence has been approximated by a straight line with the correlation coefficient of more than 0.995 which allows determining the corresponding plasma temperature. The temperatures calculated as a function of time at each position are shown in Fig. 3.6(b). The maximum plasma temperature $\sim 16700 \pm 400$ K is obtained at X_1 focal position, and it decreases to $\sim 11600 \pm 200$ K within 4.5 μs as shown in Fig. 3.6(b).

The temperature at X_1 is higher compared to the other two focal positions, and the reason can be explained as follows. The plasma shielding could be possible during the early time scales of the plasma formation (10^{-9}–10^{-8} s) where the leading edge of the laser pulse initiates it and the trailing part absorbed by the plasma [43]. However, it depends on pulse duration, ambient environment, irradiance, and sample. After initiation of the laser pulse, the absorption primarily occurs by the inverse Bremsstrahlung (IB) mechanism, which involves the absorption of a photon by free electrons in the focal volume [2, 17, 44, 45]. It further increases during the collisions with heavy particles (ions and atoms) which predominantly depends on the number density of the free electrons. In the present experiment, plasma shielding could be possible at the X_1 position where the laser beam directly interacts with the Cu sample. At X_1 focal position raising part of the laser pulse can interact with the more number of atoms (as solid density is more compared air) which favors the strong IB absorption and the trailing part may lead to the plasma shielding. Further, the plasma can be reheated[43] during the shielding process and result in higher temperature plasma at X_1. Apart from that, plasma shielding can prohibit the later part of the laser pulse to interact with the sample surface thus resulting in a lower ablation rate. It is evident from the crater studies (section 3.4.5) of the ablated samples where the crater depth obtained at X_1 is less. At the other two positions viz., X_2, and X_0, the laser pulse does not directly interact with the sample surface. At these two positions, the available number density of free electrons at the focal position is less in comparison with the X_1, and the plasma shielding mechanism is not feasible. Hence, the plasma reheating is also not favorable which leads to the formation of less temperature plasma. It is also asserted by the mass ablation measurements where the amount of ablated mass and crater depth are higher compared to the X_1 which could be due to the absence of plasma shielding effect.

3.4.4 Temporal evolution of the electron density

The electron density[38, 46] is estimated by utilizing the Stark broadening method by employing Cu -510.57 nm spectral line. The broadening corresponding to the natural linewidth is extremely small and neglected. As well as the Doppler broadening estimated for the Cu spectral line at 510.57 nm for the present experimental conditions is of the order of ~ 0.006 nm. It can also be neglected since the resolution of the spectrometer is ~ 0.1 nm. The impact width parameter 'w' corresponding to the spectral line, necessary for calculating N_e is taken from the literature[47]. To obtain the FWHM of the corresponding spectral line, the shape of the spectral line is fitted to a Lorentzian as shown in Fig. 3.7(a).

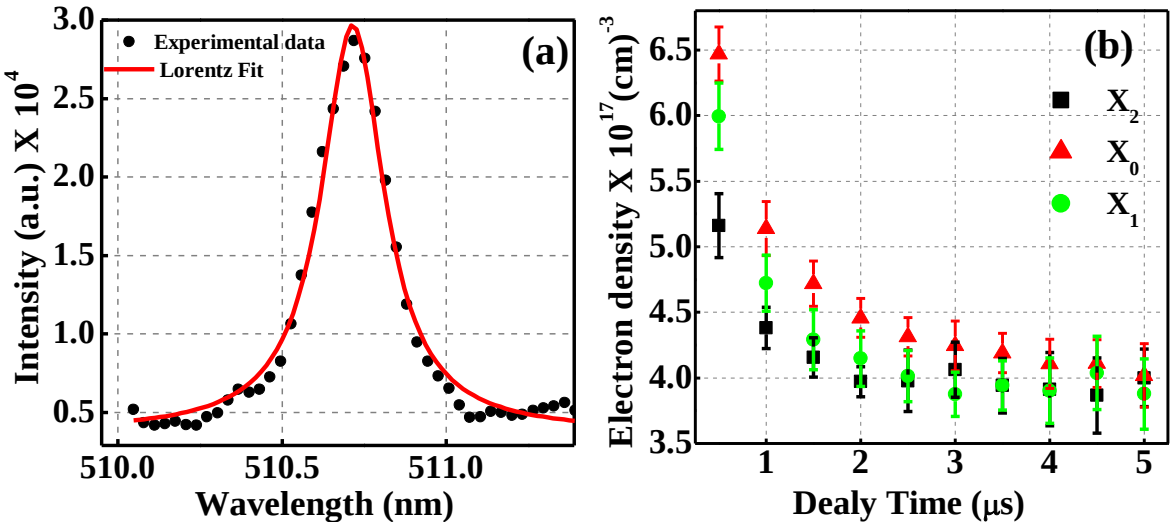

Fig. 3.7. a) Lorentzian fit of the Cu-510.57 nm spectral line. b) Variation of electron density as a function of time.

The electron densities estimated using equation (3.12) for the temporal window of 0.5 – 4.5 μs are shown in Fig. 3.7. The highest electron density is observed at X_0 and followed by X_1 and X_2. Electrons in the plasma recombine with the ions during the expansion phase of the plasma, which leads to the reduction of the electron number density at later time scales. The electron density decays rapidly in the first 2 μs, and after this, it decreases very slowly. The maximum electron density obtained at X_0 could be due to the maximum coupling of light to target leading to more ablation as observed in the crater studies (section 3.4.5). The air breakdown at X_2 can result in less ablation rate which is also revealed in the crater

studies of the sample as shown in Fig. 3.9 in section 3.4.5. The crater depth and also the amount of ablated sample is minimum compared to the other two focal positions.

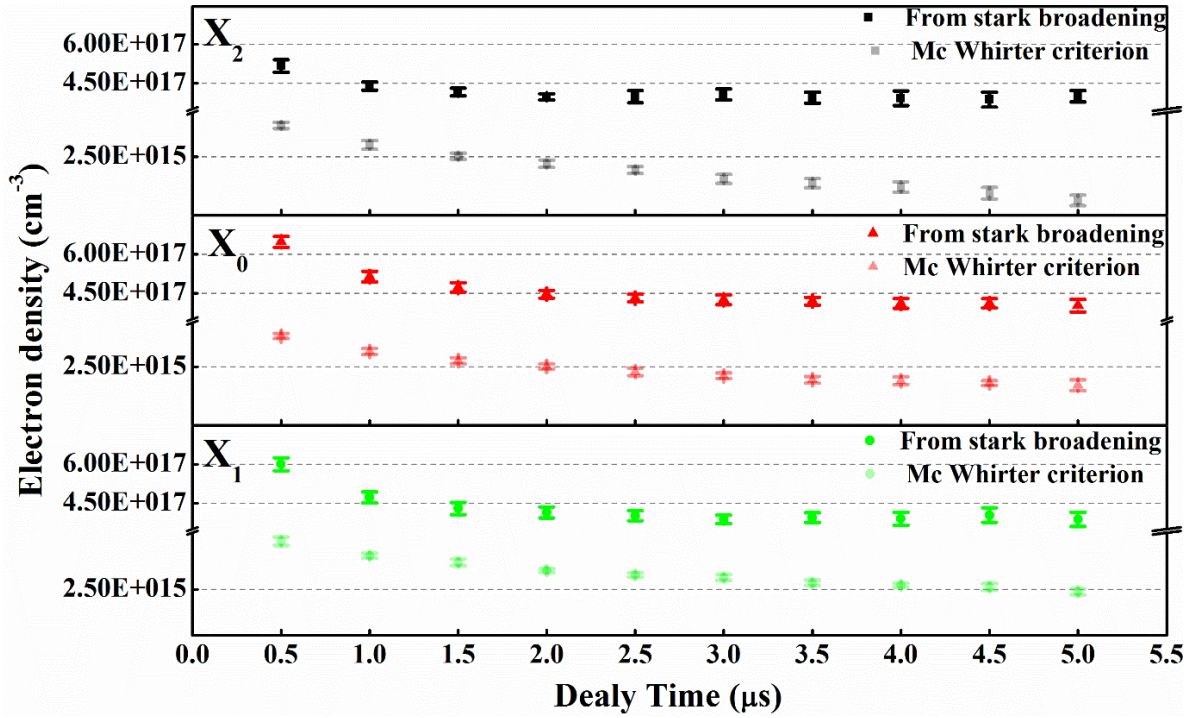

Fig. 3.8. Comparison plot of the electron densities measured from the stark broadening and Mc Whirter criterion respectively.

In addition, the validity of the local thermodynamic equilibrium (LTE) condition can be tested by evaluating the McWhirter criterion (a necessary condition). Fig. 3.8 represents the electron densities measured from the Stark broadening method and McWhirter criterion at three focal positions. It is evident from Fig. 3.8 that the measured electron densities (~ 3-7 X 10^{17} cm^{-3}) are two orders higher than the electron densities (~ 2-3 X 10^{15} cm^{-3}) obtained from McWhirter criterion. Thus, in the current study, the McWhirter criterion is satisfied at X_0, X_1, and X_2 which validate the LTE assumption.

3.4.5 Crater studies on the sample surface

Under the action of an incident laser beam, the ablation of the sample occurs and leads to the formation of a crater on the sample surface. The ablated crater was characterized by the profilometer which determines the surface and depth profile. The crater profiles

formed by the irradiation of the ten consecutive laser shots on the sample surface are shown in Fig. 3.9.

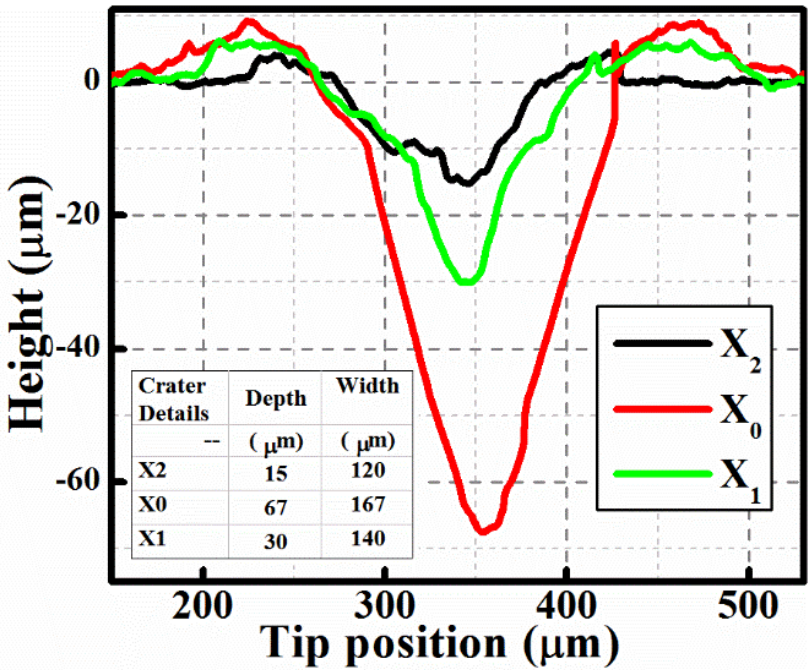

Fig. 3.9. Profilometer measurements of the crater of the Cu samples. Zero on the y-scale represents the sample surface.

The profilometer probe is scanned across the irradiated crater zone to obtain the depth and width of the crater. Position y=0 (on the y-axis) as shown in Fig. 3.9 corresponds to the surface of the initial sample while the little hill-like structure on either side of the crater indicates the re-deposition of the ejected mass of the sample from the crater. The crater formed at X_0 focal position has the greatest depth of about 67 μm while at X_1 and X_2 it is about 30 and 15 μm respectively. The amount of mass ablated from the crater is estimated by considering the crater shape as a cone (see Table 3.3). As explained in section 3.4.1 air breakdown at X_2 can lead to the reduction of the coupling of the laser energy to the sample and results in a very less ablation rate where the crater depth and amount of mass ablated is least shown in Fig. 3.9. The ablated mass is correlated with the spectral line intensities of the plasma as shown in Fig. 3.10. It represents the correlation of Cu spectral lines 324.82, 327.46, 510.71, and 515.32 nm with the ablated mass. It is observed that the spectral line intensities are increasing linearly with the ablated mass. It is due to the more ablation leads to a higher number of excited species in the plasma and results in higher intensities and vice versa.

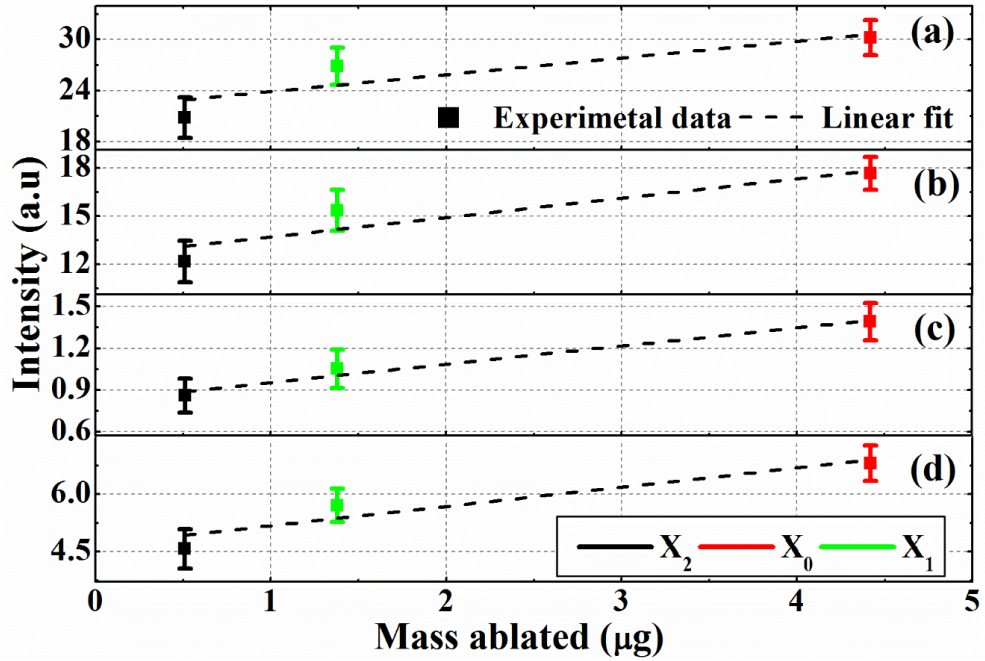

Fig. 3.10. Correlation of the Cu spectral line intensity with the mass ablated. a) 324.82 b) 327.46 c) 510.71, and d) 515.32 nm.

Various parameters of the plasma such as decay constant, electron density, and temperature are correlated with the amount of the mass ablated as shown in Fig. 3.11. The electron density is shown a positive linear correlation with the ablated mass it can be understood as follows. The electron density is proportional to the number of excited atoms, which, in turn, is proportional to the ablated mass.

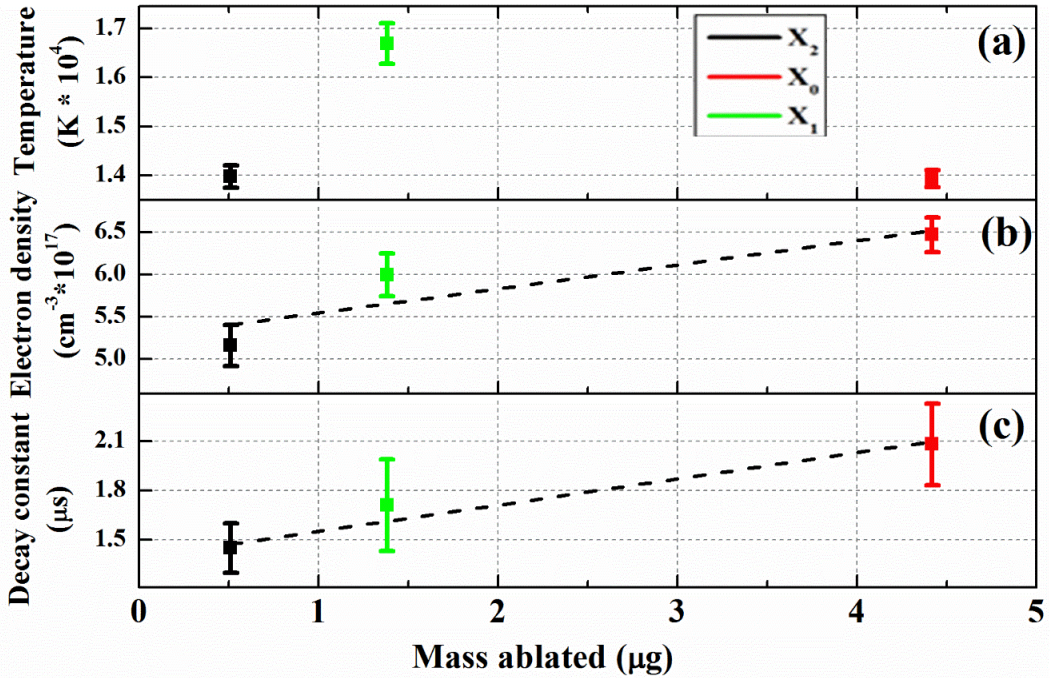

Fig. 3.11. Correlation of the different parameters of LIP with the ablated mass. a) plasma temperature, b) electron density, and c) decay constant.

On the contrary, the plasma temperature changes non-monotonously with the change in the ablated mass and has a maximum at X_1 while the maximum of ablated mass is observed at X_0. The maximum temperature at X_1 can be attributed to the reheating of the plasma during the plasma shielding process (detailed explanation is already given in section 3.4.3). Similar results were also observed in the literature for varying focusing conditions [48]. The decay constant is also varying linearly with the ablated mass. The kinetic evolution of the spectral line intensities of the plasma is generally modeled to exponential decay. However, no theory is available in the literature to understand the relation. Thus, in the next section, the theory of relaxation is proposed to explain the kinetics of the plasma temperature and validate it with the experimental data.

3.5 Theoretical model for kinetic evolution of the plasma

The plasma temperature and electron density rapidly decrease with the time after termination of the laser pulse. The study of the temporal evolution of plasma temperature and electron density is of prime importance as many kinetic reaction rates indirectly or directly depend on these parameters[21]. However, the diagnosis of LIP is a challenging job due to the fundamental plasma quantities vary dramatically in time and space. Hence, in this section, a theoretical model is proposed for the kinetic evolution of the LIP based on the radiation mechanism.

For the present study, the duration of the laser pulse Δt_L is ~ 7 ns. It is the characteristic time of the formation of the plasma plume whereas the duration of the process of plasma radiation relaxation $\Delta t_r \sim 5\ \mu s$; i.e. $\Delta t_r / \Delta t_L >> 1$. After the formation of the plasma, a decrease in temperature occurs, caused by the loss of heat due to the thermal conductivity of air and thermal radiation. The heat flux density due to thermal conductivity can be estimated by the following equation

$$q_\lambda = \frac{\lambda T}{L} \tag{3.13}$$

where λ is the coefficient of thermal conductivity of the medium, T is the plasma temperature, L is the characteristic distance at which the temperature drops from T to the ambient temperature ($T_o << T$).

The energy flux density due to thermal radiation from "Stefan-Boltzmann law" is given as

$$q_r = \sigma T^4 \tag{3.14}$$

where σ is the "Stefan-Boltzmann constant"

Further, the ratio of heat flux due to the thermal conductivity and thermal radiation is given as

$$\frac{q_\lambda}{q_r} = \frac{\lambda}{LT^3} \tag{3.15}$$

By considering λ=0.5 w/mK (for air corresponds to a temperature of $>$ 3000 K), T= 10^4 K. The estimated ratio $(\frac{q_\lambda}{q_r})$ is found to be ~ 0.01 which demonstrates that in the process under consideration, the thermal conductivity can be neglected in comparison with thermal radiation. Thus, the thermal conductivity of air cannot explain the dependences of observed Cu spectral line intensities on time. Therefore, only the radiative mechanism is considered for reducing the temperature of the plasma. In this case, the energy conservation law for the plasma can be written in the form

$$mc_v \frac{dT}{dt} = -S\sigma T^4 \tag{3.16}$$

Where m is the mass of the plasma, S is the surface area of the plasma plume, and C_v is the specific heat of the plasma cloud. All these parameters (m, S, and C_v) are assumed to be constant and the solution of the equation (3.16) is obtained as follows

$$\int \frac{dT}{T^4} = -\frac{S\sigma}{mc_v} \int dt$$

$$-\frac{T^{-3}}{3} + Int.const = -\frac{S\sigma}{mc_v} t \tag{3.17}$$

By applying boundary conditions i.e. at time t=0 (it is the time of the termination of the laser pulse), T=T_m, where T_m is the initial temperature of the plasma channel

$$Int.const = \frac{T_m^{-3}}{3}$$

by substituting the integration constant in equation 3.17

$$-\frac{T^{-3}}{3}+\frac{T_m^{-3}}{3}=-\frac{S\sigma}{mc_v}t$$

$$\frac{T^{-3}}{3}=\frac{T_m^{-3}}{3}\left(1+\frac{3S\sigma tT_m^{3}}{mc_v}\right)$$

$$T^{-3}=T_m^{-3}\left(1+\frac{3S\sigma tT_m^{3}}{mc_v}\right) \tag{3.18}$$

$$\tau=\frac{mc_v}{3S\sigma T_m^{3}} \tag{3.19}$$

Where 'τ' is the characteristic time (decay constant) of the radiative cooling of the plasma and equation 3.18 is modified as

$$T=T_m\left(1+\frac{t}{\tau}\right)^{-\frac{1}{3}} \tag{3.20}$$

The experimental data described in previous sections is modeled with the theoretical dependencies as given in equation (3.19) and (3.20). When processing the experimental data using the expression (3.20), the parameters T_m and τ are considered as fitting parameters. The experimental data obtained from the Boltzmann plot method (see Section 3.4.3) for the laser beam focused at X_0, X_1, and X_2 are shown in Fig. 3.12(a, b & c) respectively by markers. The theoretical dependences of the plasma temperature on time obtained using equation (3.20) are shown in Fig. 3.12 by solid lines.

According to equation (3.18),

$$\tau T_m^{3}=\frac{mc_v}{3S\sigma} \tag{3.21}$$

The values of the parameter τT^3_m for the different positions of the focus are indicated in Table 3.3. We see that the parameter τT_m^3 has the same order for all positions of the focus but its value is different for different positions of the focus. The biggest difference is observed for the X_2 focal position. This may be due to the difference in the mass (m) and the surface (s) of the plasma produced by the action of a laser pulse. The evaporated mass of Cu can be estimated by the expression $m=\eta J/\lambda$ where J is the energy of the laser pulse 90 mJ, η is the efficiency of Cu evaporation under the action of the laser pulse, λ is the latent heat of Cu evaporation ($\lambda=4.8\times10^6$ J/kg). As a result,

$$m\approx 19\eta\ \mu g \tag{3.22}$$

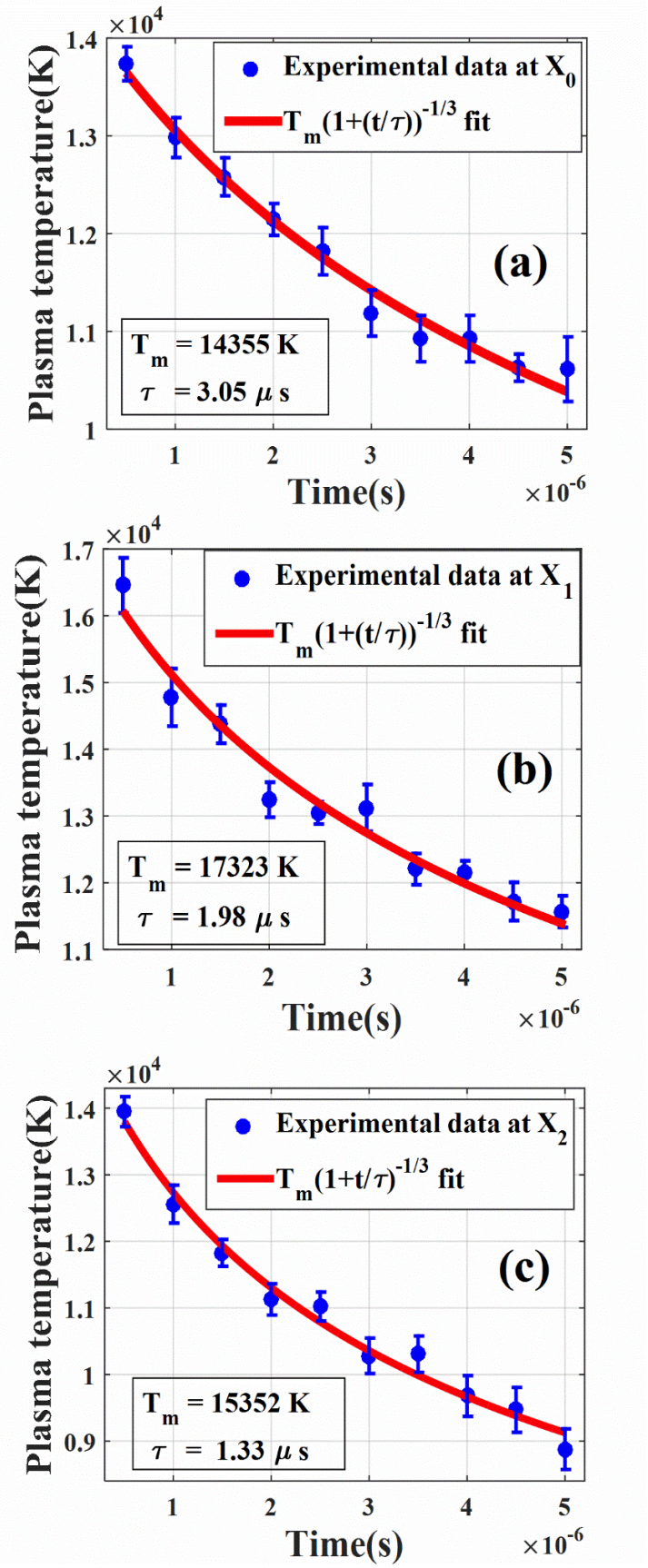

Fig. 3.12. Dependence of the plasma temperature (T) on time (t) at a) X_0, b) at X_1 and, c) at X_2. The markers and solid lines represent the experimental data and the theoretical fit respectively.

If the plasma plume has the shape of a cylinder with a diameter of 0.1 mm and a length of 1 mm, then $S = 0.3 \times 10^{-6}$ m^2

$$\tau T_m^{\ 3} = 370 X 10^6 \ \eta \tag{3.23}$$

Taking into account the data from Table 3.3, we can estimate the mass of evaporated Cu and the efficiency of Cu evaporation under the action of the laser pulse using equations (3.22) and (3.23). The results of the calculations are shown in Table 3.3. The mass 'm' determined using equation (3.22) (i.e. based on the experimental data on the change in temperature of the plasma with time) with ablated mass calculated from the results of crater measurements is compared. Taking into account that the craters (Fig. 3.9.) were obtained as a result of ten shots, the ablated mass of a sample per shot is about 10 times smaller. This result is in order of magnitude consistent with the mass determined using equation (3.22). At the same time, quantitative coincidence takes place only for X_0 focal position.

Table 3.3. Fitting parameters of the theoretical dependence of equation (3.20) for different locations of the focus.

S. No	Parameters	X_2	X_0	X_1
1	τ (μs)	1.33	3.05	1.98
2	T_m (K)	15352	14355	17323
3	Deviation in T, %	4.2	2.2	2.8
4	$\tau\ T^3_m \times 10^6$ (s·K^3)	4.81	9.02	10.3
5	Ablated mass (μg) (Experiment)	0.52	4.45	1.35
6	η	0.013	0.024	0.028
7	m (μg) (Theoretical model)	0.25	0.46	0.53

For other focal positions, the actual ablated mass, determined from the crater measurements, is less than the mass calculated by equation (3.22). To understand the reasons for this difference, it should be noted that after each shot, the sample surface shifts, so that the conditions of each subsequent shot are different from the conditions of previous shots. Thus, only the first shot corresponds to the declared focal position. Moreover, in our calculations, we used the same value of the surface area of the plasma

cloud for all focal positions. The actual values of the surface area S could improve the obtained results

3.6 Summary

An overview of thermodynamic equilibrium (TE) conditions, as well as the plasma diagnostic principles, are briefly discussed in the initial sections of this chapter. The optical emissions are utilized for the plasma characterization where the plasma temperature and electron density are estimated from Boltzmann plot and Stark broadening methods respectively. The LIBS experiment is performed on the copper sample by varying the position of the laser beam waist with respect to the sample surface (total three LSTDs). The effect of LSTD on the various parameters of the plasma viz., intensity, temperature, electron density, and decay constant are presented in subsequent sections. The maximum plasma temperature is observed at X_1 compared to the X_0 & X_2. It could be attributed to the influence of plasma shielding at X_1 where the reheating of the plasma led to the increase in temperature. Also, it is asserted by the mass ablation studies of the craters where the amount of mass ablated is less at X_1 compared to the X_0 due to the plasma shielding. It is found that maximum electron density observed at X_0, and followed by X_1 & X_2. Further, the characteristic plasma lifetime τ (decay constant) is longest for the X_0 focal position, and the shortest for the X_2 position. It is noticed that the ablated mass is linearly correlated with the electron density, decay time, spectral line intensities. In order to explain the relaxation of the plasma radiation, a theory based on the assumption that the process is governed by thermal radiation of plasma is developed. The theoretical dependence of the plasma temperature on time agrees well with the temperatures determined from the experimental data using the Boltzmann plot.

3.7 References

1. H.R. Griem, "Validity of local thermal equilibrium in plasma spectroscopy", Phys. Rev., 131, **1963**.
2. Y. Wang, A. Chen, Q. Wang *et al.*, "Influence of distance between focusing lens and target surface on laser-induced Cu plasma temperature", Phys. Plasmas, 25, **2018**.
3. J. Guo, J. Shao, T. Wang *et al.*, "Optimization of distances between the target surface and focal point on spatially confined laser-induced breakdown spectroscopy with a cylindrical cavity", J. Anal. At. Spectrom., 32, **2017**.
4. K.S. Singh, and A.K. Sharma, "Effect of lens focusing distance on laser-produced copper plasma in air in the presence of static transverse magnetic field", Phys. Plasmas, 23, **2016**.
5. S. Kumari, A. Kushwaha, and A. Khare, "Spatial distribution of electron temperature and ion density in laser induced ruby (Al2O3: Cr3+) plasma using Langmuir probe", Journal of Instrumentation, 7, **2012**.
6. S.H. Glenzer, and R. Redmer, "X-ray Thomson scattering in high energy density plasmas", Reviews of Modern Physics, 81, **2009**.
7. G.W. Faris, and H. Bergström, "Two-wavelength beam deflection technique for electron density measurements in laser-produced plasmas", Applied optics, 30, **1991**.
8. H. Tang, O. Guilbaud, G. Jamelot *et al.*, "Diagnostics of laser-induced plasma with soft X-ray (13.9 nm) bi-mirror interference microscopy", Applied Physics B, 78, **2004**.
9. S. Harilal, G. Miloshevsky, P. Diwakar *et al.*, "Experimental and computational study of complex shockwave dynamics in laser ablation plumes in argon atmosphere", Phys. Plasmas, 19, **2012**.
10. G.K. Varier, R.C. Issac, S. Harilal *et al.*, "Investigations on nanosecond laser produced plasma in air from the multi-component material YBa2Cu3O7", Spectrochim. Acta, Part B, 52, **1997**.
11. J. Hermann, A. Thomann, C. Boulmer-Leborgne *et al.*, "Plasma diagnostics in pulsed laser TiN layer deposition", J. Appl. Phys., 77, **1995**.
12. C. Aragón, and J.A. Aguilera, "Characterization of laser induced plasmas by optical emission spectroscopy: A review of experiments and methods", Spectrochim. Acta, Part B, 63, **2008**.
13. A. De Giacomo, "Experimental characterization of metallic titanium-laser induced plasma by time and space resolved optical emission spectroscopy", Spectrochim. Acta, Part B, 58, **2003**.
14. H.R. Griem, "Principles of plasma spectroscopy", Cambridge University Press**2005**.
15. G. Cristoforetti, E. Tognoni, and L. Gizzi, "Thermodynamic equilibrium states in laser-induced plasmas: from the general case to laser-induced breakdown spectroscopy plasmas", Spectrochim. Acta, Part B, 90, **2013**.
16. L.J. Radziemski, and D.A. Cremers, "Laser-induced plasmas and applications", **1989**.
17. J.P. Singh, and S.N. Thakur, "Laser-induced breakdown spectroscopy", Elsevier**2007**.
18. T. Belmonte, C. Noël, T. Gries *et al.*, "Theoretical background of optical emission spectroscopy for analysis of atmospheric pressure plasmas", Plasma Sources Sci. Technol., 24, **2015**.
19. W. Gao, N. Singh, L. Song *et al.*, "Direct laser writing of micro-supercapacitors on hydrated graphite oxide films", Nat. Nanotechnol., 6, **2011**.

20. D.H. Lowndes, D. Geohegan, A. Puretzky *et al.*, "Synthesis of novel thin-film materials by pulsed laser deposition", Science, 273, **1996**.
21. S. Harilal, B. O'Shay, M.S. Tillack *et al.*, "Spectroscopic characterization of laser-induced tin plasma", J. Appl. Phys., 98, **2005**.
22. R. Spitzer, R. Kauffman, T. Orzechowski *et al.*, "Soft x-ray production from laser produced plasmas for lithography applications", Journal of Vacuum Science & Technology B: Microelectronics and Nanometer Structures Processing, Measurement, and Phenomena, 11, **1993**.
23. M. Capitelli, A. Casavola, G. Colonna *et al.*, "Laser-induced plasma expansion: theoretical and experimental aspects", Spectrochim. Acta, Part B, 59, **2004**.
24. M. Tillack, D. Blair, and S. Harilal, "The effect of ionization on cluster formation in laser ablation plumes", Nanotechnology, 15, **2004**.
25. S. Arepalli, "Laser ablation process for single-walled carbon nanotube production", Journal of nanoscience and nanotechnology, 4, **2004**.
26. S. Mehrabian, M. Aghaei, and S. Tavassoli, "Effect of background gas pressure and laser pulse intensity on laser induced plasma radiation of copper samples", Phys. Plasmas, 17, **2010**.
27. R.A. Multari, L.E. Foster, D.A. Cremers *et al.*, "Effect of sampling geometry on elemental emissions in laser-induced breakdown spectroscopy", Appl. Spectrosc., 50, **1996**.
28. X. Li, W. Wei, J. Wu *et al.*, "The influence of spot size on the expansion dynamics of nanosecond-laser-produced copper plasmas in atmosphere", J. Appl. Phys., 113, **2013**.
29. S.S. Harilal, R.W. Coons, P. Hough *et al.*, "Influence of spot size on extreme ultraviolet efficiency of laser-produced Sn plasmas", Appl. Phys. Lett, 95, **2009**.
30. M. Chen, Y. Liu, X. Liu *et al.*, "Role of lens to sample distance during laser-induced damage in zinc targets", Laser Phys. Lett., 9, **2012**.
31. S. Zhang, X. Wang, M. He *et al.*, "Laser-induced plasma temperature", Spectrochim. Acta, Part B, 97, **2014**.
32. A. Chen, Y. Jiang, T. Wang *et al.*, "Comparison of plasma temperature and electron density on nanosecond laser ablation of Cu and nano-Cu", Phys. Plasmas, 22, **2015**.
33. D.A. Cremers, and A.K. Knight, "Laser-Induced Breakdown Spectroscopy", Wiley Online Library**2006**.
34. R. McWhirter, "Spectral intensities", **1965**.
35. H. Shakeel, S. Arshad, S. Haq *et al.*, "Electron temperature and density measurements of laser induced germanium plasma", Phys. Plasmas, 23, **2016**.
36. A. Sarkar, V.M. Telmore, D. Alamelu *et al.*, "Laser induced breakdown spectroscopic quantification of platinum group metals in simulated high level nuclear waste", J. Anal. At. Spectrom., 24, **2009**.
37. J.A. Aguilera, and C. Aragón, "Characterization of a laser-induced plasma by spatially resolved spectroscopy of neutral atom and ion emissions.: Comparison of local and spatially integrated measurements", Spectrochim. Acta, Part B, 59, **2004**.
38. E. Mal, R. Junjuri, M.K. Gundawar *et al.*, "Optimization of temporal window for application of calibration free-laser induced breakdown spectroscopy (CF-LIBS) on copper alloys in air employing a single line", J. Anal. At. Spectrom., 34, **2019**.
39. R. Junjuri, S.A. Rashkovskiy, and M.K. Gundawar, "Dependence of radiation decay constant of laser produced copper plasma on focal position", Phys. Plasmas, 26, **2019**.

40. H. Yuan, A.B. Gojani, I.B. Gornushkin *et al.*, "Investigation of laser-induced plasma at varying pressure and laser focusing", Spectrochim. Acta, Part B, 150, **2018**.
41. A. Miloshevsky, S.S. Harilal, G. Miloshevsky *et al.*, "Dynamics of plasma expansion and shockwave formation in femtosecond laser-ablated aluminum plumes in argon gas at atmospheric pressures", Phys. Plasmas, 21, **2014**.
42. S. Sai Shiva, C. Leela, P. Prem Kiran *et al.*, "The effects of electron thermal radiation on laser ablative shock waves from aluminum plasma into ambient air", Phys. Plasmas, 23, **2016**.
43. R. Coons, S. Harilal, S. Hassan *et al.*, "The importance of longer wavelength reheating in dual-pulse laser-induced breakdown spectroscopy", Applied Physics B, 107, **2012**.
44. S. Sai Shiva, C. Leela, P. Prem Kiran *et al.*, "Numerical investigation of nanosecond laser induced plasma and shock wave dynamics from air using 2D hydrodynamic code", Phys. Plasmas, 24, **2017**.
45. D.A. Cremers, R.A. Multari, and A.K. Knight, "Laser-induced breakdown spectroscopy", Encyclopedia of Analytical Chemistry: Applications, Theory and Instrumentation, **2006**.
46. J. Hermann, A. Lorusso, A. Perrone *et al.*, "Simulation of emission spectra from nonuniform reactive laser-induced plasmas", Phys. Rev. E., 92, **2015**.
47. B. Zmerli, N.B. Nessib, M. Dimitrijević *et al.*, "Stark broadening calculations of neutral copper spectral lines and temperature dependence", Phys. Scr., 82, **2010**.
48. Y. Luo, L. Zhu, J. Han *et al.*, "Effect of focusing condition on laser energy absorption characteristics in pulsed laser welding", Optics & Laser Technology, 117, **2019**.

CHAPTER 4 : LIBS as a spectroscopic tool for the identification of plastic waste

This chapter is an application towards the identification of plastic waste. It presents the efficient and rapid identification of ten different types of post-consumer plastics waste obtained from a local recycling plant. A systematic investigation is done with the aim of reducing the weight, size, and cost of the ns LIBS detection system and data acquisition & analysis time. For this, the performance of LIBS is evaluated by interrogating the samples in a single-shot as well as accumulation mode (of ten consecutive laser shots). Also, the spectral emissions of the plasma are captured by two different detection systems i.e., an Echelle spectrograph equipped with an ICCD and a low-cost portable Czerny Turner spectrometer coupled to CCD. Various data exploration methods viz., univariate (C-C bonds correlation), bivariate (C/H ratio analysis), and multivariate approaches (PCA, ANN, and RF) are utilized for the classification. The first two (uni & bi-variate) have resulted in partial discrimination and the last one (multivariate) has shown promising results where the identification accuracies up to ~99 % are achieved. The analysis performed with the CCD detector in single-shot mode resulted in a reduction of overall time by a factor of ~ 15 times compared to the ICCD. Finally, the results demonstrated here can be utilized in making a compact, and low-cost LIBS system for the rapid identification of plastics with higher accuracies for the real-time application.

Part of this chapter's work has been published as following journal article.

Rajendhar Junjuri, *C. Zhang, I. Barman, M.K. Gundawar, "Identification of post-consumer plastics using laser-induced breakdown spectroscopy", Polymer Testing, (2019).*

4.1 Introduction

The extensive use of plastic in our daily lives is creating the landfill problem by the accumulation of debris and leading to an increase in pollution. Every year, several million tons of packaging materials, water bottles, scrapped household appliances, and other mixed plastic products are being generated worldwide[1, 2]. Their higher durability adds more to the disposal problem, and the traditional disposal methods such as burying and incineration are leading to the wastage of natural resources as well. The ever-increasing industrial and domestic waste raises more concerns over the recycling of the plastics. Recycling the plastics offers an efficient solution to minimize waste output and reduces the usage of natural resources as well as pollution of the atmosphere. Identification of the type of plastic is the primary and critical step in the recycling process as it affects the quality and cost of the final products. Efficient, faster, and economic feasibility are the three prime factors for any recycling technique to become popular. Recycling techniques are specific to plastics and sometimes the additives present in the plastics need to be properly identified[3]. Manual sorting[4, 5] is the widely used traditional technique for identification based on the resin coding system[6], appearance, and color of the plastic. Sink floating measurement[7] is another conventional and low-cost separation technique used for separation based on their density. Following spectroscopic methods are reported in the literature for the identification of the plastics based on the scattering, absorption, transmission of the light: Raman spectroscopy[8, 9], fluorescence spectroscopy[10], X-ray fluorescence (XRF) spectrometry[3] and near-infrared (NIR) spectroscopy[11]. Raman and NIR spectroscopic studies provide the unique molecular fingerprint of the plastic which favors accurate discrimination by looking at their representative spectra whereas fluorescence lifetimes are used as markers for separation of plastics.

Manual sorting of plastics is an error-prone and time-consuming process. In addition, the employees involved in the sorting process need to be well protected as their exposure to hazardous plastics (industrial and medical plastic waste) could be lethal. Furthermore, the sink floating measurements require the usage of different chemical reagents in the floating medium (water) for the efficient identification of plastics. The NIR measurements have limitations with the thickness of the plastics (thickness should be greater than 20 μm) and

dark colour samples[11]. XRF has the only advantage of identifying Polyvinyl chloride (PVC) by detecting the chlorine [3, 6] however, it can be utilized to quantify the different flame retardants and elements in the pigments (Br, Sb Ti, Pb, Cd, Zn, and Si) present in the plastic. Raman spectroscopy detects the sample based on the molecular bonds nevertheless, it has limitations with the dark and black colour samples[8]. Moreover being a weak signal, the strength also greatly depends on the excitation wavelength used for the identification of samples.

LIBS being a simple technique can overcome the limitations of the conventional and other spectroscopic methods as described in chapter 1. It has been not only used for the classification of plastics but also the quantification of different trace elements present in it. Liu et. al. recently presented a comprehensive overview of works devoted to the classification and identification of the different types of the plastics using LIBS technique along with the quantitative analysis of the metallic elements present in it [12]. Table 4.1 summarizes the work done for the identification of plastics using the LIBS technique. Various intensity ratios deploying the atomic and molecular emissions were evaluated for sorting the different types of plastics in which H/C and C_2/C are found to be the prominent [13-15]. Further, the improvement in accuracy with the aid of the ratiometric approach was accomplished by utilizing the buffer gas[16]. Also, exploiting the method of adjusting spectral weights (ASW) was demonstrated the identification rates close to 100% [17]. The method of normalized coordinates and rank correlation method successfully identified plastics with a 95% confidence level [18]. Time and space resolved imaging of plasma was also used to identify the plastics in which a good correlation between the emissions of the plasma to their molecular structure was revealed [19].

LIBS combined with various multivariate tools such as ANN[20, 21], PCA[8, 22-24], PLS-DA[15, 25], SVM[17], SIMCA[26], Euclidean Distance, and Receiver Operating Characteristic (ROC)[22] have shown promising results for the identification and separation of the plastics[24, 27-29]. Nevertheless, most of these studies described in the literature were mainly reported on the standard plastics purchased from the companies/industries. Only a very few studies were performed on used/post-consumer plastics as listed in Table 4.1

Table 4.1. Summary of the work devoted to the identification of the plastics in the LIBS literature. Total no of the samples (#), Sample details (SD), Detector type (DT), no of laser shots used for recording 1 spectrum (NS), Used samples (U), Standard samples purchased from the company (S), E-Waste (E), Not mentioned in the literature (NM), and no of channels of the CCD Spectrometer (CH).

S.No	Sample names (#)	SD	Analysis (Identification rate)	DT & NS	Ref
1	HIP, PP, LD, ABS, PS, PC HD, PET, SIHET and PPCP (10)	U	Ratiometrics and PLS-DA (89 - 93 %)	ICCD & 10	[15]
2	ABS, PA, PVC, PMMA, POM, PP, PTFE and PU (8)	S	Self-organizing maps (SOM) and K-means clustering (99 %)	ICCD & 30	[30]
3	PP, PE, PET, and PS (4)	S	Euclidean distance and Pearson's correlation (73 - 87 %)	ICCD & 10	[27]
4	PP, PE, PET, PS and PVC (5)	NM	C/H and C_2/C ratio	ICCD & 10	[13]
5	PP, PE, PS, PVC, ABS, PTFE, POM, PA and PMMA (9)	NM	SVM (98-100 %) (*Ar is used as buffer*)	ICCD & 30	[17]
6	ABS, PP and HIP (3)	S	CN/He ratio (*He is used as buffer gas*)	ICCD & 60	[16]
7	PA, PE, PS and POM (4)	S	Space & time resolved imaging plasma	ICCD & 10	[19]
8	PP, PE, PC, PVC, POM, PA and PMMA (7)	NM	ANN (81-100 %)	ICCD & 1-10	[21]
9	PP, PE, PET, and PS (4)	S	PCA	ICCD & 10	[24]
10	PE, PP, POM, PVC, PTFE, POE , ABS, PC, and PBT (9)	S	Separation by PCA and C_2/H ratio	ICCD & 45	[23]
11	PP, HD, PET, and PS (4)	NM	PCA and Mahalanobis distance (80- 100 %)	ICCD & NM	[22]
12	PP, PE, PET, and PS (4)	S&U	Raman & LIBS combined with PCA and Mahalanobis distance (93 – 98 %)	ICCD & NM	[8]
13	PP, PE, PET, PS and PVC (5)	U	C/H and ANN (65-77 and PVC identified with 99 %)	ICCD & NM	[20]
14	PP, PS, LD, HD, PET, PVC and PTFE (7)	S&U	Method of normalized co-ordinates with t-test (95 %)	2CH-CCD & 15	[18]
15	ABS, HD, PC, PE, PP, PS, PMMA, POM, PU, PTFE and PVC (11)	S	Variable selection combined with PLS-DA (85-99.5 %)	3CH-CCD & 20	[25]
16	PP, LD, HD, PET, PS and PVC (6)	S	C/H ratio	4CH-CCD & 20	[14]
17	PP, PE, PET, PS, and PVC (5)	S&U	Correlation coefficients combined with student's t-test (90 -99 %).	2CH-CCD & 10	[29]
18	PP, PE, PET, PS, and PVC (5)	S&U	Non parametric correlation (90 - 99 %)	2CH-CCD & 10	[28]
19	PA, NTP, HD, and PET (4)	S&U	Commercial LIBS system, KNN and SIMCA (93-98 %)	6CH-CCD & 1	[26]
20	PET, LD, HD, PVC, PP, and PS (6)	S	Linear correlation based on the spectral library (90 %)	7CH-CCD & 1	[31]

21	ABS, PS, PE, PC, PP, PA (6)	E	KNN and SIMCA (done in ablation chamber) (92-98 %)	6CH-CCD & NM	[32]
22	Black and white plastics	E	KNN, SIMCA and PLS-DA (72.8 – 99.5 %)	6CH-CCD & NM	[33]

Polyurethane (PU), Polytetrafluoroethylene (PTFE), Polyoxymethylene (POM), Polymethylmethacrylate (PMMA), Polyamide (PA), Polyoxyethylene (POE), Polybutylene terephthalate (PBT), and Novatein thermoplastic protein (NTP).

The difficulty in the identification of plastics increases as the chances of plastic contamination increases from the time of their disposal by a consumer to their arrival at the waste collection center. To address these issues, it is necessary to build a data model using real-time post-consumer plastics. Moreover, 60 % of the total works reported in the literature (details are given in the 5th column of Table 4.1) have employed the Echelle based ICCD spectrometers. Remaining all studies have deployed the multichannel (2-6 channel) gated CCD spectrometers. Furthermore, 20 works out of 22 in Table 4.1 have acquired the spectral data by accumulating the 10-50 consecutive laser pulses depending on the experiments.

Thus, the main motive of this work is to minimize the cost, size, weight, and analysis time that incurred in identification plastics by deploying a single channel non-gated CCD (NCT-CCD/CCD) spectrometer in place of Echelle spectrometer coupled with ICCD (ES-ICCD/ICCD) and to develop robust multivariate algorithms. Generally, Echelle spectrometers are considered as the workhorse for the LIBS detection system owing to the higher resolution with a wide spectral range to detect multiple elements in a single acquisition. Nevertheless, it requires a highly sensitive area detector which leads to an increase in their size and cost[34]. Also, the Echelle based spectrometers are sensitive to the ambient atmosphere where the change in ambient temperature affects the calibration of the detector. In addition to these parameters, the cost of the ICCD makes it difficult to promote as miniaturized popular commercial equipment. Whereas the CCD spectrometers are portable, low-cost, easy to operate, posses fast frame rates, doesn't require detector cooling, filed deployable and can be operated in a wide range of temperatures in the ambient atmosphere in contrast to the ES-ICCD spectrometers[35]. On the other hand, multichannel (3-6) gated CCD spectrometers are relatively costlier compared to the single-channel NCT-CDD spectrometers. The inability of the NCT-CCDs to avoid continuum

which generated during the laser-matter interaction is the major limitation to impart these in the LIBS detection system. However, the appropriate treatment for the continuum/background in the nongated LIBS spectra has resulted in the accurate discrimination of organic samples with similar chemical composition viz., isomers[36], and pharmaceuticals[37]. Also, it has been deployed for the identification of complex samples like explosives[38], alloys, and soils[35]. Further, LIBS combined with CCD spectrometers (of resolution ~1 nm at 500 nm) have been demonstrated the discrimination of various samples viz., alloys[39], glass bottles[40], wood[41], and geological materials[42]. However, a comparative and systematic evaluation of the NCT-CDD and ES-ICCD spectrometers has not been reported for the classification of samples to the best of my knowledge.

In this chapter, the performance of LIBS with NCT-CCD and ES-ICCD spectrometers have been evaluated for the classification of the plastics. The experiment was performed on ten different post-consumer plastics obtained from a local recycling unit as their identification would be more relevant to the actual scenario. The spectra were acquired in a single shot and ten shot accumulation mode to evaluate the performance of multivariate techniques in both the conditions. Further, the ratiometric approach, C-C bonds correlation, and multivariate methods like PCA, RF, and ANN were deployed for treating the data and to validate their application for a set of ten different types of post-consumer plastics. Finally, a feature selection method based on the random forest (RF) algorithm was employed to find the essential features of the LIBS spectra and to achieve faster identification.

4.2 Characterization of the samples

The details of the ten post-consumer plastics are given in Table 4.2. It shows the sample name, chemical formula, stoichiometric ratios, and their recycling numbers. The international resin identification coding system (IRICS) has provided a consistent resin coding number (recycling number- N#) for the identification of plastics and the same is presented in the last column of Table 4.2. The number 1-6 (3 is for PVC) is a representative recycling number of each plastic. All the remaining plastics are designated as 'others' category by IRICS and number seven (#7) is assigned to it. This coding system enables the users to easily identify the type of plastic and serves as a tool for the manual

sorting of the plastics. Also, it has been adopted by various research communities in the world for implementing the recycling process.

Table 4.2. Details of the samples and various theoretical atomic ratios. Not available - (NA)

S. No	Scientific Name	Acronym	Chemical formula	C/O	C/H	H/O	Recycle No (#)
1	High impact polystyrene	HIP	$(C_{12}H_{16})$	0	0.75	0	7
2	Polypropylene	PP	$(C_3H_6)_n$	0	0.50	0	5
3	Low-density polyethylene	LD/LDPE	$(C_2H_4)_n$	0	0.50	0	4
4	Acrylonitrile butadiene styrene	ABS	$(C_{15}H_{17}N)_n$	0	0.88	0	7
5	Polystyrene	PS	$(C_8H_8)_n$	0	1.00	0	6
6	High-density polyethylene	HD/HDPE	$(C_2H_4)_n$	0	0.50	0	2
7	Polyethylene terephthalate	PET	$(C_{10}H_8O_4)_n$	2.50	1.25	0	1
8	SIHET	NA	NA	NA	NA	NA	7
9	Polycarbonate	PC	$(C_{16}H_{14}O_3)$	7.50	1.14	4.67	7
10	Polypropylene Co-polymer	PPCP	NA	NA	NA	NA	7

The following five plastics viz. PP, HD, LD, PET, and PS together account for the 2/3rd of the total plastics production [2]. LD, HD, and PP belong to the polyolefins family. The molecular structure of SIHET, PPCP, and HIP are not available nonetheless the stoichiometric composition is known for all samples except for the PPCP and SIHET. All the plastics are obtained from a local recycling plant and the sample names are provided by them. Hence, the identity of the samples was evaluated by measuring their melting points using a thermogravimetric–differential thermal analysis (TG-DTA) prior to performing the LIBS experiment. Furthermore, the samples were also characterized by the Raman spectroscopy technique which provides the characteristic molecular fingerprint of the corresponding plastic.

4.2.1 TG-DTA analysis

TG-DTA is a well-established thermal analysis technique for characterizing the plastics which quantitatively determines the physicochemical changes in the sample. DTA studies provide information about the melting point, boiling point, and crystallization temperature of a sample which are characteristic for a particular plastic and can be utilized for their identification. Crystallization is an exothermic process where the energy is released during the heating while the other two are endothermic. TG analysis provides the

weight changes of the sample as a function of temperature[43]. The analyte weight loss can be occurred due to the decomposition, desorption, vaporization, or sublimation. Whereas the oxidation process leads to an increase in the weight of the sample. All the samples were cleaned with water to remove the debris before performing the TG-DTA (Model- SDT Q600, M/s TA instruments) experiment. The TG (solid line) and DTA (dotted line) curve are shown in Fig. 4.1 where it represents the weight percentage and heat flow of the PP as a function of temperature respectively. The initial set temperature was kept at 30 °C and then it was increased up to 300 °C in with an increment of 10 °C/min. The experiment was performed in a controlled atmosphere where the chamber was purged with the nitrogen gas(100.0 ml/min). The instrument consists of two crucibles one for the sample and the other for the standard reference sample(Alumina). The plastics were cut into small pieces to place in the crucible. The thermocouple measures the temperature of the crucible. The heat flow difference between the sample and reference gives information regarding the physical and chemical changes occurring in the sample while it is heating. By analyzing the DTA curve, it is possible to find the melting temperature (T_m).

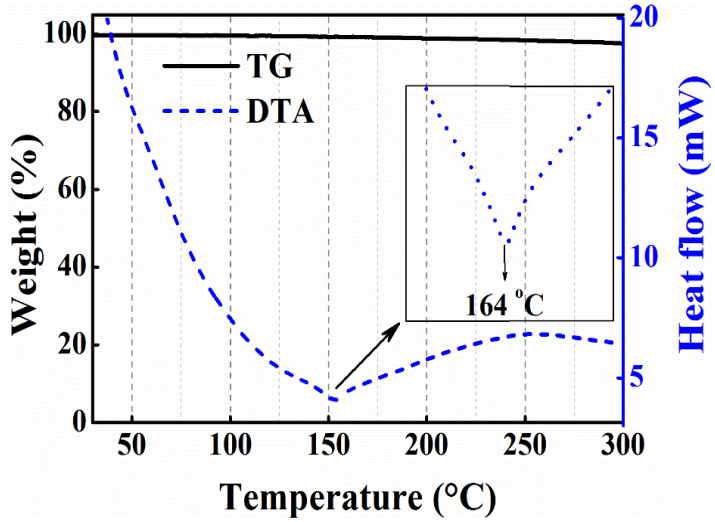

Fig. 4.1. TG-DTA plot of the PP plastic. The dashed line is the heat flow curve (DTA), and the solid line represents the weight percentage of the sample. The inset in the figure represents the close view of the dip at the melting point.

The dip at 164 °C in the DTA curve (visualized in the inset in Fig. 4.1) corresponds to the melting point of the PP. As aforementioned the weight of the sample should be constant during the melting temperature. The TG curve ascertained the same as there is no weight loss at that temperature. Similarly, the analysis was performed for all the samples, and the obtained melting points are given in Table 4.3.

Table 4.3. The melting temperature (T_m) of the samples obtained from the TG-DTA.

S. No	Sample name	T_m (°C)		Reference
		Experiment	Literature	
1	HIP	260	210-290	[44]
2	PP	164	164	[43]
3	LD	117	118	[43]
4	ABS	106	105-110	[45]
5	PS	231	230	[43]
6	HDPE	130	130	[43]
7	PET	247	248	[43]
8	SIHET	227	NA	NA
9	PC	149	147-155	[46]
10	PPCP	132	NA	NA

The results demonstrate that the measured melting points are in good agreement with the values reported literature which confirms their identity[43]. It is worth considering that some of the amorphous plastics (ex: ABS, PC, and HIP, etc.) will have a certain range of temperatures for the melting. Thus it does not have a fixed sharp melting point like crystalline/semi-crystalline plastics (ex: HD, LD, and PP, etc).

The TG-DTA analysis provided an overview of the identity of the plastic obtained from the recycling center and further Raman spectroscopy technique being utilized to evaluate their identity in the next sections.

4.2.2 Raman analysis

Raman spectroscopy is a branch of vibrational spectroscopy which is considered as one of the prominent methods for the characterization of polymers. It has been proved as a powerful spectroscopic tool that finds the applications in every branch of science as well as in a wide range of industrial disciplines. The interaction of EM radiation with matter, in particular, the specific absorption and emission of particular a wavelength provides the crucial and valuable acquaintances of chemicals. This laser-based spectroscopic technique provides the information of the sample at the molecular level. The rich vibrational content in the Raman spectra offers the details of the chemical structure and morphological nature of the analyte. Thus it serves as a valuable analytical tool for identifying the plastics by looking at their molecular fingerprint spectra. Despite numerous advantages of Raman

spectroscopy, a well-known competing process can also appear along with Raman scattering i.e. fluorescence which is observed due to the transitions of electronic excitation of the molecule. The fluorescence signal strength is two/three orders higher than the Raman signal (only 1 in 10^6 photons shows the Raman scattering) and which is sometimes buried in the fluorescence. Hence, this unwanted fluorescence could deteriorate results and limits the robust use of the Raman technique for recognizing a wide range of materials. Here, the Raman spectra were acquired by using a portable Raman spectrometer (i-Raman plus, M/s B&W Tek). All the samples were excited with continuous diode laser operating at 785 nm. Raman spectra of all the samples were recorded by averaging five single spectrums with each spectrum acquired with the integration time of 1s. A typical raw and background corrected Raman spectrum of ABS are shown in Fig. 4.2. Fig. 4.3 shows a typical background-corrected Raman spectrum of each sample along with the corresponding representative recycling number inside the triangle. It is evident from Fig. 4.3 that a specific plastic can be accurately distinguished from others except for LD and HD based on their unique spectral signature. These two have shown similar spectral signatures owing to the same molecular structure. However, the minute changes observed in the intensity and shape of a specific peak can be attributed to the changes in the percentage of crystallinity, and density of the samples.

A similar observation is demonstrated in the dendrogram plot as shown in Fig. 4.4 where the LD and HD formed as one cluster. For the present study, the Euclidian distance method is utilized and one spectrum for each sample is considered. The x-axis on the plot corresponds to the distances/dissimilarities between the samples. The Raman spectra of the PS, ABS, and HIP look similar except for some peaks due to the common spectral signature of the styrene. The dendrogram plot corroborates the same where these three are formed as one cluster. The Raman spectra of the PC, PP, PET, and SIHET are drastically different from each other and the remaining plastics also. Similar observations are noticed in the dendrogram where the maximum distances were demonstrated which corresponds to the highest dissimilarities among them. The characteristic lines observed in the Raman spectra of all the plastics are compared with the data available in the literature and corresponding spectral assignments are enumerated in Table 4.4. The results are found to be in good agreement and confirm the identity of the plastics. [8, 9, 47-49].

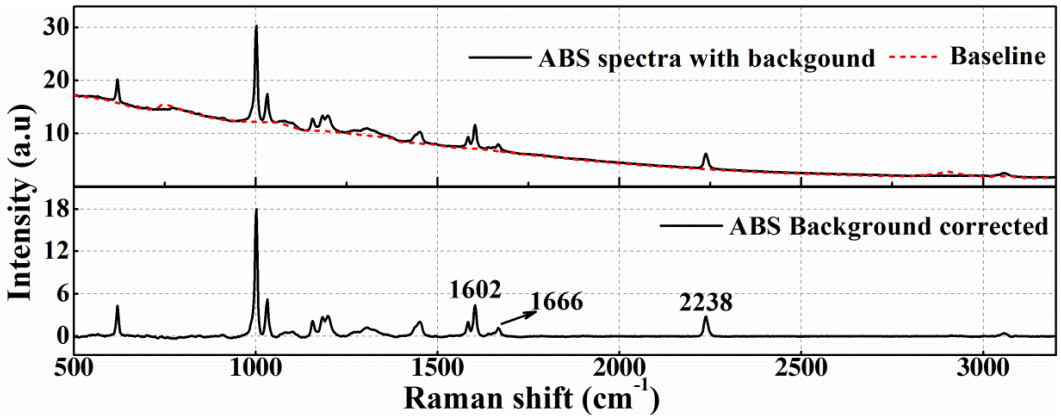

Fig. 4.2. Raman spectra of ABS with the background (Top) & after background removal (bottom).

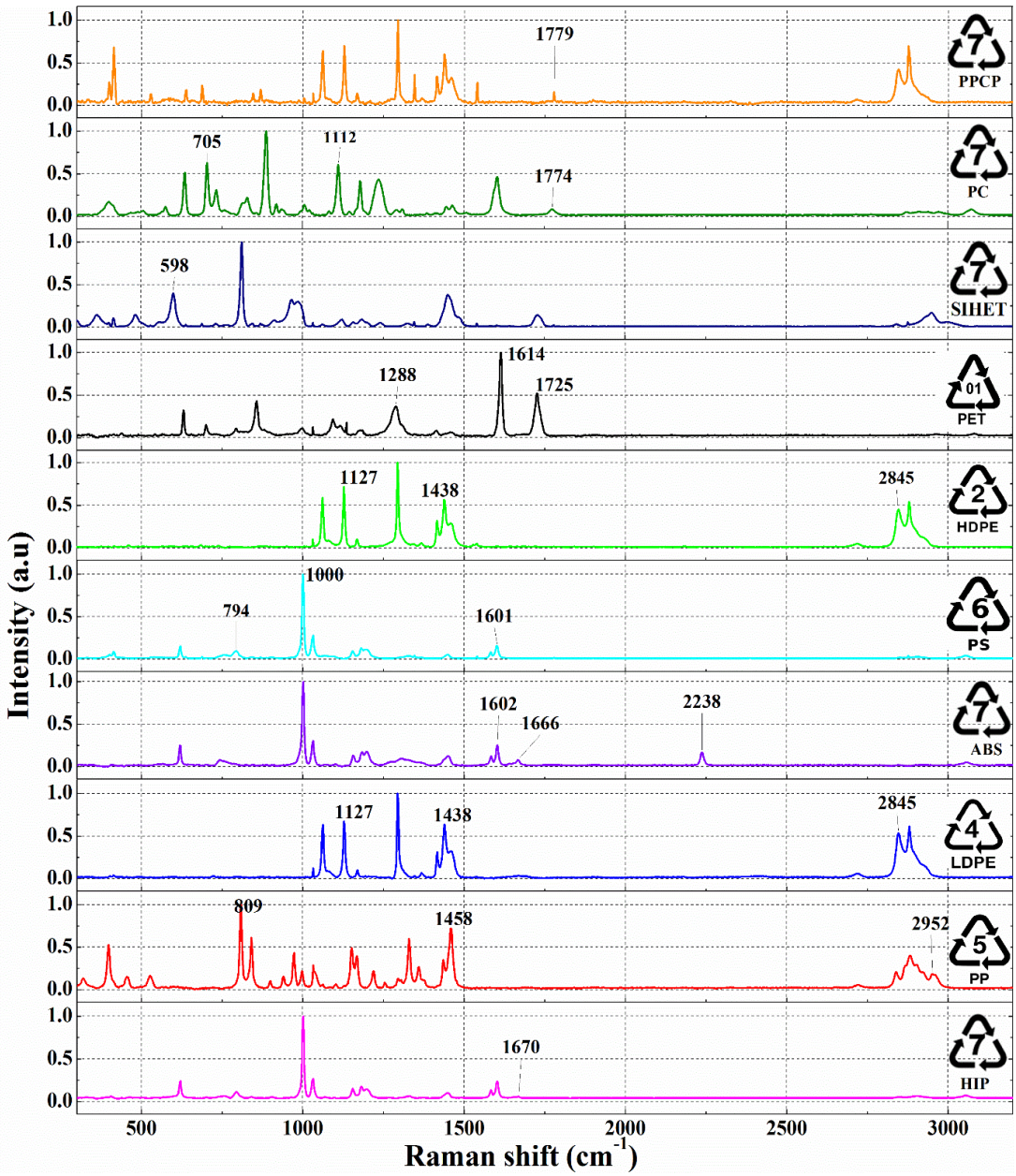

Fig. 4.3. Background corrected Raman spectra of the ten plastics. The numbers inside the triangle represent the recycling number.

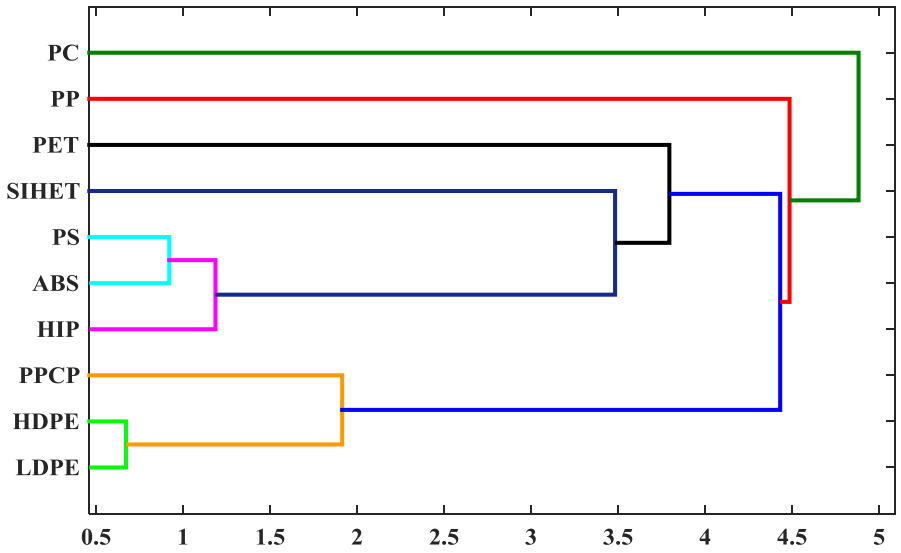

Fig. 4.4. Hierarchical clustering of the ten plastics using the dendrogram visualization

Table 4.4. The details of the characteristic Raman lines observed for all the plastics. Each peak is assigned to the corresponding bond assignment. ν - Stretching, ρ– Rocking, s –Symmetric, and δ-Deformation[50].

S No	Sample name	Raman shift (cm^{-1})		Spectral assignment
		Observed	literature	
1	HIP	1670	1671	[ν(C=C)] 1,4-trans
2	PP	809	811	[ρ(CH_2), ν(C-C), ν(C-CH_3)]
		1458	1464	[δ(CH_3), δ(CH_2)]
		2952	2959	[ν(CH_3)]
3	LD	1127	1133	[ν(C=C)]
		1438	1446	[δ(CH_2)]
		2845	2851	[ν(CH_2)]
4	ABS	1602	1603	ν_s (C-C) of benzene ring
		1666	1668	ν(C-C trans)
		2238	2239	ν(C-N)
5	PS	794	795	[α(C-C-C)]
		1000	999	[r_{adial} (C-C)]
		1601	1602	[ν_{inyl} (C-C)]
6	HD	1127	1133	[ν(C=C)]
		1438	1446	[δ(CH_2)]
		2845	2851	[ν(CH_2)]
7	PET	1288	1290	[ν_{Ring} (C-C), ν(C=O), δ(C=O)]
		1614	1614	[ν_{Ring} (C-C) and δ(C=H)]
		1725	1732	[ν(C=O)]
8	SIHET	598	NA	NA
9	PC	705	706	C-H out-of-plane bending
		1112	1110	C-O-C stretching
		1779	1781	C=O stretching
10	PPCP	413	NA	NA

In the next sections, these plastics were further investigated by the LIBS technique combined with various chemometric techniques.

4.3 Experimental details

The schematic of the experimental setup used to perform these experiments is already shown in chapter 2, Fig. 2.7 (ICCD) and Fig. 2.9 (CCD). The plasma on the sample surface is produced by focusing a 50 mJ laser beam (532 nm) through a plano-convex lens of 100 mm focal length. The photos of plastics samples taken with a mobile phone camera are shown in Fig. 4.5. The blackened area in a rectangular shape on the sample surfaces represents the laser ablated area.

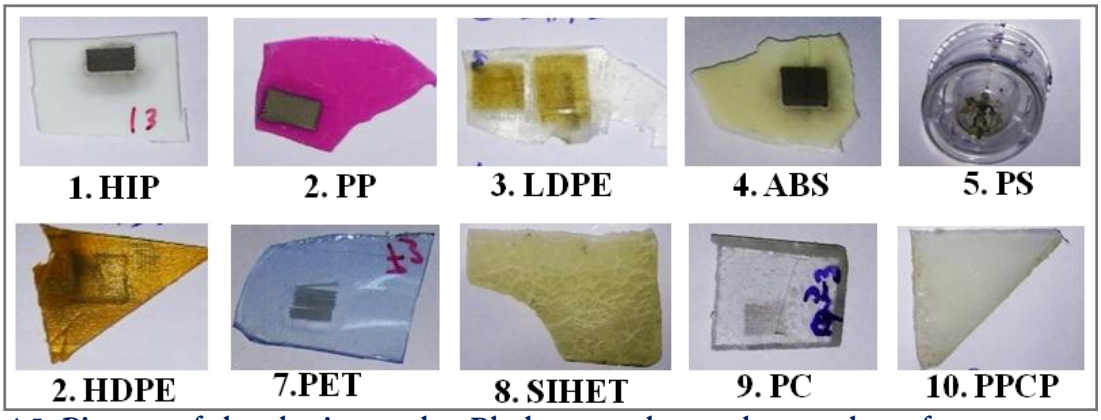

Fig. 4.5. Pictures of the plastic samples. Black rectangles on the sample surface represent the laser-irradiated area.

The spectra were acquired with the two spectrometers. The scientific details and instrument specifications are already discussed in Table 2.2 in chapter 2.

1) Non-gated Czerny Turner CCD spectrometer (Hereafter, referred as the 'CCD')
2) Mechelle spectrograph equipped with the ICCD. (Hereafter, referred to as the 'ICCD')

The integration time of 30 ms was used for recording the spectra with the CCD. The spectra were acquired with a gate delay of 1 μs and a gate width of 2 μs in the case of ICCD. Also, the data (each spectrum) was recorded in three modes

1) Accumulation of ten laser shots (ATS) with the ICCD (Hereafter referred as 1st dataset)
2) Single shot (SS) acquisition with the ICCD (Hereafter referred as 2nd dataset)
3) Single shot (SS) acquisition with the CCD (Hereafter referred as 3rd dataset)

4.4 Results and discussion

Fig. 4.6 illustrates the typical LIBS spectra of PS recorded with an ICCD (in ATS & SS mode) and CCD (in SS) acquisition modes. Each spectrum is shown in two separate windows i.e. 220-525 & 545-1000 nm to provide a clear view as shown in Fig. 4.6(a & b) respectively and the intensity scales are different for two windows. A strong continuum is noticed for the spectra recorded with the only CCD spectrometer as shown in the bottom plot of Fig. 4.6. It has appeared due to the Bremsstrahlung emissions in the early time scales of the plasma evolution which is inevitable for spectral acquisition using the non-gated CCD spectrometer. It should be noted that Carbon atomic emission peak at C I 247.8 nm was not observed in the LIB spectra recorded with CCD in contrast to the ICCD. This is due to the lack of sensitivity of CCD in the UV region. However, it is also to be noted that the oxygen atomic peak in the region 470-480 nm is only observed in the LIB spectra recorded with CCD but not with ICCD. This could be ascribed to gated acquisition in ICCD, where the information of short-lived de-excitations could be lost in the process of avoiding the continuum.

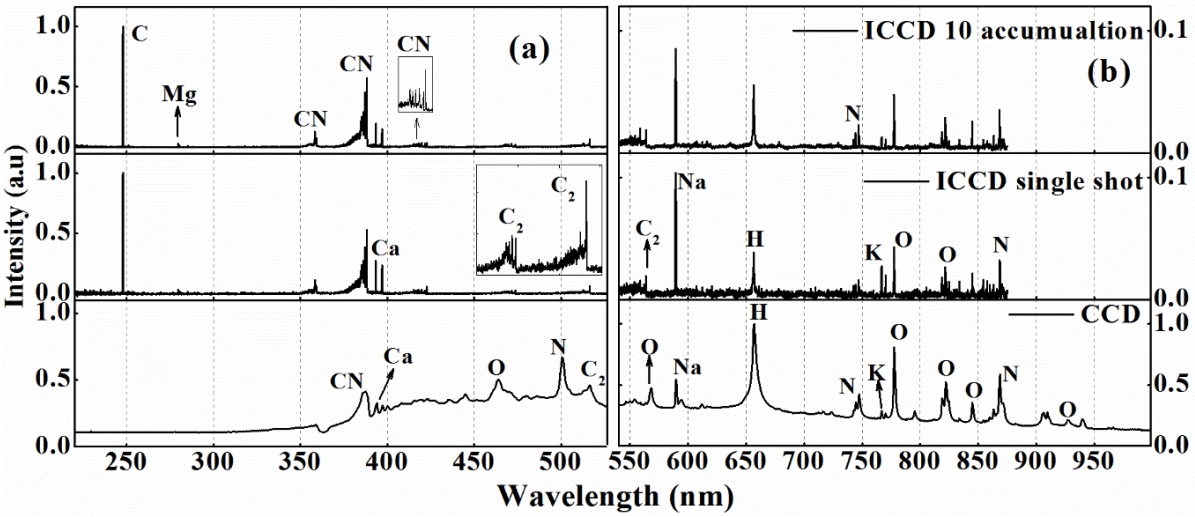

Fig. 4.6. LIBS spectra of the PS plastic acquired with the ICCD and CCD. a) & b) represent the spectra in the range of 220-525 and 545-1000 nm respectively with different intensity scales. The insets in figures represent the CN & C_2 molecular bands.

Fig. 4.7 (a-d) visualizes the plot of the individual spectral lines of H, N, O, and CN band recorded with the ICCD and CCD respectively. Some of the spectral lines are unresolved for the CCD for example, nitrogen lines and CN band as shown in Fig. 4.7 (b &d) respectively. It is due to the less spectral resolution of CCD compared to that of ICCD.

Also, the spectral lines are relatively broadened compared to the ICCD. It is attributed to acquiring the emissions from the early time scales of the plasma. At the initial time scales the electron densities are higher in the plasma and lead to the broadening of the spectral lines due to the Stark broadening.

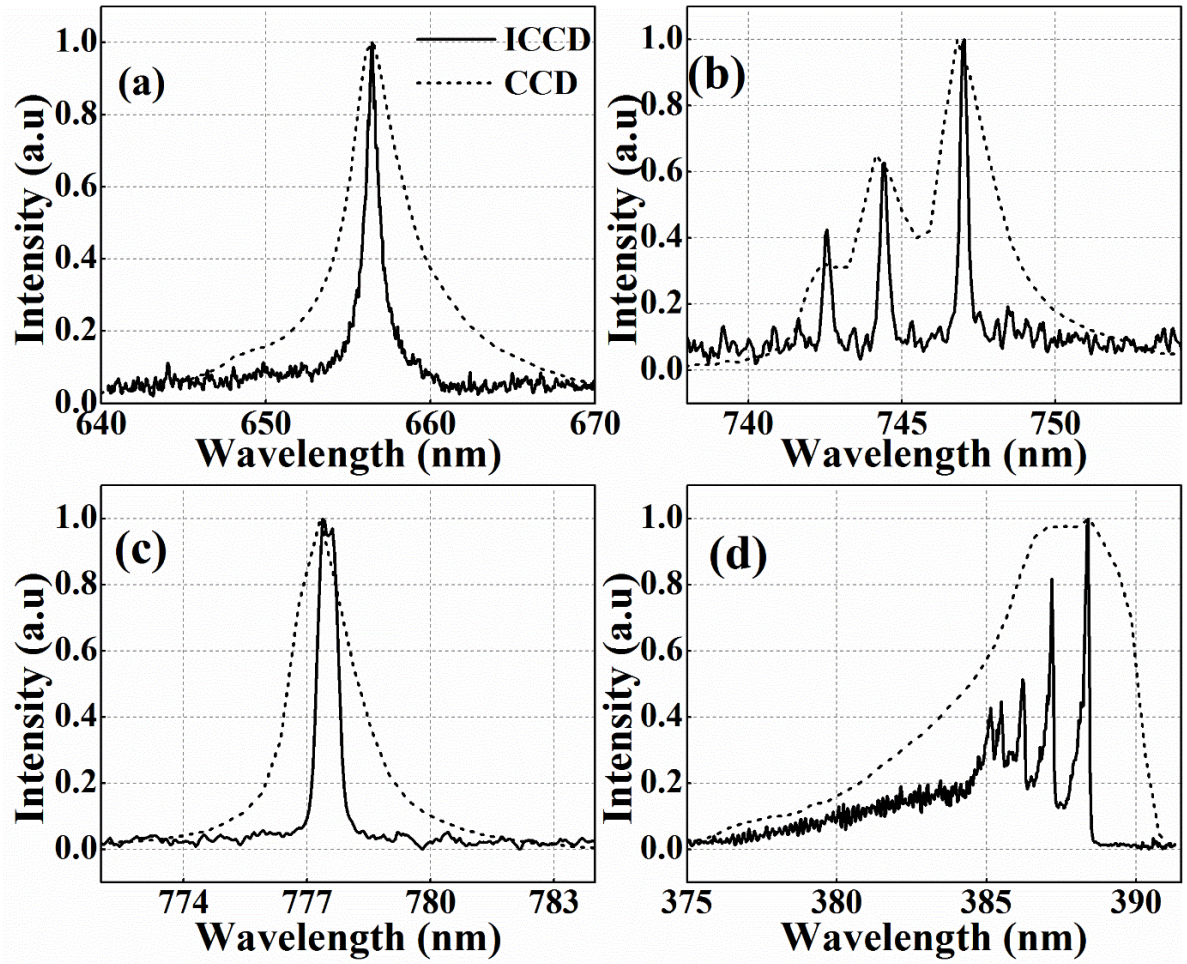

Fig. 4.7. Spectral lines recorded with ICCD and CCD. a) H-656.29, b) N-742.42, 744.35, & 746.89 c) O-777.41 (triplet) and d) CN ($\Delta\nu=0$) molecular band.

Further, signal to noise ratio (SNR) has been estimated for the three datasets at H 656.6 nm line. Here, the signal corresponds to the highest intensity of the H line. The noise is estimated from the standard deviation of the 20 data points on either side of the peak which are close to the baseline of the H line. It is important to emphasize that, the maximum SNR (~170-180) was noticed for the CCD and the minimum SNR (~30-40) for the ICCD in single-shot acquisition mode. The SNR increased by more than two times (~70-85) for the ICCD ten shots accumulation when compared to the single-shot acquisition. Furthermore, statistical variations present in the spectra were investigated by

estimating the RSD (% of variation from the 100 trials for each sample) of the intensity of a spectral line and full spectrum for the three different datasets. Then the average of the ten sample variations is represented in Fig. 4.8.

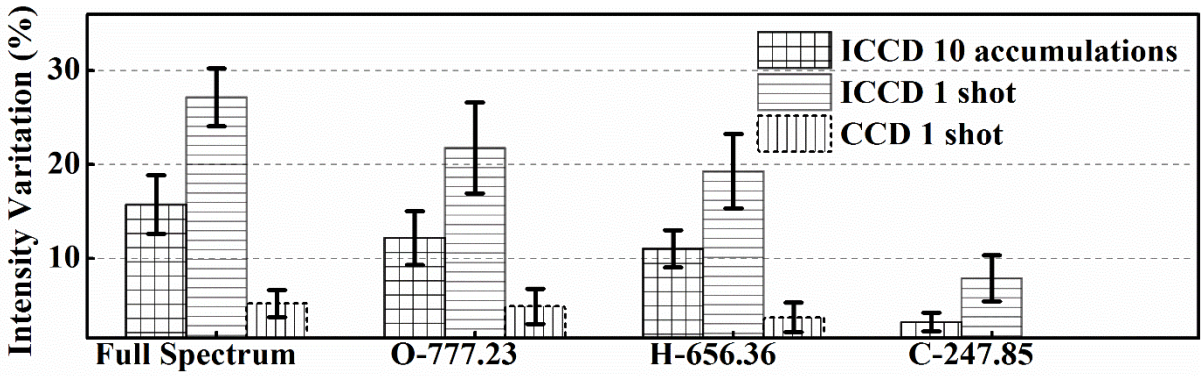

Fig. 4.8. Intensity variations measured for three data acquisitions. Full-spectrum represents the sum of the intensities estimated over the total spectral region. The carbon (C-247.85 nm) line is not observed in the spectra acquired with the CCD. Hence, the variation is not shown for the CCD.

Full-spectrum in corresponds to the intensity estimated by summing the total region for ICCD (220-880 nm) and CCD (360-950 nm). For the spectral line, intensity refers to the area under the peak estimated from the Lorentzian fit. From Fig. 4.8 it is evident that the variation in intensity is maximum for the spectra acquired with ICCD in single-shot mode, irrespective of the peaks or full spectra considered. The accumulation mode has resulted in an increase of the stability by ~2 times when compared to the singles shot acquisition mode. In the case of CCD, the intensity variation is minimum for all the peaks and full spectra. The intestines are more stable for the C-247.85 nm line and followed by H-656.36 nm and O-777.23 nm emission lines.

4.4.1 Description of the spectral lines

The background/continuum in the spectra acquired with CCD is removed by using a fifth-order polynomial fit program with an iterative least-squares curve fitting approach in MatLab [37]. Fig. 4.9 depicts the LIB spectra obtained after background correction and the spectra acquired with an ICCD are presented in Fig. 4.10. The spectra correspond to the SS acquisition looks close to the ATS spectra but with minimal changes in the intensity, hence not presented here. Typical LIBS spectra of all the samples look similar except the slight variations in line intensities as a consequence of similarities in their molecular

structures as shown in Fig. 4.9 & in Fig. 4.10. Carbon and hydrogen are common constituents among all samples with different stoichiometric ratios. Hence each spectrum recorded with the ICCD was normalized with the carbon (C) spectral line at C-247.85 nm as shown in Fig. 4.10. The spectral line of carbon was not observed in the spectra as the spectral sensitivity of the CCD is less deep UV region, thus it is normalized ((after background correction) to H-656.36 nm line (it is the strongest line in most of the plastics) as envisioned in Fig. 4.9.

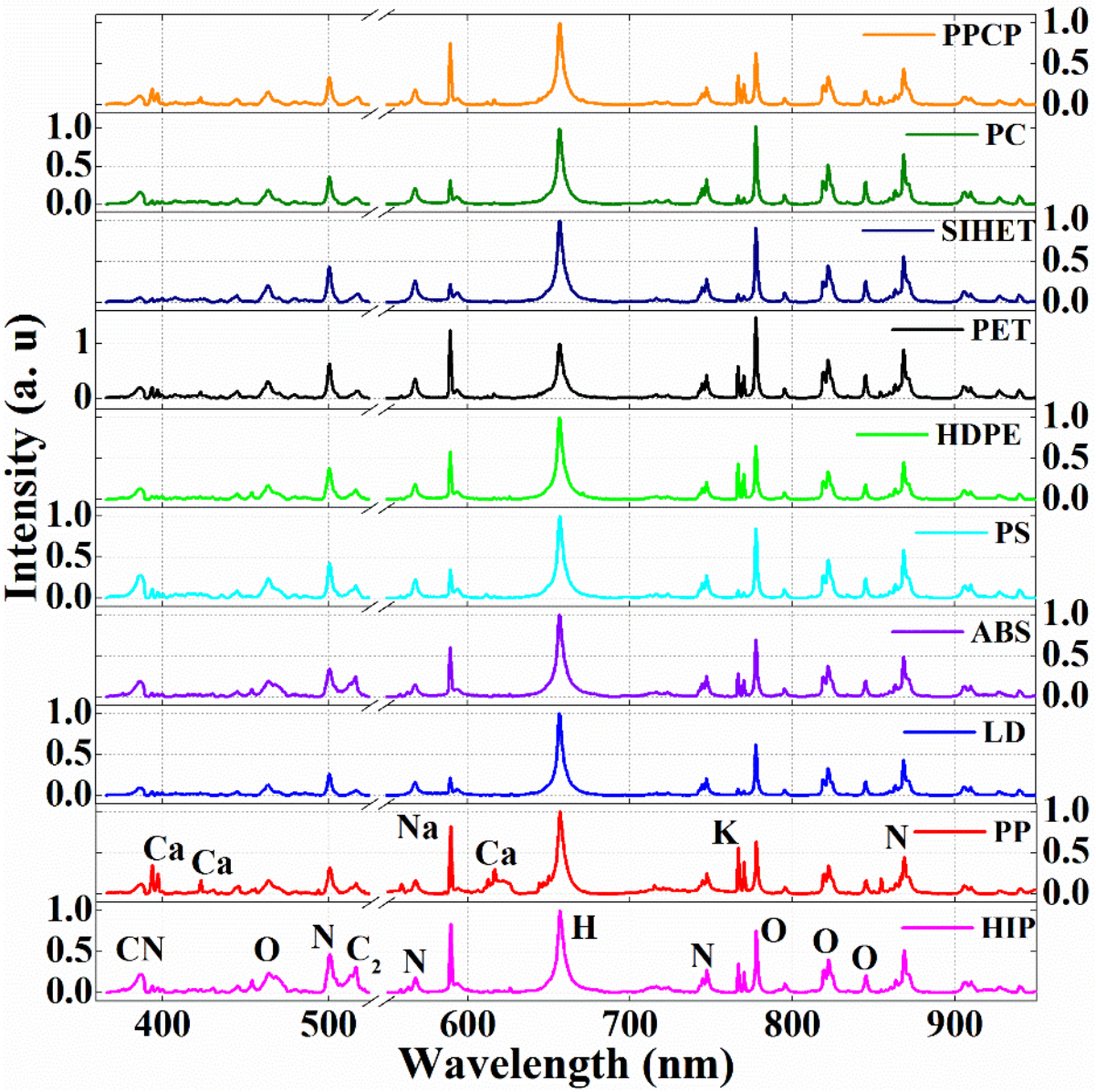

Fig. 4.9. LIBS spectra of ten plastics acquired with CCD spectrometer. All the spectra were normalized to the H-656.36 nm line after the background/continuum removal. The characteristic spectral features are represented at their corresponding positions.

These normalized datasets/spectra were utilized for the entire analysis. The following emissions are observed in the LIBS spectra recorded with both the spectrometers in 3 modes (1st, 2nd, and 3rd) viz, Magnesium (Mg-279.50 & 280.34 nm), Calcium (Ca-393.33, 396.84, & 422.67 nm), Sodium (Na-589.52, & 589.61 nm, it is an unresolved doublet for CCD), Hydrogen (H-656.29 nm), Nitrogen (N-742.42, 744.35, & 746.89 nm, it is an unresolved triplet for spectra collected with CCD), Potassium (K-766.49 nm) and Oxygen (O-777.41 (triplet) and 844.46 nm).

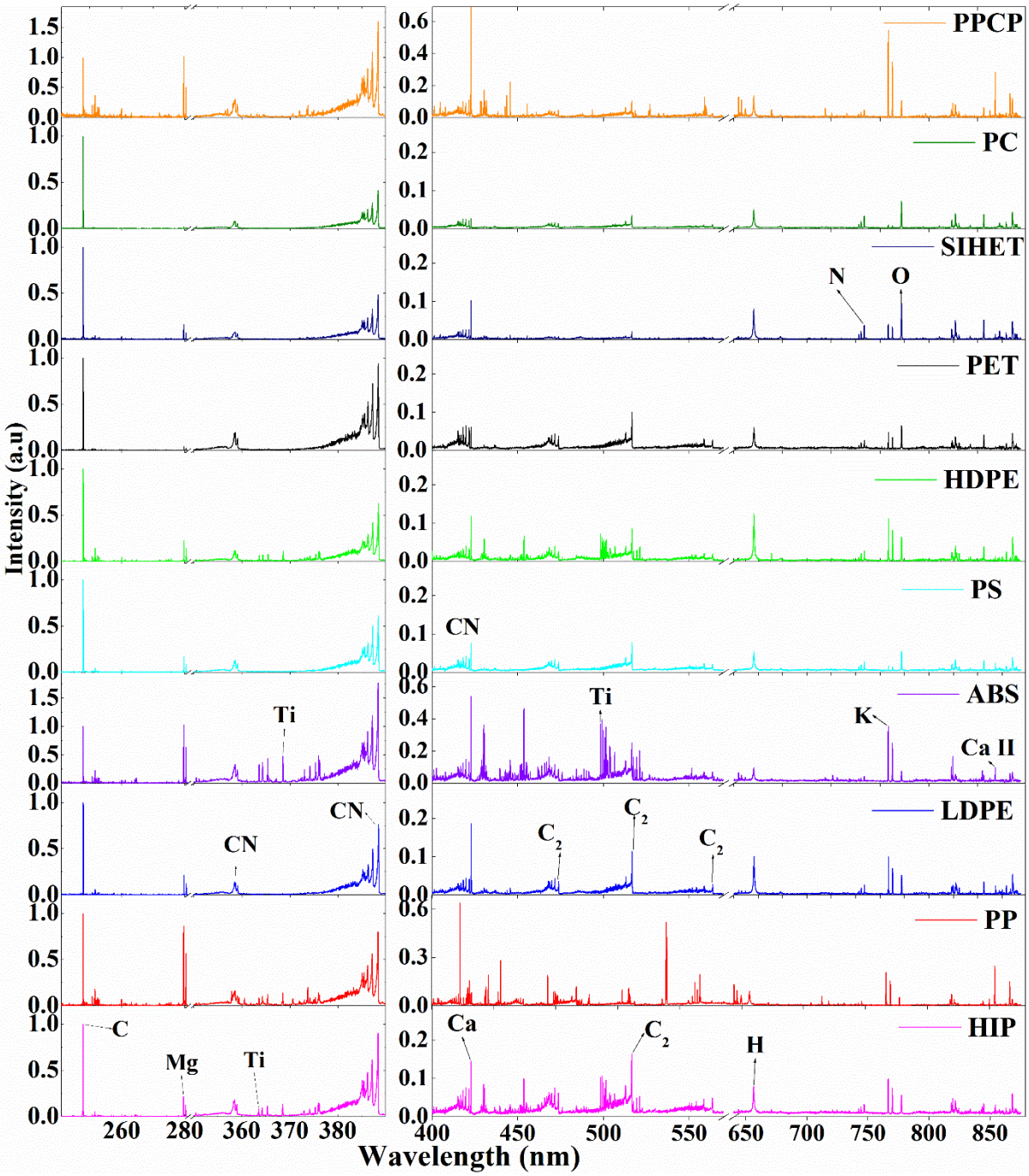

Fig. 4.10. LIBS spectra of ten plastics acquired with ICCD in ten shot accumulation mode. Each spectrum is normalized at C-247.85 nm.

Table 4.5 presents the various emission line observed in the LIBS spectra acquired in three acquisition modes. The atomic lines of C, H, N, and O are ubiquitously present in the LIBS spectra of most of the organic samples. Besides the emissions from matrix elements, the spectral lines of the non-matrix elements as Mg, Ti, and Ca, were also observed in the LIBS spectra of plastics considered in this study.

Table 4.5. The emission lines of the LIBS spectra of the ten plastics for the three datasets. Appeared in the spectra (✓), Not appeared in the spectra (×).

S. No	Element name	Emission lines (nm)	1st	2nd	3rd
1	**Carbon (C)**	C I - 247.85	✓	✓	×
2	**Hydrogen (H)**	H I - 656.29	✓	✓	✓
3	**Oxygen (O)**	O I - 777.41, O I - 844.46	✓	✓	✓
		O II - 464.12	×	×	✓
4	**Nitrogen (N)**	N I- 742.42, 744.35, 746.89, 821.78, 824.49, 868.32	✓	✓	✓
		N II -500.59, N II -567.95,	×	×	✓
5	**Sodium (Na)**	Na I - 589.52, 589.61	✓	✓	✓
6	**Magnesium (Mg)**	Mg I - 279.50, 280.34	✓	✓	×
7	**Potassium (K)**	K I - 766.49, 770.13	✓	✓	✓
8	**Calcium (Ca)**	Ca I - 393.33, 396.84, 422.67	✓	✓	✓
9	**Titanium (Ti)**	Ti I - 334.98, 363.36, 364.35, 365.42	✓	✓	×
		Ti I – 430.59, 626.10	✓	✓	✓
10	**CN ($\Delta\nu=0$)**	388.37	✓	✓	✓
11	**C_2 ($\Delta\nu=0$)**	512.96, 516.56	✓	✓	✓

These non-native metallic elements are regularly used as additives/fillers in the plastics to reduce their production cost as well as to improve the mechanical and physical properties of the materials [21, 51, 52]. Moreover, other spectral emissions (K & Na) are observed, which could be due to the contamination of the sample with their usage in daily life. In addition to atomic transitions, various molecular features corresponding to the CN violet and C_2 Swan band systems are observed. The molecular formation pathways are complex nonetheless extensive studies have demonstrated that the CN band emissions could be due to recombination of C and N in the sample or from the ambient atmosphere and partially from the native CN bands present in the samples [15, 19, 53-55]. However, the C_2 formation is mostly attributed to the inherent C=C linkages of the analyte [15, 19, 53-55]. The ambient atmosphere of the plasma plays an essential role in the evolution of the laser-

induced plasma (LIP) where the different species of the plasma plume can interact with the constituents of the surrounding environment. For the present case, the experiments were performed in ambient air only. Also, longer duration of the excitation pulse leads to the formation of high-temperature plasma due to reheating where the atomization and ionization are more favored at initial time scales in contrary to the molecular formation[54, 56]. Thus, the spectra recorded with CCD (where gating is not available to avoid the initial time scales) have shown the emission lines corresponding to ionic species of the nitrogen (N II -500.59 nm) and oxygen (O II - 464.12 nm) in comparison to the ICCD. However, air entrainment to the sample plasma plume only can be reduced by the usage of inert/buffer gas or vacuum requires a perching or vacuum chamber making the detection system bulkier), but it limits the application towards the real-time analysis.

In the next sections, the ratiometric approach, C-C correlation analysis, and various multivariate techniques have been implemented for exploring the discrimination among the samples.

4.4.2 Ratiometric analysis

Carbon is ubiquitously present in all the organic samples whereas Hydrogen, Nitrogen, and Oxygen, are three basic constituents that provide a common basis for most of the organics. The LIBS spectra of the organic samples look similar to each other and the identification of these elemental constituents has limited appeal for their discrimination owing to the complex plasma formation. However, the emission intensity ratios of the various spectral lines provide a strategy for the discrimination and identification of organic materials. Also, the spectral line intensity fluctuations in the LIBS spectra arise due to variations in the shot to shot interaction can be minimized with the analysis involving intensity ratios. The ratiometric approach correlates the theoretical/stoichiometric ratios of constituent elements to the observed peak intensity ratios in LIBS spectra. Nevertheless, the spectral line section predominantly depends on the molecular structure of the analyte and observed emission lines of the LIBS spectra. As seen from Table 4.2, only carbon and hydrogen atoms inherently present in the molecular structure/formula of all the plastics in comparison to the nitrogen and oxygen. Hence, the C/H ratio is utilized for the analysis. Moreover, it is the only one ratio which possesses minimal atmospheric contribution to

the plasma. However, for the present analysis, only 1st and 2nd datasets are considered, as the spectral signature of carbon at C-247.85 nm is not observed in the 3rd dataset (non-gated with CCD). Fig. 4.11(a&b) represents the C/H ratio plot of the 1st and 2nd datasets respectively. The actual and measured ratios in the graph correspond to their theoretical and observed intensity ratios respectively.

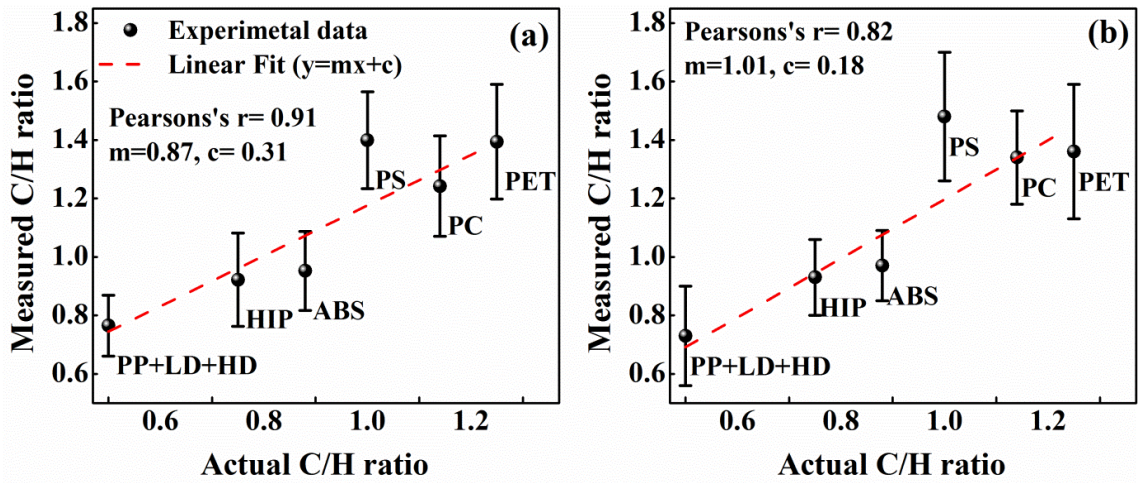

Fig. 4.11. The correlation between the actual C/H ratios to the measured intensity ratios. a) ICCD 10 shot accumulation b) ICCD single-shot acquisition. The dotted line represents the linear fit.

The solid sphere is a representative of the mean of the C/H ratios obtained from 100 measurements for each sample and the error bar corresponds to their standard deviation. The molecular structure/formula of the PPCP and SIHET is unknown hence not considered for the present analyses as well as in the next section. The actual C/H ratios of the HD, LD, and PP are the same as given in Table 4.2. Hence in the analysis, the average of (intensity ratios) these three are considered as a single point and the same is visualized in the graph as shown in Fig. 4.11(a&b). The same procedure was also considered for the analysis in the next section (correlation of no of C-C bonds). The data is fitted for a straight line equation ($y = mx + c$) as illustrated in Fig. 4.11(a&b) with a red dotted line. An improved correlation (Pearson's $r = 0.91$) is observed for the 1st dataset compared to the 2nd dataset (Pearson's $r = 0.82$). It is also observed that the measured value of the C/H ratio for the HD and LD is similar which is attributed to the similar molecular formula. Also, similar observations were reported in the literature where the linear correlation of the C/H ratio is obtained[13].

Only, partial discrimination of the plastics is achieved with the ratiometric approach as some of the ratios are overlapping with one another thus, other exploratory methods need to be evaluated for better performance. The diatomic molecular fragments and bond correlations such as CN, C=C (C_2), and C-C also provide useful indications for the discrimination of organic materials as reported in the literature [53, 54, 57]. However, molecular bonds (CN and C_2) formation pathways predominantly depend on the native bonds present in the sample along with the plasma plume interaction with the ambient atmosphere [19, 55]. Also, the origin and basic routes of the molecular formation is not yet completely understood owing to the complex phenomenon of laser-induced plasma. For the present investigation, native CN bonds present merely in ABS and inherent C_2 linkages available only in PET and PS. However, C-C bonds present in all the samples. Therefore, to see the variations among these samples the correlation analysis has been done between the C, C_2, and CN line intensities to the number of carbon single bonds present in the sample in the next section.

4.4.3 Correlation between C-C bonds to C, C_2 and CN line intensities

In this section, the number of carbon-carbon single bonds (# C-C) present in the molecular structure of each sample is correlated with the observed C, C_2, and CN line intensities. As mentioned earlier, the 3rd dataset is excluded from the analysis due to the absence of a carbon line in the LIBS spectra. It is also worth considering that the carbon line can have minimal chance of atmosphere intrusion to the plasma among all the constituents. Fig. 4.12 (a&b) illustrates the variation of the carbon line (C-247.85 nm) intensity with the number of carbon single bonds (C-C) for the 1st and 2nd datasets respectively. LD and HD considered as groups as they have the same # C-C bonds. All samples have shown a linear positive correlation with their observed spectral line intensity to the no of C-C bonds present in it except for ABS. It is the only one sample deviated from the linear approximation in which it has shown less intensity even though having the maximum number of C-C bonds in it for both the datasets as shown in Fig. 4.12 (a&b). As shown in Table 4.2, only ABS inherently contains the nitrogen atoms in their structure in contrast to the remaining samples. Further, the carbon and nitrogen present in it can lead to

recombination and favor the formation of a strong CN band. At the same time, it leads to a decrease in carbon intensity. The same is attested in the LIBS spectra of ABS where the CN violet band system is more intense compared to the carbon line C-247.85 nm as shown in Fig. 4.10. Hence, excluding ABS the correlation with carbon intensity can be considered as a good approach for the classification, and the same is envisioned in Fig. 4.12 (a&b). The data is fitted for the linear equation (y = mx + c, excluding the ABS as it has deviated from straight-line approximation). An excellent enhancement in correlation (Pearson's r = 0.97) has been observed as shown in Fig. 4.12(a) compared to the C/H correlation for the 1st data and similar behavior (Pearson's r = 0.87) noticed for the 2nd data as shown in Fig. 4.12(b). Further, Fig. 4.12 (c&d) represents the correlation of CN (Δv=0) intensities of 1st and 2nd datasets respectively.

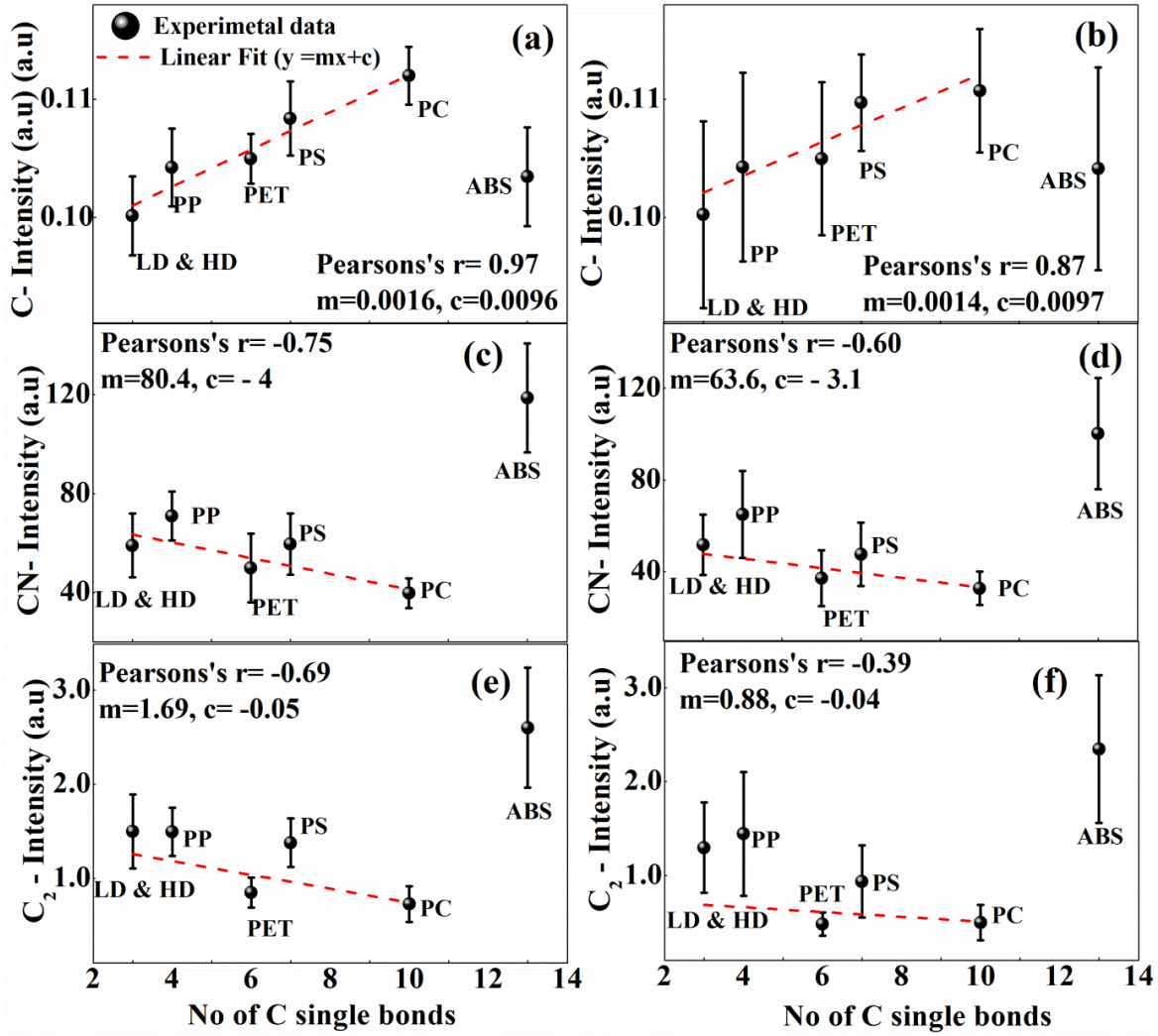

Fig. 4.12. The correlation between the number of carbon single bonds (C-C) to the C-2478.5 nm line intensity of the a) 1st dataset & b) 2nd dataset. Correlation of C_2 (Δv=0) band intensity of the c) 1st dataset & d) 2nd dataset. Correlation of CN (Δv=0) band intensity of e) 1st dataset & f) 2nd dataset. The dotted line represents the linear fit.

As discussed earlier, ABS has shown higher intensity compared to all the samples. The following mechanisms are responsible for the formation of the CN molecular bonds [54, 57, 58].

$$C + N + M \rightarrow CN + M \quad (4.1)$$

$$C + N_2 \rightarrow CN + N \quad (4.2)$$

$$C_2 + N \rightarrow CN + C \quad (4.3)$$

$$C_2 + N_2 \rightarrow 2CN \quad (4.4)$$

In the case of ns LIP, atomization is more favorable compared to the formation of molecular features which increases the carbon line intensity as shown in Fig. 4.12(a&b). Hence it has resulted in a decrease in the emission line intensities of the CN band as visualized Fig. 4.12(c&d). A negative linear correlation has been noticed for both the datasets whereas it is a positive correlation for the carbon line intensities. Moreover, the performance is decreased (Pearson's r = -0.75, -0.60) compared to the carbon line intensities. The correlation of the C_2 swan band ($\Delta v = 0$) for the 1st and 2nd datasets are illustrated in Fig. 4.12(e&f). Most of the studies in the literature suggest that these emissions could be possible due to the excitation of native C_2 (C=C) linkages and fragmentation [54, 57, 58]. The following reaction represents the formation of C_2 via fragmentation.

$$C + C + M \rightarrow C_2 + M \quad (4.5)$$

As discussed earlier, C_2 linkages only present in the PS and PET hence observed intensity mostly attributed to the fragmentation only. However, the carbon atoms formed due to fragmentation is contributed to the emission C-247.85 nm line as shown in Fig. 4.12(a&b) and increased their intensity. Hence it has affected the formation of C_2 species and a negative correlation is noticed as shown in Fig. 4.12(e&f). The performance is further degraded (Pearson's r = -0.69, -0.39) for this correlation compared to the C and CN.

It is noticed that the spectral line intensities of C, CN, and C_2 are more stable for the 1st data compared to the 2nd data which could be due to the accumulation of the spectra. It is also asserted from the SNR analysis where the SNR of the 1st data is two times greater than the 2nd dataset. Finally, these studies revealed that the formation of atomic species

favorable for the ns LIP where higher temperatures due to the reheating of plasma lead to the atomization. In the next sections, multivariate techniques are considered for exploring the classification of the plastics.

4.4.4 Classification using PCA

Rich spectral content present in the LIBS spectra combined with multivariate/chemometric techniques can enhance the identification accuracies of the samples, unlike the ratiometric analysis where only two variables are deployed [15, 23, 59, 60]. Here, PCA has been applied for three different datasets (1st, 2nd, and 3rd) where a total of 1000 normalized spectra for each dataset (10 samples and 100 spectra for each sample) are utilized. The 3D score plots obtained from the PCA for the 1st, 2nd, and 3rd datasets are illustrated in Fig. 4.13(a-c) respectively. Each data point in the score plot is representative of one spectrum. An inset in Fig. 4.13(a) is included to facilitate the clear view of separation of SIHET and PC. All the plastics are well separated from one another with an excellent clustering has been observed for the 1st and 3rd datasets. Albeit, the performance is slightly reduced for the 2nd dataset where some of the plastics (HD & LD, HIP & PS, and PC & SIHET) are overlapped with one another in contrast to the 1st and 3rd datasets. The discriminative ability of the PCA is nearly similar for the 1st and 3rd datasets as visualized in figure Fig. 4.13(a&c) albeit the data points are distributed more compactly in score plot for the 3rd compared with the 1st dataset. The accumulation of the spectra has shown more stability in the spectral measurements (i.e. less variation and high SNR) as seen from Fig. 4.8. It is also affected the performance of the PCA where the excellent clustering is observed for the 1st dataset compared to the 2nd. Further, the data spread in the 3d score plot is also less for the 1st dataset due to the accumulation. A negligible overlap is observed for the HD and LD and the interference is slightly higher for 2nd dataset which could be due to sharing the same molecular structure.

The loadings plot constructed by using the first three consecutive PCs for the three datasets (1st, 2nd, and 3rd) is visualized in Fig. 4.13(d-f) respectively. All the characteristic emission lines are labeled with unique notations at their corresponding wavelengths as envisioned in Fig. 4.13(d-f). The loadings plot of all the datasets majorly consists of the emissions lines of C, H, N, O, CN, and C_2 with different correlations strengths.

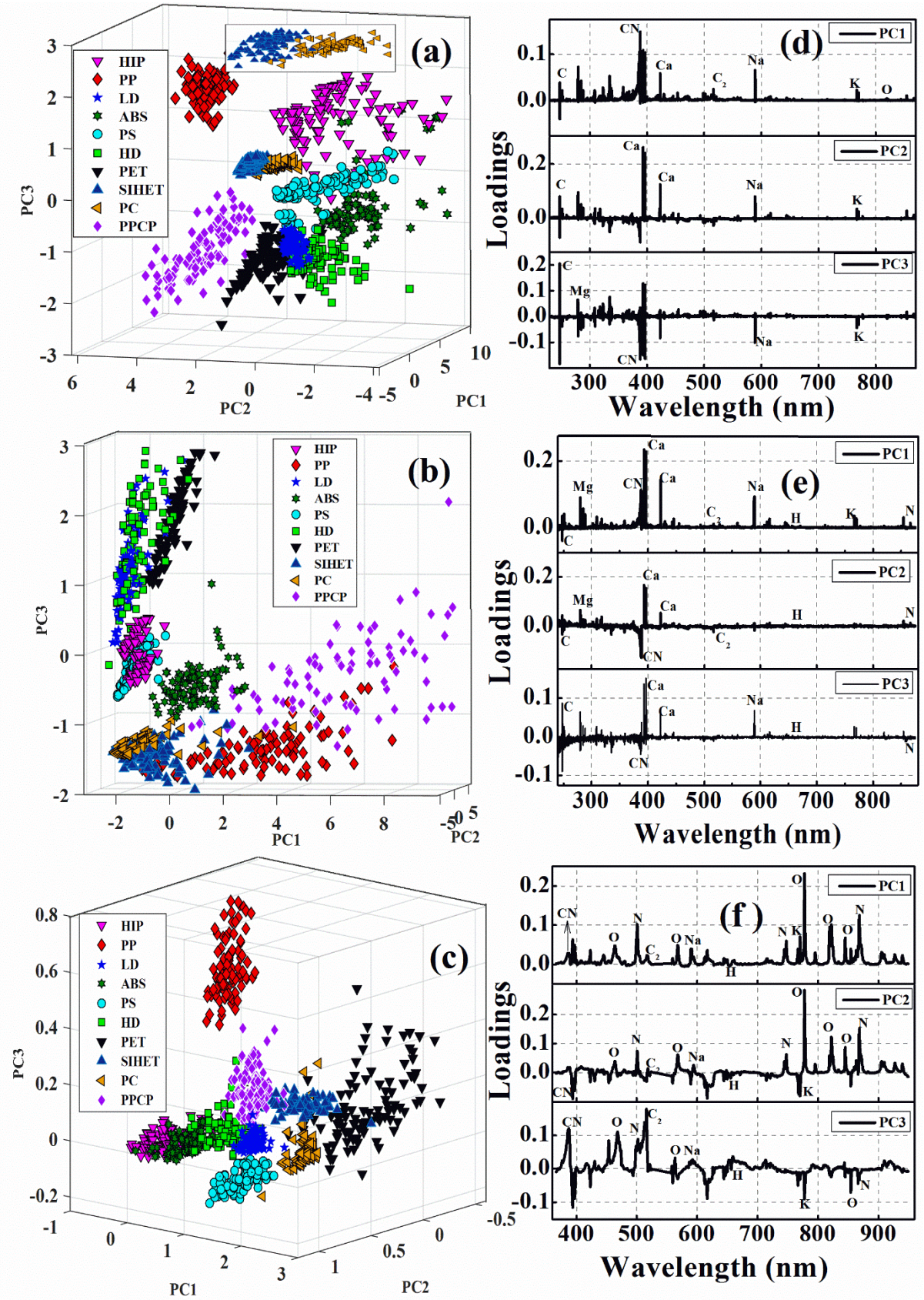

Fig. 4.13. (a-c) Correspond to the 3D score plot of 1st, 2nd & 3rd datasets respectively. The inset in figure (a) visualizes the separation between SIHET and PC. (d-f) Correspond to the loadings plot of the 1st, 2nd & 3rd datasets respectively.

In addition to these, the spectral lines of various inorganic elements viz, Ca, Mg, K, and Ca have also appeared. These non-native elements are added in the plastics manufacturing process for increasing their strength as well as for reducing the production cost. The first three consecutive PCs of the 1st dataset explain the net variance of 47.1, 26.6, and 12.4 % respectively. The CN molecular band system ($\Delta\nu=0$) at 378–390 nm is the strongest feature with positive correlation in the 1st PC followed by spectral lines of Na, Ca, C and H as shown in Fig. 4.13(d). On the other hand, PC2 represents Ca lines alongside the contributions from the C and CN. The Carbon line at C-247.85 nm line is the prominent emission with a positive correlation in the PC3 and followed by the CN swan band. In the case of 2nd dataset, the first PC itself corresponds to the fifty percent of the net variance. The subsequent two PCs explain the 15.2, and 8.2 % of the variance, and together five PCs account for the total variance of 82.1 %. It has been noticed that the PC1 looks similar to the 1st dataset with varying magnitudes of the scores.

The loadings plot of the 3rd dataset is shown in Fig. 4.13(f) where the first PC appears the same as the actual spectra except the minimal variations in intensity and negligible contribution from the hydrogen line. The first three PCs viz., PC1, PC2, and PC3 explain the variance of 55.9, 24.1, and 8.2 % present in the data respectively. Furthermore, the first five PCs cumulatively account for the net variance of 94 %. Most of the coefficients present loadings plot correspond to the several features of the atomic and molecular emissions of the LIBS spectra. The spectral line of oxygen at OI-777.41 nm has shown the highest positive correlation followed by emission lines of N, CN, C_2, and H in the PC1. Apart from these, spectral lines of Mg, Na Ca, and K are also observed. Also, similar features are observed in PC2 albeit with different correlations. The PC3 is majorly dominated by the presence of the CN violet band system and followed by the C_2 swan band, O, and N emission lines.

PCA is a good exploratory technique for the visualization of the clustering of the plastics where excellent classification has been attained. However, owing to the unsupervised nature, it can't be deployed for the labeling of an unknown plastic. Thus, in the following sections, a supervised algorithm ANN has been exploited for the one to one labeling of the plastics which is more relevant for the real-time application.

4.4.5 Identification using ANN

The ANN classifier is a widely employed supervised multivariate tool for the various applications viz, pattern recognition[61], signal processing[62], and image/sample identification [63, 64]. In the LIBS community, it has been deployed for the identification of various samples which also include plastics [15, 20, 21, 53]. For the present study, a three-layer ANN algorithm is utilized. The details of the ANN architecture are briefly discussed in chapter 1. The number of neurons in the hidden layer is optimized for better performance and the results are shown in Fig. 4.14. It has been observed that the fifteen are found to be best for the current study where the identification rates are maximum for each plastic sample.

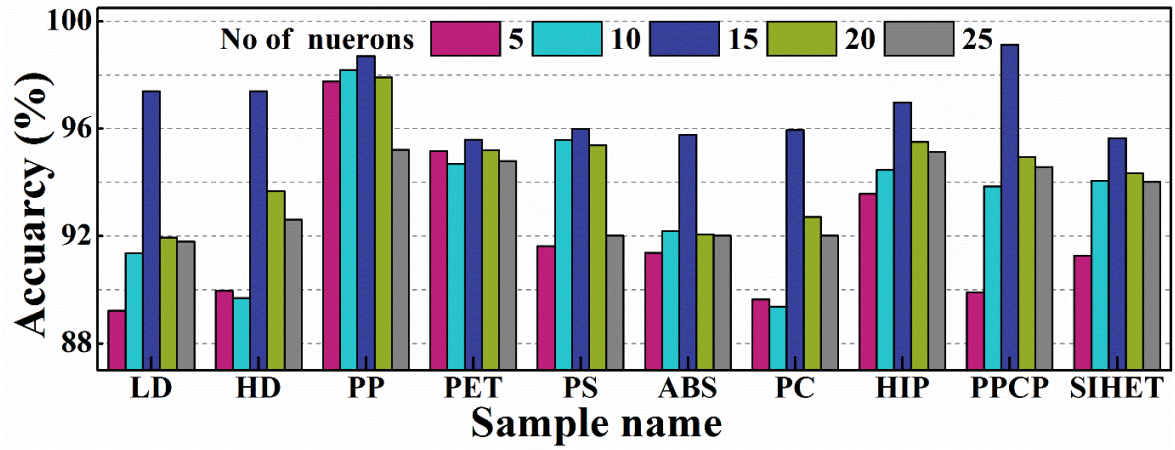

Fig. 4.14. The variation of identification accuracies with the no of neurons in the hidden layer.

The analysis performed 1000 times, and in each iteration, the input dataset was randomly divided into three subsets as training testing and validation which correspond to the 70, 15, and 15 % of the total data respectively. The target dataset composed of class labels (Binary digits) of all the ten representative plastics. Here, the analytical performance of the ANN has been evaluated for the three datasets (1^{st}, 2^{nd}, and 3^{rd}) as mentioned earlier. The analysis is done by considering the total data (22293, 1237 data points i.e. 'wavelengths for each spectrum' for ICCD and CCD respectively) as the input. The ANN results (confusion matrix) obtained for the 3^{rd} dataset are presented in Table 4.6. The diagonal elements correspond to the correct identification rate and the off-diagonal represents miss classification rate.

Table 4.6. The confusion matrix obtained for the 3rd dataset.

	Sample name	Predicted labels									
		LD	HD	PP	PET	PS	ABS	PC	HIP	PPCP	SIHET
Reference labels	LD	97.4	0.85	0.14	0.14	0.24	0.35	0.15	0.21	0.34	0.18
	HD	0.73	97.4	0.21	0.24	0.21	0.46	0.11	0.11	0.31	0.22
	PP	0.17	0.14	98.7	0.19	0.03	0.15	0.24	0.21	0.12	0.05
	PET	0.39	0.34	0.32	95.59	0.36	0.48	0.72	0.48	0.41	0.91
	PS	0.41	0.62	0.23	0.18	95.99	0.13	0.68	0.46	0.53	0.77
	ABS	0.22	1.19	0.14	0.19	0.32	95.77	0.33	1.34	0.24	0.26
	PC	0.17	0.61	0.22	0.77	0.29	0.52	95.95	0.25	0.25	0.97
	HIP	0.01	0.37	0.26	0.12	0.15	1.63	0.29	96.98	0.16	0.03
	PPCP	0.25	0.23	0.05	0.02	0.01	0.04	0.07	0.04	99.12	0.17
	SIHET	0.42	0.35	0.37	0.55	0.19	0.32	0.89	0.18	1.09	95.64

Table 4.7. The average identification rates obtained from ANN (~1000 times).

S No	Sample name	Correct identification rate (%)		
		1st	2nd	3rd
1	LD	98.00	89.96	97.40
2	HD	98.01	95.72	97.40
3	PP	99.00	94.85	98.70
4	PET	98.96	90.88	95.59
5	PS	97.07	91.98	95.99
6	ABS	96.14	93.94	95.77
7	PC	95.79	86.65	95.95
8	HIP	95.25	90.99	96.98
9	PPCP	96.12	93.03	99.12
10	SIHET	95.13	93.33	95.64
Average		**96.95**	**92.13**	**96.85**
Training time (s)		**43.80**	**49.60**	**1.40**
Testing time (ms)		**42.90**	**43.70**	**10.30**

The average identification rate acquired over 1000 times for each sample and the three datasets are enumerated in

Table 4.7. The correct labelling rates of more than ~95 % for all the plastics are obtained for the 1st and 3rd datasets. The measured errors/uncertainties are found to be ~0.1-0.9, 0.2-2.0, and 0.1-0.5 % for the three datasets respectively. Highest correct identification rates

more than ~ 99 % are accomplished for the 1st and 3rd whereas 2nd has shown ~ 96 %. The LD and HD plastics are identified with similar accuracy for 1st and 3rd datasets and LD is principally miss-classified as HD and vice versa. The score plot visualization (Fig. 4.13(a-c)) of the PCA analysis also has asserted the same where these two plastics have slightly interfered with one another for the 1st and 3rd datasets and overlap is more for the 2nd dataset. The accumulation of the spectra has improved the SNR for the 1st dataset compared to the 2nd dataset as mentioned in the previous sections. It could have also affected the performance of the ANN where the identification rates are higher for the 1st in contrast to the 2nd. Further, the average prediction rates (~ 97 % - an average for ten plastics) are similar for the 1st and 3rd datasets as given in
Table 4.7. However, the training and testing times of the developed ANN model are drastically decreased by a factor of ~31, and ~4 times respectively for the 3rd dataset compared to the 1st & 2nd dataset. Moreover, it is worth considering that, the spectral data acquisition time is 10 times faster for the 3rd dataset as it acquires only one shot in contrast to ten shot accumulation mode, thus the overall time can be reduced by a factor of ~15 times to the 1st dataset.

Further, the prediction ability of the 2nd dataset is always shown lesser in comparison with the remaining datasets. Besides that, more computational times are also required for the analysis which could be possible due to slightly noisy data acquired in addition to the shot to shot variation [21]. Finally, the results demonstrated that the correct prediction rates of ~97~ 99 % and average identification accuracies of ~97 % can be achieved for the 3rd dataset i.e. the data acquired with CCD even with a single-shot mode.

4.4.6 ANN analysis combined with feature selection

In the previous section, it is demonstrated that the recognition of plastics with average identification rates ~97 % can be attained by employing the three-layer ANN model. However, the training and testing-times required for one iteration lie in the range of ~42-44 s & ~42-44 ms respectively, for the 1st dataset and it is slightly higher for the 2nd dataset. It could be attributed to treating the total data points ~22293 as an input while developing the ANN model. Therefore, it would be beneficial to limit the investigation for only a certain number of selected lines of interest by removing the irrelevant variables

which contribute to increasing the analytical speed as well as leads to higher identification accuracy. Our previous works on the recognition of explosives with the aid of manual feature selection and GA combined with PLSDA have shown improved performance [65]. For the present investigation, the method of variable importance (VI) achieved from a multivariate random forest (RF) algorithm is chosen for variable selection. The details of the RF algorithm are presented in chapter 1. The VI scores obtained from the RF algorithm by deploying spectral data of the ten plastics for the 3rd dataset is illustrated in Fig. 4.15(a).

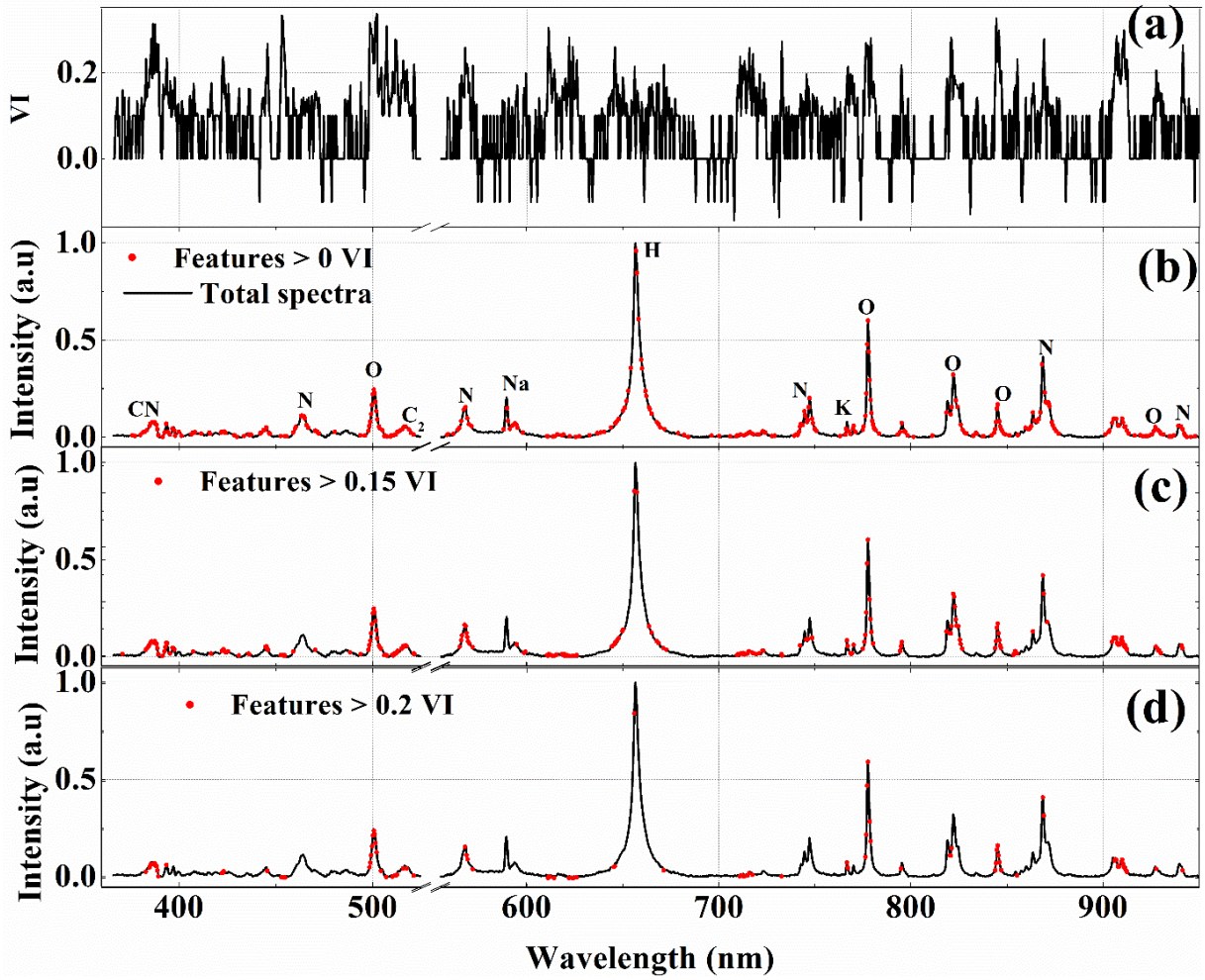

Fig. 4.15. a) Variable importance (VI) estimated by the RF model for the spectra recorded with the CCD. b) The LIBS spectra of the LD plastic. The red dots represent the features obtained with varying the different VI thresholds. (b-d) represent 0, 0.15, 0.2 VI respectively. The features with VI > 0.05 and VI > 0.1 are similar to the features with VI>0 hence not shown in the figure.

Further, the ANN analysis is performed by considering only the prominent spectral features obtained from the VI as an input. The variables are selected by opting for a certain

value of the threshold for VI as shown in Table 4.8. For example 'Threshold – 0' represents the only the features greater than '0 VI' are considered. A total of five different sets of features are selected by changing the threshold VI value i.e., 0 - 0.2 in steps of 0.05. The results obtained from these features as the input for the ANN analysis are given in Table 4.8.

Table 4.8. The identification rates obtained from the ANN by employing total data and feature selection.

Spectral input to the ANN	Data (%)			Average classification accuracy (%)			Training time (S)			Testing time (ms)		
	1st	2nd	3rd	1st	2nd	3rd	1st	2nd	3rd	1st	2nd	3rd
Total data	100	100	100	96.95	92.13	96.85	43.8	49.6	1.4	42.9	43.7	10.3
Thresold-0	6.4	7.4	24	95.21	91.93	95.00	2.6	4.2	1.0	13.2	13.6	10.3
Thresold-0.05	6.4	7.3	23	95.10	91.58	94.80	2.6	4.1	0.9	13.5	13.5	10.5
Thresold-0.1	6.4	7.2	22	94.79	91.07	94.78	2.6	4.1	0.9	13.2	13.3	10.3
Thresold-0.15	0.4	0.5	18	92.27	89.30	94.52	0.5	0.6	0.6	11.5	10.9	10.3
Thresold-0.2	0.1	0.1	8	79.43	80.15	93.06	0.4	0.5	0.4	11.5	10.3	10.0

It is observed that most of the features chosen from the RF algorithm are representative of characteristic emission lines of the C, H, N, O, CN, and C_2. The analysis performed with spectral features of VI greater than the zero threshold has shown promising results (which is utilized only ~ 8 & 25 % of total data for the ICCD & CCD respectively) where the average identification accuracies are close (barely a reduction of ~ 1.5 %) to the total data. Nevertheless, it has drastically reduced the training times which are found to be more than an order as given in Table 4.8. The training times at threshold zero compared to the total data are reduced by a factor of ~ 17, 12, and 1.4 for three datasets respectively. Similarly, the testing times are decreased by a factor of 3 times for the 1st & 2nd datasets. The identification rates and the computational times (training & testing) are almost the same for the VI threshold of 0, 0.05, and 0.1. It could be due to the number of variables (% of data) selected as the input to the ANN at these thresholds are nearly similar.

With prior information of the emission features in the LIBS spectra of plastics, it is visually inspected and found that 2/3rd of the total variables are irrelevant/noisy for the data acquired with ICCD. Hence, the variable selection has shown more influence on the spectral data acquired with ICCD and leads to a significant reduction of the analysis time. It is attributed to choosing only the most important variables from the huge number of

variables (~22300) available in the LIBS spectra in comparison to the data acquired with CCD which contains only a total of ~1240 variables. The features obtained for VI threshold greater than the 0.2 has decreased the analytical performance of ANN could be due to opting only very less number of variables (see Fig. 4.15(d)) as an input for the model. It is worth considering that the identification accuracies achieved for the 2nd dataset are always lesser than the 1st and 3rd. Feature section based on VI-RF combined with the ANN proved it as a potential candidate where the 10 fold reduction of workload can be achieved without compromising the classification accuracy significantly. Also, the data storage limitations can be overcome by the features selection and it is extremely useful while working with the large datasets which involve a higher number of samples for real-time identification.

4.5 Summary

Rapid and accurate identification of ten different post-consumer plastics obtained from a local recycling center is demonstrated in this chapter. The optical emissions from the plasma are recorded with two different spectrometers/detectors in which the first one is an Echelle spectrometer coupled with an ICCD and the second one is a compact, portable, and low-cost Czerny Turner CCD spectrometer. Also, the LIBS spectra are acquired in two different modes i.e., ten shots accumulation (for ICCD only) and one-shot acquisition (for ICCD and CCD). Initially, the analysis is performed with the ratiometric approach and correlation of C-C bonds with the C, CN, and C_2. spectral line intensities. However, it has resulted in a partial classification of the plastics. Further, the multivariate technique PCA is employed as an exploratory tool for visualizing the discrimination among the samples where the efficient separation is demonstrated. In addition to that, a supervised learning algorithm ANN is utilized for one to one labeling of the plastics. The results achieved from ANN analysis revealed that the correct identification rates (average of 1000 iterations) of more than 99 % can be attained. Apart from that, it is shown that the predictive ability of the ANN is similar for the data acquired with the ICCD in ten shot accumulations and single-shot acquisition for the CCD. Nonetheless, the training & testing times (computational workload) are greatly decreased by a factor of 31 & 4 times respectively by deploying the compact CCD spectrometer compared to the ICCD. Besides

that, the total analytical time (computation & data acquisition) can be reduced by 15 times which favors rapid identification. It is worth considering that, the correct labeling rates achieved from the single-shot ICCD analysis decreased by 5 % and analysis time increased by 4 times in comparison with the CCD. The feature selection combined with ANN has resulted in the reduction of the analysis time by more than 10 times for the ICCD without compromising the identification accuracy. Further, the LIBS detection/collection system's weight, size, and more importantly cost can be reduced by one order by utilizing the CCD spectrometer. Finally, the results demonstrate that higher accuracies with rapid identification (testing time only ~ 10 ms) can be accomplished in a single shot mode with the compact spectrometer which makes it as a field-deployable technique for the real-time investigation.

4.6 References

1. C.M. Rochman, M.A. Browne, B.S. Halpern *et al.*, "Policy: Classify plastic waste as hazardous", Nature, 494, **2013**.
2. R. Geyer, J.R. Jambeck, and K.L. Law, "Production, use, and fate of all plastics ever made", Science advances, 3, **2017**.
3. M. Chanda, and S.K. Roy, "Plastics technology handbook", CRC press**2006**.
4. K. Liu, D. Tian, C. Li *et al.*, "A review of laser-induced breakdown spectroscopy for plastic analysis", TrAC Trends in Analytical Chemistry, **2018**.
5. B. Ruj, V. Pandey, P. Jash *et al.*, "Sorting of plastic waste for effective recycling", International Journal of Applied Science and Engineering Research, 4, **2015**.
6. E.A. Bruno, "Automated sorting of plastics for recycling", North Carolina Department of Environment and natural resources, **2000**.
7. M.T. Carvalho, C. Ferreira, A. Portela *et al.*, "Application of fluidization to separate packaging waste plastics", Waste Management, 29, **2009**.
8. K.M. Shameem, K.S. Choudhari, A. Bankapur *et al.*, "A hybrid LIBS–Raman system combined with chemometrics: an efficient tool for plastic identification and sorting", Analytical and Bioanalytical Chemistry, 409, **2017**.
9. V. Allen, J.H. Kalivas, and R.G. Rodriguez, "Post-consumer plastic identification using Raman spectroscopy", Applied spectroscopy, 53, **1999**.
10. H. Langhals, D. Zgela, and T. Schlücker, "High performance recycling of polymers by means of their fluorescence lifetimes", Green and Sustainable Chemistry, **2014**.
11. T. Huth-Fehre, R. Feldhoff, T. Kantimm *et al.*, "NIR-Remote sensing and artificial neural networks for rapid identification of post consumer plastics", Journal of Molecular Structure, 348, **1995**.
12. K. Liu, D. Tian, C. Li *et al.*, "A review of laser-induced breakdown spectroscopy for plastic analysis", TrAC Trends in Analytical Chemistry, 110, **2019**.
13. J. Anzano, R.-J. Lasheras, B. Bonilla *et al.*, "Classification of polymers by determining of C 1: C 2: CN: H: N: O ratios by laser-induced plasma spectroscopy (LIPS)", Polymer Testing, 27, **2008**.
14. M.A. Gondal, and M.N. Siddiqui, "Identification of different kinds of plastics using laser-induced breakdown spectroscopy for waste management", Journal of Environmental Science and Health Part A, 42, **2007**.
15. R. Junjuri, C. Zhang, I. Barman *et al.*, "Identification of post-consumer plastics using laser-induced breakdown spectroscopy", Polymer Testing, 76, **2019**.
16. S. Barbier, S. Perrier, P. Freyermuth *et al.*, "Plastic identification based on molecular and elemental information from laser induced breakdown spectra: a comparison of plasma conditions in view of efficient sorting", Spectrochimica Acta Part B: Atomic Spectroscopy, 88, **2013**.
17. Y. Yu, L. Guo, Z. Hao *et al.*, "Accuracy improvement on polymer identification using laser-induced breakdown spectroscopy with adjusting spectral weightings", Optics express, 22, **2014**.
18. R. Lasheras, C. Bello-Gálvez, and J. Anzano, "Identification of polymers by libs using methods of correlation and normalized coordinates", Polymer Testing, 29, **2010**.
19. S. Grégoire, V. Motto-Ros, Q. Ma *et al.*, "Correlation between native bonds in a polymeric material and molecular emissions from the laser-induced plasma observed with

space and time resolved imaging", Spectrochimica Acta Part B: Atomic Spectroscopy, 74, **2012**.
20. R. Sattmann, I. Mönch, H. Krause *et al.*, "Laser-induced breakdown spectroscopy for polymer identification", Applied Spectroscopy, 52, **1998**.
21. M. Boueri, V. Motto-Ros, W.-Q. Lei *et al.*, "Identification of polymer materials using laser-induced breakdown spectroscopy combined with artificial neural networks", Applied spectroscopy, 65, **2011**.
22. V. Unnikrishnan, K. Choudhari, S.D. Kulkarni *et al.*, "Analytical predictive capabilities of laser induced breakdown spectroscopy (LIBS) with principal component analysis (PCA) for plastic classification", RSC Advances, 3, **2013**.
23. S. Grégoire, M. Boudinet, F. Pelascini *et al.*, "Laser-induced breakdown spectroscopy for polymer identification", Analytical and bioanalytical chemistry, 400, **2011**.
24. J. Anzano, B. Bonilla, B. Montull-Ibor *et al.*, "Plastic identification and comparison by multivariate techniques with laser-induced breakdown spectroscopy", Journal of Applied Polymer Science, 121, **2011**.
25. K. Liu, D. Tian, H. Wang *et al.*, "Rapid classification of plastics by laser-induced breakdown spectroscopy (LIBS) coupled with partial least squares discrimination analysis based on variable importance (VI-PLS-DA)", Analytical Methods, 11, **2019**.
26. H. Jull, J. Bier, R. Künnemeyer *et al.*, "Classification of recyclables using laser-induced breakdown spectroscopy for waste management", Spectroscopy Letters, 51, **2018**.
27. J. Anzano, B. Bonilla, B. Montull-Ibor *et al.*, "Classifications of Plastic Polymers based on Spectral Data Analysis with leaser induced Breakdown Spectroscopy", Journal of Polymer Engineering, 30, **2010**.
28. J. Anzano, I. Gornushkin, B. Smith *et al.*, "Laser-induced plasma spectroscopy for plastic identification", Polymer engineering & science, 40, **2000**.
29. J. Anzano, M.-E. Casanova, M.-S. Bermúdez *et al.*, "Rapid characterization of plastics using laser-induced plasma spectroscopy (LIPS)", Polymer Testing, 25, **2006**.
30. Y. Tang, Y. Guo, Q. Sun *et al.*, "Industrial polymers classification using laser-induced breakdown spectroscopy combined with self-organizing maps and K-means algorithm", Optik, 165, **2018**.
31. R.S. Harmon, F.C. DeLucia, A. LaPointe *et al.*, "Discrimination and identification of plastic landmine casings by single-shot broadband LIBS", SPIE**2005**.
32. V.C. Costa, F.W.B. Aquino, C.M. Paranhos *et al.*, "Identification and classification of polymer e-waste using laser-induced breakdown spectroscopy (LIBS) and chemometric tools", Polymer Testing, 59, **2017**.
33. F.W.B. Aquino, and E.R. Pereira-Filho, "Analysis of the polymeric fractions of scrap from mobile phones using laser-induced breakdown spectroscopy: Chemometric applications for better data interpretation", Talanta, 134, **2015**.
34. G. Guo, G. Niu, Q. Lin *et al.*, "Compact instrumentation and (analytical) performance evaluation for laser-induced breakdown spectroscopy", Instrumentation Science & Technology, 47, **2019**.
35. F. Trichard, S. Moncayo, D. Devismes *et al.*, "Evaluation of a compact VUV spectrometer for elemental imaging by laser-induced breakdown spectroscopy: application to mine core characterization", Journal of Analytical Atomic Spectrometry, 32, **2017**.
36. A.K. Myakalwar, S.K. Anubham, S.K. Paidi *et al.*, "Real-time fingerprinting of structural isomers using laser induced breakdown spectroscopy", Analyst, 141, **2016**.

37. A.K. Myakalwar, N.C. Dingari, R.R. Dasari *et al.*, "Non-gated laser induced breakdown spectroscopy provides a powerful segmentation tool on concomitant treatment of characteristic and continuum emission", PloS one, 9, **2014**.
38. S. Sreedhar, M.A. Kumar, G.M. Kumar *et al.*, "Laser-induced breakdown spectroscopy of RDX and HMX with nanosecond, picosecond, and femtosecond pulses", Chemical, Biological, Radiological, Nuclear, and Explosives (CBRNE) Sensing XI, International Society for Optics and Photonics, **2010**.
39. A.S. Mangsor, Z.H. Rizvi, K. Chaudhary *et al.*, "Classification of alloys using laser induced breakdown spectroscopy with principle component analysis", Journal of Physics: Conference Series, IOP Publishing, **2018**.
40. F.B. Gonzaga, W.F. de Carvalho Rocha, and D.N. Correa, "Discrimination between authentic and false tax stamps from liquor bottles using laser-induced breakdown spectroscopy and chemometrics", Spectrochimica Acta Part B: Atomic Spectroscopy, 109, **2015**.
41. J.G.R. Leandro, F.B. Gonzaga, and J.V. de Figueiredo Latorraca, "Discrimination of wood species using laser-induced breakdown spectroscopy and near-infrared reflectance spectroscopy", Wood Science and Technology, **2019**.
42. J. Savovic, M. Momcilovic, S. Zivkovic *et al.*, "LIBS Analysis of Geomaterials: Comparative Study of Basalt Plasma Induced by TEA CO2 and Nd: YAG Laser in Air at Atmospheric Pressure", Journal of Chemistry, 2017, **2017**.
43. M.N. Siddiqui, M.A. Gondal, and H.H. Redhwi, "Identification of different type of polymers in plastics waste", Journal of Environmental Science and Health Part A, 43, **2008**.
44. P.P. Nair, K. George, and N. Jayakrishnan, "Studies on mechanical behavior high impact polystyrene/vinyl clay nanocomposites: Comparison between in situ polymerization and melt mixing", Polymer Composites, 38, **2017**.
45. P. Mukherjee, A. Rani, and P. Saravanan, "Chapter 4 - Polymeric Materials for 3D Bioprinting", in: N. Ahmad, P. Gopinath, R. Dutta (Eds.) 3D Printing Technology in Nanomedicine, Elsevier**2019**.
46. Y.W. Cheung, and R.S. Stein, "Critical analysis of the phase behavior of poly (. epsilon.-caprolactone)(PCL)/polycarbonate (PC) blends", Macromolecules, 27, **1994**.
47. G. Bikulčius, I. Ignatjev, and A. Ručinskienė, "Rapid method to determine suitability of ABS plastics for metallisation", Transactions of the IMF, 92, **2014**.
48. J. Lacoste, F. Delor, J. Pilichowski *et al.*, "Polybutadiene content and microstructure in high impact polystyrene", Journal of applied polymer science, 59, **1996**.
49. D.I. Bower, and W. Maddams, "The vibrational spectroscopy of polymers", Cambridge University Press**1992**.
50. A. Dowgiallo, "Trace level pesticide detection utilizing gold nanoparticles and surface enhanced Raman spectroscopy (SERS)", Synthesis and Photonics of Nanoscale Materials XVI, International Society for Optics and Photonics, **2019**.
51. J. Fox, "Analysis of Polymer Additives in the Packaging Industry", University of Florida, **2008**.
52. J.N. Hahladakis, C.A. Velis, R. Weber *et al.*, "An overview of chemical additives present in plastics: Migration, release, fate and environmental impact during their use, disposal and recycling", Journal of Hazardous Materials, 344, **2018**.

53. R. Junjuri, and M.K.K. Gundawar, "Femtosecond laser induced breakdown spectroscopy studies for the identification of the plastics", Journal of Analytical Atomic Spectrometry, **2019**.
54. S.A. Kalam, N.L. Murthy, P. Mathi *et al.*, "Correlation of molecular, atomic emissions with detonation parameters in femtosecond and nanosecond LIBS plasma of high energy materials", Journal of Analytical Atomic Spectrometry, 32, **2017**.
55. Á. Fernández-Bravo, T. Delgado, P. Lucena *et al.*, "Vibrational emission analysis of the CN molecules in laser-induced breakdown spectroscopy of organic compounds", Spectrochimica Acta Part B: Atomic Spectroscopy, 89, **2013**.
56. S.S. Harilal, B.E. Brumfield, B.D. Cannon *et al.*, "Shock wave mediated plume chemistry for molecular formation in laser ablation plasmas", Analytical chemistry, 88, **2016**.
57. S. Mousavi, M.H. Farsani, S. Darbani *et al.*, "CN and C 2 vibrational spectra analysis in molecular LIBS of organic materials", Applied Physics B, 122, **2016**.
58. M. Dong, J. Lu, S. Yao *et al.*, "Experimental study on the characteristics of molecular emission spectroscopy for the analysis of solid materials containing C and N", Optics express, 19, **2011**.
59. A.K. Shaik, N.R. Epuru, H. Syed *et al.*, "Femtosecond laser induced breakdown spectroscopy based standoff detection of explosives and discrimination using principal component analysis", Optics express, 26, **2018**.
60. M.K. Gundawar, R. Junjuri, and A.K. Myakalwar, "Standoff Detection of Explosives at 1 m using Laser Induced Breakdown Spectroscopy", Defence Science Journal, 67, **2017**.
61. W. Al-Nuaimy, Y. Huang, M. Nakhkash *et al.*, "Automatic detection of buried utilities and solid objects with GPR using neural networks and pattern recognition", Journal of applied Geophysics, 43, **2000**.
62. A. Cochocki, and R. Unbehauen, "Neural networks for optimization and signal processing", John Wiley & Sons, Inc.**1993**.
63. F.J. Fortes, J. Moros, P. Lucena *et al.*, "Laser-Induced Breakdown Spectroscopy", Analytical Chemistry, 85, **2013**.
64. Z.-H. Zhou, Y. Jiang, Y.-B. Yang *et al.*, "Lung cancer cell identification based on artificial neural network ensembles", Artificial Intelligence in Medicine, 24, **2002**.
65. A.K. Myakalwar, N. Spegazzini, C. Zhang *et al.*, "Less is more: Avoiding the LIBS dimensionality curse through judicious feature selection for explosive detection", Scientific reports, 5, **2015**.

CHAPTER 5 : Development of ns standoff LIBS system for the identification of explosives

The development of the ns standoff LIBS (ST-LIBS) system is presented in this chapter. Initially, the experiments are performed at a distance of 1 m and further, extended to 6.5 m. The preliminary studies were demonstrated on a set of five explosives at 1 m distance. The experimental setup utilized a single Plano-convex lens in combination with the Mechelle spectrograph equipped with an ICCD for collecting the optical emissions. Further, the investigation extended for probing the samples (5 explosives and 19 non-explosives) at a remote distance of 6.5 m. However, for developing a low-cost portable detection system, a handheld non-gated CCD spectrometer is utilized. A systematic evaluation and optimization of focusing and collection systems have been done for improving the performance of the developed ST-LIBS system. The identification accuracies of over 98 % were achieved among the explosives with the ANN algorithm. Despite the huge similarities in the spectral features of the explosives and non-explosives, the correct labeling rates ~ 97 % were demonstrated.

Part of this chapter's work has been published as following journal articles.

1. ***Rajendhar Junjuri**, M.K. Gundawar, A.K. Myakalwar, "Standoff Detection of Explosives at 1 m using Laser Induced Breakdown Spectroscopy", Defence Science Journal, (2017).*

2. ***Rajendhar Junjuri,** A. Prakash Gummadi, M. Kumar Gundawar, "Single-Shot Compact Spectrometer Based Standoff LIBS Configuration For Explosive Detection Using Artificial Neural Networks ", Optik, (2020).*

5.1 Introduction

In the recent past, the efforts for the detection of hazardous materials [1](biological agents, explosives and improvised explosive devices (IEDs) have seen a major thrust in the global community as well as in India on account of antisocial elements and to counter the terrorism activities. LIBS can be a potential solution for application where the closer proximity of the operator to the sample is inaccessible/threatening or harsh environments. The standoff capability of LIBS offers a suitable choice for the identification of hazardous materials including explosives in such situations, which otherwise is not possible by other conventional vapour based techniques[2-4]. The standoff detection of explosives is a multifold challenging task where the signal strength decreases inversely with distance, inevitable losses in intensity arise due to atmospheric absorption/scattering of light and the possibility of the sample being present on varied types of materials. LIBS as compared to other optical techniques like Raman, not only gives the abundant light signal but also the instrumentation is relatively simpler.

Two distinct scenarios for the detection of explosives can be envisaged - the former is the need to distinguish a material as explosive or non-explosive, such an application is relevant in identifying the bombs in a suspected area. The latter being an identification of the specific explosive, which can give crucial inputs to the investigators to solve a bomb blast case. Also, the spectra for a large class of organic samples, particularly the secondary explosives, which are primarily of the molecular form CHNO are strikingly similar. As LIBS is an elemental technique, the resulting spectra of these samples, and numerous other non-explosive materials like sugars, grease, oils, plastics, etc. are primarily dominated by carbon, hydrogen, nitrogen, and oxygen. The atmospheric oxygen/nitrogen and hydrogen from the humidity may further compound the problem. Though visually the spectra may look similar and almost identical, but with the aid of suitable multivariate approaches, it is still possible to classify the samples. Ratiometric analysis, where the various spectral line intensity ratios have shown the partial classification [5-7]. Various multivariate techniques like PCA[8, 9], SIMCA[10], and PLS-DA[8] have been exploited for the discrimination of the explosives and their residues on different substrates. Recently, semi-supervised learning

method, K-nearest neighbour (KNN) algorithm has been applied for the explosive identification in close contact LIBS system[11].

Different standoff laser-induced breakdown spectroscopy (ST-LIBS) configurations (given in Table 5.1) [12, 13] have been employed in various fields such as process control[14], explosive detection[5, 15-17], planetary exploration[18-20], and geology [21], etc. Table 5.1 provides the technical and analytical details of the various ST-LIBS configurations reported in the literature for the different applications (only the experiments with standoff distance more than 5 m are considered).

Out of all works presented in Table 5.1, only the last seven are solely devoted to the identification of the explosives and their residues. However, only the double-pulse LIBS (DP-LIBS) configuration has been investigated. The evaluation of the DP LIBS systems for the standoff regime took advantage of enhancement in the signal strength [22], nevertheless, the system size is bulky [23]. In the DP-LIBS configuration, two lasers beams should be temporally separated to vary the inter-pulse delay time [24]. It has been achieved by splitting a laser beam using a beam splitter or two different lasers need to be synchronized through a delay generator system. Besides, the two laser beams should be spatially focused onto one point on the target surface. Nevertheless, it leads to the increase of the experimental complexity, size, and as well as cost and limits the applications as a non-portable. Moreover, it has been observed that the analytical performance of the DP-LIBS technique greatly depends on the inter-pulse delays ranging from ns to ms and pulse-energy ratios employed. Also, it is worth considering that, the excitation energies of 250-850 mJ have been deployed in DP-LIBS configuration for explosive detection. Apart from that, customized telescopes of sizes 14-18" were deployed for the light collection, the large size of aperture favors the signal collection, however, it limits the application as a non-portable owing to their size and weight. In reality, the size, weight, and robustness of the instrument are the key features for any technique that can be transformed into instrumental. Contrary to DP-LIBS systems, a single pulse LIBS system in combination with compact non-gated spectrometer has been not explored for the standoff regime to date to the best of my knowledge.

Table 5.1. Details of the different ST-LIBS systems. 1. S. No, 2. Focusing telescope (size, type), 3. Standoff distance (m), 4. Laser Energy (mJ), 5. Collection telescope (size, type), 6. Detector, 7. No of laser shots used for recording one spectrum, 8. Analysis, 9. Material. Newtonian (N), Cassegrain (CG), Galilean (G), Schmidt-Cassegrain (SC), Beam Expander (X), Two lens system (2LS), Three lens system (3LS), Spatial heterodyne spectrometer (SHS). ICCD (I), Customized three-channel gated CCD (C), Optical multichannel analyzer (O), and Double pulse (DP).

1	2	3	4	5	6	7	8	9
1	Single lens	5	250	8", N	I	100	Monitoring of Cr [14].	Steel at 1200 °C
2	Single lens	3	25	4", lens	I	400	Identification using chemometrics [21].	Rocks in CO_2 environment
3	2LS, 8.9X, G	12	1500	8", N	I	60	Fe & Cr quantification [25].	Soils & rocks
4	2LS, 3.2X, G	10	1650	8", N	I	100	Sorting various grades [26].	Steel
5	3LS	60	170	16", N	O	500	PCA for classification [27].	Metals
6	20X, G	19	100	6", lens	I	30	Elemental quantification by calibration curve [28].	Soils in a simulated CO_2 environment
7	5X	20	130	SHS	I	500	Development of spatial heterodyne LIBS spectrometer [29].	Cu and Mg
8	16" CG, DP	30	800	16", C	I	20	Method of normalized coordinates [30].	Explosive residues on glass & PMMA
9	16" CG, DP	31	850	16", C	I	35	Identification using Na and CN emissions [31].	Explosives residues on metals
10	5"	8.3	55	5"	C	200	Combined Raman LIBS analysis [32].	Calcite & silicate
11	10X	5.3	40	4", lens	C	50	Elemental quantification by calibration curve [33].	Geological samples in CO_2 environment
12	14", SC, DP	25	250	14", SC	C	1	Identification using PLS-DA [34].	Explosive residues on car panels
13	14", SC, DP	25	250	14", SC	C	1	Identification of by exploiting PLS-DA [35].	RDX residue on different substrates
14	14", SC, DP	20	250	14", SC	C	1	Identification using PCA and ROC curves [23].	Explosive residues on metals
15	14", SC, DP	30	335	14", SC	C	1	Identification using PCA and PLS-DA [36].	Explosive residues on metals dust, oils
16	16", CG, DP	30	850	16", C	C	1	Identification using supervised learning algorithms [37].	Explosive residues & organic samples on Al
17	14", SC, DP	20	335	14", SC	C	1	Classifications using PCA, SIMCA and PLS-DA [10].	Explosive residue on various surfaces.
18	14", SC, DP	20	270	14", SC	C	1	Identification using PCA and PLS-DA [38].	Biological warfare agents

For the present investigation, the overall system size is reduced because of the use of just a convex lens, instead of a traditional big telescope for the collection of the signal, compact spectrometer, and single-pulse experimental configuration. Single-pulse LIBS technique instead of DP-LIBS reduces the size of the experimental setup. Further, the cost also greatly reduces due to the usage of a non-gated compact CCD spectrometer, which is an essential factor in making a low-cost portable LIBS system. In this work, initially, the ST-LIBS experiment was performed at 1 m on five explosives using ICCD and the classification shown by employing a bi-variate ratio approach and PCA. Further, it has extended for the 6.5 m with a single shot analysis capability using a small handheld CCD spectrometer and analyzed the data using the artificial neural network (ANN). First, the focusing and collection systems have been optimized for the standoff distances of 6.5 m using a brass sample. Later, identification of explosives (five samples) and potentially interfering non-explosives (19 samples) has been demonstrated using a 2D scatter plot approach, PCA, and ANN.

5.2 Standoff detection of explosives at 1 m

5.2.1 Experimental details

The schematic of the LIBS experimental setup is shown in Fig. 5.1 [15].

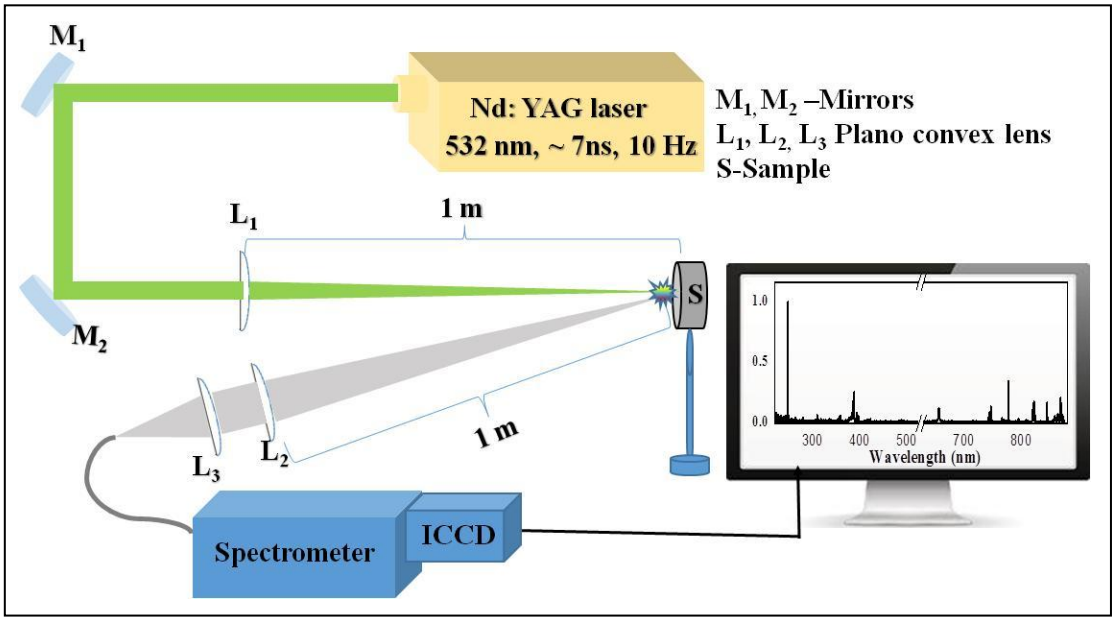

Fig. 5.1. Typical schematic of 1 m standoff LIBS Experimental setup.

The plasma was produced on the sample surface by focusing a laser pulse (532 nm, 7 ns, 1 Hz, 100 mJ) through a Plano-convex lens of 1 m focal length. The estimated theoretical spot size and irradiance on the sample surface were found to be ~100 μm and ~33 GW/cm^2 respectively. The spectral emissions were collected by a collection system (consists of two lenses) kept at 1 m away from the sample and 45^0 to the incident laser beam. The first lens (focal length 1 m) in the collection system collimates the incoming light and the second lens (focal length 10 cm) couples it to an optical fiber. The other end of the fiber was fed to the Mechelle spectrometer coupled with an ICCD. The samples were finely ground and made into pellets using a hydraulic press. All the spectra were recorded with a gate width of 10 μs and a gate delay of 1 μs. Each spectrum was accumulated over ten laser shots and a total of 8-15 spectra were acquired for each explosive based on the availability of samples.

5.2.2 Results and discussion

The LIBS spectra were recorded for five explosives, and their details are given in Table 5.2

Table 5.2. Details of the samples and different stoichiometric ratios.

S.No & Name	Chemical formulae	Stoichiometric ratios				
		C/H	C/N	C/O	O/N	H/O
1. CL 20	$C_6H_6N_{12}O_{12}$	1.00	0.50	0.50	1.00	0.50
2. TNT	$C_7H_5N_3O_6$	1.40	2.33	1.17	2.00	0.83
3. HMX	$C_4H_8N_8O_8$	0.50	0.50	0.50	1.00	1.00
4. RDX	$C_3H_6N_6O_6$	0.50	0.50	0.50	1.00	1.00
5. NTO	$C_2H_2N_4O_3$	1.00	0.50	0.67	0.75	0.67

The LIBS spectra normalized to the carbon spectral line C-247.85 nm are illustrated in Fig. 5.2. The spectra of all the explosives look similar owing to the similar elemental composition however, they differed in the intensities of the peaks. The spectra are shown in two separate windows with different intensity scales to provide a clear view of all the spectral lines. i.e. 0-1 for the 220-400, and 0-0.4 for the 400 -880 nm window. The first part (230-400 nm) represents the strongest emission line in the spectra i.e. Carbon at 247.85 nm followed by the CN band ($\Delta v = 0$, 384-389 nm). The spectral features of Mg, Na, and Ca also appeared in the spectra. The second part (400-880 nm) comprises of emission lines of

various elements Hydrogen (H-656.41), Nitrogen (N-742.36, 744.28, and 746.89) and Oxygen (O-777.34(triplet), 794.93, and 844.65). Also, the molecular emissions of C_2 Swan bands were observed at 516.35 nm.

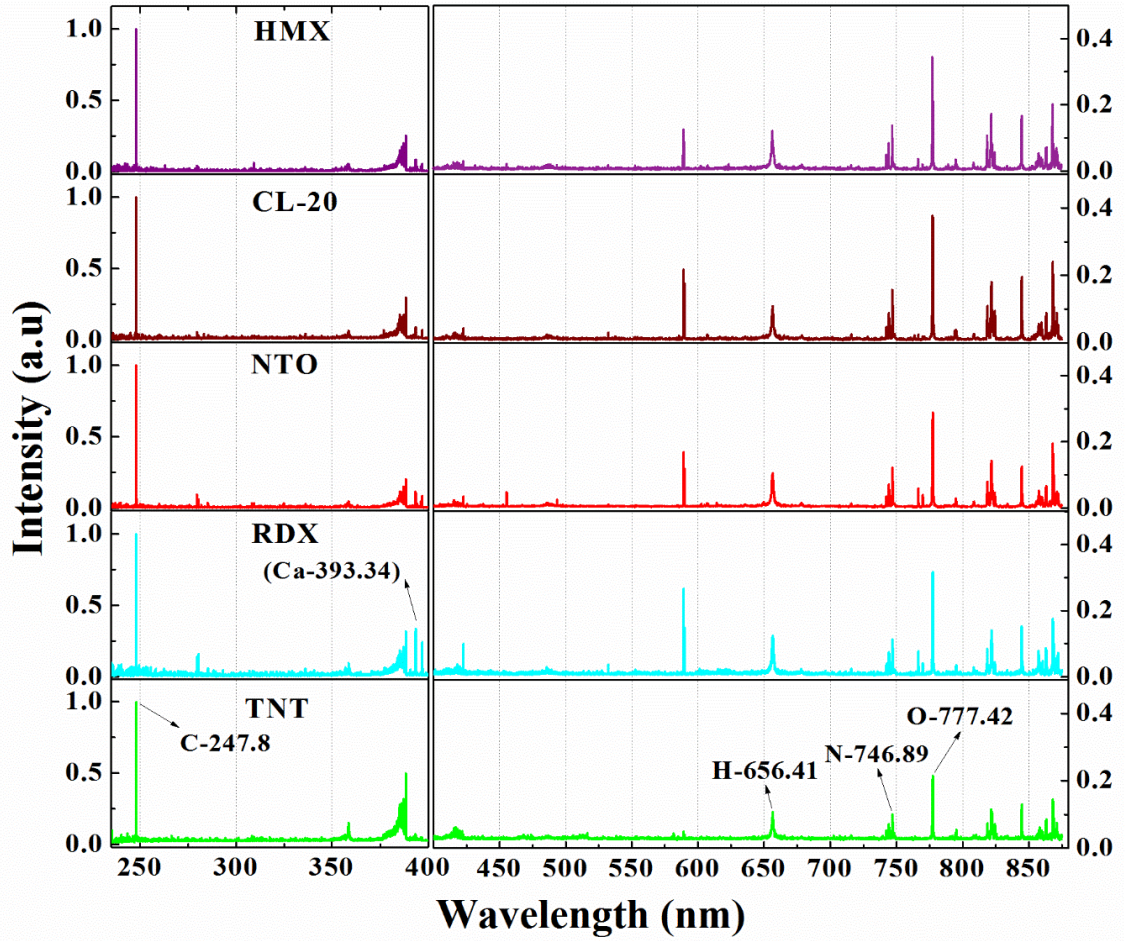

Fig. 5.2. LIBS spectra of five explosives. Two different intensity scales are considered for two spectral windows (220-400 & 400 -880 nm) for visualizing all the spectral features.

5.2.2.a Plasma diagnostic studies

Plasma temperature (T) and electron density (n_e) are the two important parameters which can influence the emission line intensities of the LIBS spectra as well as their shapes. The Boltzmann plot and Stark broadening method are utilized for the estimation of plasma temperature and electron density respectively. Three Oxygen lines at 777.34, 794.93, and 844.65 nm have been used for measuring the temperature[39] as shown in Fig. 5.3(a). All the emission lines were fitted to the "Lorentzian function" and obtained the area under the curve/peak which is considered as the intensity of the respective spectral line.

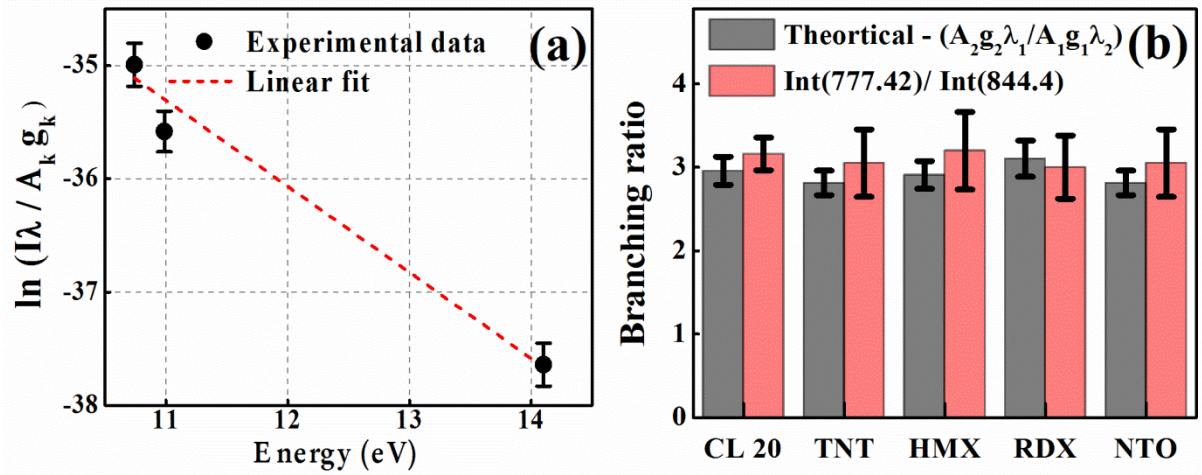

Fig. 5.3. a) The Boltzmann plot constructed, utilizing the three oxygen lines of the CL 20. b) Verifying the branching ratio condition by employing the intensity ratio of oxygen spectral lines.

The spectroscopic parameters were considered from the NIST database[40] and literature[39]. The temperature estimated for all the samples is enumerated in Table 5.3. The error corresponds to the standard deviation obtained from the multiple estimates obtained from different spectra of each sample. The evaluated temperatures are in the range of 9000 - 12750 K and the average temperature over all the samples is 10900 K.

Table 5.3. Plasma parameters. T_e (K) is the plasma temperature. n_e (cm^{-3}), and n_e (MC) (cm^{-3}) correspond to the electron density estimated from the Stark broadening method and MC Writer criterion respectively.

S.No & Name	Plasma parameters		
	T_e 10^3	n_e 10^{16}	n_e (MC) 10^{14}
1. CL 20	10.4±1.8	3.89±0.36	5.14±0.45
2. TNT	12.7±3.2	3.90±0.74	5.67±0.70
3. HMX	11.1±2.0	3.70±0.55	5.30±0.49
4. RDX	9.01±1.8	4.09±0.54	4.76±0.48
5. NTO	11.3±0.9	3.91±0.21	5.38±0.22

The electron density of the plasma has been estimated from FWHM of the spectral line of O at 844.66 nm. Doppler line width (0.015 nm) and natural line width (0.0023 nm) are considered to be negligible as the resolution of the spectrometer is ~ 0.17 nm @ 844 nm and hence only Stark broadening is considered[41]. As seen from Table 5.3 electron density does not show a significant difference across the samples. For all the samples the values are of the order of 10^{16} cm^{-3}. Further, the Local Thermodynamic Equilibrium (LTE) condition is verified from the Mcwhirter criterion. It is evident from Table 5.3 that the

plasma produced for all the samples satisfies the LTE condition as the electron density estimated from the Stark broadening method is two orders higher than the McWhirter criterion. The branching ratio has been determined for all the samples to verify the optical thin condition. The Oxygen lines at 777.42 and 844.4 nm were employed [39] for the estimation of branching ratio and results are shown in Fig. 5.3(b). It is evident from Fig. 5.3(b) that all the samples are satisfying the optical thin condition. The theoretical ratio is within the standard deviation of the actual intensity ratio for all the samples. Considering that transition probabilities itself have 10% uncertainty and hence observed branching ratios can be considered as a very good agreement[39].

In the next sections, first, different ratios and their correlation to the actual stoichiometry will be explored towards the identification of the samples. As there is an overwhelming similarity among the spectra of all the explosives, the minute differences can be exploited by the judicious use of multivariate analysis. The multivariate analysis uses the intensity information available at all the 22290 wavelengths in the range of 220-850 nm.

5.2.2.b Ratiometric analysis

In this section, ratios of different emission lines viz., C/H, and H/O from all the samples were considered to explore the correlation with the actual stoichiometry. The actual stoichiometric ratio implies the ratio of the number of atoms per molecule. For example, CL 20 ($C_6H_6N_{12}O_{12}$) has an H/O ratio of 0.5. As discussed in the last section, the area under the curve for an emission line is considered as intensity for the evaluation of ratios. Fig. 5.4(a&b) shows the correlation of C/H and H/O ratios of all the samples respectively. The standard deviation obtained from multiple trails is depicted as an error bar. The other possible ratios like C/O, O/N, and C/N have not considered for the analysis as their stoichiometric ratios are similar for three explosives (RDX, HMX, and CL20) out of five as given in Table 5.2. The data is fitted for the straight-line equation ($y = mx + c$) as visualized in Fig. 5.4(a&b). The H/O ratio (Pearson's $r = 0.99$, $m=0.54$ and $c=0.32$) has shown better correlation compared to the C/H (Pearson's $r = 0.96$, $m=0.37$ and $c=0.15$). The C/H ratio forms three sets of samples, it is not possible to distinguish among the samples with the same value for the ratio.

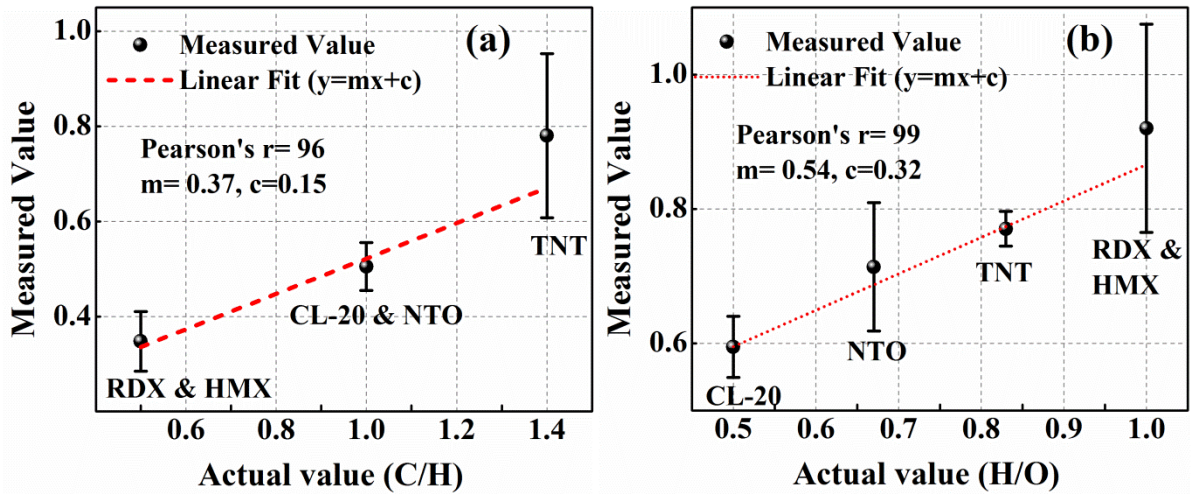

Fig. 5.4. The comparison of the stoichiometric ratios with the measured values. a) C/H and b) H/O ratios.

However, an unknown sample can be identified as belonging to one of the three groups – a) RDX/HMX b) CL20/NTO and c) TNT. With H/O, as shown in Fig. 5.4(b), the samples can be very well-identified with the RDX and HMX forming a single group. C/H ratio has an advantage over other ratios as it has the minimum effect of the atmospheric contribution to the plasma. Although, ratiometric performance is limited as none of them provide a clear distinction between all the samples studied. Hence in the next section, a multivariate method utilized for the analysis which considers the inherent contribution from all the spectral lines.

5.2.2.c Classification of explosives by PCA

As seen in earlier sections, typical LIBS spectra of all the five samples were overwhelmingly similar and the application of ratios yielded limited success in identification. In this section, multivariate analysis is employed to systematically investigate the presence of subtle differences between the spectra of each type of explosives. The advantage with the multivariate approach is that it considers the intensities at all the wavelengths rather than at some selected peaks. PCA is a technique that transforms the data into an '*abstract*' space where the variables are the linear combinations of the original variables (the intensities at different wavelengths). Fig. 5.5 shows the PCA cluster plot. Each data point, represented by coefficients of first and the second principal components (PCs), represents a single LIBS spectrum in the transformed space.

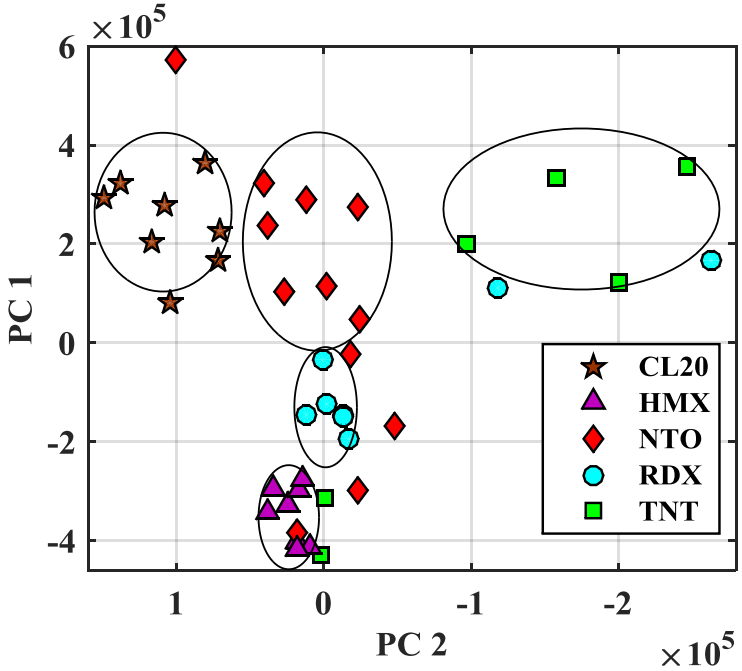

Fig. 5.5. Score plot of the first two PCs of five explosives.

It can be seen that the spectra corresponding to an explosive sample now cluster together. Each spectrum is now represented by only two coordinates PC1 and PC2 as shown in Fig. 5.5. There are two outliers for TNT, three for NTO and one for RDX. The clear separation of the spectra in the PC plane indicates that there are subtle but reproducible differences between the spectra of different explosives recorded from a distance of 1m and enable their clear separation. The chemical basis of clustering, that is, the reason behind the clear separation of the clusters can be understood by looking at the individual PCs in loadings plot as shown in Fig. 5.6. The first and second PCs account for 75 and 8 % of the variance respectively. The first five PCs, together account for 92.15 % of the net variance in the spectral dataset. The first PC, which is the most dominant, contains the information from the CN, Oxygen, Nitrogen, Sodium, and Calcium. The second is mainly dominated by carbon, CN, Oxygen, Nitrogen Calcium, and Sodium. The 3rd PC has contributions from the emission lines of Carbon, Hydrogen, Sodium, and Nitrogen. The PCA data clearly establishes that the explosives studied in this work can be easily identified from the signal collected at a distance of 1 m. The clustering is a clear indication that the spectra of different explosives have subtle but reproducible variations among themselves and can be harvested by applying the suitable multivariate approach.

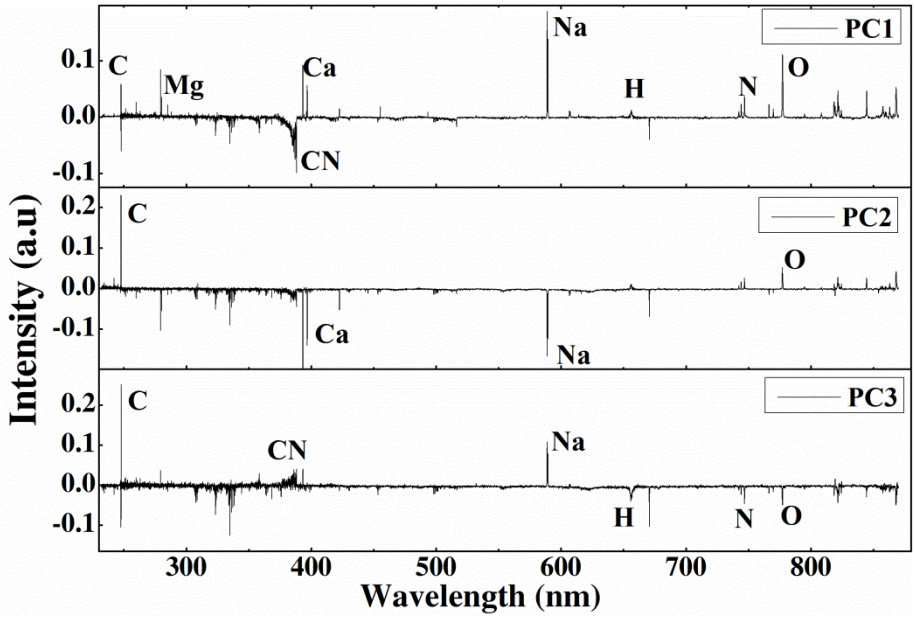

Fig. 5.6. Loadings plot of the first three PCs of explosives.

5.3 Standoff detection at 6.5 m

ST-LIBS measurements on a set of five explosives at 1 m distance have been demonstrated in the previous section. That experimental setup has utilized a 1 m focal length Plano-convex lens for focusing the laser beam on to the sample. However, in real-time applications, the target/sample distance is unspecified before performing the experiment. Thus, single-lens focusing configuration for creating the plasma on the given sample is always not feasible for the unknown standoff distances. Even in the case of the single-lens LIBS application, most of the standard companies only provide fixed focal lengths insteps of 5 cm such as 100/105 cm but not any required focal length for example 101 cm. Further, the probing distance may also change randomly while interrogating the samples in different situations however within a specified range. In such a scenario, the required standoff distance can be accomplished by using a combination of lenses, either it maybe two or three depending on the requirement. As well as specifications of the lenses such as focal length and diameter can be chosen depending on the application of interest. Further, the optimization of the focusing system is necessary for achieving the higher irradiance at the focal position which improves the signal strength.

Apart from that, the collection system also plays a crucial role in the development of the ST-LIBS system. Earlier section, Mechelle based ICCD detector has been utilized

nevertheless it increases the size and overall cost. Hence it is necessary to deploy a low-cost, compact detection system. In real-time ST-LIBS measurements, first, the suspected sample needs to be identified as an explosive or not. This scenario may get encountered in different situations such as identifying a sample in a bus stop/ in a stadium/ mass gathering in public meetings/ theatres. Further, if the suspected is an explosive it needs to identify as a specific explosive such as RDX or HMX. Hence the ST-LIBS experiments need to be performed on explosives and non–explosives to tackle real-life problems. However, the selection of samples depends on the requirement of the user and their availability.

ST-LIBS experiment at 1 m serves as standardization and provides hands-on experience for working in a standoff regime. Hence, in the next section, the experiment has been performed by considering the aforementioned requirements for working towards the real-time measurements. As well as, the probing distance has been extended to 6.5 m. A double lens system that consists of a Plano-convex and Plano-concave has been exploited for focusing the laser beam. Later, a different set of lenses have been used for the collection system optimization. The spectral emissions were captured by a portable non-gated spectrometer which drastically reduces the cost and size of the LIBS detection system, which is a prime factor in real-time applications. Further, the experiment has been performed on the five explosives and a wide range of nineteen non-explosives. Bivariate and multivariate approaches have been utilized for the classification of the samples.

5.3.1 Optimization of the focusing system

The single-lens focusing system has a limitation for varying the focusing distance for the real-time measurements. However, this hurdle can be overcome by the utilization of a double lens focusing configuration (Galilean) which employs a concave and convex lens. It is also worth considering that the selection of lenses depends on the application of interest as given below

1. Focusing range - focusing the laser beam at different standoff distances with a given set of lenses, for example, the combination of -10 & 20 cm focal length lenses can focus the laser beam in the range of 2-30 m.

2. The total size of the focusing system i.e. length and diameter is a crucial factor in developing a compact ST-LIBS system. The length is decided by the maximum separation between the lenses and diameter can be controlled by the aperture size of the lens.
3. Precision in measurements – the effective focal length (focusing distance) varies with the separation between the lenses. However, sometimes a slight change in separation greatly affects focusing distance for a given set of lenses. i.e. the separation decides how precisely a laser beam can be focused onto the sample.
4. Optical quality and reflectivity of the lenses. It should consider the reflected light from the back surface of the lens which may damage the optical components of the setup.

Here for the optimization, two different lens systems have been utilized as given below

1. -100 & 100 cm focal length lenses of each 50 cm diameter (Referred to as 1st)
2. -10 & 20 cm focal length lens of diameter 25 & 50 mm respectively (Referred to as 2nd)

Here the standoff distance refers to the back focal length (BFL- the distance from the last surface of the focusing system to the focal point, and the same is also illustrated in Fig. 5.13)

$$BFL = \left(\frac{f_2(L - f_1)}{L - (f_1 + f_2)} \right) \tag{5.1}$$

Where L is the distance between the two lenses, f_1 & f_2 is the focal length of first and second lens respectively. The required focusing distance can be achieved by varying the distance between the two lenses as shown in Table 5.4. It also represents the estimated spot size and fluence for two lens systems (1st & 2nd).

Table 5.4. Details of the two double lens systems. BFL- back focal length (lens to sample distance), L – the distance between the lenses, W_o radius of the spot size.

BFL (m)	-100 cm & 100 cm lenses (1st)			-10 cm & 20 cm lenses (2nd)			Fluence (1st) / Fluence (2nd)
	L (cm)	$2W_o$ (mm)	Fluence (J/cm²)	L (cm)	$2W_o$ (mm)	Fluence (J/cm²)	
3	59.21	0.32	125.9	11.43	0.12	914.9	7.27
4	40.83	0.48	55.3	11.03	0.16	497.6	9.00
5	31.72	0.64	30.9	10.83	0.20	306.1	9.91
6	25.32	0.80	19.7	10.69	0.26	210.5	10.69

Further, the focused spot size at different standoff distances has been estimated from the ABCD matrix approach and thin lens approximation. The input laser beam parameters are taken as diameter-8 mm, Gaussian, and quality factor (M^2) as 1. The laser beam propagation through the 2nd lens system is illustrated in Fig. 5.7 and the inset represents a focused laser beam waist obtained at 6 m. The analysis and visualization have been performed in MatLab and the final outputs are presented in Table 5.4. The 2nd lens system also works as a 2X beam expander which favors in achieving the lower spot size and leads to higher irradiance. The theoretical focal beam waist radius obtained at 6 m for the 2nd lens system is 3 times lesser compared to the 1st lens system and fluence is 10 times as enumerated in Table 5.4.

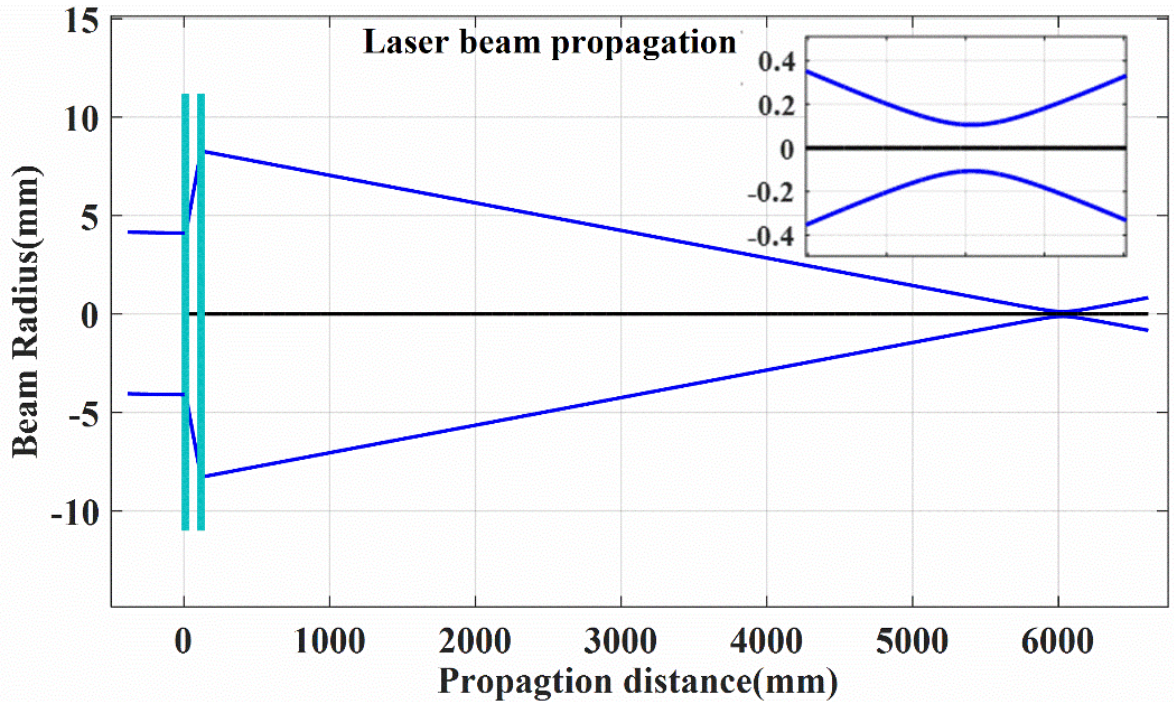

Fig. 5.7. Laser beam propagation through the -10 & 20 cm lens system. Inset in the figure represents the close view of the beam waist at 6 m focusing distance.

Also, the ST-LIBS experiments were performed for the Al sample at 6.5 m. Two lenses are kept on the optical rail for better alignment and measurement. The laser beam is aligned in such that it passes through the center of both the lenses (see Fig. 5.13). Ten consecutive laser shots irritated on the sample for measuring the spot size. The optical microscope image of the focal spot size at 6.5 m obtained by focusing the laser beam for two lens systems is shown in Fig. 5.8(a&b). It is evident from Fig. 5.8 the experimental spot size is higher than the theoretical spot size estimated.

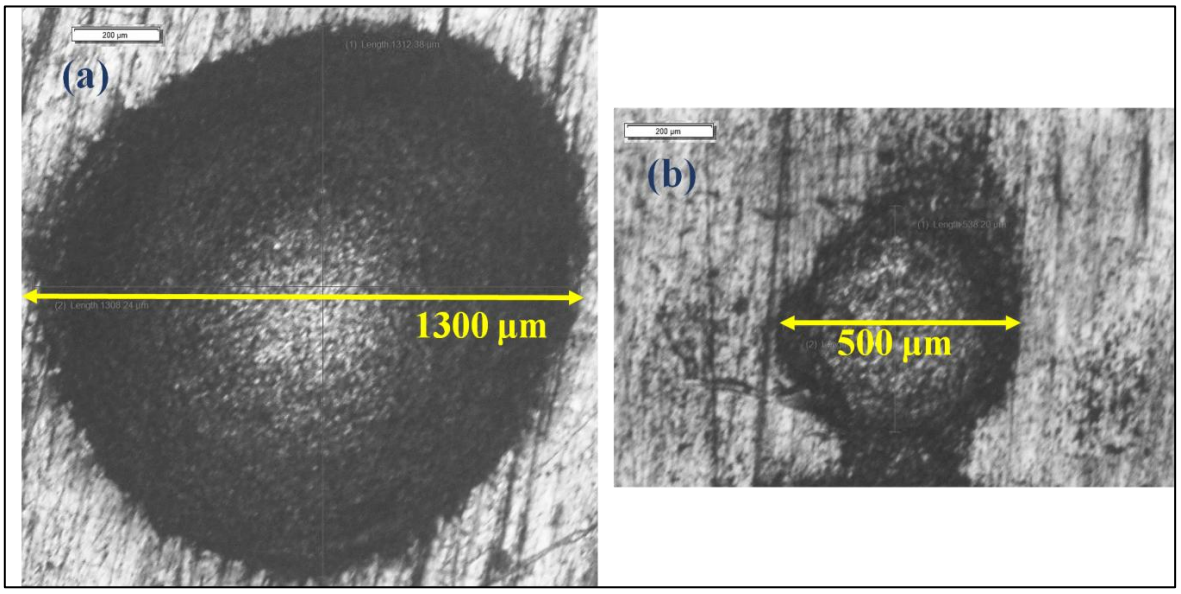

Fig. 5.8. The images of the irradiated craters on Al sample taken from the optical microscope. a) & b) correspond to the laser irradiated with the 1st and 2nd lens system at 6.5 m respectively.

The LIBS spectra of the aluminium sample acquired at 6.5 m standoff distance with both the lens system are shown in Fig. 5.9. The spectra have been recorded in a single-shot mode with the pulse energy of 50 mJ. Only strong Al lines are shown in the spectra for better visualization. As seen in Fig. 5.9, the spectra recorded at 6.5 m with the 2nd lens system have shown more intensity (ten times) owing to the higher laser intensity at the focal spot size.

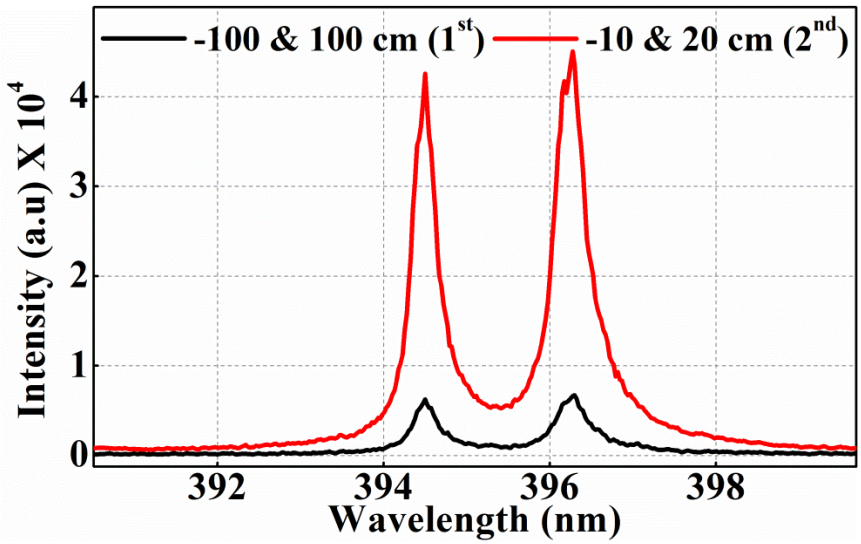

Fig. 5.9. The LIBS spectra of Al acquired at 6.5 m distance with two lens systems.

Further, the 2nd lens system has been utilized for focusing the laser beam in the ST-LIBS experiment for the identification of explosives and non-explosives.

5.3.2 Optimization of the collection system

ST-LIBS has an inevitable signal loss that increases with distance and it is a critical factor in general, and particularly while working with a CCD spectrometer. Hence, the proper optimization of the collection system is necessary for acquiring the maximum signal. The collection system is optimized for the best signal by choosing the proper lens configuration to match the F-number of the portable spectrometer (F#4). It is worth considering that any collection system (it may be a lens or telescope) having F#, equal or more than that of a spectrometer can couple maximum light into the system. Three different lenses were employed for the optimization, viz.,

I. 5 cm diameter and focal length 10 cm (F#2)
II. 5 cm diameter and focal length 20 cm (F#4)
III. 10 cm diameter and focal length 50 cm (F#5)

The efficient coupling of plasma light to the spectrometer depends on the telescope size [42], i.e., the diameter of the primary mirror (present case a lens), as given in equation 5.2 and F-number of the collection system.

$$d\phi = Id\Omega = I\frac{dA}{r^2} \tag{5.2}$$

Where dϕ is the plasma luminous flux, dA is the area of the collection optics, dΩ is the solid angle at the point source, r is the distance between source and collection system.

The standoff LIBS spectra obtained at a distance of 6.5 m with these three lenses are presented in Fig. 5.10. The continuum/background observed in the spectra due to the free –free transitions in the plasma and it can't be avoided as the gating is not available in the CCD spectrometer utilized for the experiment. The background has been removed for accurate estimation of the signal enhancement and the inset in Fig. 5.10 represents strong lines of Cu after background correction. The f-number matching is necessary for maximum throughput which is clearly demonstrated in Fig. 5.10. The intensity (Cu - 522.01 nm line) acquired with the F#4 lens is twice to the F#2 lens even though both have the same aperture size owing to the F-number matching (spectrometer F# 4). Also, the

intensity has further doubled when the spectra were recorded with a 10 cm aperture lens due to the large aperture size as shown in Fig. 5.10. Also, the SNR has been calculated at 510.61 nm line and it found to be 42, 24, and 11 for the F#5, F#4 and F#2 lenses respectively. Hence by using the appropriate F# number of the collection system with a large size can enhance the signal significantly.

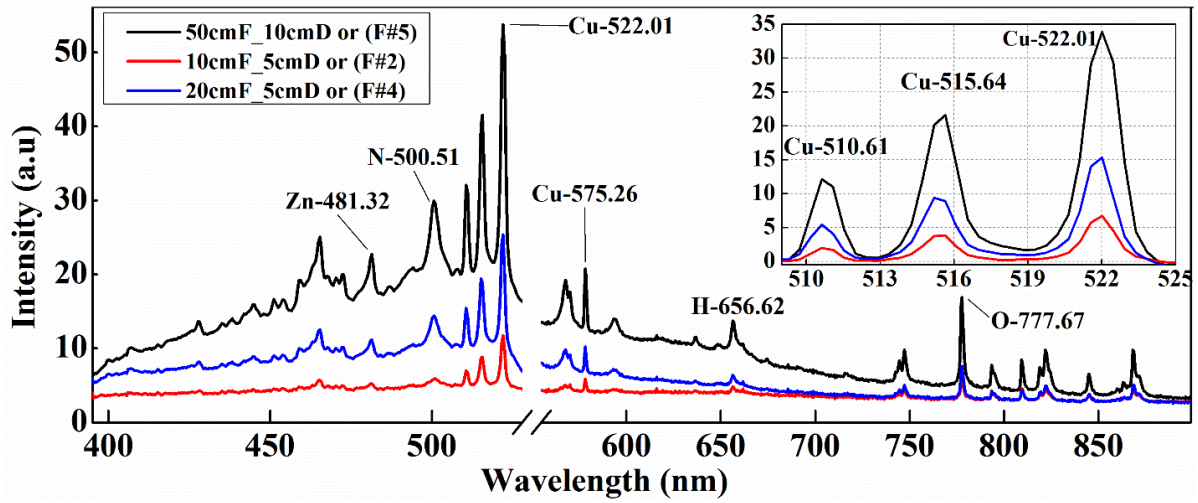

Fig. 5.10. The ST-LIBS spectra of Brass acquired at 6.5 m with the Plano-convex lens of different F-numbers. In legend F & D represents focal length and diameter of the lens respectively. The inset figure represents the Cu prominent lines with background correction.

Further, the efficient coupling of light from the lens to fiber is a crucial factor for achieving maximum signal. i.e. the total light from the lens should couple to the core of the optical fiber and proper optimization of the fiber tip position is also vital. In the experiment, the fiber was mounted on a bidirectional translation stage to facilitate the x-y movement and also along the direction of the pump laser beam direction. The fiber tip was positioned exactly at the focal plane of the Plano-convex lens (F#) and aligned to obtain a maximum signal. To check the efficient light coupling to the fiber, the plasma plume was imaged onto a separate CCD (OPHIR, GRAS20). The plasma image captured by CCD kept at the focal point of the collection lens shown in Fig. 5.11. A circle with a diameter of 600 μm has been drawn around the image to show the size. It is also observed that the image size increased gradually when the CCD moved either side of the focal position. From Fig. 5.11 it is evident that the maximum coupling of light can be achieved by properly positioning the fib tip (as the plasma image size is less than the fiber core size).

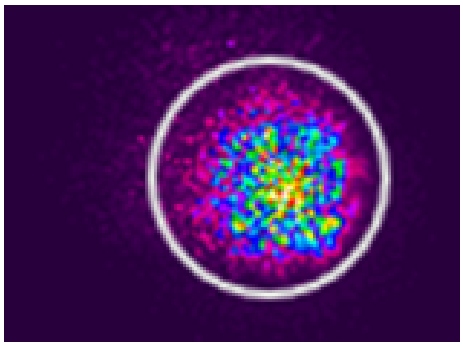

Fig. 5.11. The image of the plasma captured by the CCD kept at 6.5 m from the plasma source. F#5 lens used for imaging the plasma. The circle with a diameter of 600 μm has been drawn to compare the size of the image.

Further, the ST-LIBS spectra of brass recorded with F#5 lens at various energies of 10- 100 mJ are shown in Fig. 5.12(a). The spectra have two contributions, one from the broad continuum and the other from the sharp peaks. It has been observed that the continuum increases with excitation energy. The ST-LIBS spectra can be acquired even in a single shot with a minimum pulse energy of 10 mJ. The spectral lines are fitted to a Lorentzian and obtained the area under the curve is obtained, which will be referred to as its Intensity. The intensity (after the background correction) of the Cu-522.01 spectral line is increasing almost linearly with the energy as shown in Fig. 5.12(b).

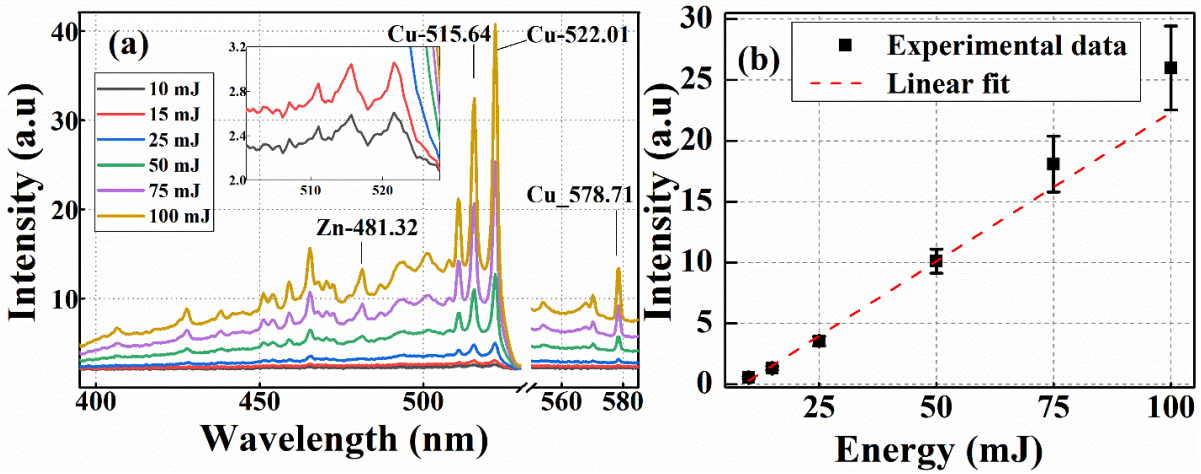

Fig. 5.12. a) The ST-LIBS spectra of brass recorded at 6.5 m standoff distance for different energies. The strong lines at 10 and 15 mJ energy are shown in the subset for the clear view. b) A linear fit obtained for the intensity of Cu 522.01 nm line as a function of energy.

Identification explosives and non-explosives are presented in the next section with the optimized standoff LIBS setup.

5.4 Identification of explosives and non-explosives

5.4.1 Experimental details

The schematic of the experimental ST-LIBS system is shown in Fig. 5.13. The laser beam (1064 nm, 7 ns, 1 Hz, 100 mJ) was focused onto the sample surface using the telescopic lens arrangement which consists of a Bi-concave and Plano-convex lens of focal length -10 cm and 20 cm respectively. A single Plano-convex lens is used as a telescope for the collection of spectral emissions from the plasma. The light from the collection lens coupled to a compact nongated spectrometer (Maya 2000-Ocean optics) via an optical fiber of core diameter 600 μm and numerical aperture (NA) 0.22. The spectrometer provides a wide spectral range of 350-1000 nm in single acquisition with a resolution of 1 nm at 500 nm. A holographic notch filter (Kaiser Optical system HNF-1064.0-10, OD > 4.0, AOI 0^{O}) was mounted in front of the optical fiber to avoid the excitation source in the LIB spectra.

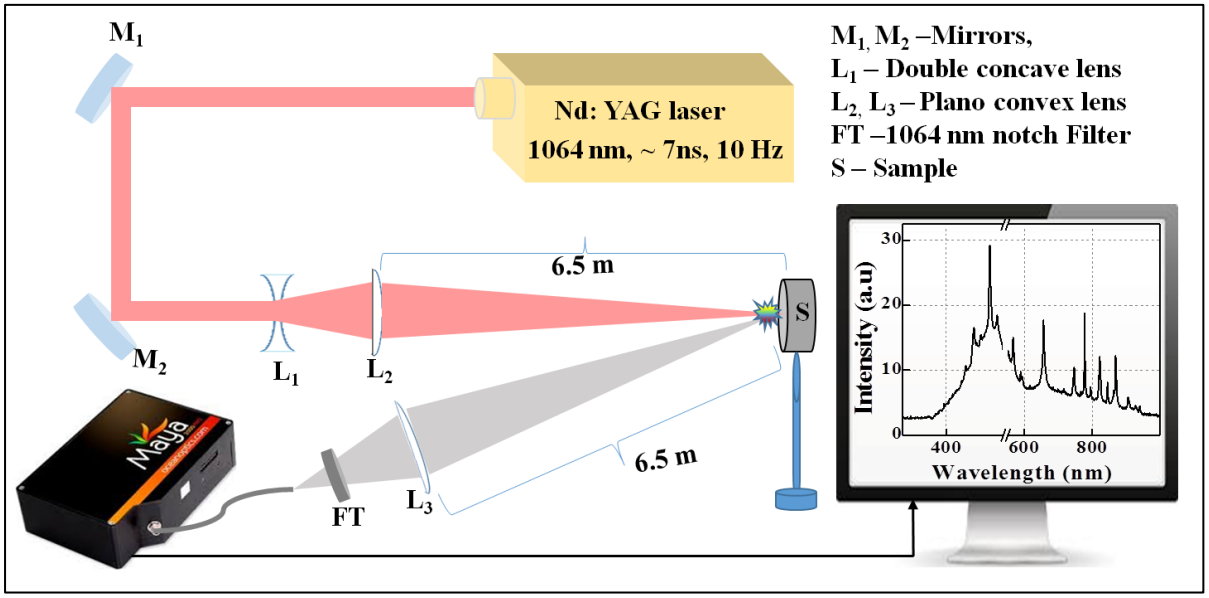

Fig. 5.13. The schematic of the Standoff LIBS system at 6.5 m.

The details of the samples used in the experiment are given in Table 5.5. The first five are explosives and the remaining nineteen are non-explosives (6-24). These non-explosives include the most extensively used eight plastics (6-13).

Table 5.5. Details of the samples. 1st five are explosives (*) and remaining are non-explosives.

S. No	Sample name	Chemical Formula	S. No	Sample name	Chemical Formula
1	AN*	NH_4NO_3	13	ABS	$(C_{15}H_{17}N)_n$
2	DNT*	$C_7H_6N_2O_4$	14	Pyridine	C_5H_5N
3	TNT*	$C_7H_5N_3O_6$	15	Triethanolamine	$C_6H_{15}NO_3$
4	NTO*	$C_2H_2N_4O_3$	16	Thymine	$C_5H_6N_2O_2$
5	RDX*	$C_3H_6N_6O_6$	17	Paracetamol	$C_8H_9NO_2$
6	HDPE	$(C_2H_4)_n$	18	Cytosine	$C_4H_5N_3O$
7	HIP	$(C_{12}H_{16})$	19	Dextrose	$C_6H_{12}O_6$
8	LDPE	$(C_2H_4)_n$	20	DL-Alanine	$C_6H_{12}N_2O_3$
9	PC	$(C_{16}H_{14}O_3)$	21	DL-Methionine	$C_5H_{11}NO_2S$
10	PET	$(C_{10}H_8O_4)_n$	22	Glycine	$C_2H_5NO_2$
11	PP	$(C_3H_6)_n$	23	Hypoxanthine	$C_5H_4N_4O$
12	PS	$(C_8H_8)_n$	24	Neomycin	$C_{23}H_{46}N_6O_{13}$

Among all, plastics can be considered to be potentially interfering agents for the identification of explosives as they are commonly used as transport containers/boxes in airports and public transport systems[11].

5.4.2 Results and discussion

Here the experiment is performed on the nineteen non-explosives and five explosives. All the non-explosives are organic samples hence their LIBS spectra exactly resemblance to explosives spectra and lead to the identification strategy more challenging. 100 spectra for each sample were acquired except for RDX (30 are acquired due to the limited sample and the pellet is not intact). Each spectrum is acquired with only a single laser shot and the sample was moved for every acquisition. The spectrum of TNT with a continuum/background is shown in Fig. 5.14(a). The continuum is observed in the spectra due to the Bremsstrahlung emissions. The spectra were background removed/corrected for 5th order polynomial fit by an iterative least-square based curve fitting algorithm in MatLab [30]. The background-corrected spectrum of TNT is shown in Fig. 5.14(b). The spectral line of carbon at C-247.85 nm is not observed in the spectra as the spectral sensitivity is very low in the deep UV region. The filter used to avoid the pump beam also suppressed the spectral window of 528 -552 nm hence omitted from the spectra.

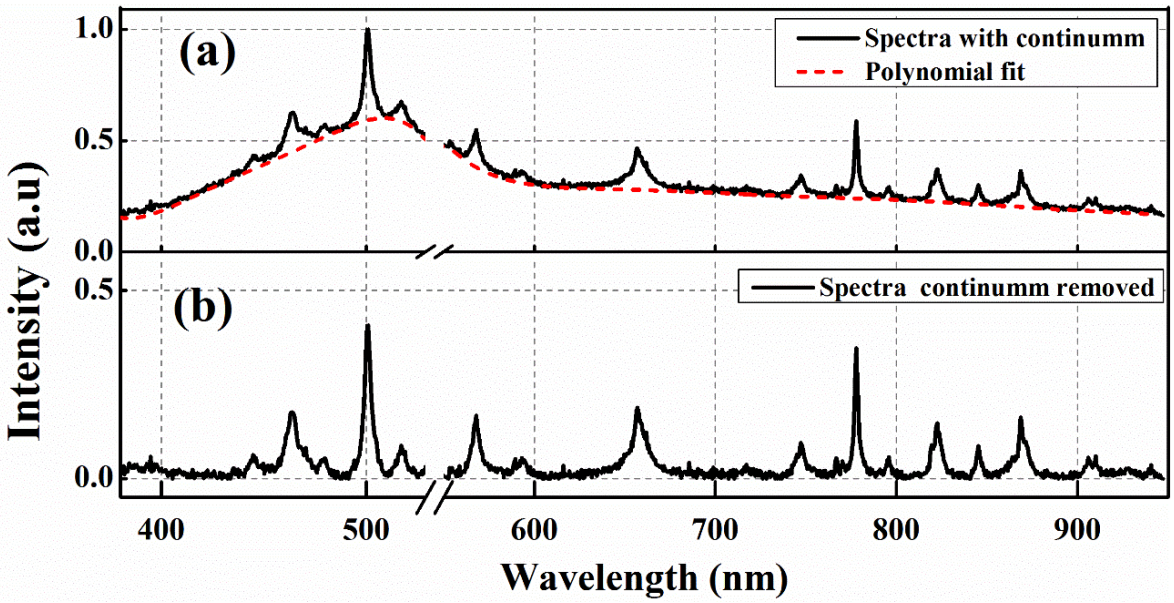

Fig. 5.14. ST-LIBS spectra of the TNT a) The black solid and red dotted lines represent the spectra with continuum and polynomial fit to remove the continuum respectively. b) Continuum corrected spectra.

The background-corrected spectra of the ten non–explosives and one explosive are shown in Fig. 5.15. Only one explosive is shown in Fig. 5.15 to compare it with non-explosives LIBS spectra due to space constraints. The spectral lines corresponding to Hydrogen (H I - 656.9 nm), Nitrogen (N I - 747.2 it is an unresolved triplet, N I – 822.1, N II – 500.5, N II - 567.9, and N II - 868.6 nm) and Oxygen (O I – 777.46, O I – 844.7, and O II- 464.1 nm) have appeared in the spectra. The emission lines of Sodium (Na I – 589.6 nm) and Potassium (K I – 766.7 nm) are also observed in the spectra. The molecular emissions of the CN band are not observed in the spectra. It is due to the notch filter (it suppressed the data in the spectral window of 375-390) but the strong C_2 Swan band ($\Delta v = 0$, 516.9 nm) has been observed. The spectra of all the samples look identical except the variations in the intensity and possibly widths which is the most ambitious challenge to identify the given analyte whether explosive or not. The emissions of the Hydrogen (656.6 nm) and Oxygen (777.7 nm) lines differ in intestines for the sample to sample in non-explosives. The N II 500.5 nm is the intense emission line among all and the spectra were normalized to it. For the entire analysis, background corrected and normalized data was used.

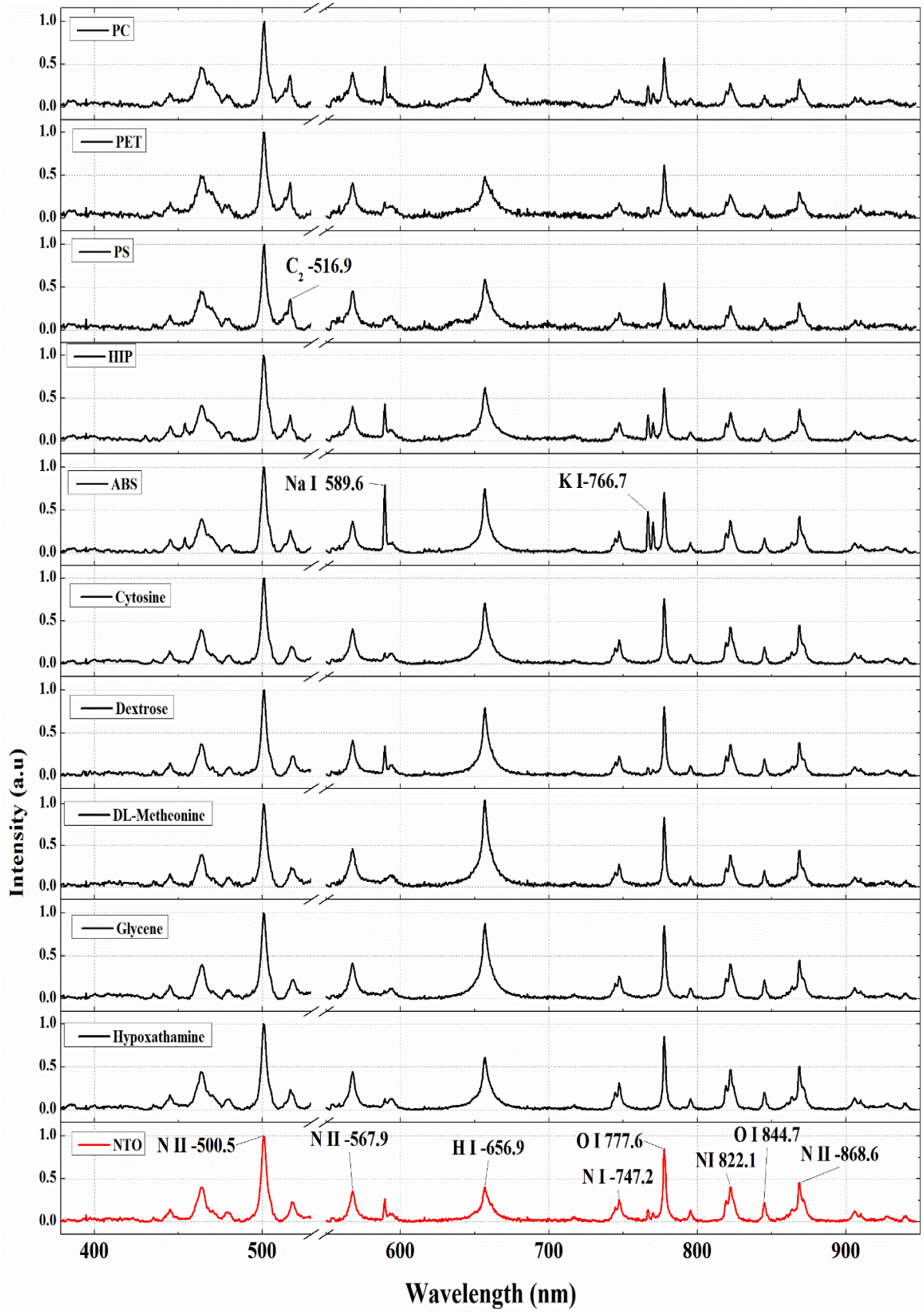

Fig. 5.15. ST-LIBS spectra of the ten non-explosives and one explosive (it is NTO, represented with red colour) recorded at 6.5 m. (The spectra of the other also looks similar but not shown here due to space constraints).

5.4.2.a Plasma diagnostic studies

The properties of the plasma viz, temperature (T), and electron density (N_e) are estimated using the Boltzmann plot and Stark broadening method respectively. Three spectral lines of Oxygen at 777.6, 794.9, and 844.7 nm are considered for estimating the plasma temperature [39, 43, 44]. The plasma temperature measured for all the samples is given in Table 5.6 and lies in the range of 20000-22000 K.

Table 5.6. Plasma properties. T_e (K) is the plasma temperature. n_e (cm^{-3}) and n_e (MC) (cm^{-3}) correspond to the electron density estimated from the Stark broadening method and MC Writer criterion respectively.

S. No	Sample name	T_e	N_e 10^{18}	N_e (MC) 10^{16}
1	AN	21520 ± 980	1.47 ± 0.16	1.58 ± 0.04
2	DNT	21430 ± 990	1.49 ± 0.11	1.58 ± 0.03
3	TNT	21830 ± 1200	1.74 ± 0.24	1.60 ± 0.04
4	NTO	21500 ± 970	1.70 ± 0.21	1.58 ± 0.03
5	RDX	21920 ± 1030	1.87 ± 0.25	1.60 ± 0.04
6	HDPE	22170 ± 1720	1.29 ± 0.25	1.66 ± 0.06
7	HIP	20130 ± 1770	1.37 ± 0.24	1.53 ± 0.07
8	LDPE	22170 ± 1770	2.05 ± 0.43	1.70 ± 0.13
9	PC	22320 ± 2200	2.17 ± 0.49	1.58 ± 0.23
10	PET	22160 ± 2230	2.18 ± 0.45	1.70 ± 0.17
11	PP	22310 ± 2370	2.30 ± 0.35	1.82 ± 0.14
12	PS	20400 ± 2200	2.25 ± 0.25	1.58 ± 0.19
13	ABS	21230 ± 1750	1.50 ± 0.30	1.57 ± 0.09
14	Pyridine	21700 ± 1900	1.56 ± 0.25	1.60 ± 0.09
15	Triethanolamine	22000 ± 1510	1.75 ± 0.26	1.60 ± 0.16
16	Thymine	21970 ± 1510	1.56 ± 0.20	1.60 ± 0.05
17	Paracetamol	21590 ± 570	1.15 ± 0.15	1.58 ± 0.02
18	Cytosine	21670 ± 1040	1.43 ± 0.14	1.59 ± 0.13
19	Dextrose	21880 ± 1470	1.65 ± 0.22	1.60 ± 0.06
20	DL-Alanine	21820 ± 1540	1.49 ± 0.26	1.60 ± 0.23
21	DL-Methionine	22110 ± 1880	1.93 ± 0.33	1.60 ± 0.13
22	Glycine	21880 ± 1010	1.38 ± 0.13	1.60 ± 0.04
23	Hypoxanthine	21910 ± 780	1.46 ± 0.09	1.60 ± 0.03
24	Neomycin	21870 ± 1400	1.82 ± 0.26	1.60 ± 0.17

Further, the electron density is determined from full–width at half maximum (FWHM) of the Stark broadening method[43, 44]. The spectral line Hydrogen at H-656.6 nm has been utilized for the estimation of electron density. The measured electron densities are found

to be in the order of 10^{18} cm^{-3} for all samples as enumerated in Table 5.6. In addition, the McWhirter criterion should be satisfied (a necessary condition) to ascertain the validity of local thermodynamic equilibrium (LTE). For the current investigation, the McWhirter criterion has been satisfied (see Table 5.6) as the measured electron densities (~ 1.2 – 2.3 X 10^{18} cm^{-3}) are two orders to the electron densities (~ 1.5-1.8 X 10^{16} cm^{-3}) obtained from McWhirter criterion and validates the LTE assumption. Apart from that, the branching ratio has been determined for all the samples to verify the optical thin condition by employing two oxygen lines at 777.42 and 844.4 nm [15]. The estimated theoretical branching ratios of all the samples are in a good agreement within the actual intensity ratios which ascertains the optical thin condition.

LIBS spectra of all the investigated samples have a similar signature owing to the similar chemical composition. However, the reproducible variations in the spectral intensities were utilized for the 2D scatter plot/projection and multivariate analyses (PCA & ANN) for the identification of the samples in the next sections.

5.4.2.b 2D Scatter plot analysis

An overview of the 2D scatter plot approach is presented in chapter 1. Carbon, Hydrogen, Nitrogen, and Oxygen are the common elements present in all the samples. In addition, the spectral emissions of the CN and C_2 bands are influenced by the molecular structure and the ambient atmosphere. As mentioned earlier, the emission lines of Carbon and CN molecular bands are not observed in the LIBS spectra. Consequently, the emission lines of Hydrogen-656.9 (H), Nitrogen – 500.5 (N), Oxygen- 777.6 (O), and C_2 -5169.9 nm are exploited for the 2D correlation. Further, the spectral line intensities are suitably paired in 2D projection/scatter plots[37, 45] to look for the distinctions among the explosives and non-explosives, for example, H-N combination as shown in Fig. 5.16 (a). Total six combinations are possible viz., H-N, H-O, H-C_2, O-N, C_2-O, and C_2-N for the aforementioned spectral emissions (H, N, O, and C_2) where first four are presented in Fig. 5.16 (a-d) respectively. A least-square fitting based approach has been utilized to find the best fit of an ellipse for the distributions corresponding to explosives and non-explosives as shown in Fig. 5.16 (a-d).

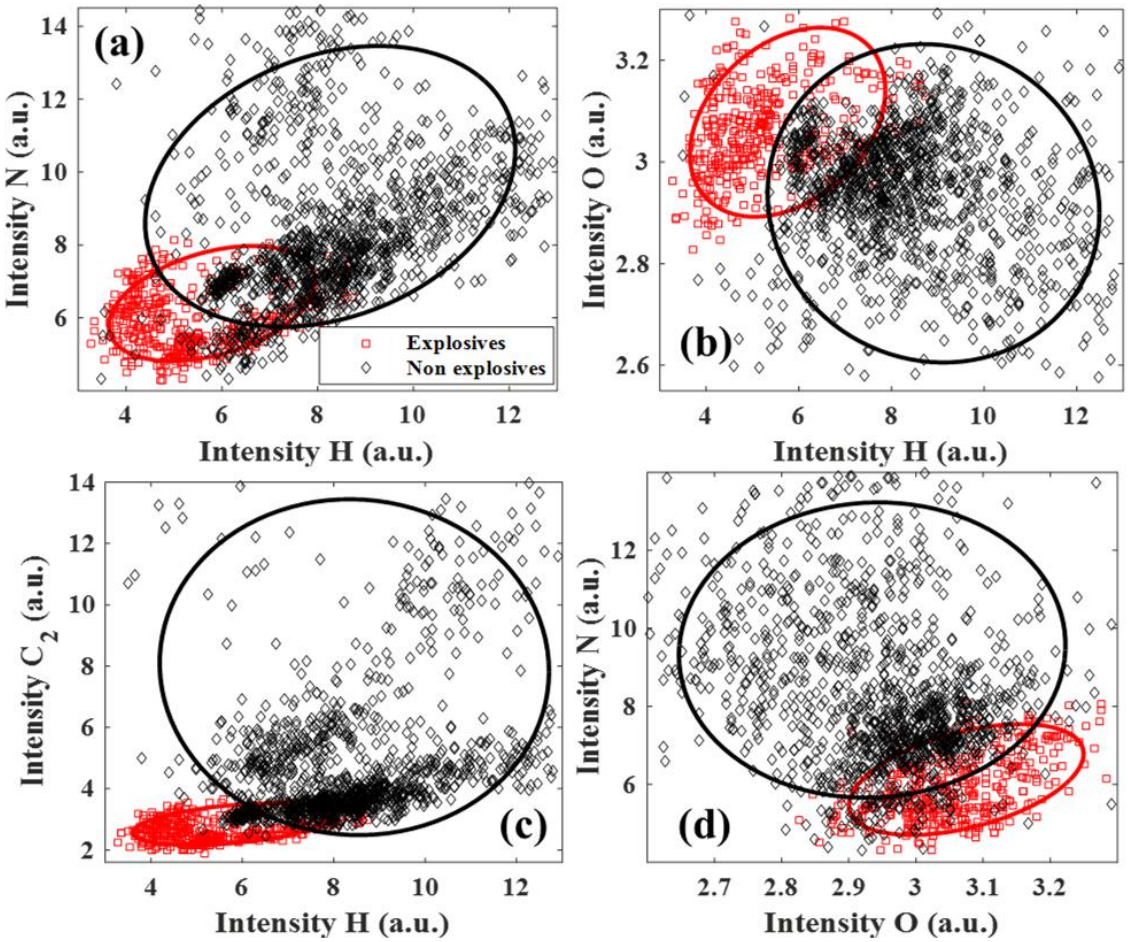

Fig. 5.16. The 2D scatter plots of the explosives and non-explosives a) H-N, b) H-O, c) H-C_2 and d) O-N.

Total 2330 spectra were acquired where 430 spectra belong to the explosives and rest for the non-explosives (same data used for PCA and ANN analysis in the next sections also). All the points of each dataset are well fitted for the ellipse with a confidence of 95 %. The non-explosives are scattered more in 2D space in contrast to the explosives as visualized in Fig. 5.16. However, in the case of the H-C_2, the results are promising where only sight overlap has been noticed. Similar behavior was observed for the C_2-O and C_2-N combinations (Not shown in the figure). The C_2 intestines of the non-explosives are higher than the explosives as shown in Fig. 5.16(c). Further, the discriminatory ability of the 2D scatter plot approach is evaluated by (RDR) [37] as defined in chapter 1. The RDR values obtained for the six combinations viz, H-N, H-O, H-C_2, O-N, C_2-O, and C2-N are 0.65, 0.55, 0.24, 0.43, 0.22, and 0.18 respectively. The combination involving the C_2 as one of the components of the 2D scatter plot has shown promising separation. In which, H-C_2 can be considered as good approach as these lines are less influenced by atmospheric contribution.

5.4.2.c PCA Analysis

Here the PCA has been performed on the background-corrected and normalized single spectra. Further, the analysis (in the next sections also) was done for two different spectral windows. The main objective for this consideration is to verify the effect of the non-sample analyte emissions on the performance of employed multivariate techniques which is a challenging task while working mainly with explosives.

1. Total data **(R1)**.
2. Total data excluding contaminants (Na 589–595 & K 765–772 nm) **(R2)**.

In the first step, we employed the PCA for the total spectral region R1 as an input to the PCA. Excellent segregation was demonstrated with the aid of the first three PCs as shown in Fig. 5.17(a). The first five PCs cumulatively describe the total variance of 95.64 %. The explosives are scattered in a more compact manner in the PC space and distinctly separated from the non-explosives. However, non-explosives have shown more scattering which could be owing to the wide range of the samples utilized for the investigation. A similar performance is obtained for the other input R2 as shown in Fig. 5.17(b).

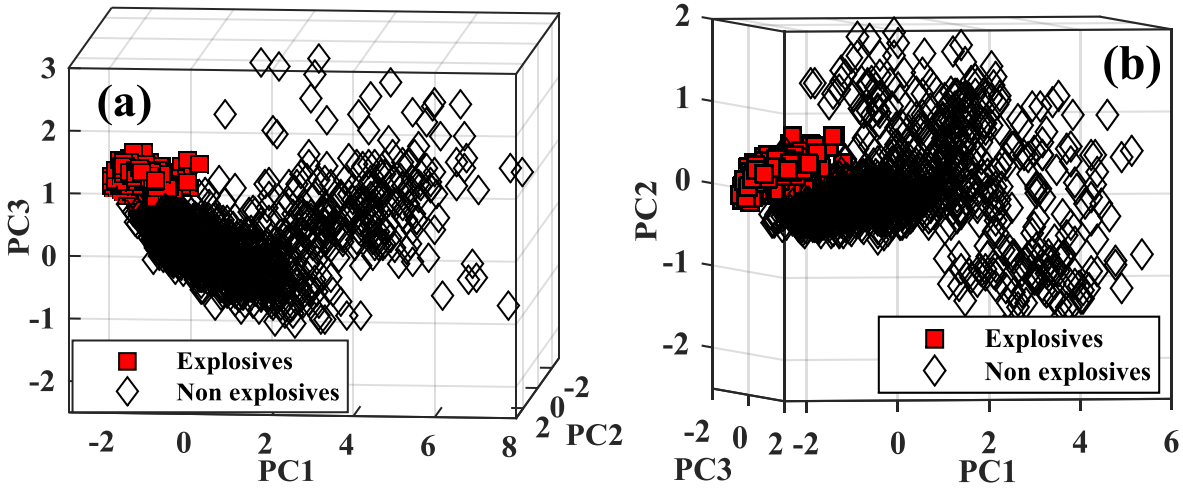

Fig. 5.17. 3D score plots of the explosives and non-explosives. a) R1 as input, b) R2 as input.

PC loading plot provides information about the significant spectral features responsible for sample set clustering under the investigation which are illustrated in Fig. 5.18 (a&b) corresponds to the input R1 and R2 respectively. The first PC of the loadings plot (R1) alone corresponds to one-third of the total variance present in the data, and the two subsequent PCs explain 17.71, 5.94 % of the variance respectively. The spectral features of

the Nitrogen (N II – 500.5 nm), Oxygen (O II – 464.1 nm), Hydrogen (H I – 656.9 nm), C_2 Swan band system (C_2-516.9 nm), Sodium (Na I - 589.6 nm), and Potassium (766.7, 769.9 nm) are dominant in the three PCs as shown in Fig. 5.18 (a).

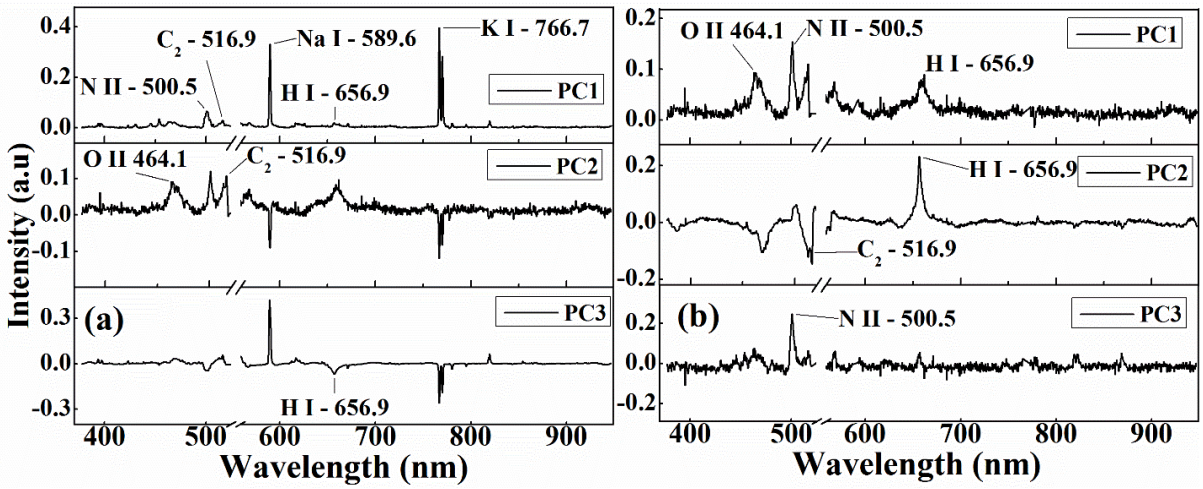

Fig. 5.18. Loadings plot of the first three PCs. a) R1 as input, b) R2 as input.

Fig. 5.18(b) visualizes the loadings plot obtained by the R2 as input to the PCA. The atomic lines of the matrix elements viz., H I – 656. 9, N - II 500.5, and O II – 464.1 are observed in the loadings plot. The molecular features of the C_2 Swan band 516.9 nm is more pronounced in all the three PCs. PC1, PC2, and PC3 explain the variance of 65.01, 9.65, and 8.02 % respectively and the first five PCs together account for ~ 91.35 % of the variance. This result demonstrates that excellent segregation of explosives and non-explosives can be achieved with PCA and the influence of the impurities can be considered as negligible for the classification.

5.4.2.d ANN Analysis

For the present investigation, a three-layer neural network has been utilized with the two different inputs are (as aforementioned R1 and R2) given to the network. Initially, the network has been optimized by varying the number of neurons (2-50) for better performance and twenty-five neurons found to be optimum. The ANN analysis was performed over 1000 times. In each iteration, the data set was randomly divided into training (70%), testing (15 %), and validation (15%). The results achieved from the 1000 iterations are represented in Table 5.7. It presents the correct classification rate

determined from the confusion matrix. The analysis has been performed for R1 & R2 as an input to the model. Further, the model was also evaluated for the total data as input (5 explosives and 19 non-explosives – referred to as 1st dataset) and by considering the equal number of samples (5 explosives and 5 non-explosives – referred to as 2nd dataset).

Table 5.7. The results obtained from the ANN for the explosives and non-explosives.

	5 explosives & 19 non-explosives (Referred as 1st data)		5 explosives & 5 non-explosives (Referred as 2nd data)	
	R1	R2	R1	R2
Explosives	97.71	94.18	99.51	99.65
Non-explosives	99.83	99.83	99.62	99.78

The idea behind considering these inputs is to evaluate the effect of class imbalance on the predictive ability of the trained ANN model. The correct labelling rates obtained for the 2nd data are found to be higher compared to the 1st dataset. It could be attributed to the consideration of the equal number of inputs for the explosives and non-explosives which can minimize the biasing while training the model[46]. It was also found the classification rates are equal for R1 and R2. Similar results were observed in literature where the misclassification rate is higher for the minority dataset however it can be overcome by deep learning methods[47]. In the case of the 1st dataset, it is noticed that identification accuracies are higher for the non-explosive in contrast to the explosives regardless of the input chosen for the ANN analysis. The ACCR achieved through R1 as input is merely 2 % higher than R2, i.e., ~ 98.77 %. Along with that, the result reveals that the identification rate of non-explosives is identical irrespective of the input which is already demonstrated visually in the earlier section through PCA. A slight reduction in the correct identification rate of the explosives has been noticed with R2 as input in contrast to the R1. This could be possible due to considering the only native spectral features of the samples. Nevertheless, the results presented here demonstrate the performance of ANN analysis for recognizing the explosives from non-explosives in the standoff regime with false alarm rates lower than the 6 %.

Further, the analysis has been extended to the identification among explosives in the next section.

5.5 Standoff detection of explosives at 6.5 m

The details of the five explosives are presented in Table 5.5. All the spectra were background corrected and normalized as mentioned in section 5.4.2. Typical LIBS spectra (background corrected) of the five explosives are illustrated in Fig. 5.19.

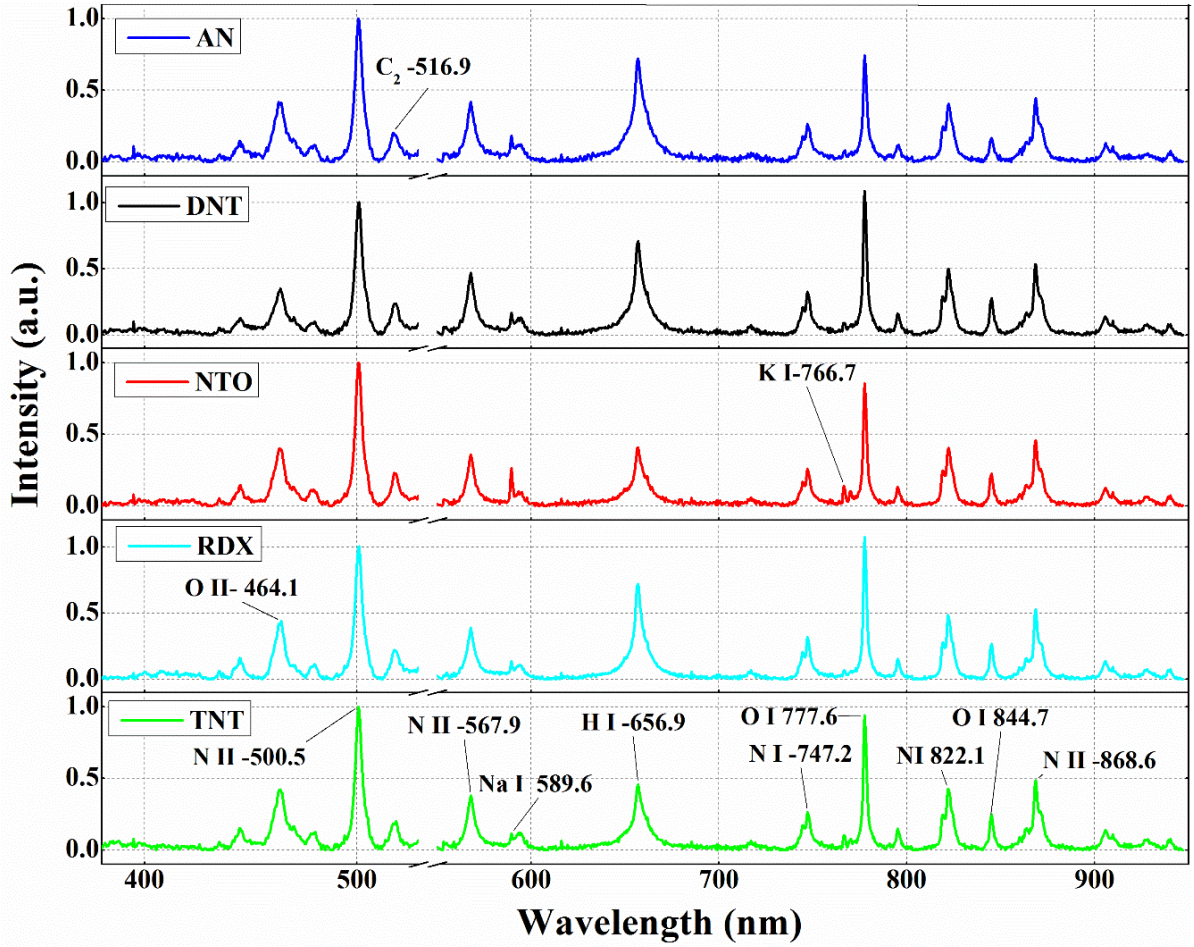

Fig. 5.19. ST-LIBS spectra of the five explosives recorded at 6.5 m. All are background corrected and normalized to the N II- 500.5 nm line.

5.5.1 2D scatter plot analysis

The analysis is done similarly as mentioned in section 5.4.2.b. The 2D scatter plot of four combinations viz., H-N, H-O, H-C_2, and O-N are shown in Fig. 5.20 (a-d). Each point in the plot is a representative of one spectrum and 100 spectra for each sample are employed (except RDX). H-N and H-C_2 scattered plot offered good discrimination among all the samples as shown in Fig. 5.20(a&c) respectively. However, a slight overlap observed

between NTO and TNT. The scatter plot of H-O is illustrated in Fig. 5.20(b) where the RDX and AN are well separated from each other and also from the rest. Nevertheless, the overlap has been noticed between the NTO & TNT, NTO&DNT, and TNT&DNT. The plot involving the oxygen and nitrogen has exhibited the overlap of all the data sets as shown in Fig. 5.20(d) which could be attributed to the immense air contribution to the LIB spectra contrary to other pairs[37]. The C_2-O and C_2-N plots are not shown in Fig. 5.20 where the outcomes are more or less similar to the O-N scatter plot.

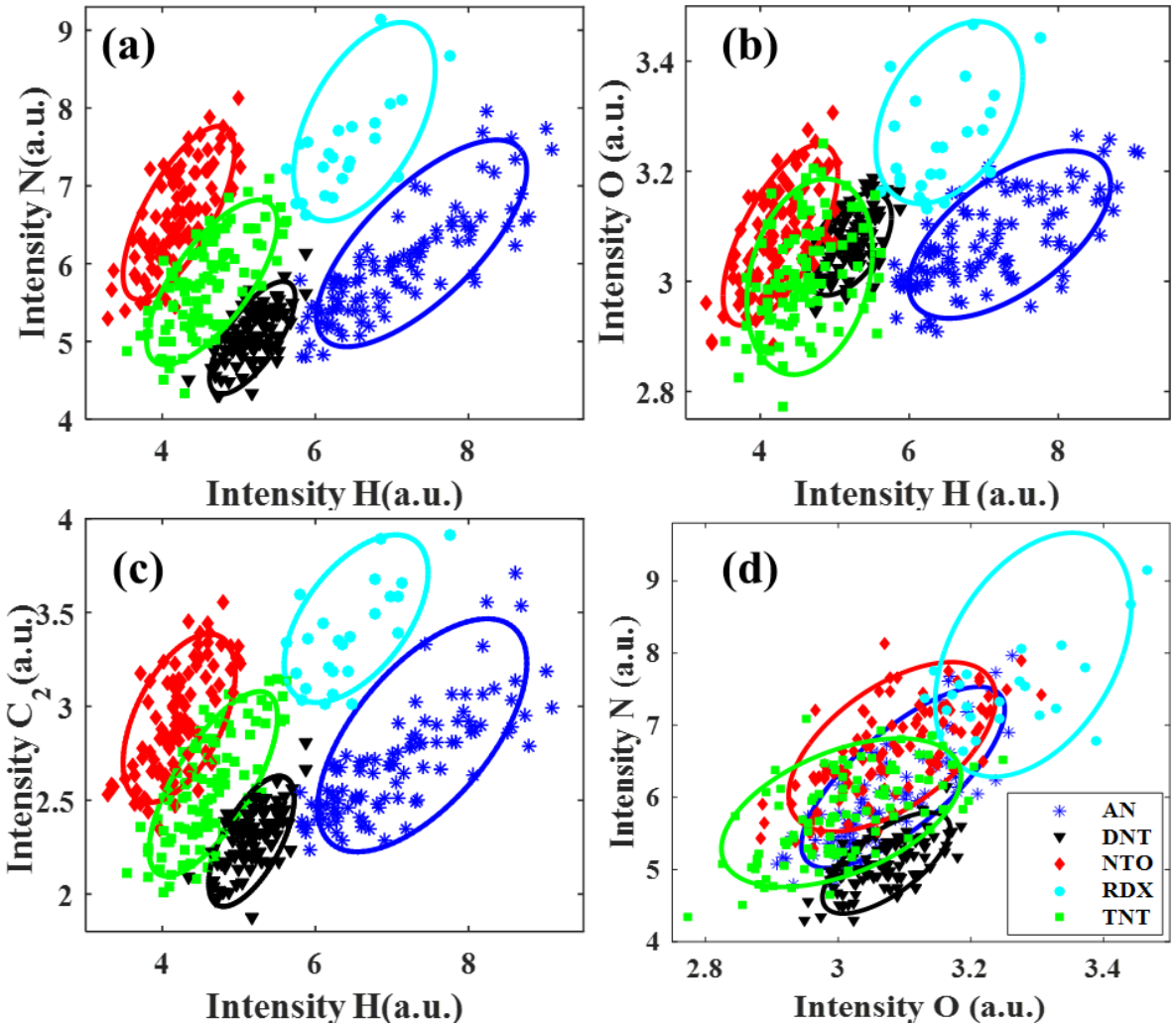

Fig. 5.20. 2D scatter plots of the explosives a) H-N, b) H-O, c) H-C_2 and d) O-N. Symbols are the actual data and ellipses are drawn to visualize the clustering.

Finally, the discriminative ability has been evaluated by determining the RDR values for all the plots. The RDR for all the scatter plots are evaluated and computed values are enumerated in Table 5.8. The RDR value estimated from the H-N scatter plot for TNT &

NTO is close to zero (~ 0.08) where the remaining are well distinguished from each other. Almost, similar behaviour is noticed for the H-C_2, however, a slight additional overlap has been observed between the TNT, and NTO in contrast to the H-N plot where the RDR is 0.25. Besides that, a small overlap region has been noticed between the TNT & DNT with RDR of 0.06. Nevertheless, it has less chance to prone to the atmospheric contribution which makes it as a reliable marker for the accurate/critical evaluation.

Table 5.8. The RDR values evaluated from the 2d scatter plots.

Scatter plots	TNT & NTO	TNT & DNT	NTO & DNT	DNT & AN	TNT & AN	RDX & NTO	RDX & AN	NTO & AN
H-N	0.08	0	0	0	0	0	0	0
H-O	0.92	1.04	0.06	0	0	0	0	0
H-C_2	0.25	0.06	0	0	0	0	0	0
O-N	0.92	0.47	0	0.30	1.17	0.34	0.35	1.32
C_2-O	0.93	0.74	0	0.31	1.02	0.32	0.33	1.52
C_2-N	0.91	0.99	0.11	0.51	1.22	0.45	0.31	1.41

The RDR values of the O-N, C_2-O, and C_2-N are high compared to the other combination due to the more overlap. These results suggest that, apart from the spectral intensities, the choice of the spectral lines is the crucial factor/stage for the efficient identification of the explosives. The findings from the 2d projection approach demonstrate the reliable classification of the explosives with good discrimination ability by employing only 2 % of the total data.

5.5.2 Classification of explosives by PCA

Here the PCA has been performed on the five explosives and the procedure similar as mentioned in section 5.4.2.c. Fig. 5.21 illustrates the 3d score plot corresponding to the first three PCs (R1 as input). The first three PCs account for the variance of 39, 34.61 %, and 10.17 % respectively and five PCs collectively explain the variance of 91.72 % present in the data. All the samples are well clustered, which demonstrates the presence of differences among the spectra and can be employed for discrimination among the samples. AN is well isolated from the rest of the samples. DNT has shown less dispersion among all

the samples and it is slightly overlapped with the RDX. The loadings plot of the first three PCs is shown in Fig. 5.22 (R1 as input).

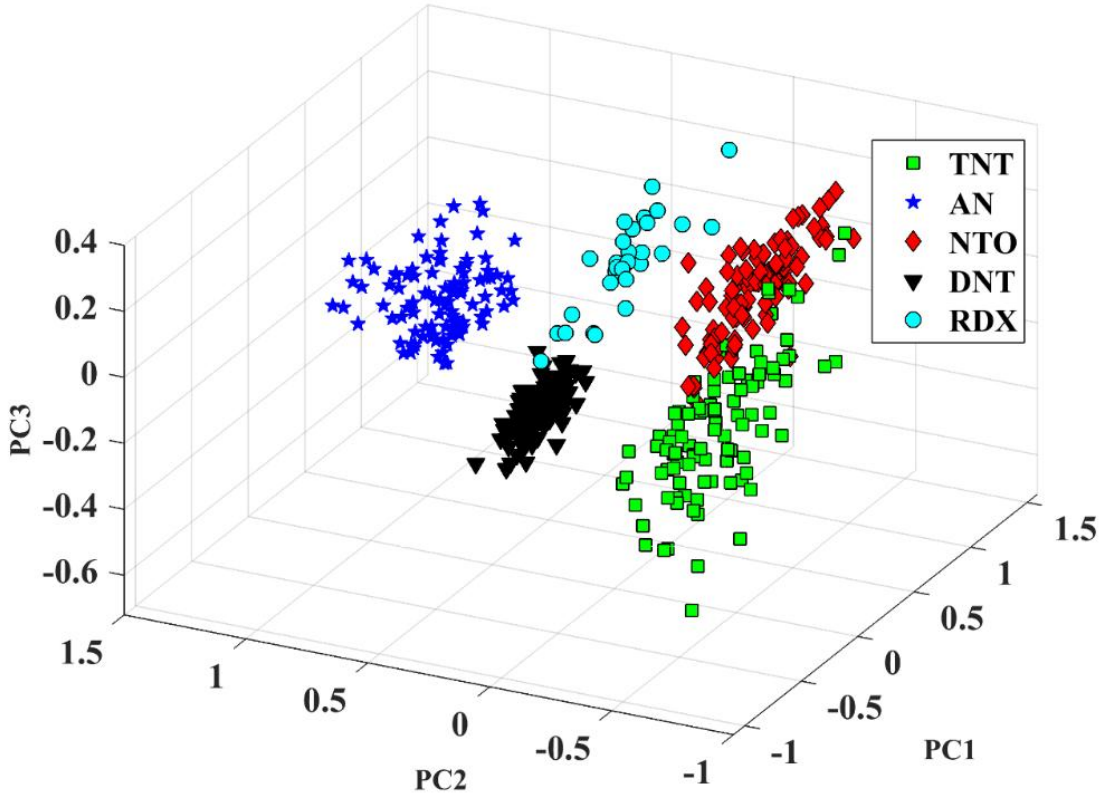

Fig. 5.21. 3D score plot of the five explosives. R1 is used as input to the PCA.

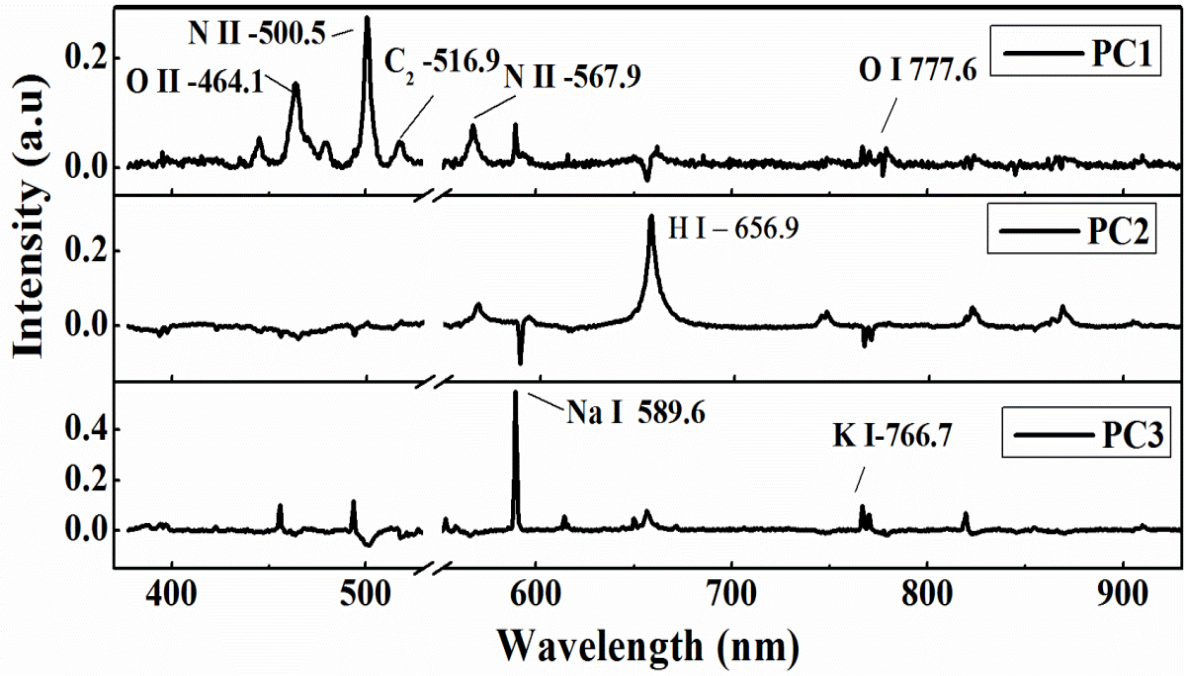

Fig. 5.22. Loadings plot of the first three PCs. R1 is used as input to the PCA.

Nitrogen (N II-500.5, N II-567.9 nm) and Oxygen (O II-464.1 nm) spectral lines are the most dominant features in the PC1. Also, the molecular C_2 Swan band at 516.9 nm prevailed in the loadings plot. Hydrogen (H I -656.9 nm) is the strongest line that appeared in PC2 followed by Na I 589.6 nm as shown in Fig. 5.22. The Na I 589.6 nm & K 766.7 nm spectral lines are majorly contributed to the PC3.

The 3d score plot for the R2 as input to the PCA is shown in Fig. 5.23. The segregation is observed almost similar to R1 as input. The first three PCs describe 43.68, 38.1, and 6.63 % of the total variance within the data set respectively. The cumulative variance obtained by the first five PCs is approximately the same as the R1 ~ 91.95 %.

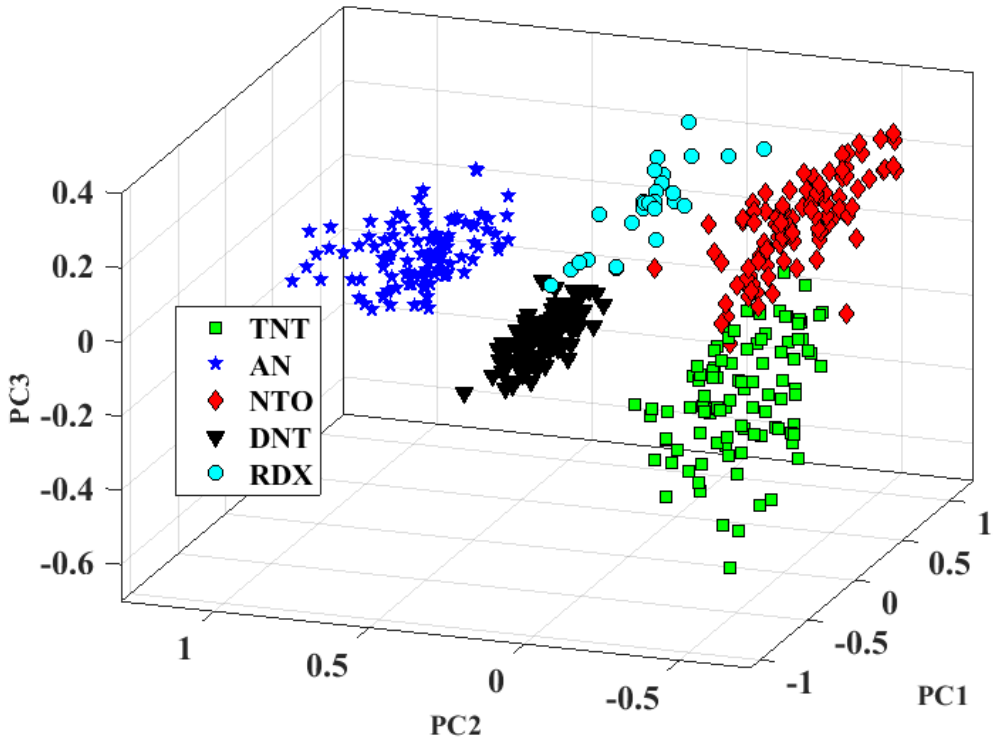

Fig. 5.23. 3D score plot of the five explosives. R2 is used as input to the PCA.

The loadings plot are also has shown the nearly identical spectral features for PC1 with slight variations in the intensities as shown in Fig. 5.24. Hydrogen (H I -656.9 nm) is the strongest feature observed in PC2 followed by Nitrogen lines (747.2, 822.1 & 868.3 nm). Whereas N II- 868.6 nm is the strongest emission in the PC3 followed by N-822.1 and O I-777.6 nm lines. These results reveal that the performance of the PCA for the explosives discrimination hardly depends on the impurities of the interrogated samples.

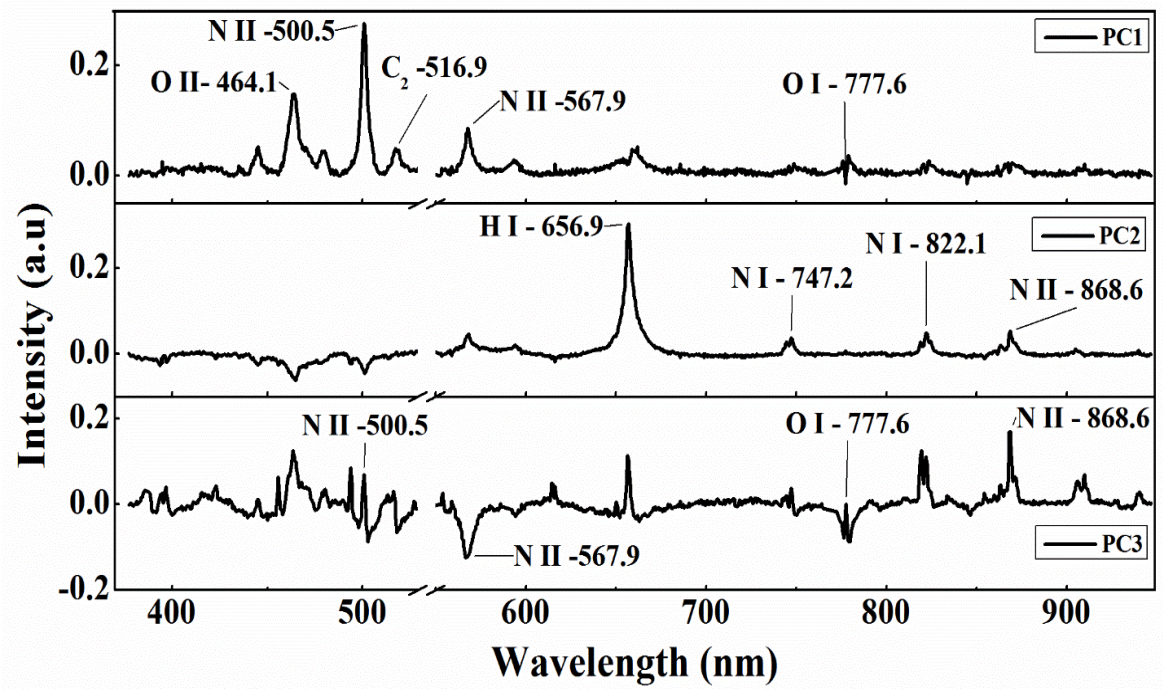

Fig. 5.24. Loadings plot of the first three PCs. R2 is used as input to the PCA.

An excellent classification among the explosives has been already demonstrated in this section with the aid of PCA albeit one to one labelling is not viable. Hence, here, we employed a supervised learning algorithm i.e. ANN in the next section.

5.5.3 Classification of explosives by ANN

The analysis has been performed similarly as mentioned in section 5.4.2.d. The results (R1 as input) obtained from the average of the 1000 iterations are presented in Table 5.9. The analytical performance of the ANN can be accessed from the confusion matrix.

Table 5.9. Confusion matrix obtained from the ANN (R1 as input).

		Predicted labels				
		TNT	AN	NTO	DNT	RDX
Reference labels	TNT	98.67	0.07	0.27	0.03	0.97
	AN	0.00	98.33	0.07	0.57	1.03
	NTO	0.37	0.00	97.73	0.07	1.83
	DNT	0.13	0.53	1.03	97.01	1.29
	RDX	0.00	0.37	0.30	0.37	98.97

As shown, in Table 5.9 the correct predictions rate is above 97 % for all the samples and close to 99 % for the TNT and RDX. The average of the correct classification rate (ACCR) is around 98.14 %. Also, few performance metrics were determined from the confusion matrix to evaluate the performance of the ANN model as enumerated in Table 5.10.

Table 5.10. Performance parameters of the samples determine from ANN (R1 as input).

	Accuracy	Precision	Sensitivity	Specificity
TNT	99.63	99.50	98.66	99.87
AN	99.46	99.02	98.33	99.75
NTO	99.20	98.32	97.73	99.57
DNT	99.18	98.94	97.02	99.74
RDX	98.75	95.08	98.96	98.70
Average	99.24	98.17	98.14	99.53

The performance metrics reflect that the identification accuracies of ~ 99 % can be achieved for all the samples which minimize the arbitrariness in decision making. Along with that ANN presents high sensitivity and specificity where the average specificity close to 99.5 %. The results for the R2 as input to ANN are given in Table 5.11.

Table 5.11. Confusion matrix obtained from the ANN (R2 as input).

		Predicted labels				
		TNT	**AN**	**NTO**	**DNT**	**RDX**
Reference labels	**TNT**	99.60	0.07	0.17	0.07	0.10
	AN	0.37	99.03	0.47	0.00	0.13
	NTO	1.00	0.20	96.83	0.90	1.07
	DNT	1.17	1.07	1.70	95.00	1.07
	RDX	0.13	0.60	1.07	0.17	98.03

The results are almost similar to R1 where the ACCR is 97.70 % which is only differed by the ~ 0.5 %. Nevertheless, the individual identification rate attained is ~ 100 % for TNT. Also, it is observed that DNT correct prediction is decreased by 2% and it is principally misclassified as TNT (~1.2 %). Similarly the average of all the performance parameters also closely resemble (which only differ by less than 0.5 %) to the input R1. These results demonstrate that the accuracies up to 99 % can be achieved for the standoff detection of explosives.

5.6 Summary

Initial, ST-LIBS experiment has been performed at 1 m where the atomic ratios and PCA have been used for the classification of the five explosives. Further, it extended for probing the five explosives and a wide range of non-explosives at 6.5 m. Proper optimization of the focusing has resulted in higher irradiance which favours the formation of intense plasma. The captivating principle of f-number matching of the collection system to that of the spectrometer was utilized in designing an optimized compact portable detection system consists of a single lens and a small spectrometer. This helps in increasing the spectral throughput of the detection system even with small aperture size. The 2D scatter plots of two selected spectral lines have shown promising/good clusters where only 2 % of the total spectral data was utilized. An excellent classification of explosives has been achieved with the aid of PCA which has also demonstrated the discrimination of explosives and non-explosives. The results from the ANN analysis of non-explosives and explosives have resulted in the correct prediction rates of 99.83 % and 94.18 % respectively. The obtained false alarm rates, being less than ~ 6%, suggests that the identification, as well as labelling of explosives with high accuracy, can be achieved using the ANN algorithm coupled to LIBS data. The overall results present the efficacy of the miniaturized ST-LIBS and can be utilized as a field-deployable technology for the rapid identification of the explosives.

5.7 References

1. N.C. Dingari, I. Barman, A.K. Myakalwar *et al.*, "Incorporation of support vector machines in the LIBS toolbox for sensitive and robust classification amidst unexpected sample and system variability", Analytical chemistry, 84, **2012**.
2. R.L. Grob, and E.F. Barry, "Modern practice of gas chromatography", John Wiley & Sons**2004**.
3. J.S. Caygill, F. Davis, and S.P. Higson, "Current trends in explosive detection techniques", Talanta, 88, **2012**.
4. M.J. Lefferts, and M.R. Castell, "Vapour sensing of explosive materials", Anal Methods-Uk, 7, **2015**.
5. S. Sreedhar, M.K. Gundawar, and S.V. Rao, "Laser Induced Breakdown Spectroscopy for Classification of High Energy Materials using Elemental Intensity Ratios", Defence Sci J, 64, **2014**.
6. S. Sreedhar, S.V. Rao, P.P. Kiran *et al.*, "Stoichiometric analysis of ammonium nitrate and ammonium perchlorate with nanosecond laser induced breakdown spectroscopy", SPIE Defense, Security, and Sensing, International Society for Optics and Photonics, **2010**.
7. F.C. De Lucia, Jr., R.S. Harmon, K.L. McNesby *et al.*, "Laser-induced breakdown spectroscopy analysis of energetic materials", Appl Opt, 42, **2003**.
8. Q.-Q. Wang, K. Liu, H. Zhao *et al.*, "Detection of explosives with laser-induced breakdown spectroscopy", Front Phys-Beijing, 7, **2012**.
9. V. Lazic, A. Palucci, S. Jovicevic *et al.*, "Analysis of explosive and other organic residues by laser induced breakdown spectroscopy", Spectrochim Acta B, 64, **2009**.
10. J.L. Gottfried, F.C. De Lucia Jr, C.A. Munson *et al.*, "Strategies for residue explosives detection using laser-induced breakdown spectroscopy", J Anal Atom Spectrom, 23, **2008**.
11. Q. Wang, G. Teng, C. Li *et al.*, "Identification and classification of explosives using semi-supervised learning and Laser-induced Breakdown Spectroscopy", Journal of Hazardous Materials, **2019**.
12. W. Li, X. Li, X. Li *et al.*, "A review of remote laser-induced breakdown spectroscopy", Applied Spectroscopy Reviews, **2018**.
13. B. Sallé, P. Mauchien, and S. Maurice, "Laser-induced breakdown spectroscopy in open-path configuration for the analysis of distant objects", Spectrochim Acta B, 62, **2007**.
14. J.M. Vadillo, P.L. García, S. Palanco *et al.*, "Remote, real-time, on-line monitoring of high-temperature samples by noninvasive open-path laser plasma spectrometry", Analytical and bioanalytical chemistry, 375, **2003**.
15. M.K. Gundawar, R. Junjuri, and A.K. Myakalwar, "Standoff Detection of Explosives at 1 m using Laser Induced Breakdown Spectroscopy", Defence Sci J, 67, **2017**.
16. C. Lopez-Moreno, S. Palanco, J.J. Laserna *et al.*, "Test of a stand-off laser-induced breakdown spectroscopy sensor for the detection of explosive residues on solid surfaces", J Anal Atom Spectrom, 21, **2006**.

17. F.C. De Lucia, J.L. Gottfried, C.A. Munson *et al.*, "Double pulse laser-induced breakdown spectroscopy of explosives: Initial study towards improved discrimination", Spectrochim Acta B, 62, **2007**.
18. A. Laxmiprasad, V.S. Raja, S. Menon *et al.*, "An in situ laser induced breakdown spectroscope (LIBS) for Chandrayaan-2 rover: Ablation kinetics and emissivity estimations", Advances in Space Research, 52, **2013**.
19. S. Maurice, R. Wiens, M. Saccoccio *et al.*, "The ChemCam instrument suite on the Mars Science Laboratory (MSL) rover: Science objectives and mast unit description", Space Sci Rev, 170, **2012**.
20. A. Laxmiprasad, V. Sridhar Raja, A. Goswami *et al.*, "Realization of empirical database and generation of calibration curves for precise quantitative analysis employing a mini-LIBS for Chandrayaan-2 rover", 39th COSPAR Scientific Assembly**2012**.
21. J.-B. Sirven, B. Salle, P. Mauchien *et al.*, "Feasibility study of rock identification at the surface of Mars by remote laser-induced breakdown spectroscopy and three chemometric methods", J Anal Atom Spectrom, 22, **2007**.
22. R. Ahmed, and M. Baig, "A comparative study of enhanced emission in double pulse laser induced breakdown spectroscopy", Optics & Laser Technology, 65, **2015**.
23. J.L. Gottfried, F.C. De Lucia, C.A. Munson *et al.*, "Double-pulse standoff laser-induced breakdown spectroscopy for versatile hazardous materials detection", Spectrochim Acta B, 62, **2007**.
24. G. Galbacs, "A critical review of recent progress in analytical laser-induced breakdown spectroscopy", Anal. Bioanal. Chem., 407, **2015**.
25. C. Lopez-Moreno, S. Palanco, and J. Laserna, "Remote laser-induced plasma spectrometry for elemental analysis of samples of environmental interest", J Anal Atom Spectrom, 19, **2004**.
26. C. Lopez-Moreno, S. Palanco, and J.J. Laserna, "Stand-off analysis of moving targets using laser-induced breakdown spectroscopy", J Anal Atom Spectrom, 22, **2007**.
27. R. Grönlund, M. Lundqvist, and S. Svanberg, "Remote imaging laser-induced breakdown spectroscopy and laser-induced fluorescence spectroscopy using nanosecond pulses from a mobile lidar system", Applied spectroscopy, 60, **2006**.
28. A.K. Knight, N.L. Scherbarth, D.A. Cremers *et al.*, "Characterization of laser-induced breakdown spectroscopy (LIBS) for application to space exploration", Applied Spectroscopy, 54, **2000**.
29. P.D. Barnett, N. Lamsal, and S.M. Angel, "Standoff Laser-Induced Breakdown Spectroscopy (LIBS) Using a Miniature Wide Field of View Spatial Heterodyne Spectrometer with Sub-Microsteradian Collection Optics", Applied spectroscopy, 71, **2017**.
30. R. González, P. Lucena, L. Tobaria *et al.*, "Standoff LIBS detection of explosive residues behind a barrier", J Anal Atom Spectrom, 24, **2009**.
31. P. Lucena, I. Gaona, J. Moros *et al.*, "Location and detection of explosive-contaminated human fingerprints on distant targets using standoff laser-induced breakdown spectroscopy", Spectrochimica Acta Part B-Atomic Spectroscopy, 85, **2013**.
32. R.C. Wiens, S.K. Sharma, J. Thompson *et al.*, "Joint analyses by laser-induced breakdown spectroscopy (LIBS) and Raman spectroscopy at stand-off distances", Spectrochimica Acta Part A: Molecular and Biomolecular Spectroscopy, 61, **2005**.

33. B. Sallé, D.A. Cremers, S. Maurice *et al.*, "Evaluation of a compact spectrograph for in-situ and stand-off laser-induced breakdown spectroscopy analyses of geological samples on Mars missions", Spectrochim Acta B, 60, **2005**.
34. F.C. De Lucia, and J.L. Gottfried, "Classification of explosive residues on organic substrates using laser induced breakdown spectroscopy", Applied optics, 51, **2012**.
35. J.L. Gottfried, F.C. De Lucia Jr, and A.W. Miziolek, "Discrimination of explosive residues on organic and inorganic substrates using laser-induced breakdown spectroscopy", J Anal Atom Spectrom, 24, **2009**.
36. F.C. De Lucia Jr, J.L. Gottfried, C.A. Munson *et al.*, "Multivariate analysis of standoff laser-induced breakdown spectroscopy spectra for classification of explosive-containing residues", Applied optics, 47, **2008**.
37. I. Gaona, J. Serrano, J. Moros *et al.*, "Range-adaptive standoff recognition of explosive fingerprints on solid surfaces using a supervised learning method and laser-induced breakdown spectroscopy", Analytical chemistry, 86, **2014**.
38. J.L. Gottfried, F.C. De Lucia, C.A. Munson *et al.*, "Standoff detection of chemical and biological threats using laser-induced breakdown spectroscopy", Applied spectroscopy, 62, **2008**.
39. H. Hegazy, "Oxygen spectral lines for diagnostics of atmospheric laser-induced plasmas", Appl Phys B-Lasers O, 98, **2010**.
40. T. Huth-Fehre, R. Feldhoff, T. Kantimm *et al.*, "NIR-Remote sensing and artificial neural networks for rapid identification of post consumer plastics", Journal of Molecular Structure, 348, **1995**.
41. H. Griem, "Spectral Line Broadening by Plasmas, Acad", Press, New York, **1974**.
42. W. Li, X. Yang, X. Li *et al.*, "A portable multi-collector system based on an artificial optical compound eye for stand-off laser-induced breakdown spectroscopy", J Anal Atom Spectrom, 32, **2017**.
43. A. Moosakhani, P. Parvin, S.Z. Mortazavi *et al.*, "Effect of hydrocarbon molecular decomposition on palladium-assisted laser-induced plasma ablation", Appl. Opt., 56, **2017**.
44. A. Moosakhani, P. Parvin, A. Reyhani *et al.*, "Propane decomposition and conversion into other hydrocarbons using metal target assisted laser induced plasma", Physics of Plasmas, 24, **2017**.
45. J. Moros, J. Serrano, C. Sanchez *et al.*, "New chemometrics in laser-induced breakdown spectroscopy for recognizing explosive residues", J Anal Atom Spectrom, 27, **2012**.
46. J.M. Johnson, and T.M. Khoshgoftaar, "Survey on deep learning with class imbalance", Journal of Big Data, 6, **2019**.
47. R.A. Bauder, and T.M. Khoshgoftaar, "The effects of varying class distribution on learner behavior for medicare fraud detection with imbalanced big data", Health information science and systems, 6, **2018**.

CHAPTER 6 : Femtosecond and Filamentation LIBS Studies

This chapter explores the extending femtosecond (fs) laser-induced breakdown spectroscopy (Fs-LIBS) for the discrimination of plastics waste and characterization of the Cu plasma produced by fs filaments. The utilization of the fs pulses particularly favors the molecular species formation and also minimizes atmospheric entrainment to the plasma, which can greatly increase the identification accuracies. PCA has been utilized for the exploratory analysis where excellent segregation was achieved. Further, the data was analyzed through a supervised algorithm, ANN. For efficient identification, an ANN model was constructed and evaluated by exploiting five different spectral windows/regions. The average identification rates obtained for all samples are in the range of 97 to 99 % depending on the spectral window. The correct prediction rates with 100 % accuracy were achieved when ten prominent spectral features were employed. Further, it presents the filamentation induced breakdown spectroscopy (FIBS) studies of Cu. The filaments of various intensities were generated with the aid of three different focusing lenses. Further, the FIBS measurements were carried out for each filament at three different positions along the length. The filaments were spatially characterized by estimating the plasma temperature and electron density via Boltzmann and Stark broadening methods respectively. The investigation has demonstrated that the maximum spectral line intensity for Cu plasma is attained at the central part of the filament. It also revealed that the persistence time of the spectral lines is highest for the centre of the filament. Further, it has been demonstrated that the persistence time decreased linearly with increasing the focal length of the focusing lens.

Part of this chapter's work has been published as following journal article.

Rajendhar Junjuri, *M.K. Gundawar, "Femtosecond laser-induced breakdown spectroscopy studies for the identification of plastics", Journal of Analytical Atomic Spectrometry, (2019).*

6.1 Introduction

The first part of the current chapter briefly explains an overview of Fs-LIBS and explores its application for the recognition of plastic waste. Whereas the second part presents the Spatio-temporal characterization of the Cu plasma produced by different fs filaments generated by different focal length lenses.

6.1.1 Overview of Fs-LIBS

Laser-matter interaction of the ultrafast pulses (fs) highly differs from the long duration pulses (ns) in the energy dissipation mechanism. In the case of interaction with fs pulse, the rapid creation of the hot plasma with the absence of liquid phase along with a decrease in the size of the heat-affected zone leads to much more controllable material removal[1]. Whereas in the case of interaction with long pulses, the matter undergoes transient changes in thermodynamic pathways starting from solid to the plasma via the liquid state. Apart from that, the poor coupling of laser energy to the sample in ns LIBS leads to the usage of higher pulse energies and leaves a scar due to the melting. Fs-LIBS has attractive features like the absence of laser-plasma interaction (plasma shielding) and negligible heat transfer from the laser interaction zone to the surrounding lattice leading to improvement in sensitivity[2]. Whereas in the case of ns-LIBS, the plasma undergoes reheating due to the persistent plasma-pulse interaction. Thus it results in a plasma with a higher temperature where atomization dominates compared to the molecular formation at initial time scales. In contrast, the fs pulse forms a lower temperature plasma and favors the molecular formation.

CN and C_2 are the dominant molecular band systems observed in the LIBS spectra of organic samples such as biological specimens (bacteria, tissues) [3, 4], explosives[5], and polymers[6]. Their formation pathways are complex but extensive works have demonstrated that C_2 formation is mostly due to the native C=C linkages whereas CN emissions could be due to the recombination of C and N and partially from native CN bands [5, 7, 8]. The detailed mechanisms/reactions are given in section 6.3.1(c). Baudelet et al. have done extensive work for the identification of biological samples using ns and fs-

LIBS techniques [3, 4]. They have identified the samples based on CN emissions and have shown that these emissions are purely due to the direct ablation of bonds present in the sample in fs case. Also, it has been widely reported in the literature that, the less plasma temperature in fs case leads to the negligible oxygen and nitrogen emissions from excited ambient air[4, 7, 9]. Thus employing the fs-LIBS technique can efficaciously help in identifying the organic samples. Also, it has figures of merit for the quantitative and qualitative analysis in terms of minimal damage to the surface by precise ablation, improved spatial resolution, lack of fractional evaporation and better reproducibility[10]. However, the smaller plasma size and the time of persistence are limitations in acquiring the signal. These challenges can be expected to be overcome by future technological advances leading to more sensitive detectors and high power lasers. Over the past decade, the overall size of fs amplifier laser systems has been gradually decreasing with the advent of new technologies. New generation compact, less expensive fiber femtosecond lasers are available and being utilized in portable LIBS investigations along with a few standoff applications[11].

An overview of the plastics identification and the motivation behind applying LIBS for their discrimination is already presented in chapter 4. Also, a brief review of the identification of the plastics using LIBS is given in table 4.1 in chapter 4. To date, all the works devoted to the identification of plastics using LIBS technique have been employed nanosecond lasers (ns) as an excitation source to produce the plasma. The use of fs laser pulses for the identification of plastic waste has not been explored to the best of my knowledge hence in this chapter the feasibility of fs-LIBS for their identification is presented.

6.1.2 Overview of Filamentation LIBS (FIBS)

The standoff detection capability is the key attribute of the LIBS technique which enables the identification of hazardous materials in hostile environments where the physical access to the sample is not viable nevertheless optical access can be envisaged [12, 13]. The conventional ST-LIBS technique relies on the ns pulse has been reported in the literature for various applications such as identification of explosives, contaminants, and nuclear

materials, etc.[12, 14, 15]. Nevertheless, it has limitations for achieving the maximum standoff distances owing to the atmospheric turbulence and diffraction effects [16-19]. However, this hurdle can be overcome by utilizing the advantage of complex but favorable nonlinear dynamics of ultrafast fs laser propagation in ambient air which produces the filaments for probing samples for long-range applications. Filamentation has got significant attention of the research community owing to the wide range of applications viz., artificial lighting[20], filament induced breakdown spectroscopy (FIBS)[21], LIDAR[22], THz generation[23], and others[24]. FIBS is a promising spectroscopic method where the intensities of fs filaments are in the range of 10^{13} W/cm^2 which is sufficient to ablate the samples even at longer standoff distances[25, 26]. The fs filaments can propagate and deliver energies over very long distances without any diffraction effects in contrast to the conventional ns pulses and demonstrates it as a potential candidate for the remote sensing applications[27]. These unique feature has demonstrated the fs laser beam propagation over the ranges of a few kilometers [28, 29]. Most of the FIBS studies have been focused on the capability of standoff measurements and the recognition of atomic and molecular spectra. It has been applied for the remote identification of the materials in different applications such as defense[16, 30], archeology[31], biology[21, 32, 33], nuclear technology[34] and environment monitoring[35], etc. [10, 36-38].

Although it has been reported that the FIBS is a promising spectroscopic tool for the standoff detection of materials, the characteristic properties of FIBS are still under investigation. The enhancement of the spectral line intensity for the remote FIBS is reported with spatio-temporally chirped pulses[39]. Harilal *et al.* demonstrated the temperature clamping in FIBS and it is attributed to the intensity clamping in a filament. They have also investigated the effect of loosely focused (2- 4 m focal length) and freely propagated filaments (no focusing optics used) on the evolution of the aluminum oxide (ALO) molecular species[40, 41]. Fs laser ablation studies of steel and titanium alloys with tightly focused fs pulses, sharply focused and unfocused filaments have been demonstrated that the ablation efficiency is more for the tightly focused fs pulses followed by sharply focused filaments[42]. The longitudinal variation of the filament intensity in ambient air qualitatively determined by the acoustic measurements. The change in the acoustic signal is attributed to the cumulative effect of change in plasma temperature and electron density.

Xu *et al.* characterized the lead FIBS plasma produced by the loosely focused filaments by measuring the plasma temperature and electron density [43]. Skrodzki et al. have demonstrated the transition from single to multiple filament regime with the shadowgraphy technique and quantified the laser coupling efficiency to the metal target [44]. It is worth considering that the properties of the LIP greatly depend on the irradiation conditions. A better understanding of the plume properties at different positions of filament is an essential factor for improving the figures of merit of the FIBS technique. Hence, it is of the vital role to study and compare the spatial and temporal characterization/dynamics of the FIBS measurements generated by different filaments which are very less explored in the literature.

The second part of this chapter presents the characterization of the Cu plasma produced by the filaments with various intensities generated by different focal length lenses. Each filament is characterized at different positions along the spatial length.

6.2 Experimental details

6.2.1 Fs-LIBS

The details of the Fs-LIBS are already given in chapter 2 (section 2.3.1). A laser pulse of 2 mJ is guided by a set of mirrors and focused onto the sample surface using a 100 mm focal length plano-convex fused silica lens to produce the plasma. Fs- LIBS spectra were acquired with the gate delay of 20 ns and the gate width of 5 μs. A constant ICCD gain of 2600 was used for the spectral acquisition. Thirty spectra were acquired for each sample and each spectrum corresponds to an accumulation of 1000 laser pulse corresponds to 1 second of acquisition time.

6.2.2 Filamentation LIBS

A typical schematic of the FIBS setup is shown in Fig. 6.1(a). The details of the fs laser system are described in chapter 2 (section 2.1.2). The filaments of three different lengths were produced by focusing the laser beam of 2 mJ energy through a Plano-convex lens of focal lengths 50, 100, and 200 cm respectively, and the images of the three filaments are

shown in Fig. 6.1(c). The FIBS experiment has been performed on the Cu target in an ambient atmosphere.

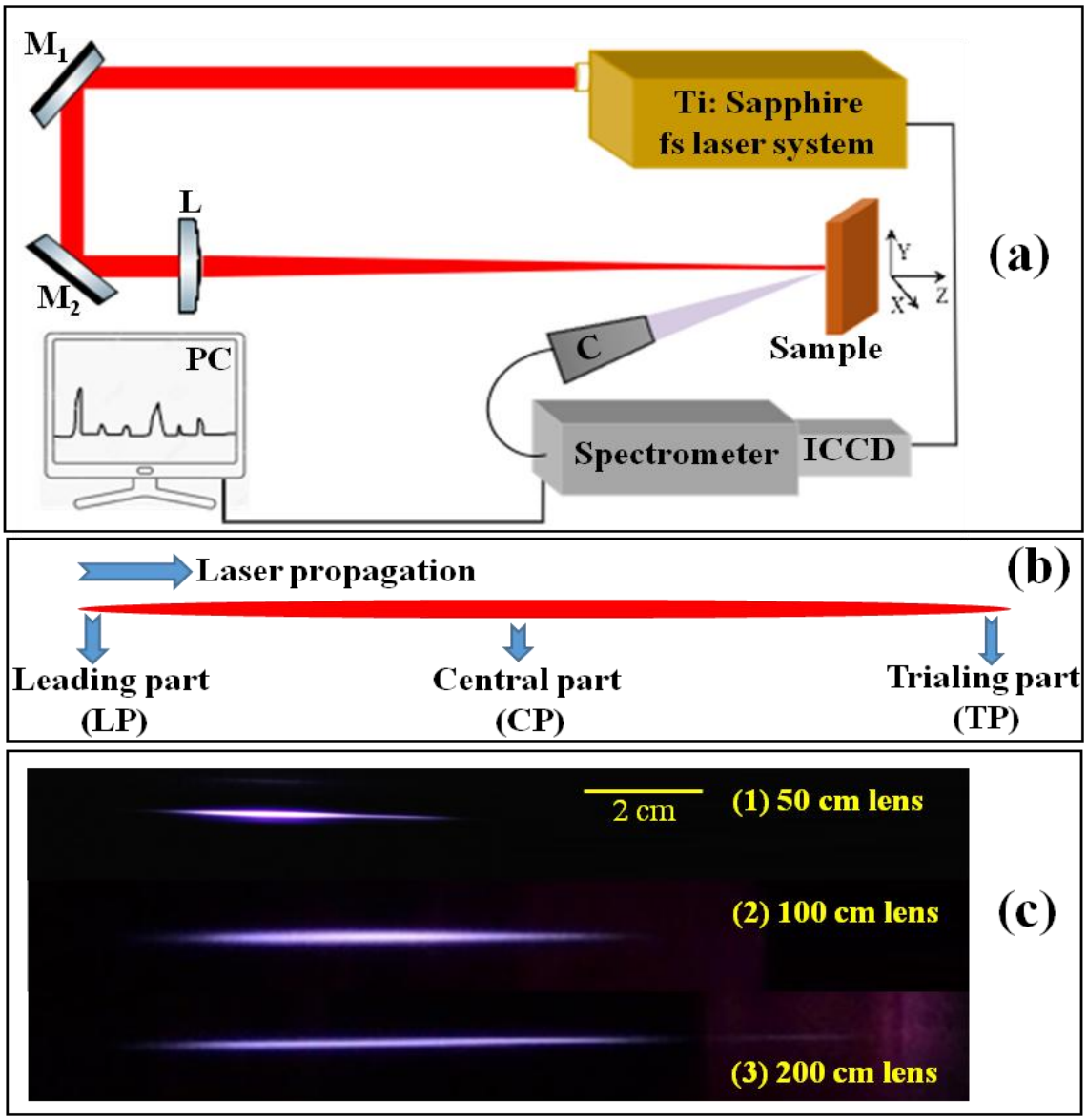

Fig. 6.1. a) Typical schematic of the FIBS setup. M_1 and M_2 are mirrors, L is focusing lens, and C is the collection system. b) FIBS measurements at three different positions of the filament. LP, CP, and TP correspond to the exposure of the Cu target by keeping at leading, central, and trailing parts of the filament respectively. c) Images of the filaments captured by a camera.

The sample was kept on the X-Y translation stage which was perpendicular to the incident laser beam propagation. The Cu sample was exposed by the filament at three different parts along its length by moving the lens along laser propagation as shown in Fig. 6.1(b). To maintain reproducibility in experimental data, the lens was placed on a rail which can have access in +z and –z directions. The optical emissions from the filament induced Cu plasma were acquired by the collection optics (Andor, ME OPT-007) which is positioned

at 45° relative to the incident laser beam and kept at a distance of 18 cm from the Cu target. The Cu target and collection optics were held fixed at a position on the optical bench for the constant collection efficiency. The spectral emissions from the collection system were guided to the Mechelle spectrometer through an optical fiber. The Echelle spectrograph coupled to an ICCD (for details see chapter 2, section 2.2.1).

Two types of FIBS spectra were acquired for the present study for the spatial and temporal characterization.

a) Time-integrated spectra recorded with a gate width of 2 μs.

b) Time-resolved spectra acquired for the temporal characterization in the time window 0.02-1.82 µs by increasing the delay in steps of 0.2 µs with a constant gate width of 0.2 µs.

The initial delay (20 ns) and gain (1200) was fixed for these two datasets and each spectrum corresponds to an accumulation of 1000 laser pulses. Ten spectra were acquired at each position

6.3 Results and discussion

The first part represents the application of Fs-LIBS for the identification of plastic waste. Further, the characterization of Cu plasma generated by different fs filament intensities is discussed in the second part.

6.3.1 Fs-LIBS for the identification of the plastic waste

The experiment was performed for five plastics namely, PET, HDPE/HD, LDPE/LD, PP, and PS. The details are given in chapter 4 (Table 4.2). All the samples were characterized by TG-DTA (See chapter 4, section 4.2.1) and Raman spectroscopy (See chapter 4, section 4.2.2). The results from both techniques have confirmed their identity.

6.3.1.a Description of the spectral lines

The LIBS spectra were normalized to the carbon line at C-247.85 nm and normalized spectra of the five plastics are envisioned in Fig. 6.2. The spectra are shown in two spectral regions 220-450 and 450-880 nm with different intensity scales to facilitate the clear view of

spectral features with low intensities. The second spectral region, i.e., 450-880 nm consists of C_2 Swan band system, and atomic peaks of hydrogen, nitrogen, and oxygen.

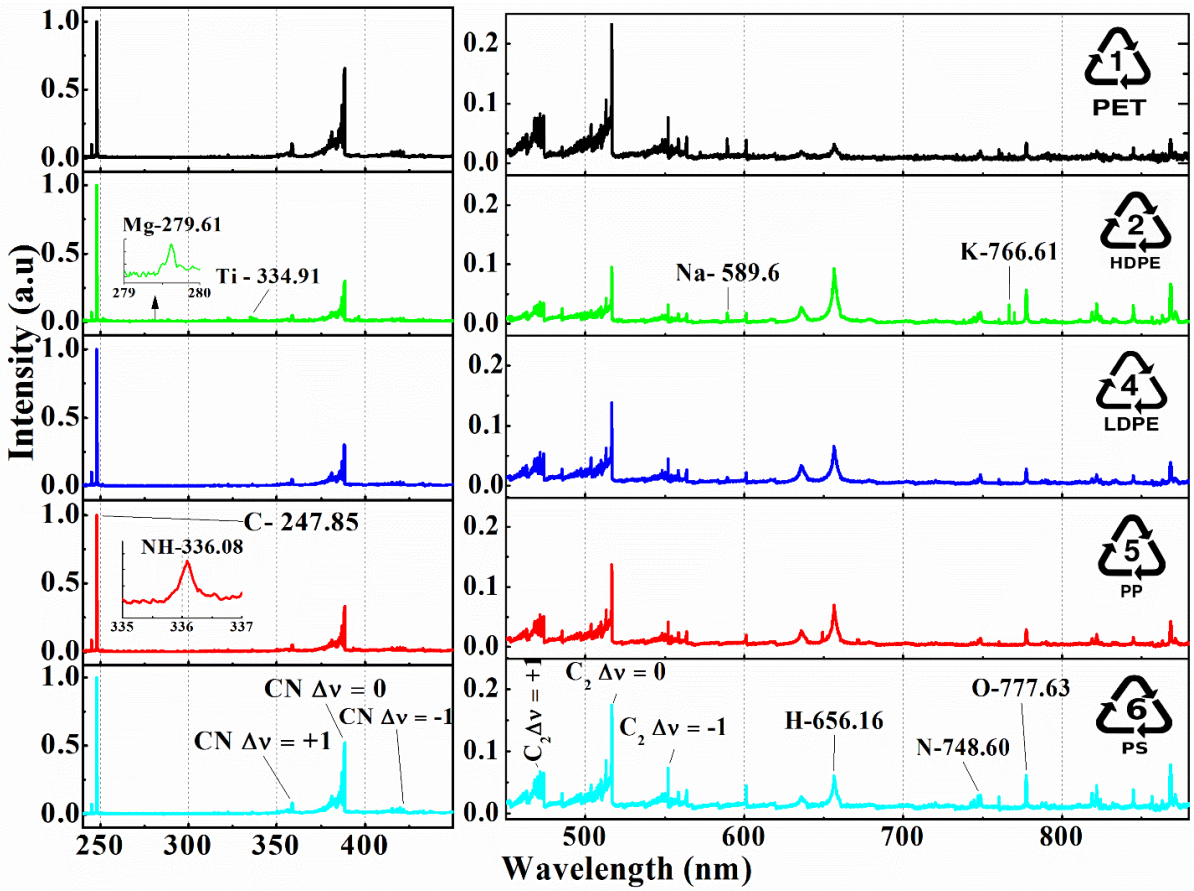

Fig. 6.2. Fs-LIBS spectra of the five plastics. The number in the triangle represents the respective recycling codes.

The prominent spectral features are depicted in Fig. 6.2 and their corresponding wavelengths are presented in Table 6.1. The number inside the triangle in Fig. 6.2 represents the standard recycling number of plastic. The atomic lines of Ti were also observed in all the samples. The metallic elements of Ti, Ca, Na, and K are commonly utilized as additives for improving the mechanical and physical properties along with the aim of reducing their cost [45]. CN ($\Delta v=0$) molecular band head at 388.37 nm had the strongest intensity next to the carbon and followed by C_2 ($\Delta v=0$) Swan band head at 516.56 nm, and other atomic transitions of hydrogen, oxygen, and nitrogen. In total, a seven molecular band systems were observed in which three corresponds to CN violet band system [CN ($\Delta v=+1, 0, -1$)] and three corresponds to C_2 Swan band system [C_2 ($\Delta v=+1, 0, -1$)], and the last one is NH (336.08 nm) molecular emission[46]. It is evident

from Fig. 6.2 that intensities of C_2 and CN band heads ($\Delta v=0$) are observed to be varying from sample to sample. PET and PS have shown higher intensities of C_2 ($\Delta v=0$) molecular band head at 516.56 nm in contrast to other samples which could be attributed to the presence of native C=C linkages (aromatic rings)[6].

Table 6.1. The emission lines observed in the fs-LIBS spectra of the five samples. # represents the band head wavelength. *Lines/Bands used for the ANN input.

Atomic species	Emission lines (nm)	Molecular species	Emission lines (nm)
C	247.85*	CN ($\Delta v=0$)*	385.13, 385.50, 386.21, 387.19, 388.37 (0-0)#
H	656.36*	CN ($\Delta v=+1$)	358.45, 358.62, 359.08 (1-0)#
O	777.63*, 844.84*	CN ($\Delta v=-1$)	415.87, 416.80, 418.13, 419.75, 421.61 (0-1)#
Na	589.12*, 589.71*	C_2 ($\Delta v=0$)*	509.83, 512.96, 516.56 (0-0)#
Mg	279.61*, 280.27, 285.26	C_2 ($\Delta v=+1$)	467.86, 468.55, 469.80, 471.54, 473.73 (1-0)#
K	766.64*, 770.13	C_2 ($\Delta v=-1$)	554.11, 558.58, 563.62 (0-1)#
N	742.65*, 744.43*, 747.09*, 818.67, 821.78, 824.49, 868.32*	C_2 ($\Delta v=+2$)	436.52, 437.22, 438.17 (3-1)#
Ti	334.98*, 363.36, 364.35, 365.42	NH ($\Delta v=0$)*	336.08

The CN molecular band head intensity in PET and PS is also strong as shown in Fig. 6.2. The higher intensity of this could be due to the recombination of the C_2 radicles or atomic carbon in the plasma with the omnipresent nitrogen [7, 8, 47]. Our observations are consistent with the previous LIBS studies on the polymers and other organic compounds[7, 8]. Further, the entire analysis was done by using the normalized data.

6.3.1.b Ratiometric analysis

The analysis performed here is similar to the analysis reported in chapter 4, section 4.4.2. It utilizes the intensity ratios of two spectral lines (carbon and hydrogen). As discussed earlier, all the five plastics inherently contain the carbon and hydrogen in their molecular structure and their stoichiometric ratio can be used as a marker to identify the plastics. The correlation among the actual to measured intensity ratios of the samples was fitted to a straight line ($y = mx + c$) as shown in Fig. 6.3. It is well correlated with the straight-line

approximation (Pearson's r = 0.97). It is noticed that the actual ratios are matching with the measured intensity ratio for all the samples except for the PET, in case of PET is slightly deviated from the actual value. It could be possible due to the following scavenging reactions

$$C_2 + O \rightarrow CO + C \quad (6.1)$$

$$C_2 + O_2 \rightarrow 2CO \quad (6.2)$$

PET contains the native oxygen atoms in their molecular structure and the reaction between the C_2 with oxygen can lead to the emission of the carbon line as given equation 6.1 and enhances the carbon line intensity. Further, it is evident from Fig. 6.3, five samples can be classified into three categories with their C/H value.

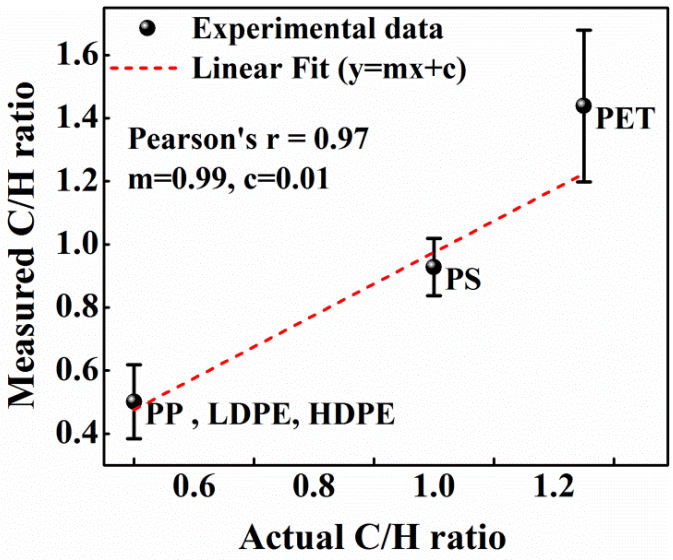

Fig. 6.3. The correlation between the actual C/H ratios to the measured intensity ratios.

The polyolefins (PP, LD, and HD) as one group (0.37-0.62) and remaining are two can be considered as two groups PS (0.82-1), and PET (1.21-1.69). However, this correlation can't able to classify the LD, HD, and PP due to sharing the same C/H value. In the next sections, C, CN, C_2 emissions are explored for the correlation.

6.3.1.c Correlation between C-C bonds to C, C2 and CN line intensities

Only PET and PS contain the native C_2 bonds and CN bonds are absent in all the samples, hence only C-C bonds are utilized for the correlation. The intensities of C, C_2 ($\Delta v = 0$), and

CN (Δv=0) emission lines are correlated with the no of C-C bonds present in the sample as shown in Fig. 6.4(a-c) respectively. The intensity of the carbon (C-247.85 nm) line has not shown variation with the no of C-C bonds whereas a linear positive correlation noticed for the C_2 and CN emissions. In the case of the carbon line, the intensities are almost constant for all the samples except for PET, where it has shown higher intensity. As discussed earlier, the native oxygen present in the PET increases the carbon line emissions (see equation 6.1 & 6.2). Further, it has the highest number of carbon atoms compared to all the samples which can lead to an increase in carbon line intensity.

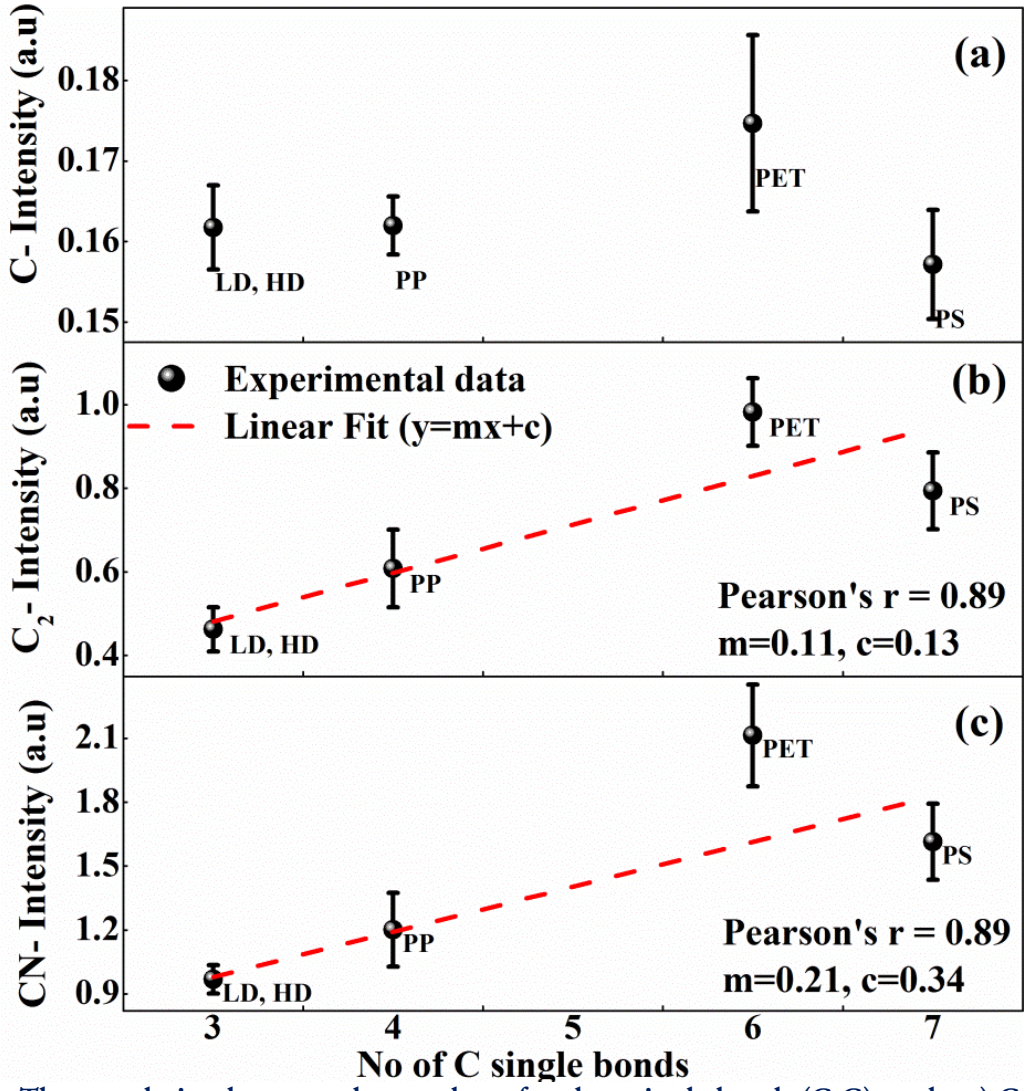

Fig. 6.4. The correlation between the number of carbon single bonds (C-C) to the a) C-2478.5 nm line intensity, b) C_2 (Δv=0) band intensity, and c) CN (Δv=0) band intensity.

In the case of ns LIBS, an increase in carbon line intensity is observed due to the atomization which has resulted in a decrease of intensities of molecular emissions (See Fig. 4.12 in chapter 4). Here, the intensities of molecular emissions are increased with no of C-

C bonds, and the correlation is fitted for the straight line as shown in Fig. 6.4(b & c). It can be understood from the following equations[8]

$$C + N + M \rightarrow CN + M \quad (6.3)$$

$$C + N_2 \rightarrow CN + N \quad (6.4)$$

$$C + C + M \rightarrow C_2 + M \quad (6.5)$$

The carbon species in the plasma can react with nitrogen and carbon species and leads to the formation of the CN and C_2 radicals as given equations (6.3 to 6.5). Fs LIBS offers the formation of a lower temperature of plasma compared to ns LIBS and leads to the molecular formation in contrast to the atomization. Similar observations were reported where; atomic line intensities are stronger in the case of ns LIBS and molecular emissions are predominant in fs LIBS[5, 7].

6.3.1.d 2D scatter plot analysis

The details of the 2D scatter approach are given in chapter 2 (section 1.4.1). Carbon and hydrogen are the common elements present in all the five samples and C_2 linkages/bonds inherently present in PS and PET. In addition, the spectral emissions of the CN and C_2 bands are influenced by the molecular structure and the ambient atmosphere. Consequently, the atomic lines of C-247.85, H-656.36, along with the molecular CN and C_2 bands are exploited for the 2D correlation. Initially, all the atomic lines are fitted for the Lorentzian function using MATLAB and obtained the area under the curve (considered as the intensity of the line). For CN and C_2 molecular bands, the sum of the intensities of the $\Delta v = 0, +1, -1$ transition were considered. The relative standard deviation (RSD) of the spectral intensity of carbon atomic transition (obtained from the thirty trails of each sample) was observed to be less around ~ 2-6 % while the RSD of hydrogen, CN, and C_2 bands is around ~ 5-11 %. A total of six combinations of 2D plots (C-H, C-CN, C-C_2, H-CN, H-C_2, and CN-C_2) are possible for the four spectral features (C, H, CN, and C_2) and the same are presented in Fig. 6.5(a) to Fig. 6.5(f). Each point in the graph is a representative of one spectrum. First three combinations involve the carbon as one of the components on x-axis and H, C_2 and CN are in combination with carbon respectively as shown in Fig. 6.5(a) to Fig. 6.5(c) respectively. A least square fitting method has been

employed to find the best fit of the ellipse for the scattered data of each sample as shown in Fig. 6.5(a) to Fig. 6.5(f). All the clusters were well fitted for the ellipse with a confidence of 95 %. Further, a numerical parameter, residual discriminatory region (RDR) has been defined (see section 1.4.1, chapter 1) for the quantitative evaluation of the discriminatory power of a 2D scatter plot [48].

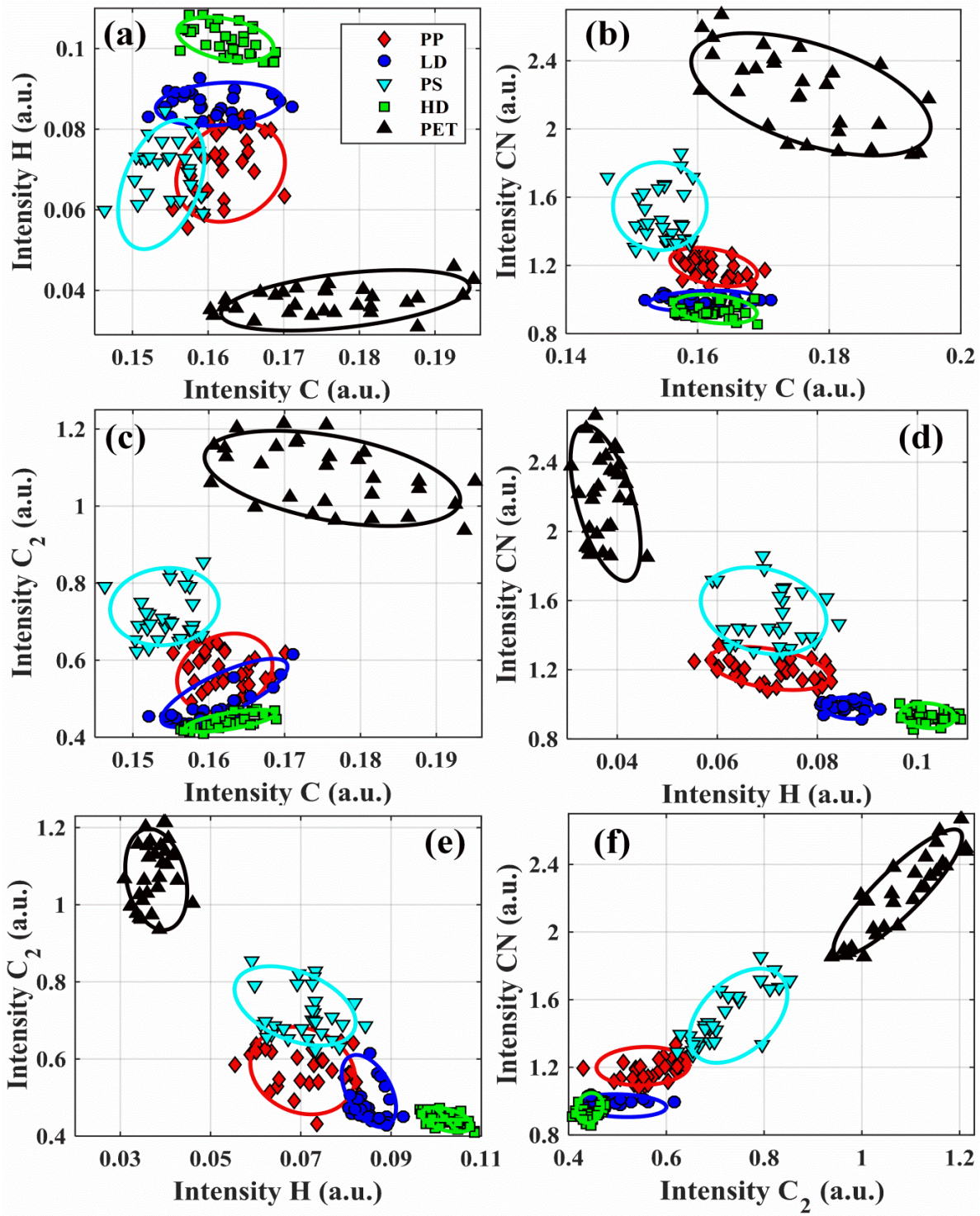

Fig. 6.5. The 2d correlation plots of the plastics with different combinations. (a) C-H and (b) C-CN, (c) C-C_2, (d) H-CN, (e) H-C_2, and (f) C_2-CN.

The RDR values determined from the aforementioned six combinations of 2D plots are presented in Table 6.2.

Table 6.2. RDR values measured for the 2D scatter plots.

S.No	Spectral features	LD & HD	PS & PP	PS & LD	PP & LD
1	C-H	0	0.33	0.02	0.01
2	C-CN	1.01	0	0	0
3	C-C_2	0.10	0	0	1.15
4	H-CN	0	0.07	0	0
5	H-C_2	0	0.11	0	0.19
6	C_2-CN	0.88	0	0	0

All the combinations have shown good separation among the samples. However, LDPE and HDPE have interfered for three combinations viz., C-CN, C-C_2, and C_2-CN. PET is well separated from the rest of the samples in all the combinations. It could be possible due to the maximum number of the carbon, hydrogen atoms present in it contrary to other samples. The scatter plot employing the atomic lines of C and H is shown in Fig. 6.5(a) where a slight overlap has been noticed among the PS and PP which corresponds to the RDR of 0.33. The scatter plot of CN and C_2 intensities have shown a linear correlation as shown in Fig. 6.5(a). The linear correlation can be understood from the following equations.

$$C_2 + N \rightarrow CN + C \quad (6.6)$$

$$C_2 + N_2 \rightarrow 2CN \quad (6.7)$$

The nitrogen presents in the ambient atmosphere can react with the C_2 radicals in the plasma and results in the formation of CN molecular bonds as given in equations (6.6 & 6.7). i.e. increase in C_2 species can increase CN emissions. Further, as mentioned earlier, PS and PET have shown maximum C_2 and CN intensities as it contains native C_2 linkages in itself. The H - CN scatter plot is well discriminated all the samples however, a negligible overlap (RDR ~ 0.07) has noticed among the PS and PP. Overall, the three combinations (H-CN, C_2-CN, and C-CN) have shown promising results for the discrimination of the samples which accounts for only ~ 6 % of the total data

6.3.1.e PCA analysis

PCA demonstrates the classifying capability by correlating dominant spectral features with the output PCs. No data pre-processing was done except the normalization (normalized to the C-247.85 nm line) which minimizes the fluctuations in data. The CN, C_2 molecular bands systems are the prominent spectral features contributing to the first PC as shown in the loadings plot in Fig. 6.6(a). Carbon, nitrogen, oxygen, sodium, titanium, and magnesium lines are prevailed in second and the third PCs. The carbon atomic line is observed in all the PCs, but it is more pronounced in the 2nd and 3rd PCs. The 3D score plot of the first three PCs is shown in Fig. 6.6(b).

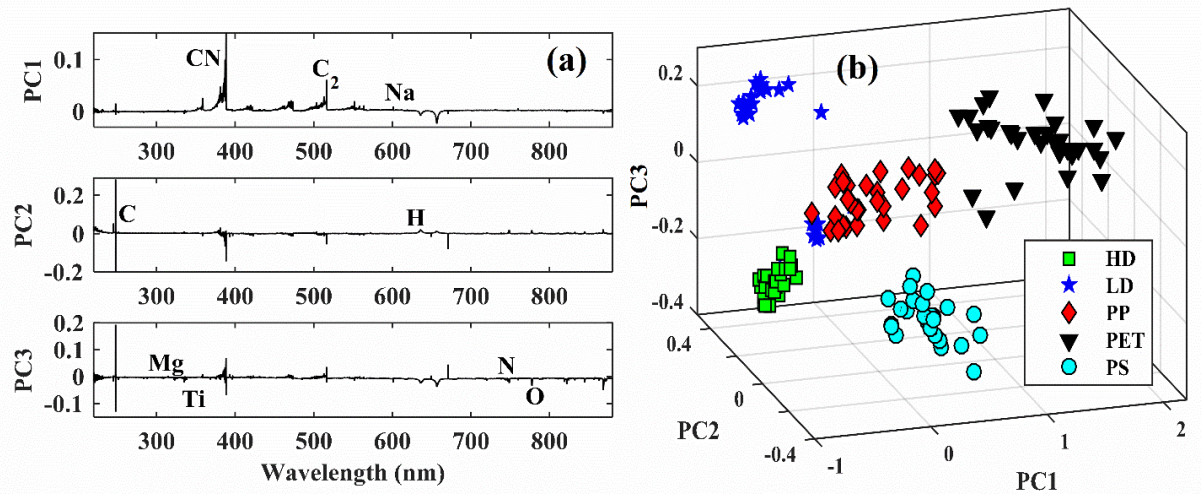

Fig. 6.6. a) Loadings plot of the first three PCs of the plastics. All the spectral features are represented at their characteristic wavelengths. (b) Score plot of the first three PCs.

Excellent segregation among all the samples has been achieved as shown in Fig. 6.6(b). However, a very slight overlap has been noticed between the PP and LD. The first three PCs individually explain the variance of 77.2, 5.3, & 4.7 % respectively and five PCs together account for the 92 % of net variance present in the data. It is evident from Fig. 6.6 (b) that the PCA has successfully differentiated all the samples with well-separated clusters from each other. ANN is employed in next the sections for the labeling of plastics.

6.3.1.f ANN analysis

The details of the ANN architecture can be found in chapter 1 (section 1.4.3). The number of neurons is optimized for better performance and fifteen are found to be optimum.

Selecting the proper spectral input to chemometric/multivariate methods reduces the complexity of the neural network and computing time [49, 50]. For the present analysis, five spectral windows (W1-W5) comprising of different spectral lines have been chosen as given in Table 6.3. The spectral lines (wavelengths) of each element used for the ANN are given in Table 6.1 with a star (*) mark, for example, in the case of magnesium Mg I 279.61 nm. For CN and C_2 molecular bands, only the lines involving in $\Delta v=0$ transitions have been used.

Table 6.3. Different spectral regions of the data used for the ANN model.

S No	Spectral region	Data (%)
W1	Total data	100.0
W2	C and H lines	2.5
W3	C, H, N, O, Ti, Mg, Na and K lines	5.5
W4	C, H, N, O lines, NH, CN and C_2 bands	7.7
W5	C, H, N, O, Ti, Mg, Na, K lines, NH, CN and C_2 bands	8.3

The aforementioned five spectral features (W1-W5) are fed to ANN one after another, and the performance is evaluated. Initially, the input dataset was divided into training, validation, and testing sets which correspond to 70, 15, and 15 % of the input dataset respectively. For each spectral window, ANN has been performed for 100 iterations. In each iteration, the ANN algorithm randomly chooses the data for the training, validation, and testing. The ANN results obtained from the W5 spectral window are shown in Table 6.4. The correct identification rates of all the samples achieved through ANN is more than 99 % except for LD. HD, PET plastics are 100 % identified correctly and the identification of PP is close to 100 % (99.7 %).

Table 6.4. Confusion matrix of obtained by ANN analysis W5 as the input.

		Predicted labels				
		LD	HD	PP	PET	PS
Reference labels	LD	97.77	1.27	0.60	0.00	0.36
	HD	0.00	100.00	0.00	0.00	0.00
	PP	0.00	0.30	99.70	0.00	0.00
	PET	0.00	0.00	0.00	100.00	0.00
	PS	0.07	0.73	0.00	0.00	99.20

LD is slightly miss-identified as HD which could be a possible outcome of a similar chemical structure. The average correct classification rate (ACCR) for each input is obtained from the mean of the five diagonal elements of the confusion matrix. The ACCR obtained for W5 is 99.3. A similar analysis has been done for the remaining inputs (W1-W4) and the obtained ACCR is given in Table 6.5.

Table 6.5. The average correct classification rate obtained for five spectral inputs and their testing time

S No	Data (%)	ACCR (%)	T (mS)
W1	100.0	97.5	14.96
W2	2.5	97.3	2.71
W3	5.5	98.4	4.08
W4	7.7	98.9	4.09
W5	8.3	99.3	4.38

The four spectral windows except the first one (W1), constitute less than 10 % of the total data nevertheless better classification was achieved over the total data (100 %) utilized. It is also worth mentioning that, the W2 spectral window, which is only 2.5 % of the total data, has exhibited equal performance as of the total data. This could be possible due to the minimal influence of the ambient atmosphere along with the inherence presence of C and H atoms in all the samples. The other spectral windows are the combinations of the various atomic lines and molecular band systems considered from the literature dealing with the identification of plastics exploiting ANN[49]. Maximum identification accuracies ~ 99.3 % were achieved for the W5 spectral window as given in Table 6.5. This could be attributed to the utilization of the selective spectral features of atomic and molecular lines correspond to the 8.3 % of the overall data. Further, it is noticed that the testing time is reduced by 3-5 times compared to the total data as input. These results clearly demonstrate that 100 % identification accuracies can be achieved with ANN combined with fs-LIBS.

In the next sections results of the filamentation LIBS (FIBS) studies of Cu are presented. It presents the characterization of the FIBS Cu plasma produced by different filament intensities.

6.3.2 Filamentation LIBS (FIBS) studies of Cu

Filamentation is a result of a dynamic interplay between the self-focusing of the laser beam due to the optical Kerr effect and the defocusing of the plasma generated through multi-photon or tunnel ionization process of air molecules. In principle, the fs laser pulse self-focuses when its power exceeds the 'critical power' (P_{cr})

$$P_{cr} = \left(\frac{3.72\lambda^2}{8\pi n_0 n_2} \right) \tag{6.8}$$

Where n_o and n_2 are the linear and non-linear refractive indices respectively, λ is the laser wavelength. By considering the excitation wavelength of 800 nm, the estimated P_{cr} in air is 3 GW[51]. The power utilized in the current experiment is ~40 GW which exceeds P_{cr}.

6.3.2.a Description of spectral lines

The FIBS spectra acquired for the Cu target irradiated by the three parts of the filament for the 50 cm focal length lens is shown in Fig. 6.7. It represents the spectral features in the window of 323-590 nm. All the prominent spectral lines were indicated at their characteristic wavelengths. The spectral transitions at 324.79 and 372.46 nm are strongly self-absorbed irrespective of the irradiating conditions.

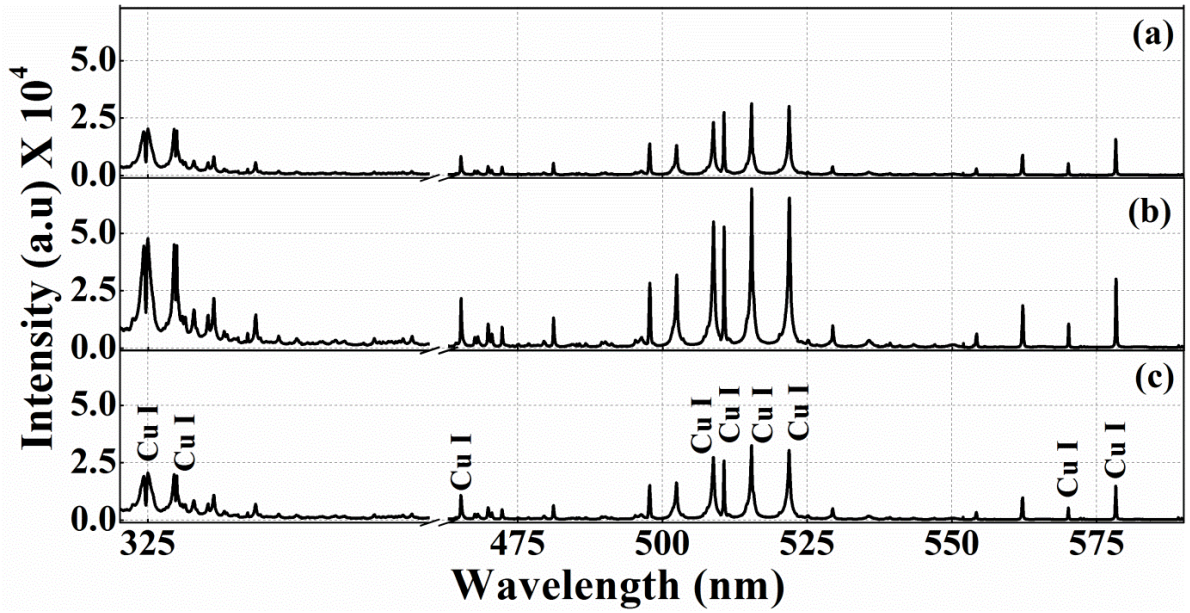

Fig. 6.7. The LIBS spectra acquired at three different parts of the filament produced by the 50 cm focal length lens. a, b, and c correspond to the leading edge, central position, and the trailing edge of the filament respectively.

The emission intensities of the spectral lines have shown significant changes when the Cu plasma produced by the different parts of the filament. Most of the emission features are neutral transitions lines of the Cu plasma. Similar observations were noticed in the previous studies where the FIBS spectra predominantly provide neutral emissions due to the absence of plasma reheating [52, 53]. The signal strength is observed maximum for sample irradiated by the central part of the filament and it is almost double to the intensity when exposed by the leading and trailing part of the filament as shown in Fig. 6.7. The results were almost similar (spectra is not shown here) when the sample interrogated by the filaments produced by the other two lenses of focal lengths 100 cm and 200 cm. The prominent spectral lines viz., 465.11, 510.55, 515.32, and 521.82 nm were fitted for the Lorentzian function and extracted the area (considered as the intensity for the further analysis), width and height of the peaks. Fig. 6.8 represents the bar plot of the intensities of the four spectral lines for three different filaments.

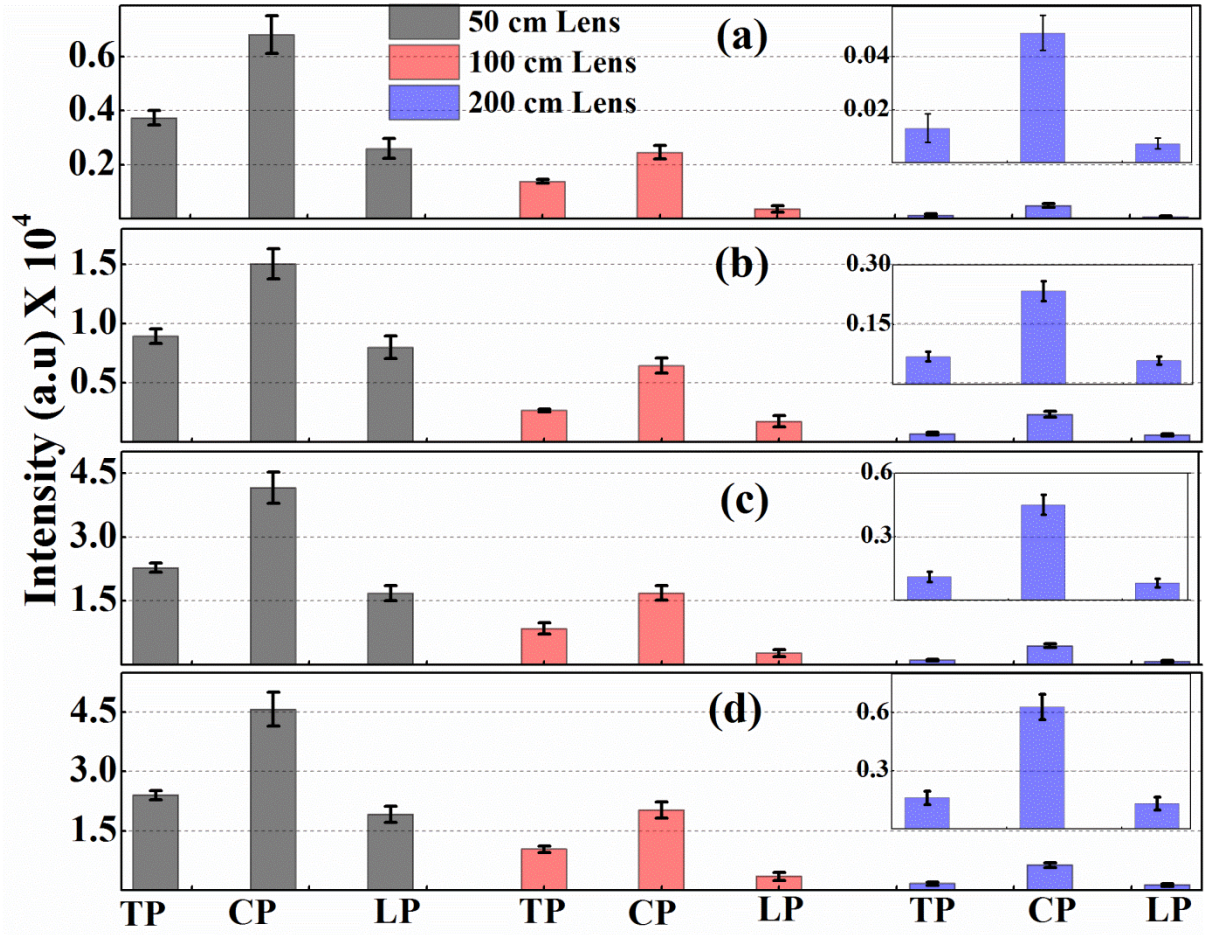

Fig. 6.8. The bar plot of the intensities of the four spectral lines. a) 465.11 nm b) 510.55 nm c) 515.32 nm d) 521.82 nm. The figure in inset represents the close view of the intensities obtained for a 2 m focal length lens.

TP, CP, and LP in Fig. 6.8 correspond to the Cu target exposed with the trailing part/edge leading part, central position, and the of the filaments respectively. It is evident from Fig. 6.8, the spectral line intensities are higher when Cu target is at the central part of the filament than the either ends, and it is observed for three different lenses and for remaining spectral lines. It is also noticed that the spectral intensities at the trailing edge of the filaments are always higher in comparison to the leading edge of the filaments. This is in line with the reports that the trailing edge of the filament has enhanced intensities in comparison with the leading stage of the filament[54].

The significant changes in emission line intensities along the filament channel can be linked to variation in plasma properties[53].

$$I_{ij} = \frac{N_o hcg_i A_{ij}}{\lambda_{ij} Z(T)} \exp\left(-\frac{E_i}{k_B T}\right) \tag{6.9}$$

All the symbols have their usual meaning (see chapter 3, section 3.2.2).

As seen from equation (6.9), the intensity of a particular spectral transition/line depends on the temperature of the plasma and the number density of emitting species. Both of these parameters are crucial to characterize the plasma and are highly transient in nature. Hence, the density and temperature measurements were performed at different positions along the filament.

6.3.2.b Measurement of plasma temperature

The plasma temperature is estimated from the Boltzmann plot method. The following spectral lines at 465.11, 510.55, 515.32, and 521.82 nm are utilized for estimating the plasma temperature[55]. All the remaining spectroscopic parameters are taken from the literature[55]. The temperatures estimated for the three lenses are shown in Fig. 6.9(a). It has been clearly visualized in Fig. 6.9(a) that the measured plasma temperature is varying with the different parts of the filament channel. The variation is ~9200-10700, 8300-9800, and 7500-9100 K for the filaments produced with the 50, 100, and 500 cm focal length lenses respectively. It has been found that the estimated plasma temperatures are linearly decreasing with increasing the focal length of the lens as shown in Fig. 6.9(b) which can be understood as follows. The filament intensity decreases with increasing the focal length of

the lens. In the case of higher focal length, the photon density is low and, the interaction is weak compared to the focusing with short focusing condition. Hence, it results in the formation of the filament with less temperature and vice-versa.

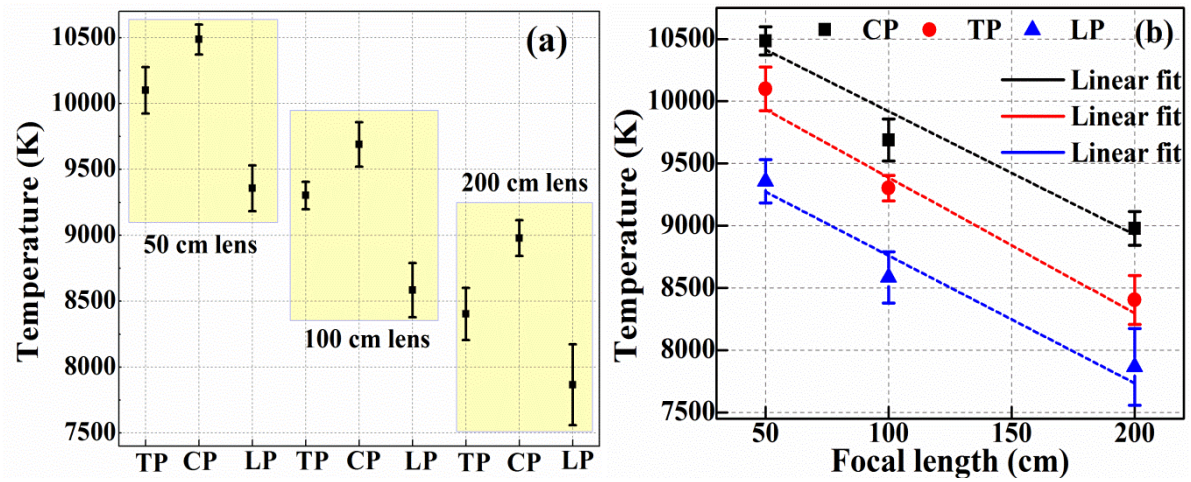

Fig. 6.9. a) The estimated plasma temperature for the different parts of the three filaments. The boxes in the figure help to visualize the variation of the plasma temperature at three different points along the length of the filament. b) A linear fit of the plasma temperature with the focal length of the lenses.

The plasma generated with the interaction of the leading edge of the filament with the Cu target has shown minimum temperature compared to the other two positions. Further, the central part has shown maximum temperature and similar observations were noticed for the remaining filaments of different lengths, generated with different focusing lenses. These results suggest that the intensity measurements can be correlated with corresponding plasma temperature. According to the Boltzmann distribution, the increase in temperature leads to the excite the more number of species/atoms into a particular excited energy level and populates it. Further, the de-excitation of the atoms results in higher intensity for that respective spectral transition. The same observation is noticed in our present investigation where the temperatures are highest for the ablation with the central part of the filament and resulted in the emission of spectral lines with maximum intensity. A similar performance is noticed for all the spectral features and also for all the three focusing lenses. The electron density measurements were performed in the next sections.

6.3.2.c Estimation of electron density

The electron density measurements have been performed for all the filaments. Stark broadening method is utilized for the estimation of the electron density. The Cu spectral line transition at 510.57 nm is used and the corresponding electron impact width parameter obtained from the literature [55]. The electron densities estimated for all the filaments are shown in Fig. 6.10.

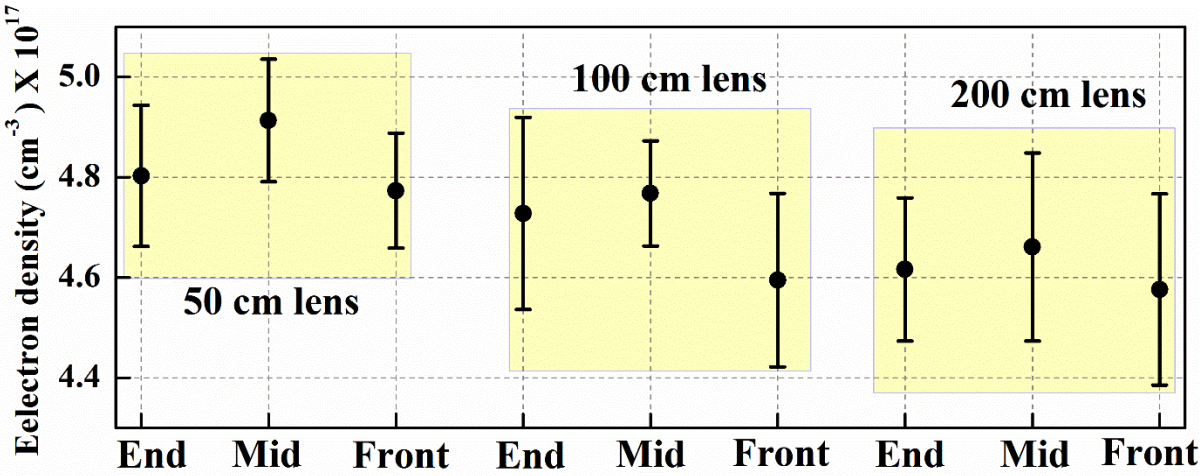

Fig. 6.10. The electron density measured for the three filaments.

It has been found that the electron densities are in the same order (10^{17}/ cm^3), however with slight variations for one filament to another. It is also observed that the variation in electron density between the ends of the filament to the center of the filament reduces with increasing focal length, this is due to increased intensity clamping as we progress towards higher focal length. The energy in the core of the filament is continually replenished by the surrounding energy reservoir of the filament while the peak intensity in the filament is restricted by the plasma formation, resulting also in the prolonged propagation of the filament. Both the electron density (Fig. 6.10.) and temperature measurements (Fig. 6.9) are performed with the FIBS spectral data collected in time-integrated mode and are highly dynamic. Thus the numerical values are given in Fig. 6.9 and Fig. 6.10 should be considered as the average temperature and density during the evolution of the plasma lifetime. However, the change in spectral line intensity is significant compared to the electron density. It can be possible due to the variation in

plasma persistence time. Further, to explore this observation, the time evolution studies were performed in the next sections.

6.3.2.d Time evolution studies

The temporal evolution of the FIBS spectra were recorded and analyzed in the time window of 0.02-1.82 µs. The kinetic evolution of the FIBS spectra (510 -524 nm region) acquired at the central part of filament produced with the 50 cm lens is illustrated in Fig. 6.11(a). After the formation of the plasma, as time progresses, the plasma decays and expands into the surrounding atmosphere[56]. As a result, the intensity of spectral lines gradually decreases with the delay time as shown in Fig. 6.11(a). Maximum intensities were observed at the initial dealy, and it decayed continuously with increasing the delay time. Fig. 6.11 (b) visualizes the decay of the 521.82 nm spectral transition. The intestines are fitted for the exponential decay function and obtained the plasma persistence times. Symbols represent the actual data and solid line corresponds to the exponential fit. The error bar represents the standard deviation of the ten trails at each position.

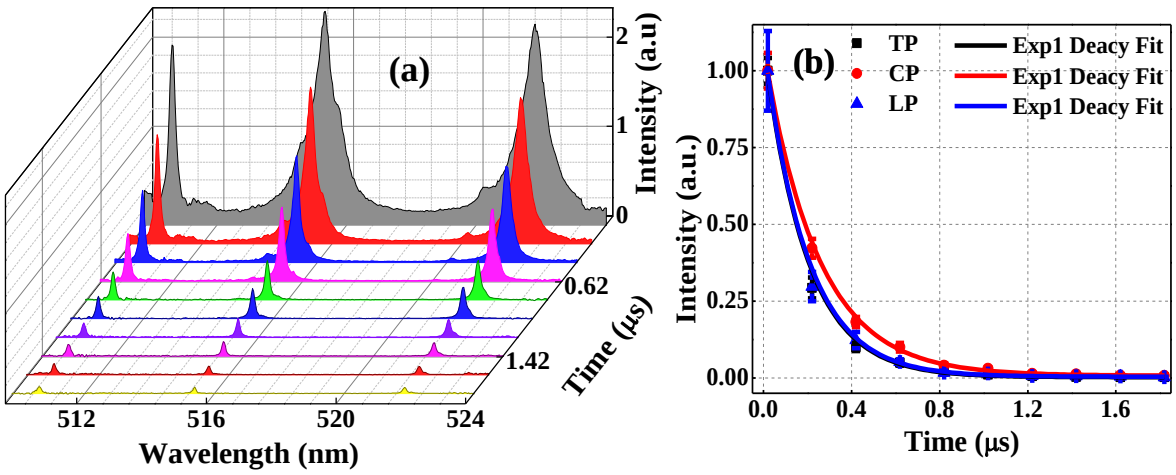

Fig. 6.11. a) The time evolution Cu FIBS spectra. The spectra recorded at the middle part of the filament in the time window of 0.02-1.82 *µs*. b) The kinetic evolution of the Cu-521.82 nm spectral line for the Cu target exposed by three different parts of the filament. Both the figures correspond to the filament produced by a 50 cm focal length lens.

The spectra acquired with the central part of the filament persists for a longer time compared to the other two positions as shown in Fig. 6.11 (b). The intensity decay for the Cu-521.82 nm is almost similar for the leading and trailing edge of the filament. The

intensity is drastically decreased to 44 % of the initial intensity in the first 0.2 μs for the central part of the filament and further decays slowly to zero in the 1 μs. In the case of irradiation with the leading and trailing edge of the filaments, it is decayed to 30 % of the initial intensity. The intensities are approximately the same and approach zero in the time window of 1.22 - 1.82 µs irrespective of the focusing conditions. Similarly, the analysis has been performed to the other two filaments and obtained the decay constants. Fig. 6.12(a) represents the decay constants estimated for the Cu -521.82 nm line for the three different filaments.

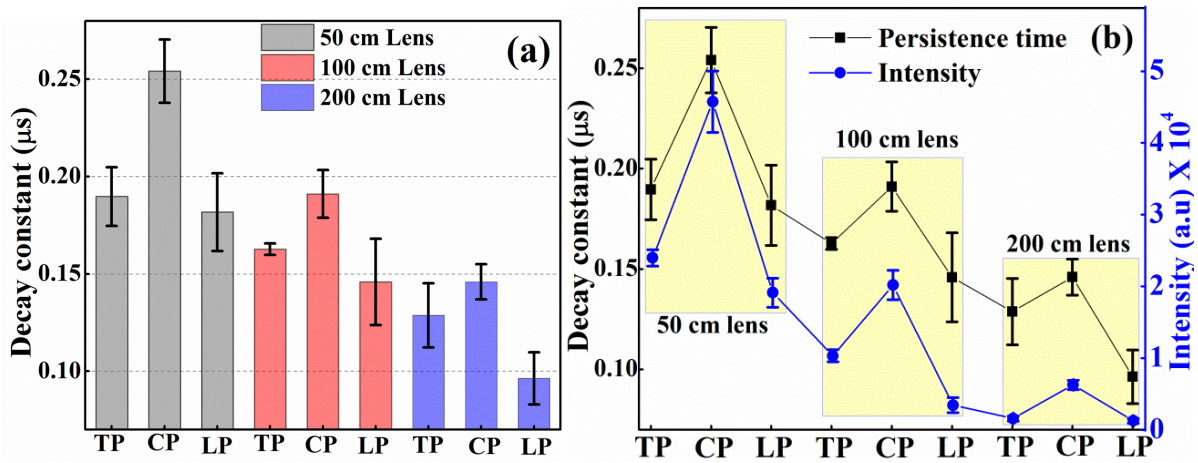

Fig. 6.12. a) Representation of the decay constants /persistence time obtained for the 521.82 nm line for three positions of each filament. b) Correlation between the persistence time and spectral line intensity.

A similar trend has been exhibited for the other spectral lines thus not shown here. It has been noticed that the plasma is persisting for a longer time when the target exposed with the filaments generated by a lower focal length lens. The persistence time decreasing linearly with increasing the focal length. This could be attributed to the decrease in irradiance/fluence with an increase in the focal length of the lens. Also, it is observed that plasma persists for a longer time when irradiated with the central part of filament in contrast to the other two ablation conditions. The higher persistence can results in the emission with a maximum intensity which is exactly resembled intensity measurement as shown in Fig. 6.12 (b). It is envisioned from Fig. 6.12 (b) the higher plasma persistence time resulted in higher spectral line intensity and vice-versa.

These results suggest that the irradiation with a different part of the filaments have different properties and lead to the variation of the emission line intensities.

6.4 Summary

In this work, the post-consumer plastics obtained from a local recycling unit were examined and identified using the fs-LIBS technique combined with multivariate analysis. Strong CN, C_2 molecular bands and C, H, N, O atomic lines were observed. The differences in the intensities corresponding to prominent spectral features were utilized for drawing 2D scatter plots. The pairs of H-CN and CN-C_2, have shown good separation. Besides that, excellent separation of the samples with an efficient clustering has been demonstrated with the aid of PCA which was prominently aided by strong molecular features in the spectra. A three-layer ANN analysis has been performed with the different selected spectral features as the input. The combination of spectral window input involving atomic and molecular features has shown correct identification rates up to 100 %. Achieving identification rates up to 100 % greatly helps in increasing the quality of the final recycled plastics. The use of fs pulses particularly favors the formation of molecular species and also minimizes the atmospheric contribution to the plasma, which greatly increases the identification accuracies obtained by multivariate analysis. Further, the characterization of the Cu plasma generated by the fs filaments with three different intensities was demonstrated. The measurements were carried out by exposing the Cu target at three different positions of each filament. It is revealed that the intensities are strong at the central part of the filament compared to either ends. These observations are attributed to the changes in the plasma properties where the plasma temperature is maximum for the central part of the filaments. Moreover, it is noticed that the plasma persisted for a longer time when it is generated with the central part of the filament.

6.5 References

1. B.N. Chichkov, C. Momma, S. Nolte *et al.*, "Femtosecond, picosecond and nanosecond laser ablation of solids", Applied Physics A, 63, **1996**.
2. T. Gunaratne, M. Kangas, S. Singh *et al.*, "Influence of bandwidth and phase shaping on LIBS with ultrashort laser pulses", Chemical Physics Letters, 423, **2006**.
3. M. Baudelet, J. Yu, M. Bossu *et al.*, "Discrimination of microbiological samples using femtosecond LIBS", Applied physics letters, 89, **2006**.
4. M. Baudelet, L. Guyon, J. Yu *et al.*, "Spectral signature of native CN bonds for bacterium detection and identification using fs LIBS", Applied Physics Letters, 88, **2006**.
5. E.N. Rao, P. Mathi, S.A. Kalam *et al.*, "Femtosecond and nanosecond LIBS studies of nitroimidazoles: correlation between molecular structure and LIBS data", Journal of Analytical Atomic Spectrometry, 31, **2016**.
6. S. Gregoire, M. Boudinet, F. Pelascini *et al.*, "Laser-induced breakdown spectroscopy for polymer identification", Anal Bioanal Chem, 400, **2011**.
7. S.A. Kalam, N.L. Murthy, P. Mathi *et al.*, "Correlation of molecular, atomic emissions with detonation parameters in femtosecond and nanosecond LIBS plasma of high energy materials", Journal of Analytical Atomic Spectrometry, 32, **2017**.
8. S. Mousavi, M.H. Farsani, S. Darbani *et al.*, "CN and C 2 vibrational spectra analysis in molecular LIBS of organic materials", Applied Physics B, 122, **2016**.
9. Y. Dikmelik, C. McEnnis, and J.B. Spicer, "Femtosecond and nanosecond laser-induced breakdown spectroscopy of trinitrotoluene", Optics Express, 16, **2008**.
10. T.A. Labutin, V.N. Lednev, A.A. Ilyin *et al.*, "Femtosecond laser-induced breakdown spectroscopy", Journal of Analytical Atomic Spectrometry, 31, **2016**.
11. A.W. Schill, D.A. Heaps, D.N. Stratis-Cullum *et al.*, "Characterization of near-infrared low energy ultra-short laser pulses for portable applications of laser induced breakdown spectroscopy", Optics Express, 15, **2007**.
12. F.C. De Lucia Jr, J.L. Gottfried, C.A. Munson *et al.*, "Multivariate analysis of standoff LIBS spectra for classification of explosive-containing residues", Applied optics, 47, **2008**.
13. S. Wallin, A. Pettersson, H. Östmark *et al.*, "Laser-based standoff detection of explosives: a critical review", Analytical and bioanalytical chemistry, 395, **2009**.
14. R. Junjuri, A. Prakash Gummadi, and M. Kumar Gundawar, "Single-shot compact spectrometer based standoff LIBS configuration for explosive detection using artificial neural networks", Optik, 204, **2020**.
15. J.L. Gottfried, F.C. De Lucia, C.A. Munson *et al.*, "Standoff detection of chemical and biological threats using LIBS", Applied spectroscopy, 62, **2008**.
16. A.K. Shaik, N.R. Epuru, H. Syed *et al.*, "Femtosecond laser induced breakdown spectroscopy based standoff detection of explosives and discrimination using principal component analysis", Optics express, 26, **2018**.
17. H.L. Xu, and S.L. Chin, "Femtosecond laser filamentation for atmospheric sensing", Sensors, 11, **2011**.
18. J. Kasparian, and J.-P. Wolf, "Physics and applications of atmospheric nonlinear optics and filamentation", Optics express, 16, **2008**.

19. J. Laserna, R.F. Reyes, R. González *et al.*, "Study on the effect of beam propagation through atmospheric turbulence on standoff nanosecond laser induced breakdown spectroscopy measurements", Optics express, 17, **2009**.
20. M. Singh, D. Gupta, and H. Suk, "Efficient second-and third-harmonic radiation generation from relativistic laser-plasma interactions", Physics of Plasmas, 22, **2015**.
21. H. Xu, G. Méjean, W. Liu *et al.*, "Remote detection of similar biological materials using fs filament-induced breakdown spectroscopy", Applied Physics B, 87, **2007**.
22. J. Kasparian, M. Rodríguez, G. Méjean *et al.*, "White-light filaments for atmospheric analysis", Science, 301, **2003**.
23. C. D'Amico, A. Houard, M. Franco *et al.*, "Conical forward THz emission from femtosecond-laser-beam filamentation in air", Physical review letters, 98, **2007**.
24. N. LaHaye, S. Harilal, P. Diwakar *et al.*, "Characterization of laser ablation sample introduction plasma plumes in fs-LA-ICP-MS", Journal of Analytical Atomic Spectrometry, 29, **2014**.
25. E. Gurevich, and R. Hergenröder, "Femtosecond laser-induced breakdown spectroscopy: physics, applications, and perspectives", Applied spectroscopy, 61, **2007**.
26. S.L. Chin, "Femtosecond laser filamentation", Springer**2010**.
27. K. Stelmaszczyk, P. Rohwetter, G. Méjean *et al.*, "Long-distance remote LIBS using filamentation in air", Applied Physics Letters, 85, **2004**.
28. I. Ghebregziabher, K.C. Hartig, and I. Jovanovic, "Propagation distance-resolved characteristics of filament-induced copper plasma", Optics Express, 24, **2016**.
29. M. Rodriguez, R. Bourayou, G. Méjean *et al.*, "Kilometer-range nonlinear propagation of femtosecond laser pulses", Physical Review E, 69, **2004**.
30. D. Mirell, O. Chalus, K. Peterson *et al.*, "Remote sensing of explosives using infrared and ultraviolet filaments", JOSA B, 25, **2008**.
31. S. Tzortzakis, D. Anglos, and D. Gray, "Ultraviolet laser filaments for remote LIBS analysis: applications in cultural heritage monitoring", Optics letters, 31, **2006**.
32. S. Chin, H. Xu, Q. Luo *et al.*, "Filamentation "remote" sensing of chemical and biological agents/pollutants using only one fs laser source", Applied Physics B, 95, **2009**.
33. H. Xu, W. Liu, and S. Chin, "Remote time-resolved filament-induced breakdown spectroscopy of biological materials", Optics Letters, 31, **2006**.
34. K.C. Hartig, I. Ghebregziabher, and I. Jovanovic, "Standoff detection of uranium and its isotopes by femtosecond filament laser ablation molecular isotopic spectrometry", Scientific reports, 7, **2017**.
35. J.-F. Daigle, G. Méjean, W. Liu *et al.*, "Long range trace detection in aqueous aerosol using remote filament-induced breakdown spectroscopy", Applied Physics B, 87, **2007**.
36. J. Martin, M. Baudelet, M. Weidman *et al.*, "Stand-off detection of organic samples using filament-induced breakdown spectroscopy", Optics and Photonics in Global Homeland Security V and Biometric Technology for Human Identification VI, International Society for Optics and Photonics, **2009**.
37. E.J. Judge, G. Heck, E.B. Cerkez *et al.*, "Discrimination of composite graphite samples using remote filament-induced breakdown spectroscopy", Analytical Chemistry, 81, **2009**.
38. A.K. Shaik, and V.R. Soma, "Discrimination of bimetallic alloy targets using femtosecond filament-induced breakdown spectroscopy in standoff mode", Optics letters, 43, **2018**.

39. B. Zeng, T.-J. Wang, S. Hosseini *et al.*, "Enhanced remote filament-induced breakdown spectroscopy with spatio-temporally chirped pulses", JOSA B, 29, **2012**.
40. S.S. Harilal, J. Yeak, B.E. Brumfield *et al.*, "Consequences of femtosecond laser filament generation conditions in standoff LIBS", Optics express, 24, **2016**.
41. S.S. Harilal, J. Yeak, B.E. Brumfield *et al.*, "Dynamics of molecular emission features from nanosecond, femtosecond laser and filament ablation plasmas", Journal of Analytical Atomic Spectrometry, 31, **2016**.
42. A. Valenzuela, C. Munson, A. Porwitzky *et al.*, "Comparison between geometrically focused pulses versus filaments in femtosecond laser ablation of steel and titanium alloys", Applied Physics B, 116, **2014**.
43. H. Xu, J. Bernhardt, P. Mathieu *et al.*, "Understanding the advantage of remote femtosecond LIBS of metallic targets", journal of Applied Physics, 101, **2007**.
44. P. Skrodzki, M. Burger, and I. Jovanovic, "Transition of femtosecond-filament-solid interactions from single to multiple filament regime", Scientific reports, 7, **2017**.
45. Y. Yu, L.B. Guo, Z.Q. Hao *et al.*, "Accuracy improvement on polymer identification using LIBS with adjusting spectral weightings", Opt Express, 22, **2014**.
46. J. Serrano, J. Moros, and J.J. Laserna, "Exploring the formation routes of diatomic hydrogenated radicals using femtosecond laser-induced breakdown spectroscopy of deuterated molecular solids", Journal of Analytical Atomic Spectrometry, 30, **2015**.
47. J. Serrano, J. Moros, and J.J. Laserna, "Molecular signatures in femtosecond laser-induced organic plasmas: comparison with nanosecond laser ablation", Physical chemistry chemical physics : PCCP, 18, **2016**.
48. J. Serrano, J. Moros, C. Sánchez *et al.*, "Advanced recognition of explosives in traces on polymer surfaces using LIBS and supervised learning classifiers", Analytica chimica acta, 806, **2014**.
49. M. Boueri, V. Motto-Ros, W.Q. Lei *et al.*, "Identification of polymer materials using LIBS combined with artificial neural networks", Applied Spectroscopy, 65, **2011**.
50. V.K. Unnikrishnan, K.S. Choudhari, S.D. Kulkarni *et al.*, "Analytical predictive capabilities of Laser Induced Breakdown Spectroscopy (LIBS) with Principal Component Analysis (PCA) for plastic classification", RSC Advances, 3, **2013**.
51. A. Couairon, and A. Mysyrowicz, "Femtosecond filamentation in transparent media", Physics reports, 441, **2007**.
52. S. Harilal, N. Farid, J. Freeman *et al.*, "Background gas collisional effects on expanding fs and ns laser ablation plumes", Applied Physics A, 117, **2014**.
53. S.S. Harilal, J. Yeak, and M.C. Phillips, "Plasma temperature clamping in filamentation laser induced breakdown spectroscopy", Optics express, 23, **2015**.
54. X. Sun, S. Xu, J. Zhao *et al.*, "Impressive laser intensity increase at the trailing stage of femtosecond laser filamentation in air", Optics express, 20, **2012**.
55. R. Junjuri, S.A. Rashkovskiy, and M.K. Gundawar, "Dependence of radiation decay constant of laser produced copper plasma on focal position", Physics of Plasmas, 26, **2019**.
56. J.P. Singh, and S.N. Thakur, "Laser-induced breakdown spectroscopy", Elsevier**2007**.

CHAPTER 7 : Conclusions and future scope

This chapter comprehends the inferences derived from the research work carried out in the thesis as well as the future plan. It has primarily focused on the development of a portable, low-cost, LIBS system for the standoff and near filed applications. It includes the optimization of the experimental setup, evaluating it for a wide variety of samples, and finally exploring the different data analysis methods for improving the analytical performance. It has successfully demonstrated the rapid identification of explosives, explosives & non-explosives (in standoff mode at 6.5 m) and ten different types of plastics waste (in situ mode) using various machine learning algorithms. Further, it has proposed a new theoretical model for the understanding of the temporal evolution of LIP and validated with the experimental data. Also, it explored the investigation of fs and filamentation LIBS for in situ and futuristic standoff measurements respectively. Finally, it presents the future scope of the work.

7.1 Conclusions

The present thesis aimed at the development of a low-cost field-deployable LIBS & ST-LIBS system for the in situ identification of plastic waste and standoff detection of HEMs respectively. LIBS being an AES technique, working with these organic samples (explosives, and plastics, etc) is a challenging task as their elemental constituents (C, H, N, and O) are similar and all the spectra look almost identical with minute variations in spectral line intensities. Moreover, the entrainment of the ambient environment (humidity, N, and O) to the plasma complicates their identification, but it can be minimized by purging argon gas or utilizing the DP-LIBS approach. However, it is inevitable for real-time standoff measurements. Mechelle based ICCD spectrometer is considered as a workhorse for the LIBS detection system which offers the acquisition of time-resolved emissions and high spectral resolution however, the cost and size are the limiting factors to make it field deployable. At another extreme, non-gated CCD spectrometers are compact and cheaper nevertheless; the resolution is low and suffers from a continuum background. Hence, the performance of LIBS is evaluated for both the

spectrometers in view of classification approach by treating various data analysis methods. The following methods, such as ratiometrics, 2D scatter plots, the correlation between the number of bonds to the observed line intestines, PCA, and ANN are explored for understanding the correlation among the samples and classification. Further, feature selection based on the RF algorithm is utilized for the rapid identification which reduces the computational time by removing the irrelevant variables in the data. The following are the major conclusions of the present work

1. A theory of radiative relaxation mechanism is proposed for explaining the temporal evolution of the LIP and evaluated the performance. The experiment was performed for three different focal positions. The temporal studies revealed that the decay of the spectral line intensities at X_2 is faster than at X_o because the LIB occurs in ambient air above the sample surface. Consequently, less energy coupled to the sample, and the same is asserted by the mass ablation studies where the amount of ablated mass is minimum. At X_1 and X_o, the formation of laser-plasma begins directly on the sample surface and strong laser-plasma interaction is observed. Further, it is found that, observed spectral line intensities, electron density, and decay constant are linearly correlated with the corresponding ablated mass. However, a deviation is noticed for the plasma temperature at X_1 due to the plasma shielding. The plasma shielding increased the temperature of the plasma due to the reheating phenomenon at X_1. In order, to explain all these results a new theoretical model based on radiation cooling is proposed. The model not only considers the temperature alone but also includes the ablated mass and surface area of the plasma. It is demonstrated that the plasma temperatures obtained from the model are in good agreement with the temperatures reported from the experimental data. Further, the ablated mass is in order of magnitude consistent with the mass determined from the crater studies. *[Published in Physics of plasma, 2019[1]].*

2. The rapid identification of the ten types of plastics waste collected from the local recycling unit is demonstrated. TG-DTA and Raman spectroscopy studies have confirmed the identity of the samples. Ratiometric and correlation analysis have given limited results for the classification albeit PCA has shown excellent clustering among the samples. Further, identification rates up to ~99 % are achieved with ANN. The

analytical performance of LIBS with the ICCD in the accumulation of ten shots is similar to the CCD spectrometer in a single-shot acquisition. Nevertheless, reduction of the analysis time by more than one order is achieved with the CCD compared to the ICCD. Further, the ANN analysis based on feature selection drastically reduced the investigation time without losing the identification accuracy which favors rapid identification. Finally, the detector/collection system size, weight, and cost also can be reduced by ~ 10 times by employing a CCD spectrometer which can be utilized in making a compact and low-cost LIBS system for the rapid identification in real-time measurements. *[A part of this published in Polymer testing, 2019[2], and under review in Waste management].*

3. The development of the ST-LIBS system is demonstrated for the identification of the HEMs. Initial, studies were performed on a set of five HEMs at 1 m distance using a Mechelle spectrometer equipped with ICCD. The atomic ratios have shown a good correlation with the actual stoichiometric ratios and an excellent classification has been attained with PCA. Further, the ST-LIBS measurements were performed on a set of five HEMs and nineteen non- HEMs by extending the standoff distance to 6.5 m. A single lens and a small handheld CCD spectrometer were utilized for collecting the optical radiation which mimics a compact portable system for real-time measurements. The optimization of the focusing system has resulted in an increase of spectral line intensities by more than an order. Later, the collection system efficiency has improved by four times with the proper optimization of f-number. Further, 2D scatter plots and PCA have demonstrated an excellent separation among the HEMs as well as HEMs & non-HEMs. The identification rates of ~94 and ~98 % were demonstrated for HEMs and HEMs & non-HEMs respectively. *[Published in Defense science Journal, 2017 [3] and Optik 2020 [4]].*

4. Femtosecond (fs) LIBS is explored for the first time for the discrimination of the plastics waste to the best of our knowledge. Strong molecular features of CN violet and C_2 swan bands were observed in the spectra along with the atomic emission lines of C, H, N, and, O. A strong positive linear correlation (Pearsons'r=0.90) is observed between the spectral features of the molecular bands CN and C_2. It is attributed to the fs ablation,

where lower temperature plasma favors the formation of molecular species. An efficient clustering has been achieved with the PCA where the emission lines of molecular species predominantly contributed to their discrimination. The ANN analysis has revealed that the identification rates up to 100 % can be achieved. Further, filamentation LIBS studies were performed on the Cu target with different filaments generated by different focal length lenses. The results revealed that spectral emissions are stronger at the middle part of the filament and persisted for a longer time compared to the other parts and for all the filaments. The variations in the spectral line intensities and persistence time are attributed to the differences in the temperature of the filaments at different positions. It is found that the temperatures and electron densities of the filaments are decreased by increasing the focal length of the filaments. *[A part of this published in Journal of Analytical Atomic Spectrometry, 2019 [5]].*

7.2 Future scope

1. The theoretical model proposed for explaining the temporal evolution of the LIP should be evaluated for the following conditions for improving the performance.

a) It is assumed that the surface area of the plasma plume is similar for the three focal conditions however it should be measured experimentally. The surface area can be estimated from the self-emission images or the shadowgraphy experiments.

b) Moreover, mass ablation studies need to be performed for a single laser shot instead of the ten shots irradiated at one place as the sample surface shifts for each shot.

c) Further, it should be verified for the following conditions for the generalization of the model. (i) Same sample with different excitation energies, (ii) energy with different samples, (iii) Vary laser wavelengths, and ambient conditions such as gas and pressure (iv) For fixed laser energy, vary the lens to sample distance significantly.

2. The identification of the plastics using LIBS needs to be explored for the wide range of samples including e-waste which has great potential for the reuse. Different additives are added in the manufacturing of the plastics to improve strength, reduce cost, and modify color. Hence, a study on the effect of additives on the classification accuracy is required

and their quantification is helpful for the industrial applications. In the present study, the dust layer/debris on the sample surface is removed by cleaning it in water however, it can be performed by using a 'cleaning shot' with the laser beam which is crucial for the real-time measurements and it also increases the analysis speed. A study on the conveyor belt model sample movement is desirable for the realtime investigation of the samples.

3. The standoff detection of HEMs has been demonstrated up to 6.5 m distance due to space constraints in the lab and to be extended for longer distances in the future. However, increasing the probing distance has an inevitable signal loss and proper optimization is further required. For the present study, the experiment has been performed on samples in pellet form nevertheless actual scenario demands the identification of HEMs in trace quantities. Also, the trace identification on different substrates is essential for mimicking the real-time measurements. Further, a wide range of HEMs, potentially interferent non HEMs, HEM mixtures, and their traces need to be identified for creating a standard library which is critical for the real-time application. The current ST-LIBS setup comprises two separate geometries for the collection and focusing systems and it needs to be integrated into one system with a collinear configuration. Therefore, focusing the laser beam and plasma emissions can be collected by the same path for various standoff distances. Moreover, the collection system should be changed into reflective mode by using a set of convex and concave mirrors which can avoid the aberrations observed due to the transmissive optics.

4. Further, enhancing the detection efficiency of the current CCD spectrometer in the 230-360 nm range can improve the performance of the LIBS for the identification of the samples (HEMs and plastics). As it covers the emission line of carbon at 247.85 nm which present in all the organic samples and also the strongest feature among most of the lines with the least contribution from the air. Hence, the inclusion of the carbon line (it is not present the spectra acquired with current CCD spectrometer) is beneficial for the analysis of HEMs and plastics. Also, exploring the various LIBS data analysis and cross-validation methods is encouraged for attaining the robust classification. The experimental configuration should be changed for the autofocusing conditions for

creating the plasma on the sample surface. It is essential for the identification of a wide range of samples with different geometrical shapes and sizes.

5. Fs LIBS is utilized for the identification of the set of five plastics and it requires further studies on more number of samples. A systematic investigation on the effect of number native bonds of the analyte (C-C, C=C, CN) to different emission lines (C, N, CN, and C_2) of the plasma is essential to understand complex plasma formation pathways. It would be beneficial if the experiment is performed in the different atmospheres (Ar, O, and N gas) so one can infer the correlation among the different species of the plasma and the effect of ambiance can be interpreted. Further, filamentation LIBS has a great potential to work in a standoff regime at longer distances. In the current study, the effect of different filaments on the spatiotemporal evolution of the Cu plasma is investigated. This interrogation can be extended by generating different filaments by changing the chirp, pulse duration, and wavelength of the laser. Consequently, their effects on the LIBS plasma will enable the development of an efficient technique for ST analysis of samples in different applications, for example, monitoring of HEMs for civilian security, plastics –recycling, calcified tissues-archelogy, and monitoring of impurities –steel industry, etc.

6. Finally, the hyphenation of LIBS and Raman techniques provides complimentary spectral information to each other. i.e. LIBS gives the elemental information of the samples whereas fingerprint molecular information can be obtained by the Raman studies. Hence, multiplexing both the spectral data leads to the efficient identification of the samples. However, the Raman signal is very weak and LIBS has matrix effects hence the proper optimization is necessary for accurate results. Moreover, integration of both into one system with a single-pulse excitation source requires numerous efforts in the experimentation. For example, the Raman signal only lasts for tens of ns as the pulse duration of the laser is typically 10-30 ns (for the ns laser) hence more excitation energy is required for attaining the higher signal, albeit it leads to the ablation of material. Further, the optimization of the gate delay and gate width is critical and the effect of fluorescence should be considered otherwise it deteriorates the performance.

7.3 References

1. R. Junjuri, S.A. Rashkovskiy, and M.K. Gundawar, "Dependence of radiation decay constant of laser produced copper plasma on focal position", Physics of Plasmas, 26, **2019**.
2. R. Junjuri, C. Zhang, I. Barman *et al.*, "Identification of post-consumer plastics using laser-induced breakdown spectroscopy", Polymer Testing, 76, **2019**.
3. R. Junjuri, M.K. Gundawar, and A.K. Myakalwar, "Standoff Detection of Explosives at 1 m using Laser Induced Breakdown Spectroscopy", Defence Science Journal, 67, **2017**.
4. R. Junjuri, A.P. Gummadi, and M.K. Gundawar, "Single-shot compact spectrometer based standoff LIBS configuration for explosive detection using artificial neural networks", Optik, 204, **2020**.
5. R. Junjuri, and M.K.K. Gundawar, "Femtosecond laser induced breakdown spectroscopy studies for the identification of the plastics", Journal of Analytical Atomic Spectrometry, **2019**.

List of publications

1. ***Rajendhar Junjuri***, S.A. Rashkovskiy, M.K. Gundawar, "Dependence of radiation decay constant of laser produced copper plasma on focal position", Physics of Plasmas **26**(12) 122107 (2020). **(Chapter 3)**

2. ***Rajendhar Junjuri***, C. Zhang, I. Barman, M.K. Gundawar, "Identification of post-consumer plastics using laser-induced breakdown spectroscopy", Polymer Testing **76** 101-108 (**2019**). **(Chapter 4)**

3. ***Rajendhar Junjuri***, M.K. Gundawar, A.K. Myakalwar, "Standoff Detection of Explosives at 1 m using Laser Induced Breakdown Spectroscopy", Defence Science Journal **67**(6) 623 (**2017**). **(Chapter 5)**

4. ***Rajendhar Junjuri***, A. Prakash Gummadi, M. Kumar Gundawar, "Single-Shot Compact Spectrometer Based Standoff LIBS Configuration For Explosive Detection Using Artificial Neural Networks ", Optik 163946, (**2020**). **(Chapter 5)**

5. ***Rajendhar Junjuri***, M.K. Gundawar, "Femtosecond laser-induced breakdown spectroscopy studies for the identification of plastics", Journal of Analytical Atomic Spectrometry **34**(8) 1683-1692 (**2019**). **(Chapter 6)**

6. ***Rajendhar Junjuri***, Akash Kumar Tarai, Akshay Dhobley, and Manoj Kumar Gundawar, Identification of the calcified tissues using LIBS, WRAP 2019, Conference proceedings, (**2020**).

7. ***Rajendhar Junjuri***, G.M. Kumar, "Laser Produced Plasma Diagnosis for Classification of Optical Isomers", International Conference on Fibre Optics and Photonics, Optical Society of America, (**2016**), p. W3A. 34.

8. ***Rajendhar Junjuri***, Arun Prakash Gummadi, Manoj Kumar Gundawar, Identification of the explosive mixtures using LIBS, ICOL-2019, Conference proceedings (In Press)

Co-authored publications

9. Jakub Vrábel, Erik Kepes, Ludovic Duponchel, Vincent Motto-Ros, Cécile Fabre, Sven Connemann, Frederik Schreckenberg, Paul Prasse, Daniel Riebe, ***Rajendhar Junjuri***, Manoj Gundawar, Xiaofeng Tan, Pavel Porizka, Jozef Kaiser, Classification of challenging LIBS soil sample data - EMSLIBS contest, Spectrochimica Acta Part B: Atomic Spectroscopy, 2020. **(EMSLIBS contest publication- I secured 4th position in the data analysis competition)**

10. Arun Prakash Gummadi, ***Rajendhar Junjuri***, and Manoj Kumar Gundawar, Development of picosecond Standoff LIBS system for the identification of the metals and alloys, (WRAP 2019, Conference proceedings), (**2020**).

11. Eshita MAL, ***Rajendhar Junjuri,*** Manoj Kumar Gundawar, Alika Khare, Temporal characterization of laser induced plasma of tungsten in air, Laser and Particle Beams. 1-11, (**2020**).

12. P. Thomas, ***Rajendhar Junjuri***, N. Joy, M. Siemer, M.K. Gundawar, R. Philip, K. Al-Shamery, G.P. Joseph, "Influence of MnCl2 on the properties of an amino acid complex single crystal-l-arginine perchlorate (LAPCl) for optical limiter applications", Journal of Materials Science: Materials in Electronics **30**(9) 8407-8421 (**2019**).

13. P. Thomas, G.C. Jose, V.R. Mathew, P. Dominic, ***Rajendhar Junjuri***, R. Philip, M.K. Gundawar, G.P. Joseph, "Tuning the optical, electrical and thermal properties of l-arginine maleate dihydrate (LAMD) single crystals for optical limiter applications", Journal of Materials Science: Materials in Electronics **30**(18) 17322-17332 (**2019**).

14. E. Mal, ***Rajendhar Junjuri***, M.K. Gundawar, A. Khare, "Optimization of temporal window for application of calibration free-laser induced breakdown spectroscopy (CF-LIBS) on copper alloys in air employing a single line", Journal of Analytical Atomic Spectrometry **34**(2) 319-330 (**2019**).

15. S.K. Anubham, ***Rajendhar Junjuri***, A.K. Myakalwar, M.K. Gundawar, "An Approach to Reduce the Sample Consumption for LIBS based Identification of Explosive Materials", Defence Science Journal **67**(3) 254 (**2017**).

Under Review:

1. ***Rajendhar Junjuri***, Manoj Kumar Gundawar, A low-cost LIBS detection system combined with chemometrics for rapid identification of plastic waste, March 2020, Waste management. **(Chapter 4).**

2. Akash Kumar Tarai, ***Rajendhar Junjuri***, S.A. Rashkovskiy, M.K. Gundawar, "A Simple intensity ratio based approach for modelling the temporal dynamics of laser produced plasma", June (2020), Physics of Plasmas.

Under Preparation

1. ***Rajendhar Junjuri,*** Samuel Anurag, E. Manikanta, Srikantaiah Sree Harsha, P. Prem Kiran, Manoj Kumar Gundawar, "Spatial and temporal characterization Cu plasma produced by femtosecond filaments" **(Chapter 6).**

Awards/Achievements

1. **Secured top 4th position globally** in LIBS data analysis competition conducted by the Euro-Mediterranean Symposium on Laser-Induced Breakdown Spectroscopy (EMSLIBS) 2019 organizing committee in the conference. **September 2019**, Brno, Czech Republic.

2. **Received DST-SERB, India travel grant** to present research work at 10th EMSLIBS 2019, **September 2019**, Brno, Czech Republic.

3. **Best Oral presentation Award** entitled paper "Femtosecond and nanosecond LIBS Studies of Postconsumer Plastics", **Feb-2018**, MeghnadSaha Memorial International Symposium-cum-Workshop on LIBS -2018, University of Allahabad, Allahabad.

4. **Best poster Award** entitled paper "Laser Induced Breakdown Spectroscopy (LIBS) based standoff detection of explosives", **April -2015**, Recent Advances in optics conference, UOH, Hyderabad

Workshops/Schools selected

1. "DST-SERB School on Ultrahigh Intensity Laser Produced Plasmas: Physics and Applications" organised during **7– 25h Jan-2018**, RRCAT, Indore

2. "Horiba optical school", organised during **22- 26th May-2017**, Jointly Organized by JNCASR, Bangalore and HORIBA Scientific Group

3. "2nd Hands-on course on Optical Instruments Technology", organised during **22– 26th Feb-2016**, CSIR- Central Scientific Instruments Organisation, Chandigarh

Oral presentations in conferences:

1. ***Rajendhar Junjuri,*** and Manoj Kumar Gundawar, Femtosecond and nanosecond LIBS Studies of Postconsumer Plastics, **Jan-2018**, MeghnadSaha Memorial International Symposium-cum-Workshop on Laser Induced Breakdown Spectroscopy -2018.

2. ***Rajendhar Junjuri,*** G. Manoj Kumar, Identification of Explosives using Standoff LIBS Combined with Multivariate Analysis, **Nov-2017**, HEMCE 2017 international conference.

Conference presentations- poster (National and International):

1. ***Rajendhar Junjuri***, Akash Kumar Tarai, Akshay Dhobley, and Manoj Kumar Gundawar, Identification of the calcified tissues using LIBS, **December 2019,** WRAP 2019, IIT Gouhathi.

2. **Rajendhar Junjuri,** G. Arun Prakash and G. Manoj Kumar, Identification of the explosive mixtures using laser induced breakdown spectroscopy (LIBS), **Oct-2019**, International Conference on Optics & Electro-Optics, XLIII Symposium of Optical Society of India. Dehradun, Uttarakhand (INDIA).

3. **Rajendhar Junjuri,** and G. Manoj Kumar, Rapid identification of the plastics using laser-induced breakdown spectroscopy (LIBS), **Sep-2019**, 10th Euro-Mediterranean Symposium on Laser-Induced Breakdown Spectroscopy, Brno University of Technology, Czech Republic.

4. ***Rajendhar Junjuri,*** G. Arun Prakash and G. Manoj Kumar, Standoff detection of explosives using compact LIBS setup, **Dec-2018**, National Laser Symposium-27. RRCAT, Indore

5. ***Rajendhar Junjuri,*** G. Manoj Kumar, Combined Raman and Laser Induced Breakdown spectroscopy for Identification of post-consumer plastics, **Dec-2017,** National Laser Symposium-26, BARC, Mumbai.

6. ***Rajendhar Junjuri,*** G. Manoj Kumar, Identification of Explosives using Standoff LIBS Combined with Multivariate Analysis, **Nov-2017,** 11th International High Energy Material Conference and Exhibits, HEMRL-Pune.

7. ***Rajendhar Junjuri,*** G. Manoj Kumar, Classification of recyclable plastics using Femtosecond Laser Induced Breakdown spectroscopy, **Nov-2017**, UFS, University of Hyderabad.

8. ***Rajendhar Junjuri,*** G. Manoj Kumar, Laser Produced Plasma Diagnosis for Classification of Optical Isomers, **Nov-2016**, The International Conference on Fiber Optics and Photonics, IIT –Kanpur.

9. ***Rajendhar Junjuri,*** Ashwin Kumar Myakalwar, G. Manoj Kumar Detection of Explosives at 1 Meter with Laser Induced Breakdown Spectroscopy, **Dec-2016,** 25th National Laser Symposium, KIIT- Bhubaneswar.

10. ***Rajendhar Junjuri,*** Ashwin Kumar Myakalwar and G. Manoj Kumar, Laser Induced Breakdown Spectroscopy (LIBS) based standoff detection of explosives, **April -2015**, Recent Advances in optics conference.

11. Arun Prakash Gummadi, ***Rajendhar Junjuri***, and Manoj Kumar Gundawar, Development of picosecond Standoff LIBS system for the identification of the metals and alloys, **December 2019**, WRAP 2019, IIT Gouhathi.

12. Eshita Mal, ***Rajendhar Junjuri,*** Manoj Kumar Gundawar and Alika Khare, Quantitative analysis of Brass using Calibration-Free Laser Induced Breakdown Spectroscopy (CF-LIBS) Technique in Air, **Dec-2018,** National Laser Symposium-27, RRCAT-2018

13. Eshita Mal, ***Rajendhar Junjuri,*** Manoj Kumar Gundawar and Alika Khare, Spectroscopic Characterization of Laser Induced Molybdenum Plasma in Air, **Feb-2018**, MeghnadSaha Memorial International Symposium-cum-Workshop on LIBS -2018. University of Allahabad, Allahabad.

14. Arnab Sarkar**,** ***Rajendhar Junjuri,*** G. Manoj Kumar and Manjeet Singh, Simulation of laser induced breakdown molecular spectra to calculate rotational and vibrational temperature of molecular species, **Dec-2017,** National Laser Symposium-26, BARC, Mumbai.

15. Eshita Mal, ***Rajendhar Junjuri,*** Manoj Kumar Gundawar and Alika Khare, Characterization of Laser Produced Tungsten Plasma in air using Time-resolved Laser Induced Breakdown Spectroscopy (LIBS), **Dec-2017,** National Laser Symposium-26, BARC, Mumbai.

16. Ashwin Kumar Myakalwar, ***Rajendhar Junjuri***, and Manoj Kumar Gundawar, Explosive Identification: Unfolding the requirements for a LIBS Device, **Feb-2016,** 10th International High Energy Material Conference and Exhibits. Hyderabad

Nanosecond, femtosecond (fs) and fs filamentation LIBS studies combined with machine learning for the identification of plastic waste and standoff detection of HEMs

by Rajendhar Junjuri

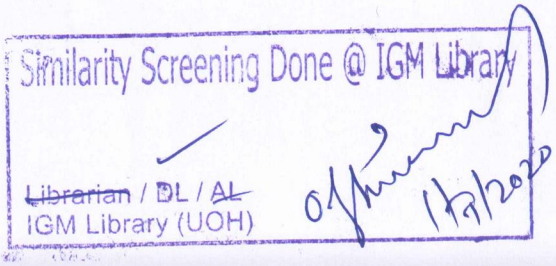

Nanosecond, femtosecond (fs) and fs filamentation LIBS studies combined with machine learning for the identification of plastic waste and standoff detection of HEMs

ORIGINALITY REPORT

33%	9%	29%	7%
SIMILARITY INDEX	INTERNET SOURCES	PUBLICATIONS	STUDENT PAPERS

PRIMARY SOURCES

1	Rajendhar Junjuri, Arun Prakash Gummadi, Manoj Kumar Gundawar. "Single-shot compact spectrometer based standoff LIBS configuration for explosive detection using artificial neural networks", Optik, 2020 Publication	11%
2	Rajendhar Junjuri, Manoj Kumar Gundawar. "Femtosecond laser-induced breakdown spectroscopy studies for the identification of plastics", Journal of Analytical Atomic Spectrometry, 2019 Publication	6%
3	aip.scitation.org Internet Source	6%
4	Submitted to Florida International University Student Paper	3%
5	Rajendhar Junjuri, Chi Zhang, Ishan Barman, Manoj Kumar Gundawar. "Identification of post-	1%

1/7/2020 (1/6)

1/7/2020 (2/6)

Similarity Screening Done @ IGM Library
Librarian / DL / AL
IGM Library (UOH)
1/7/2020

1/7/2020 (3/6)

1/7/2020 (4/6)

1/7/2020 (5/6)

It is certified that S No.s 1-5 and 7 belong to Student's own publications.

Dr.G. Manoj Kumar
Advanced Centre of Research in High Energy Materials
University of Hyderabad
Hyderabad-500 046. Telangana, India

1/7/2020

consumer plastics using laser-induced breakdown spectroscopy", Polymer Testing, 2019
Publication

6	Submitted to University of Hyderabad, Hyderabad Student Paper	1%
7	Rajendhar Junjuri, Sergey A. Rashkovskiy, Manoj Kumar Gundawar. "Dependence of radiation decay constant of laser produced copper plasma on focal position", Physics of Plasmas, 2019 Publication	1%
8	Submitted to Higher Education Commission Pakistan Student Paper	1%
9	epdf.tips Internet Source	<1%
10	"Laser-Induced Breakdown Spectroscopy", Springer Science and Business Media LLC, 2014 Publication	<1%
11	Rajendhar Junjuri, Akash Kumar Tarai, Arun Prakash G, Akshay Dhobley, Manoj Kumar Gundawar. "Identification of the calcified tissues using laser induced breakdown spectroscopy", 2019 Workshop on Recent Advances in	<1%

6/6

1/7/2020

Dr.G. Manoj Kumar
Advanced Centre of Research in High Energy Materials
University of Hyderabad
Hyderabad-500 046. Telangana, India